Modelling foam flow through confined geometries

PhD Thesis

Carlos Torres-Ulloa PhD Student

Supervisor: Paul Grassia

Department of Chemical and Process Engineering

University of Strathclyde, Glasgow

July 28, 2021

Abstract

Despite their apparent simplicity, multiphase fluids such as liquid-foam exhibit a very rich dynamics, which is often difficult to predict, much more so than would be the case for single-phase fluids. The physics of liquid foams can be hard to capture mathematically, even in static and equilibrium systems. As external forces are applied on the foam structure, driving the system into motion, the amount of required information to characterize the system also increases, depending on factors such as the number of individual bubbles, and the geometry of the system's container. This work takes a step forward into expanding the understanding of the nature of liquid-foam, where its physics, methods and techniques used to model its dynamics, and possible applications are reviewed. Two related models for modelling macroscale and bubble-scale liquid-foam dynamics, respectively, are further analysed. The first of these is the pressure-driven growth model, which aims to capture the location over time of a two-dimensional foam front propagating through a porous medium, in the context of foam improved oil recovery, particularly in the surfactant alternating gas process. It is shown that this model admits solutions containing sharp corners or kinks, in which a foam front reorients over a length scale small compared with the distance over which the front has propagated. The second of these is the viscous froth model, which is used to model bubble-scale foam flow of a layer of bubbles in a channel between closely-spaced parallel flat plates, and hence is a two-dimensional foam model. It is shown that this model admits topological transformations in which sets of bubbles flowing in a channel exchange neighbours as the flow velocity increases.

Acknowledgements

I would like to thank and acknowledge my supervisor Dr Paul Grassia, mainly for giving me the opportunity of working with him and helping me on my academic path, even before I started my PhD studies with him. I am grateful for his dedication, patience, and empathy. He has always had a kind and efficient way of explaining difficult concepts and providing valuable and useful feedback.

I also would like to thank the staff in the Department of Chemical and Process Engineering. They have been of great help towards my PhD studies, both before and during the process. I also would like to acknowledge all my PhD colleagues, for their help, for sharing experiences, and guidance during the process.

I would like to express my gratitude to my parents, grandparents, siblings, and all my family who in one way or another, even at a distance, were always present. I would like to thank my fiancée, who always had the correct words to encourage me in the process, for her patience, and mainly for make me happy. To my fiancée's parents for always being present, I say thank you.

Having the opportunity of learning everyday is a priceless privilege that I deeply value. Therefore, I would like to thank life, and all the things that have happened, and have taken me to this stage of my journey.

Finally, and not less important, I would like to express my gratitude to ANID Becas-Chile for funding my PhD studies. I also acknowledge to Universidad Católica de Temuco for supporting me all these years.

Contents

List of Figures

List of Tables

Chapter 1

Introduction

Bubbles, consisting of gas dispersed in liquid, play an important but not always noticeable role in people's daily life. They are present in different size scales in food, in drinks, and in many domestic tasks. People are used to having them around and interact naturally with them, as with many other multiphase substances, suspensions, powders, emulsions, aerosols, amongst others. However, understanding the physics and dynamics behind the behaviour of these substances can be challenging, particularly due to their multiphase nature [1–3]. Bubbles, as we have said, consist of a gas phase dispersed inside a liquid phase, where the liquid fraction is generally less than the gas fraction [1, 4]. Using nothing more sophisticated than water and soap (a detergent or any other surfactant), bubbles can be easily created. The mechanisms to make bubbles including mixing or agitation, release of a dissolved gas (due to a change in temperature, pressure, or as an effect of a catalyst), and blowing gas through a liquid [5]. Nonetheless, it might be complicated to make them exactly with some desired size characteristics, and even more, to keep them in that state for long periods of time [6, 7]. The lifetime of bubbles depends on factors such as surfactant concentration, liquid drainage rate, film thinning processes (that lead to film rupture), gas diffusion (leading to coarsening), surface tension distribution, external stresses, capillary

pressure, amongst others, as will be discussed later [5, 7]. Bubbles are by their nature unstable entities, they shrink, stretch or burst easily [5, 8, 9].

What makes it possible to enclose gas within a thin liquid interface is the presence of surfactants. Surfactants (surface-active agents) are amphiphilic molecules, i.e. they are comprised of both a hydrophobic and a hydrophilic group in the same molecule [10]. In fluids, when surfactants are in low concentrations they diffuse predominantly onto the fluid surface, decreasing the minimum free energy necessary to create that interface [11]. Generally, the hydrophilic group of these molecules is directed to the (aqueous) liquid phase, while the hydrophobic group is directed to the gas. In bubble films, surfactants maintain structural stability by exerting a disjoining pressure at both sides of the gas-liquid interface [10], which opposes both the capillary pressure (that sucks liquid out of the films) and attractive van der Waals forces [12]. Surfactants give stability to bubbles, and therefore, pure liquids cannot generate bubbles so easily. In fact, when a gas is injected below the surface of a pure liquid, it dissipates to the air as soon as it reaches the surface [10]. If the liquid contains surfactant however, as the gas-liquid interface is perturbed by the injected mass of gas (bubble), it expands exhibiting elasticity, where as a result of the Gibbs-Marangoni effect, the surfactant concentration in that expanded interface (now the bubble film) reaches a new equilibrium state locally [11, 13]. Surfactants therefore move and redistribute inside and along the bubble films as an effect of surface tension gradients [14, 15]. The majority of surfactants are organic in character, and a wide range of them can be found in nature, hence the reason why bubbles can be seen in various media, e.g. rivers, sea water, produced by animals and/or plants [10]. The capacity of a liquid to generate bubbles can be seen as a direct measure of how much organic load this contains [13]. In these sorts of situations, bubbles within liquid are regularly grouped together in bulk, i.e. many of them

packed together, which is called foam or more specifically liquid-foam [9].

1.1 Physics of liquid-foam

The study of liquid-foam had already drawn the attention of scientists by the 19th century. Therefore, by late that century, several studies on liquid-foam and its applications had already been carried out [1]. However, many of these works were focused more on empirical observation rather than theoretical analysis: a more systematic approach however was pioneered by the physicist Joseph A. F. Plateau in 1876 [1]. In his research Plateau studied the inner geometry of bubbles, finding a very complex system [1]. Plateau discovered that a static soap film consists of an unbroken smooth surface that always seeks to reach a minimum energy state, which corresponds to the minimum surface area necessary to balance the pressure difference across the film with the film's curvature. Film curvature when coupled to the effect of the surface tension produces a force and this is what then balances the force associated with pressure difference. This was later corroborated by Taylor [16,17], who proved that the so-called Plateau's rules for foam structure are a consequence of the minimization of the interfacial energy [1, 9, 18]. In addition, Plateau found that the (mean) curvature at any location on a static bubble film surface is uniform. Moreover, when bubbles with a uniform surfactant concentration are attached together, i.e. in a foam system, soap films meet three by three at the edges, subtending an angle of 120° (or $\pi/3$). These edges are called Plateau borders, and they also meet at a four fold vertex subtending an angle of 109.47° [5]. Based on Plateau's studies, many research articles have emerged through the years, greatly expanding the knowledge about the configuration of liquid-foam [2, 5, 15, 19–24].

1.1.1 Liquid-foam structures

As was mentioned before, liquid foams consist of a gas dispersion contained in a liquid and surfactant solution. Depending on how bubbles are created, the foam structure can be organized in a wide range of length scales, the typical size of bubbles being in a range of $10\,\mu$m–$1\,$cm [9]. Foams comprised of bubbles of different sizes are known as polydisperse systems, while in a monodisperse system the bubbles sizes are equal [25]. Depending on the liquid fraction F_l and the bubble size distribution of the foam, the system can exhibit different structures. In the dry limit, $F_l \ll 1$, the bubbles take a polyhedral cell form with curved faces, satisfying Plateau's rules [25]. In contrast for larger F_l, bigger than the close packing limit ($F_l \approx 0.36$ for monodisperse foams and $F_l \approx 0.26$ typically for polydisperse foams [18]), the system is found to behave as a bubbly liquid. For F_l less than the close packed limit but not $\ll 1$, the foams are called wet foams [25], and bubbles tend to be only slightly perturbed from spherical. Close to the dry limit however, the equilibrium structure of the foams is described by Plateau's rules as we have said [5, 18, 25].

1.1.2 Instabilities of liquid-foam

The instability of liquid-foam is a consequence of the large interfacial energy associated with dispersing gas in liquid, which is proportional to the surface area [5, 9, 25]: adding surfactant reduces the surface energy per unit of area, but energy still remains large provided the area is large. Complex dynamics result from foams seeking to reduce their interfacial energy [25]. In the absence of an external stress, the liquid-foam structure evolves over time as a consequence of a number of coupled processes (also known as ageing processes) [18]. First, since Plateau borders (edges where films meet) consist of micro channels, liquid can flow through the channel network from the top to the bottom as an effect

of gravity, a process which is known as foam drainage [5, 26, 27]. This process makes the foam dry at the top of the structure and wet at the bottom. As the liquid within the foam flows down, surfactant can potentially be carried away with it, increasing the attractive forces between each side of the films [5, 28]. This can change the film stability. Therefore, if the surfactant concentration is not sufficient to maintain the film stability, foam films between bubbles will break generating bigger bubbles [18]. This is known as foam coalescence or film rupture. Another factor affecting the bubble lifetime is the capillary pressure. Generally the capillary pressure is quantified in terms of the curvature between the liquid and the gas phase at the Plateau borders [5]. Specifically, the capillary pressure corresponds to the pressure difference between the gas and the liquid phase there. Low capillary pressures favour stability, while higher capillary pressures (which tend to suck liquid from films to Plateau borders) make the system susceptible to film rupture for any small perturbation [29]. The last ageing process is known as (diffusive) coarsening, which is governed by the von Neumann's law [30], and takes place when the gas diffuses between the bubbles owing to the pressure difference across the films. This pressure is known as Laplace pressure and can be expressed as a ratio of the surface tension σ to the mean curvature radius r as $\Delta P = 2\sigma/r$ [1]. These processes lead to periodic bubble rearrangements, which help to relax the interfacial energy. The rate at which these processes occur decreases as the foam ages [25].

1.1.3 Moving away from the static structure

Static foams manage to find an equilibrium state in which structures are determined via total area minimization, following Plateau's laws. These constraints on film meeting angles can be considered to apply even when the foam is set into motion [24]. Even though liquid foams are comprised of two fluids (generally Newtonian), their behaviour is non-Newtonian, exhibiting different mechanical

properties depending on different external applied forces [5, 19, 31–33]. For low applied stress the foam behaves like a solid, in contrast, for high applied stress beyond the yield stress, the foam behaves like a viscous non-Newtonian fluid [9,32]. The yield stress point varies as a function of the liquid fraction F_l, being bigger in the dry limit ($F_l \ll 1$) and lower for wet foams. As the stress rises towards the yield stress point, the foam behaves like a plastic solid. As foam moves, the individual gas-liquid interfaces or films may either increase their size or else decrease their size until disappearing, leading to rearrangements of the structure, also called topological transformations [5,19,32]. Rheological complexity thereby results as a consequence of the evolution of the microstructure of the foam [21].

When the films deform, surface energy increases, producing stress. In order to compute the films' energy and the stress they produce, it is necessary to know in detail the films' positions, areas, orientations, and shapes. In fully three-dimensional foam models, it is computationally expensive to determine the films' energy and stress, owing to the very considerable topological and geometric complexity of the system [20]. Nevertheless, this complexity can be reduced by studying the foam system as a collection of interconnected foam monolayers confined between two glass plates with a small separation (known as a Hele-Shaw cell), which gives a quasi-two-dimensional foam structure. This is addressed in detail in section 2.2.

1.1.4 Topological transformations

A topological transformation can be described as a bubble neighbour exchange, and can occur in principle via various distinct mechanisms [32]. If a bubble film breaks as a consequence of the ageing process (as described above), the structure will experience stress i.e. the equilibrium structure will be perturbed, where a dissipative process typically associated with the viscous forces will start to

relax the structure [19]. The system will seek to reach a new equilibrium configuration, minimizing the total surface energy, measured as the total interfacial surface area [5]. This process can lead in turn to topological changes [34]. On the other hand, if an external constant force is applied to the system, the foam structure will deform, while at the same time, viscous forces will try to reach a new equilibrium state (a minimum energy state) [19]. If the applied force is low enough, the foam will be essentially always at local mechanical equilibrium without topological change [19], even though deformed relative to the stress free state. In contrast, when the force is bigger, topological transformations occur. Moreover when the flow rate that it induces is bigger than the relaxation rate, films will be in constant deformation [19, 33]. As the deformation rate increases, the system energy will keep increasing [24]. In this case, different bubbles will move at different speeds, relative to their container, and in some cases even in different directions. In both situations (i.e. slow deformation and fast deformation) some films will shrink while others will stretch, although the amount of shrinking/stretching tends to be greater for larger forces and faster deformations. In the case where films shrink, eventually they can go to zero area. A collision of films and/or Plateau borders and/or vertices then takes place, which then immediately disassociate into the surrounding bubbles, in concordance with Plateau's rules [35]. A new film and/or new Plateau border can also be created in place, but now connecting different bubbles. In the various cases described above therefore, the foam structure undergoes topological transformations (bubble neighbour exchanges), which help to relax the system energy [5, 19].

1.2 Liquid-foam applications

Foam's mechanical properties such as high effective viscosity, low mobility, and high elasticity, which depend on factors like liquid fraction, bubble size distribu-

tion, bubble stability, and liquid composition, make them ideal working fluids for a wide range of industrial applications such as for example: mining/minerals processing, food and cosmetics, production of glass, foam fractionation, firefighting, as well as pharmaceutical and medical processes [3, 3, 5, 11, 32, 36–38]. In general these applications can be found in separation processes, stabilisation processes, control and active transport of microscale elements, as a contrast agent and also as a driving fluid. Various of these are reviewed below. Specifically, and what is studied in the present thesis, are applications which involve foam flow through confined channels (e.g. in a porous media). We will come back to this point later.

Foam fractionation, is a separation process which uses bubbles to remove a pollutant (organic waste), particles or material from a liquid solution. In this process, gas is typically injected from the bottom of the liquid's container. Since the liquid contains surfactant, this helps to stabilize the gas-liquid interface, generating bubbles [39]. As bubbles flow up due to buoyancy force (density difference between liquid and gas), particles and/or surface active species adhere on their surfaces [39–41]. The type of surfactant and gas used in each case depends on the nature of the process [40]. In the mining industry for example, a related process known as froth flotation operates on the same principle. Bubbles are used to extract mineral particles of interest from a liquid slurry. The minerals to be recovered are ultimately collected from the bubbles [42–45].

Foams are also used in the production of materials like glasses, metals, concrete and paper-making [3, 46–49]. In these applications, the foam is used to control the process' stability, and in some cases also to confer mechanical properties to materials [3]. In such applications, often the strength of a solid foam depends on the structure of a liquid-foam precursor, and the resulting solid foam is also lightweight being much less dense than the bulk liquid in the precursor. On the

other hand, foam can also be used as a firefighting agent, where bubbles are made of a non-flammable gas and liquid. The foam then displaces the air, which helps to suffocate the fire [50, 51]. Other more indirect applications of foams can be found in architecture/construction, where the bubbles' geometry can be used as a template for designing structures [52, 53].

Foam applications are also present in the food industry, as, for example, in baking and/or dessert making (breads, whipped creams, and mousses), and also in the production of drinks such as beers, sodas, wines, and champagne, amongst others [3, 54, 55]. In the food industry in particular, aerated mixtures comprised of dispersed bubbles in a continuous liquid solution (or solid medium), help to reduce the cost of the final product by reducing the amount of required solution per volume (relative to the pure liquid or solid phase). By stabilizing the bubbles within this media, the product structure can be stabilized giving control over desirable characteristics like texture, crustiness, and caloric density [56].

On the other hand, foam can also be used in a process to produce pharmaceutical powders from a solution in a systematic and controlled fashion [57–59]. This process is based on bursting bubbles. When bubbles burst, small droplets are created. Then, they are immediately dried out. This allows the creation of nanoparticulates or powders [27].

Modelling foam flow through confined channels with complex geometry is relevant for processes such as medical testing [32], and also in the treatment of varicose veins [60]. Moreover, in medical procedures, properties like the low density and the low solubility of microbubbles, that depend on the bubble coatings (phospholipid, surfactants, or synthetic polymer), make them effective for specific delivery of drug through the blood stream, treatment of thrombosis, pulmonary

embolism, and even to improve the quality of ultrasonic images since sound waves travel more slowly through the air than through tissues or liquids [61, 62].

Specifically, applications combining liquid foams with microfluidics occur in processes like enhanced oil recovery (EOR) [63, 64] and soil remediation [63], are those of primary interest in this thesis. In these applications the foam is used as a driving fluid to sweep a specific material, colloid pollutant or particles from porous media [65–67]. Using foam allows a more uniform sweep through the porous medium since foams are less sensitive to permeability heterogeneities than a Newtonian fluid would be [4]. Moreover, using foam in applications like these helps to reduce the quantity of the working fluid required, in comparison with a single-phase fluid [4]. In particular in foam EOR or, as it is often called, foam improved oil recovery (foam IOR) processes, as the foam displaces, perhaps only around 10% of it consists of liquid solution, significantly reducing the need for surfactants in the displacement process [65]. This liquid fraction (F_l) of the foams has an important role in the structure of foams [18] and also in the relation between structure and driving velocity [23], as will be discussed later. In any of the above mentioned applications, how foam moves and rearranges inside porous media, is a matter of great interest since the bubble-scale processes may affect the global foam behaviour.

1.3 Overview and scope

Up to here, the basic concepts about the physics and dynamics of liquid foams and their various applications have been reviewed. In what follows however, this work is to be focused on reviewing methods and mathematical models used to capture the foam dynamics as it flows through different systems, considering a number of very different length scales. This is presented in Chapter 2. Primarily,

models used to predict how foam flows through a porous media will be addressed, particularly those related with the foam improved oil recovery process (or foam IOR). In this context, previous works related to the so-called pressure-driven growth model for foam IOR are studied, specifically those which form the basis for the new results of this thesis, presented in chapters 3 and 4. These new results themselves will be also discussed, comparing with prior work and highlighting their importance, as pertinent. Works in chapters 3 and 4 correspond to research papers already published in the literature, which are presented here as part of this thesis. The pressure-driven growth model is used in these works to capture how a propagating foam front moves in the foam IOR process.

On the other hand, the theory, methods and models used to capture the dynamics on the bubble-scale of a finite number of bubbles as they flow through a confined geometry are also studied here. Specifically, works based on the so-called viscous froth model are reviewed in detail in Chapter 2. Novel results obtained by applying this model are therefore also addressed, emphasising their importance to the field as relevant. These results are presented in Chapter 5, which corresponds to a research manuscript already submitted for publication, but not yet published.

Therefore, based on what is discussed above, Chapter 2 is divided into two parts: macroscale models, and bubble-scale models. An important connection between these two types of models is that bubble-scale dynamics can be used as a source of information for the behaviour of macroscale models, e.g. by furnishing information about foam rheology and thereby foam mobility. Moreover despite the pressure-driven growth model (on the porous medium scale) and viscous froth model (on the individual bubble-scale) applying on very different physical length scales, there turns out to be a mathematical analogy between them as we will discuss.

In summary, the main novel contribution of this thesis to literature relies on the results in three research papers and/or manuscripts, which are available in chapters 3, 4 and 5. The scope and key background underpinning each of these chapters will be mentioned throughout Chapter 2, where relevant. Overall conclusions for the thesis are captured in Chapter 6. Possibilities for future work as discussed in Chapter 7

Chapter 2

Literature Review

This chapter is divided into two parts. In the first part, previous research outcomes that are ultimately related with the work in chapters 3 and 4 are analysed, where the theory, methods, and models used to predict foam motion in porous media are reviewed, particularly those related with foam IOR process. A number of these works use the pressure-driven growth model to predict how the foam propagates inside an oil reservoir, in the context of foam IOR. The work in chapters 3 and 4 expands the understanding of this process by taking two different approaches: using an Eulerian model in Chapter 3 (solved numerically), and a Lagrangian model in Chapter 4 (solved via an analytical similarity solution approach).

The second part of this chapter is focused on models and works based on predicting foam dynamics on the bubble-scale, as the bubbles flow within different confined geometries. Therefore, mathematical models used to predict how a finite number of bubbles move inside confined geometries will be reviewed. Specifically, the models discussed in most detail are those related with the work in Chapter 5. This work is based on the viscous froth model, which incorporates information not just about the amount a bubble structure deforms, but also the rate at which

deformation is applied. In Chapter 5, a simple three-bubble system is studied as a model for a more complex foam. Steady state (but out of equilibrium) configurations are obtained as a function of how rapidly the system is driven along a confining channel.

2.1 Models to capture foam dynamics in porous media

Foams' comparatively low mobilities make them excellent control agents in various industrial applications involving fluid flow through porous media [64, 68]. Since generally foam mobility is orders of magnitude lower than other fluids within the media, by controlling the foam flow it is possible to govern the entire system dynamics [69, 70]. Foam applications in porous media include processes like foam IOR, remediation of contaminated aquifers, clean up of polluted soils, and subsurface sequestration of CO_2 [12, 63, 66, 67, 71–74]. The rheology of foams, as they flow through these media, can be affected by factors such as the medium permeability, pore size distribution within the soil, liquid and gas relative permeabilities and viscosities, drag forces on the foam, type of surfactant, brine salinity, temperature, mechanical properties of the fluid to be displaced or recovered, gas and liquid injection method, injection pressure, capillary pressures, and ageing processes, such as those mentioned in section 1.1.2 [12, 69, 75, 76]. All these various factors can affect the mechanisms in which bubbles are created or destroyed, and therefore characterise the foam texture, which at the same time defines foam mobility inside the porous media [77]. Specifically the foam texture is measured as the number of films (or "lamellae") per unit of gas volume [12, 77] and the finer the texture, the less mobile the foam becomes. Several models developed to predict foam mobility can be found in literature, where the foam rheology is predicted as a function of the aforementioned factors governing texture, either

directly (i.e. explicitly involving the texture) and/or indirectly (i.e. implicitly, involving just the factors that govern texture) [12, 78, 79]. How much each one of the aforementioned factors contributes to the modelling overall, and under which conditions each factor is considered depends on each specific model type [12]. However, these models all recognize that the foam mobility as a key parameter within porous media flows [12]. Foam mobility is reflected within the gas relative permeability and/or gas effective viscosity, both of which are also mainly affected by the foam texture [76]. Foam can considerably restrict gas mobility, while its impact on the liquid phase in a porous medium (aqueous surfactant solution in the case of foam IOR) is almost negligible [12, 70, 80]. In the absence of other fluids, such as oil (which can destabilise foam), the presence of foam can cause the mobility of gas to be very severely reduced indeed.

There are two well recognised classes of models for foam in porous media namely local-equilibrium models, and population-balance models [12]. A key variable in these models is, as one might expect, the foam texture (or the mobility implicitly deriving from it), where the main difference between these two foam-modelling methods relies on the mechanism in which the foam texture is determined [12]. Local-equilibrium models do not necessarily explicitly relate foam texture with as relative permeability and effective viscosity of foamed gas, instead they adjust these variables based on physical observation, and empirical approaches [12]: thus the texture is implicit. In population-balance models in contrast, foam texture is determined explicitly by dynamically tracking how texture varies based on conservation equations for mass and for film number density [12]: processes creating and destroying foam films need not be in local equilibrium. These conservation equations lead to complex differential expressions which to be solved sometimes require extensive computational time [12]. Local-equilibrium implicit models are therefore often preferred.

Additional models to predict foam behaviour in porous media have been proposed in literature, such as the percolation theory which is based on pore-network analysis, and the fractional-flow theory [12, 81]. Fractional-flow theory in particular has been widely used to predict the foam mobility and dynamics in processes such as foam IOR [76,82]. This theory is typically based on solving a local-equilibrium model for foam mobility coupled to a mass conservation/continuity equation for foamed gas and/or for liquid, the resulting equation then being solved using the method of characteristics [76, 82]. Fractional-flow theory is actually relevant here since it turns out to underlie the pressure-driven growth model for foam IOR [64, 83], which is one of the main models we will employ in this thesis.

2.1.1 Foam improved oil recovery

The increasing oil demand as an effect of the world's growing energy needs [84], the lack of new oil fields being explored or exploited, the reservoirs' low quality (e.g. tar sands and heavy oils) and difficult accessibility of the recently discovered oil reservoirs (e.g. deep in the ocean bed and/or in low permeability formations), and the number of existing reservoirs that have already reached a mature production stage, have triggered the development of new oil extraction techniques that can make the most of existing fields [75,85]. Oil recovery processes generally rely on pressure gradients between the oil reservoir and the extraction well [86]. Maintaining these pressure gradients sufficiently high is essential to permit a continuous oil recovery process, even though the pressure may be expensive to maintain [86]. Usually, in an oil well, just a fraction of the oil is extracted using the original internal pressure of the reservoir as a driving force [85]. This stage is called primary recovery, and thereafter large amounts of oil remain to be recovered [85]. Once the reservoir's own pressure has dropped, so that no extra oil can be expelled, it is possible to inject other fluids into the reservoir in order

to maintain a high reservoir pressure and/or to displace additional oil to an extraction well (secondary extraction): common secondary extraction fluids include injection of single-phase fluids like water or carbon dioxide [87]. Typically up to a third of the oil originally present in the reservoir is recovered, after the primary and secondary stage of extraction [85]. Following this, there are technologies, processes or mechanisms known as tertiary or enhanced oil recovery (EOR), the application of which can help to recover additional oil [85,86]. EOR is defined as the set of methods that use external energy sources or materials to recover immobile oils retained in porous media, which due to viscosity and capillary forces cannot be produced by conventional means employed during primary and secondary recovery [75,88]. EOR processes can be divided into two groups, thermal and non-thermal [75]. Thermal methods include hot water flooding or steam injection, while non-thermal methods include the injection of a miscible fluid (e.g. alcohol), a chemical compound (e.g. a polymer), an immiscible gas (e.g. carbon dioxide or nitrogen), or a multiphase fluid (e.g. foam) [75]. Therefore, the methods and techniques used not just to maintain such high pressure gradients, but also to improve the production efficiency more generally are known as enhanced and/or improved oil recovery (IOR) processes [75]. IOR is a wider term that is usually understood to encompass all of EOR plus other approaches (e.g. various drilling strategies and/or hydraulic fracturing). In the present thesis though we do not consider those other approaches, only the use of foam, so we use the terms EOR and IOR interchangeably.

As mentioned above, one of the tertiary oil extraction techniques is the use of foam. Foam improved oil recovery (or foam IOR) employ liquid-foam as a control agent to sweep out the remaining oil within porous media [64,80]. Understanding the foam dynamics is fundamental in order to control and improve the efficiency of the process, however, modelling how foam propagates inside the reservoir can

be challenging, since we cannot see what is happening underground. Fortunately there have been numerous studies of the mechanisms by which foam is generated within and propagates within porous media [12, 64, 69, 80, 83, 89–93], so insights into the elements that are required within a model are available. The foam IOR method is based on the fact that the foam (particularly finely-textured foam) is relatively immobile compared with the mobility of other fluids within the oil reservoir. In porous media, foam films can severely restrict the motion of gas; the gas mobility falls due to the presence of foam films blocking the flow paths of gas [12]. In the region in which gas has very low mobility, foam is finely-textured [64], recalling here that mobility is a reflection of texture. Foam's low mobility is associated therefore with the large force required to drive the foam films through channels in a porous medium [80]. Being less mobile, foam controls the flow of any of the other reservoir fluids such as foamed gas, liquid and surfactant solution, as well as oil. By extension, to control the overall fluid flow through the reservoir, it is sufficient to control the flow of the foam, leading to a more uniform displacement of fluid from the reservoir [64]. Hence, the use of foams makes it possible to improve the process efficiency [64].

The foam is typically created inside the oil reservoir either by the co-injection of gas and liquid which contains surfactant, or via surfactant alternating gas (SAG) injection [94]: SAG is the process of main interest here, and consists of an alternate injection of a liquid surfactant solution and a gas. Upon contacting the surfactant, the gas generates foam, that propagates pushing the liquid (oil and surfactant solution) to the extraction well. This is discussed in section 2.1.3. The ratio of flow rates between the gas and the gas plus liquid determines what is defined as foam quality [68, 69]. A high foam quality, although it decreases the amount of surfactant liquid required may imply unstable foam, which can collapse if the capillary pressure increases above a critical limiting value [68, 89]. In

contrast, low foam quality makes the foam stable and decreases the gas relative permeability, but requires more surfactant [70,79]. The process relies on the foam films that are formed being stable enough to survive as they propagate through the porous medium, displacing reservoir liquids ahead of them.

In the presence of oil, stability of propagating foam films in porous media can be significantly affected, and therefore mobility might be more complicated to predict [76]. When foam films come into contact with the oil phase, the oil can either destabilize the bubble films (lamellae) breaking them up, or a gas/liquid/oil interface can be created [76], the properties of this new interface then being different from the original gas-liquid interface [12]. The surfactant solution used for displacement of a gas-liquid interface might not be appropriate for a more complex gas/liquid/oil interface [76], although, surfactant formulations can be found that, for particular oil types, impart good stability to the films [95–99]. Despite phenomena such as these which can complicate modelling, a model known as fractional-flow theory has been widely used to determine foam mobility in porous media (under conditions without or with oil), specifically to describe processes like foam IOR [76, 82]. This model is discussed in what follows.

2.1.2 Fractional-flow theory

Fractional-flow theory has been widely used to predict foam mobility (and mobility of fluids more generally) in porous media, and more recently to model processes including the presence of oil, and also including SAG injection related processes [75]. Despite the assumptions of this theory, like incompressible phases, Newtonian mobilities, one-dimensional displacement, absence of dispersion and absence of any gradients of capillary pressures, and that steady local-equilibrium conditions are considered wherever the gas meets the liquid, it captures the foam dynamics remarkably well [76]. This has been corroborated via labora-

tory measurements, and also via comparison with more complex models, such as population-balance models [64, 77]. Fractional-flow theory consists of solving a governing partial differential equation for liquid (or equivalently for gas) in pores, which is based on mass conservation laws. This governing equation establishes that the variation of the liquid saturation over time is proportional to the variation of liquid fractional flow over space, considering the spatial domain in which foam has displaced [100]. The variation of fractional flow (i.e. flowing liquid relative to overall flow) in the presence of foam can be determined as a function of the gas and liquid relative permeabilities and viscosities, which can be computed in terms of the liquid saturation [101]. It is supposed that at certain limiting capillary pressure [102, 103], which is determined as a function of the liquid saturation, the foam collapses, i.e. becomes coarsely textured [68]. Upstream then, in the region where the liquid saturation is lower than this limiting value, even though foam films might be present blocking certain pores, if there are sufficient unblocked pores so that gas is able to find a flow path, then mobility is much higher [70]. Moreover the mobility of pure liquid (i.e. primarily aqueous surfactant solution in foam IOR applications) is *not* being affected by foam in any region [12]. Hence what restricts motion is the zone of finely-textured foam where injected gas meets liquids [104] already in the reservoir, not drier and coarser foam upstream, nor unfoamed reservoir liquids downstream [12, 105]. Therefore, the total fluid mobility either side of the region where the foam is being generated is substantially larger than that at the generation region itself, possibly by as much as four orders of magnitude [105, 106].

In a SAG process, based on what fractional-flow theory predicts, it is possible to consider that all the pressure drop occurs across a (typically thin) finely-textured foam region [64] at which gas meets liquid, where the entire dynamics is focussed [29, 64, 104, 105]. Thus the effective viscosity of the finely-textured

foam is much larger than that of the surfactant solution (downstream) or the coarsely-textured foam (upstream) [80]. This prevents various operational problems associated with the injection process, in comparison to single phase fluids with lower density than the oil, such as gravity segregation (or gas override), where the injected gas might rise to the top of the reservoir and thereby override most of the oil, and the fingering phenomena, where the gas might predominantly flow through high permeability strata and therefore leaving oil unrecovered [64]. The finely-textured region where gas and liquid meet can be treated as a "shock" at which a sharp change in liquid saturation occurs. It has been proven, based on the fractional-flow theory analysis, that the finely-textured region close to the shock thickens over time but since the shock itself also migrates, the thickness of the shock region remains small relative to the distance it migrates [64].

Owing to hydrostatic effects, the net pressure drop driving foam IOR is depth dependent, although such depth dependence is not captured in a one-dimensional fractional flow model. These depth-dependent effects are however captured in the pressure-driven growth model (the main model to be used here) which is a two-dimensional or even three-dimensional model that derives from one-dimensional fractional flow [80]. How the shock at which gas meets liquid moves through the porous medium in a two-dimensional or three-dimensional system is a matter of great interest for applications such as foam IOR [70].

Returning to the one-dimensional case, the resulting partial differential equation for fractional flow can be readily solved via the method of characteristics [100]. In the one-dimensional case, fractional flow curves are then derived, from which time-distance characteristic lines are obtained for each fixed liquid saturation (and therefore for each fixed foam mobility) [82]. The slopes of these curves also determine the velocity at which foam at that particular saturation advances in

the porous medium [82].

Although the information provided by the fractional-flow theory comes as we have said from an one-dimensional analysis, it can be used to provide input on foam mobility to macroscale models, and therefore to predict foam flow into two or three dimensions (see section 2.1.3), such as it does for the pressure-driven growth model, which is discussed in section 2.1.4.

2.1.3 Propagating foam front

As gas is injected in a porous medium filled with liquid and surfactant, a finely-textured foam zone forms at the boundary where the gas meets the liquid and surfactant solution (also called the "shock"), with coarsely-textured foam also being left behind further back [64]. By applying the fractional-flow theory discussed above, we can track the foam propagation by considering just the region where foam is being generated. The thickness of this region, compared to other length scales, i.e. the depth to which the foam penetrates, and the trajectory through which the front has moved, is relatively small, such that it can be considered as a sharp propagation front [64]. As was proven in [64] via considering a two-dimensional model against an axisymmetric flow from an injection well, provided the fronts are sufficiently sharp, the shapes of the propagating foam fronts are the same in either case, despite the volume of liquid and gas injected to achieve the given front shape turning out to be particular to each geometry. Therefore, for simplicity, we can consider just a two-dimensional system with the advancing front treated as a curve of negligible thickness [80,104] (see Figure 2.1). Hence, as Figure 2.1 shows, the front itself consists of the zone of finely-textured foam, separating (as mentioned above) coarsely-textured, collapsed foam upstream from liquids (surfactant solution and oil) downstream. Foam in porous media is of course a rheologically complex fluid (which amongst other things) can exhibit

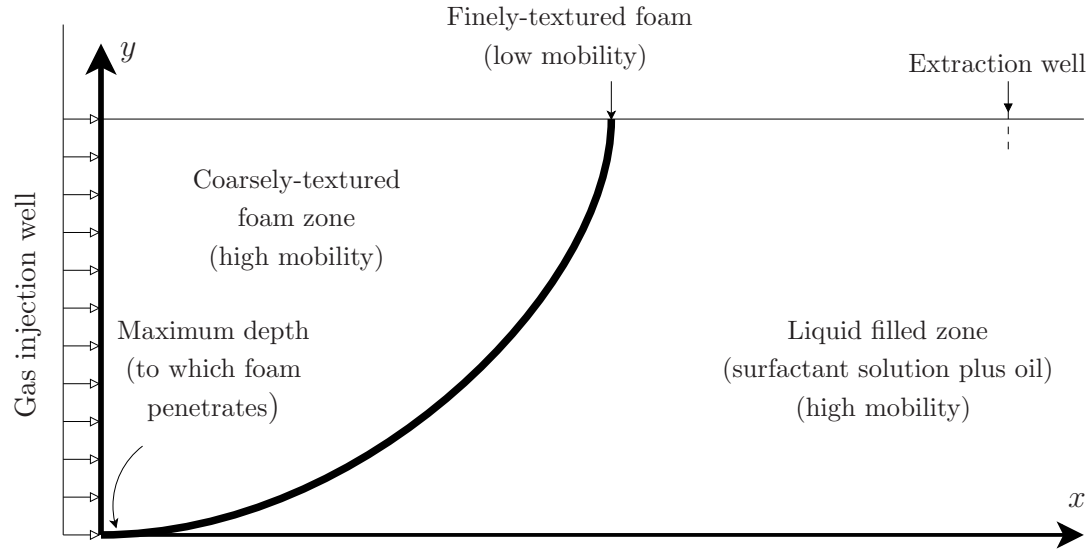

Figure 2.1: Two-dimensional representation of the liquid-foam front propagating in an isotropic and homogeneous oil reservoir. The front is sketched as line of negligible thickness, which corresponds to the finely-textured foam zone.

shear thinning behaviour [12, 89, 93, 106–108]. For the purposes to be considered here though, what matters is that at the front (as we have discussed in section 2.1.2), we have a finely-textured foam which has very low mobility. Consequently, the front is pushed along the reservoir by pressure, and at the same time, is retarded by dissipation across the finely-textured foam zone, the width of this zone gradually increasing with time (as follows from fractional-flow theory) but always remaining thin relative to front displacement [80]. As the front motion is driven by the pressure difference across it, its velocity decreases with depth, since the injection pressure behind remains fixed, but the hydrostatic pressure ahead increases with depth. Therefore, there is a maximum depth (used to non-dimensionalise length scales in the system) to which the foam can penetrate, i.e. the depth at which the injected gas pressure equals the hydrostatic pressure (see Figure 2.1) [104]. This maximum depth scales proportionally to gas injection pressure and inversely with liquid-gas density difference and gravitational acceleration.

2.1.4 Pressure-driven growth model

Pressure-driven growth is a model derived ultimately from Darcy's law [64], developed to capture the foam propagation front in foam IOR, specifically in SAG injection related processes. Darcy's law, as is well known [109, 110], involves a proportionality between flow through a porous medium and the imposed pressure gradient, the coefficient of proportionality being then the total mobility of the fluids that are flowing. Pressure-driven growth [80] is however a special case of Darcy's law in which all the driving pressure drop is lost across a thin, finely-textured foam region adjacent to a shock at which foamed gas meets liquid. The mobility within and also the (small but finite) thickness of this finely-textured region follow from one-dimensional fractional-flow theory (see section 2.1.2). Indeed the pressure-driven model was first deduced in [64], based on a fractional-flow theory analysis, and it was used to determine the evolving position of a foam front in a porous medium in an idealized two-dimensional system. As already alluded to in section 2.1.3, the generalisation of pressure-driven growth to axisymmetric three-dimensional systems turns out to be relatively straightforward (easier to handle certainly than a three-dimensional generalisation of Darcy's law would be) so is not considered any further here, although readers can consult [64] for details. Thus the development from [80], specifically in two dimensions, is recalled below, where the following assumptions are considered.

- The porous medium (oil reservoir) is geologically homogeneous and isotropic.
- Just gas and liquid (water plus surfactant) phases are considered to flow, in an effort to understand in the first instance how foam propagates through the medium and which parts of the medium it reaches over time. The residual oil trapped in the porous medium is not explicitly considered, although the model could be extended to included it.
- Surfactant concentration in the pure liquid zone (downstream of any gas)

is homogeneous.

- The mobility on both sides (coarsely-textured foam upstream and liquid filled region downstream) of the low-mobility region (finely-textured foam), is orders of magnitude higher than at the shock itself, so is treated as being arbitrarily large.

- The thickness of the finely-textured foam zone is much smaller than the trajectory through which the front (or shock) has moved. Therefore, the zone of finely-textured foam can be considered to be a curve (an idealised representation of an area of comparatively small thickness), which propagates through the petroleum reservoir. Any singularities that the model might predict in the shape of the front correspond physically to the front reorienting itself on a length scale comparable with the thickness of the finely-textured zone.

- The finely-textured zone is pushed along by a net driving pressure: At the top boundary of the domain the net driving pressure is maximal and at the lower boundary the net driving pressure is zero.

Therefore, based on these assumptions the finely-textured foam zone can be then represented as a curve of negligible thickness, and it propagates through the reservoir over time. This curve or propagating foam front, can be modelled by following the derivation of the model presented in [64] and [70] and realized in [80]. From Darcy's law, the superficial velocity of a gas phase in porous media is expressed as

$$u_s = -\frac{k\, k_{rg} \nabla P}{\mu_g}, \tag{2.1}$$

where k corresponds to the medium's permeability, k_{rg} and μ_g to the gas relative permeability and gas viscosity, and ∇P to the driving pressure gradient in the finely-textured foam zone (or low-mobility zone). The interstitial velocity can

then be obtained as

$$u_i = -\frac{k\,\lambda_{rg}\nabla P}{(1-S_w)\varphi}, \tag{2.2}$$

where $\lambda_{rg} = k_{rg}/\mu_g$ corresponds to the relative mobility of the gas in the low-mobility zone, S_w to the liquid saturation, and φ to the porosity of the medium. The interstitial velocity then gives the rate of change with respect to time of the location (in dimensional variables) of a material point $\mathbf{x}_D$ in the low-mobility zone, i.e. it captures the rate at which the finely-textured foam zone advances in the porous media. By defining ∇P as $-(\Delta P_D/\tau)\mathbf{n}$, with ΔP_D as the pressure difference (in dimensional variables) across the low mobility zone, with τ as the thickness of the low-mobility zone, and with $\mathbf{n}$ as the unit normal direction of motion of $\mathbf{x}_D$ (downstream), it is possible to deduce that

$$\frac{\mathrm{d}\mathbf{x}_D}{\mathrm{d}t_D} = \frac{k\,\lambda_{rg}\Delta P_D}{(1-S_w)\varphi\tau}\mathbf{n}, \tag{2.3}$$

where t_D denotes the dimensional time. Based on the fractional-flow theory [64], it was determined that the thickness of the low-mobility zone can be determined as $\tau = \epsilon\, s_D$, with ϵ being assumed constant such that $\epsilon \ll 1$, and s_D as the total distance that a local material point on the foam front has displaced. In addition, considering that the pressure difference across the low-mobility zone can be determined as the injected driving pressure P_{driv} (assumed to be uniform in the coarsely textured foam zone) minus the hydrostatic pressure P_{hyd} in the pure liquid zone (so that $\Delta P_D = P_{\mathrm{driv}} - P_{\mathrm{hyd}}$), it is possible to deduce that there must be a maximum depth to which foam can penetrate. This corresponds to the point where $P_{\mathrm{driv}} = P_{\mathrm{hyd}}$. Here P_{hyd} is computed as $P_{\mathrm{hyd}} = \rho\, g(d_{\max} - y_D)$, where ρ corresponds to the *density difference* between the liquid and gas, g to the magnitude of acceleration due to gravity, $d_{\max}$ to the maximum depth to which the foam penetrates, and y_D to the vertical distance measured from this point, such that $y_D = 0$ corresponds to the maximum depth, and $y_D = d_{\max}$ to

the surface. Since at $y_D = 0$ the hydrostatic pressure P_{hyd} equals the driving pressure P_{driv}, it can be deduced that $d_{\max} = P_{\text{driv}}/(\rho\, g)$. On the other hand, the time scale of the process turns out to be proportional to the following quantities: gas saturation at the front, porosity of the medium, maximum penetration depth squared, and the (assumed roughly constant, based on fractional-flow theory) ratio between front thickness and front displacement, and inversely proportional to medium permeability, relative mobility of foamed gas, and pressure used to drive the foam [64, 80]. Then, time can be scaled as

$$t_{\text{scale}} = \frac{(1 - S_w)\varphi\, d_{\max}^2 \epsilon}{k \lambda_{rg}\, P_{\text{driv}}}. \tag{2.4}$$

From equation (2.3), the dimensionless form of the pressure-driven growth model, developed in [64, 70, 80, 104] and used in this work, can be derived by rescaling lengths and thickness by $d_{\max}$, pressures by P_{driv}, and time by equation (2.4), obtaining that

$$\frac{\mathrm{d}\mathbf{x}}{\mathrm{d}t} = \frac{y}{s}\mathbf{n}, \tag{2.5}$$

where $\mathbf{x}$ corresponds to the dimensionless $\mathbf{x} = (x, y)$ location of a material point on the front in Cartesian coordinates (x and y represent the horizontal and vertical coordinates respectively), t to the dimensionless time, and s corresponds to the dimensionless distance travelled by a front's material points, and $\mathbf{n}$ is the local normal direction, which is measured as an angle α from the horizontal (see Figure 2.2). Here $y \in [0, 1]$ represents the distance above the maximum depth (which also equals dimensionless pressure difference). Thus, $y = 1$ at the top of the reservoir, and $y = 0$ at the maximum depth to which foam penetrates. Note that equation (2.5) is just a statement of Darcy's law, recognising that the lowest mobility in the system is at the finely-textured foam front, which is where the bulk of the Darcy pressure drop occurs, making it no longer necessary to solve a conventional two-phase flow Darcy model [64]. The front orientation angle α,

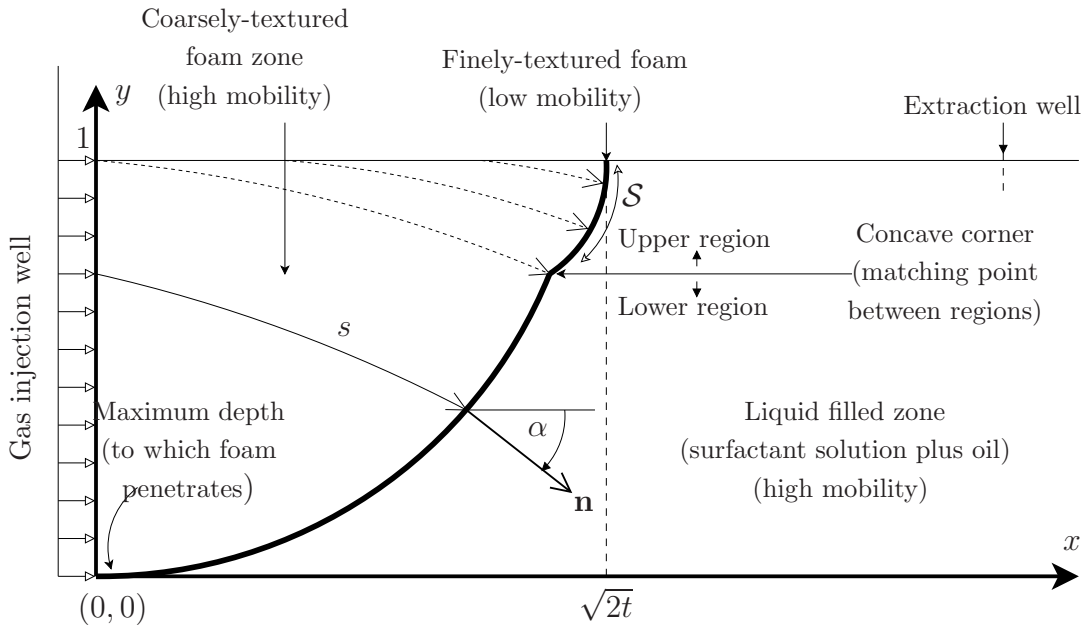

Figure 2.2: Definition sketch: Foam front propagation across a vertical domain $y \in [0, 1]$ and a horizontal domain $x \in [0, \infty)$. Variables are non-dimensionalised as established in [64, 80, 111]. Here $\mathcal{S}$ (which will be considered further in section 4.3.1) is the distance along the front measured downward, and s corresponds to the distance travelled by material points. At each point the front evolves in the local normal direction $\mathbf{n}$, which is measured as an angle α from the horizontal.

defined to be between the front normal and a horizontal line, can be obtained in terms of

$$\tan(\alpha) = \frac{\mathrm{d}x}{\mathrm{d}y}, \tag{2.6}$$

or equivalently $\alpha = \arctan(\mathrm{d}x/\mathrm{d}y)$. Here the derivative with respect to time t is considered by following a material point, whereas the derivative with respect y denotes a spatial derivative along the foam front from material point to material point [104]. If the normal $\mathbf{n}$ is expressed in terms of the angle α as $\mathbf{n} = (\cos(\alpha), -\sin(\alpha))$, then the model becomes

$$\frac{\mathrm{d}x}{\mathrm{d}t} = \frac{y}{s}\cos(\alpha), \tag{2.7}$$

$$\frac{\mathrm{d}y}{\mathrm{d}t} = -\frac{y}{s}\sin(\alpha). \tag{2.8}$$

On the other hand, by following the path of a fixed material point on the foam front, it is possible to deduce that the dimensionless evolution of such a point, i.e. the length of the trajectory s, evolves according to

$$\frac{\mathrm{d}s}{\mathrm{d}t} = \sqrt{\left(\frac{\mathrm{d}x}{\mathrm{d}t}\right)^2 + \left(\frac{\mathrm{d}y}{\mathrm{d}t}\right)^2}. \tag{2.9}$$

Inserting the model equations (2.7) and (2.8) into (2.9) gives

$$\frac{\mathrm{d}s}{\mathrm{d}t} = \frac{y}{s}. \tag{2.10}$$

The Lagrangian model for the foam-liquid front propagation consists of equations (2.5) and (2.10). Two boundary conditions are then considered. (i) At $y = 1$ the front location over time is found to be at $\sqrt{2\,t}$ (in dimensionless variables), which corresponds to the leading edge or maximum horizontal displacement, at least in the homogeneous and isotropic case [64]. (ii) At $y = 1$ the front meets the top of

the reservoir perpendicularly [64]. In homogeneous systems, these two conditions turn out to be equivalent. In strongly heterogeneous systems this equivalence does not always apply, which is discussed later (see also [112] for details). An initial condition meanwhile establishes that the front location at time $t = 0$ corresponds to a vertical line along the gas injection well (see Figure 2.2). A typical value of this time scale has been estimated as around 11–14 days [91,113]. However the important point for the current work is that this time scale is defined such that, at dimensionless time $t = 1/2$, the front has displaced horizontally by an amount equal to its maximum penetration depth [80]. As time proceeds, far above this maximum depth however, the pressure-driven growth model turns out to predict a concave corner or kink when seen from downstream [104] (see Figure 2.2), which starts off right at the top and migrates downward. This kink divides the propagating front vertically in an upper region and a lower region (see Figure 2.2). Determining how this concave corner moves, is one of the issues we address in this thesis. Further details are given in sections 2.1.4.1 and 2.1.4.2.

Although physically and mathematically the pressure-driven growth model is relatively easy to formulate (see equations (2.5) and (2.10)), it has shown a very rich and complex dynamics in cases where it has been applied to different porous media conditions. This complex dynamics arises since the equation governing the model (see equation (2.5)) turns out to be a hyperbolic partial differential equation [80]; in this hyperbolic equation, the speed of material points over time is directly proportional to vertical position y and inversely proportional to distance travelled s, where the direction of motion is given by the local normal $\mathbf{n}$ which changes over time and also along the front. This system leads to non-smooth solutions [80, 114]: singularities that emerge from the model have been determined both numerically, and via obtaining asymptotic analytical solutions. These singularities have been widely studied via both Eulerian and Lagrangian

formulations of the model [64, 70, 104]. Eulerian and Lagrangian versions of the model are further investigated in chapters 3 and 4, respectively. The model has been employed to explore the foam front motion in different scenarios which are discussed below.

2.1.4.1 Analysis and predictions of the model

Equation (2.5) and (2.10) can be studied via both, numerical, and analytical methods. Numerical solutions were first presented in [64], and then were improved in [80]. Analytical solutions were first obtained in [70], which subsequently were improved in [80]. For the purpose of Lagrangian computation, the propagation front since time $t = 0$ can be discretized into a finite number of material points, the motion of which we can readily track, and the front shape itself at any given time can be reconstructed by following a collection of such points. Then by applying a discretized version of equations (2.5) and (2.10) it is possible to track the motion of each individual point, and therefore to have a representation of the front over time [80]. However, as the front propagates, numerical artifacts may appear, specifically owing to the nature of model: the hyperbolic behaviour admits non-smooth solutions. These manifest as discontinuities such as concave corner (or kinks) which may arise (concave in this context means as seen from downstream) [112]. In such concave regions, points can intersect each other generating spurious loops which destroy the solution's stability and artifacts then occur [80]. On the other hand, in convex regions (convex in the sense seen from downstream) the distance between material points tends to increase as the front propagates, so the points do not intersect. Numerically the aforementioned spurious loops could be easily avoided by correcting velocities to evolve concave regions slightly faster than surrounding convex ones [12]. Physically, concavities represent an abrupt front's reorientation over a short distance (much less distance than the front has propagated), but there is a physical limit

to how sharp concave corners can be permitted to become owing to the front's small but finite thickness. However, concavities do not necessarily imply concave corners. In a concavity, material points need to propagate a distance comparable with the curvature radius of the concavity before they form a corner [114]. In physical terms, a locally non-smooth front shape, such as this concave corner represents, may induce fingering phenomena, or also it can be a potential indication of the gas override phenomena (in points above such a corner, gas can be much further forward than at the corner itself), any of which can decrease the process efficiency. Predicting the position and evolution of such corners might be useful for designing strategies to prevent or control override [104]. For this reason then, establishing whether the corners are an essential model feature, or just a numerical artifact, is of interest.

To maintain a reliable and stable solution, material points in the concave corners have to be either removed (or destroyed) or be evolved differently from their neighbours (velocity corrections can be included for them as mentioned earlier and as proposed in [80,112]). Additionally, new material points eventually have to be placed on the front as it stretches in convex regions. These new material points can be injected at locations estimated via asymptotic analytical solutions near the top of the front. This has been addressed by [80], effectively finding numerical solutions up to arbitrarily long times avoiding the aforementioned spurious loops that otherwise destroy stability, and matching solutions obtained in [64,70]. Solutions obtained out to the long-time limit demonstrated the SAG process can prevent gas override even up to very long times. In addition, in [80] an alternative strategy to avoid concave corners (and hence avoid spurious loops) forming altogether was also suggested, which consists of the inclusions of a diffusive (surface tension force) term in the model. However diffusive strategies generally need small time and spatial steps, making the numerical scheme expensive [80].

As studied in [80], concave corners can also appear when the driving pressure is abruptly increased [115], or when the surfactant concentration decreases near the top of the foam front (also known as slumping), which affects the bubble stability, causing film collapse, and therefore increasing the gas relative permeability. In the cases like those mentioned above, the shape of the propagating front can change and/or concave corners might appear. In the slumping scenario a reduction in the surfactant concentration can lead to a faster moving front [91]. Slumping of surfactant is typically undesirable though, since it can potentially trigger foam collapse at the top of the reservoir and hence gas override, which as mentioned before might decrease the effectiveness of the process [80].

Another case leading to concave corners is that where the porous medium is comprised of strata with different permeabilities. This was studied in detail in [114] and also in [113], where the pressure-driven growth model was used to represent the foam front, considering heterogeneous (and possibly also anisotropic) porous media. In this type of system, concave corners are likely to appear since at different depths different permeabilities (and also different ratios between vertical and horizontal permeability) can lead to having material points on the front moving at distinct velocities (a more substantial velocity variation along the front than in a pure isotropic and homogeneous case). To determine the motion of points on the front where concave corners form, a new computation technique was developed in [114]. This method consists (as already alluded to earlier) of speeding up points at the concave corner, effectively evolving the propagating front with its corners correctly, and therefore avoiding the aforementioned spurious loops. This study also proved that in anisotropic reservoirs the gravity override increases (gas rises to the top of the reservoir), which means that more oil is left behind than in an isotropic and homogeneous porous medium [114].

Then in [112] a system with strong heterogeneities was studied. A strongly heterogeneous porous medium in this context was defined as a system with very different permeabilities in different strata. In particular it was considered that permeabilities vary with depth by such a large amount that in parts of the medium this exceeds the variation with depth of net driving pressure (injection pressure less hydrostatic pressure), so net driving pressure does not entirely govern the flow dynamics. The top of the front does not now correspond to the maximum horizontal distance that the front has travelled, neither must the front meet the top boundary in a right angle. In contrast, the front exhibits local maxima of horizontal displacement away from the top, located in the high permeability strata. This study showed that sharp concave corners appeared at early times on the front in the region where strata connect, however as time proceeded they are driven down to the bottom of the front, where any further propagation is highly restricted by hydrostatic pressure. Material elements of the front as they migrate alternate between concave zones and convex zones. Thus, although material elements shrink in the concavity, before they shrink away to a corner, they manage to migrate to the next convexity and stretch again [112]. Indeed, only smooth concavities (not concave corners) persist out to long times [112]. This study also proved that gravity override (i.e. gas override) should not take place in a strongly heterogeneous system.

Returning to homogeneous systems, another interesting case (distinct from the pressure increase discussed earlier) is a net pressure *decrease*, which can lead in turn to a flow reversal (a change in the direction of the front's motion) at depth on the front. This happens as we have said, whenever the net driving pressure is decreased, thereby falling below hydrostatic pressure at depth, as studied in [83]. Flow reversal at depth such as described here, would take place [83] if the

injection pressure is suddenly reduced, or if the pressure field downstream of the front is increased by external factors, such as new gas injection wells away from the original one, or indeed if a gas injection well is shut in (so forward flow on the upper part of the foam front is necessarily balanced by reverse flow lower down). The flow reversal case is interesting because the sense of what is concave and convex (seen from the direction in which the front is propagating) is likewise reversed. This means any erstwhile concave corners now become convex corners, whilst former convex regions (which account for most of the front) become concave. Whether or not these now concave regions actually focus down into sharp concave corners is an open question. It is conceivable that before any sharp corners develop, these concave regions may simply find a new depth at which driving pressure and hydrostatic static pressure balance, and propagation of this section of the front then stops.

2.1.4.2 Solution procedures for model

The above sections considered various physical situations in which concave corners might appear on the foam front. In particular, as mentioned above, numerical solutions of the pressure-driven growth model indicate that concave corners might tend to appear even in homogeneous and isotropic porous media [104]. According to equation (2.5), the speed of the points closer to $y = 1$ is faster, hence the sign of the $\hat{\mathbf{j}}$ component of the normal $\mathbf{n}$ becomes negative (as in Figure 2.2), which implies that material points on front migrate not only sideways but also downwards. A gap is thereby created between the topmost point originally on the front at time $t = 0$ and the top of the reservoir, therefore new material points have to be injected in order to have a front shape that joins up continuously with material points that were originally on the front, avoiding instabilities. In Figure 2.2 the trajectory that has been followed by the new material points constituting what is termed the upper region is drawn with dotted lines, originating at the

top boundary, those points having been injected from the top and hence having been part of the front, during less time than the original ones (present from $t = 0$, trajectories drawn with solid line) that constitute what is termed the lower region. Mathematically, the corner can thereby be a manifestation of an incompatibility when trying to match (Lagrangian) material points that have been on the propagation front since the start of the injection process (all found in the lower region below the corner) and material points that have been newly injected at the top boundary since the initial time (the upper region) [104]. Therefore, it arises due to an incompatibility between boundary and initial conditions. Literature indicates that it was unclear at first however whether (as was discussed earlier) these corners were an essential feature of the model or merely a numerical artifact due to a poor choice of placement of the newly injected points, that could be mitigated by an algorithm that placed them more carefully [80,104,116]. This was studied in [104] by obtaining an analytical asymptotic solution, which focused on to determine the front shape at early times near top of the reservoir. From [104] the existence of a concave corner was then proven, which arises as alluded to above, owing to an incompatibility between newly injected material points (boundary condition), and points originally on the front since time $t = 0$ (initial condition). It was then determined, via first-order similarity equations valid for early times that this concave corner migrates downwards on the front at a constant speed, whilst the amount that the front propagates ahead of and above it remains comparatively limited, at least at early times. This then supports the notion, as mentioned above, the front itself can then be divided vertically into two regions, an upper region above the concave corner, and a lower region below it.

The existence of this concave corner was corroborated by solving the pressure-driven growth model via using Eulerian coordinates (as opposed to Lagrangian ones). This coordinate system does not require us to track the evolution of in-

dividual material points, instead, it evolves an objective function over a well specified solution domain. The Eulerian version of the model, as presented in Chapter 3 constitutes one of the main results chapters of this thesis which is now published as [116]. It formulates the pressure-driven growth model as a coupled system of Hamilton-Jacobi equations [116]. Numerical solutions at different times were then obtained in [116], where the concave corner appeared as a jump in the front orientation angle (see Chapter 3 for details). In [116] the position of the concave corner on the propagating front was tracked, suggesting that the velocity at which this migrates downwards decreases over time. To determine then whether the behaviour deduced in [104] (constant downward migration velocity of the corner), or that in [116] (velocity decreasing over time) corresponds to the real dynamics of the concave corner, further research was carried out as described below.

One of the issues with [104] was that the upper and lower regions of the front were computed to different orders of accuracy (first and second-order respectively), and the motion of the corner was predicted by matching these regions. It is possible then that the predictions in [104] for the velocity of the concave corner were an error due to having different solutions for the upper and lower region (different order early-time analytical solutions) as studied in [104]. Alternatively it is relevant to ask whether the velocity of the corner might have been affected by numerical truncation error in [116], and hence differed from [104] merely for that reason. To explore this further, a second-order (in time) analytical solution was formulated (expanding a leading-order similarity solution up to second-order in time [104]) as another of the main results chapters of this thesis (see Chapter 4 for details), now published as [117]. The work presented in Chapter 4 [117] is focused on improving upon the analytical similarity solutions obtained in [104] to predict the front shape on the upper region. These higher-order solutions

recognize the existence of strong spatio-temporal non-uniformities in the front dynamics as it propagates, which makes obtaining the higher-order solution particularly difficult. Despite the difficulties, the solutions effectively prove that the velocity at which the concave corner migrates downwards on the front decreases over time (see Chapter 4 for details).

This completes the section of the literature survey dealing with modelling on the scale of an entire foam front. In the next section we look at models of foam on the scale of individual bubbles.

2.2 Modelling foam flow in confined channels

Modelling liquid foams as they flow through confined geometries (e.g. in microfluidic devices) is of great interest in a number of processes in different industries (see section 1.2). As discussed in section 1.2, the study of microfluidics more generally has applications in various industries such as pharmaceuticals, medical treatment, and materials formation, including metals, polymers, inorganic crystals, and ceramics [32, 118]. Understanding foam microfluidics in particular relies on understanding foam at the bubble-scale. In turn, capturing and predicting foam dynamics at the bubble-scale, 10 μm–1 cm depending on the system of interest, implies taking into account factors such as surfactant concentration, surface tension (three-dimensional bubbles) or line tension (two-dimensional case comprised of a single layer of bubbles) [119], capillary pressures, ageing processes, bubble size distribution, gas diffusion across films, external applied forces (or stresses), viscous drag forces, system energy (measured as total film's surface area), film to film interactions which are based on Laplace pressures and Plateau's rules, and bubble rearrangement (see section 1.1). Despite this complexity, models have been developed from underlying fluid mechanical principles leading to

sophisticated mathematical descriptions [20, 119, 120].

Models aside, the experimental study of foam flow in confined channels is often performed by using microfluidic devices, with a view towards the sorts of application areas mentioned above [121]. These devices allow control of the flow of two fluid phases, such as liquid and gas, or analogously two immiscible liquids (emulsions), such that a dispersion of one fluid (bubbles or droplets) can be contained within the other [122]. The rheology of the multiphase flow is directly related to the physical properties of each phase, and their respective flow fractions, as well as the properties of the interface between them [123]. In microscale or bubble-scale flows, the effect of inertial forces is much less than the viscous forces, i.e. small Reynolds numbers are considered, which tends to makes the flow laminar and therefore easier to characterize in detail [124, 125]. By using the gas-liquid (or liquid-liquid) interface as a membrane it is possible to control reactions, to refine biochemical processes, and also to control drug delivery rates [61, 122, 126].

In microfluidic devices, bubbles are generally created by a continuous injection of liquid (e.g. water plus surfactant) through a tube or in between two glass plates, and intermittent injection of gas [127, 128]. Gas phases are divided via the so-called pinch-off method, which interrupts the gas injection at a well defined rate [127]. This interruption rate, in addition to the gas and liquid flow rates themselves determine the size of each bubble, and the liquid fraction of the foam. By manipulating liquid fraction, foam (i.e. many bubbles packed together) can then be changed from the dry limit towards a bubbly dispersion (see section 1.1.1). Depending on the bubble size with respect to the channel, different foam structures can be found. These vary from the bubbly dispersion case (wet limit), to packing in regular structures such as the Kelvin structure or Weaire-Phelan structure [129] (in three-dimensional dry foam) or else (for a monolayer of bubbles

in the dry limit, i.e. a two-dimensional foam) in so-called honeycomb structures (dry limit), where bubbles are characterized by their hexagonal shape (see section 1.1.1). Confinement however also determines shape, when the channel size shrinks to become comparable with the bubble size.

Three-dimensional foams systems are geometrically and topologically complex systems, even more so when they are flowing. One of the issues with studying rapidly sheared, out-of-equilibrium three-dimensional foam systems, is that the dissipation mechanisms are not well established [130]. The dissipative process in three-dimensional of extracting a film from a Plateau border is different from the somewhat more easily characterised dissipation that occurs in a quasi-two-dimensional foam (i.e. a bubble monolayer), whereby a Plateau border at a solid boundary typically moves over that boundary [130, 131]. Indeed the complexity of studying dynamics of foams as they flow in confined channels can be greatly reduced (as alluded in section 1.1.3) by considering quasi-two-dimensional channels, hence the reason we consider this limit [20]. These channels generally are comprised of two glass plates with a small separation between them, where their extension greatly exceeds that separation, such that gravity, foam drainage, and surfactant concentration gradient effects across the gap between the plates can be neglected [34]. Typically then there is just a single layer of bubbles across the gap between the plates as we have said. This two-dimensional foam system simplifies modelling, whilst at least some of the insights gained can be extrapolated to three-dimensional systems [20]. Thus in the interests of simplicity, consideration here is restricted to flow of two-dimensional foams. Several models to predict foam rheology have adopted this two-dimensional approach [19–21, 32, 120], in some cases as a preliminary to a full three-dimensional formulation. Some of the relevant models are: the vertex model [132,133], network modelling [134], the bubble model [135–137], the Potts model [138–140], and the quasi-static/equilibrium

foam model [141]. Each model considers a well defined set of assumptions and constructs the foam out of a well-defined set of model elements. However, not all physically relevant properties are included in these models, such as bubble shapes, Plateau's rules, pressure differences across films, surface tension forces, or indeed viscous drag forces, which might become relevant as the speed of flow increases. Unlike some of the other models mentioned above (like the vertex model), network based models establish the importance of considering hydrodynamic effects, and looking at all the physically important elements, such as films, Plateau borders, and vertices [142]. Nonetheless, there is a two-dimensional foam model, known as the viscous froth model [19] that incorporates all these aspects: this is the model of choice in this thesis. However, before formally introducing the viscous froth model, it is necessary to describe in more detail how the viscous drag forces arise in a flowing foam system, particularly when the foam is two-dimensional (confined between plates). This is discussed in section 2.2.1.

2.2.1 Forces governing film dynamics in two-dimensional channels

In two-dimensional models, although films are treated as one-dimensional curves, this disguises the fact that they are actually two-dimensional surfaces that are embedded in a three-dimensional space, whilst as the foam flows, the film surfaces can be curved both along and across the glass plates (see Figure 2.3). Therefore, as was indicated in [20], the three-dimensional physics can be included in two-dimensional mathematical representations of models. The main forces governing the dynamics of films are the surface tension σ, the viscous drag forces (associated with a viscous drag coefficient that we denote $\mathcal{C}$) and pressure difference across films Δp. Since the films have two surfaces, the film tension (2σ) is twice the surface tension σ. In addition, as can be seen in Figure 2.3, the orientation change

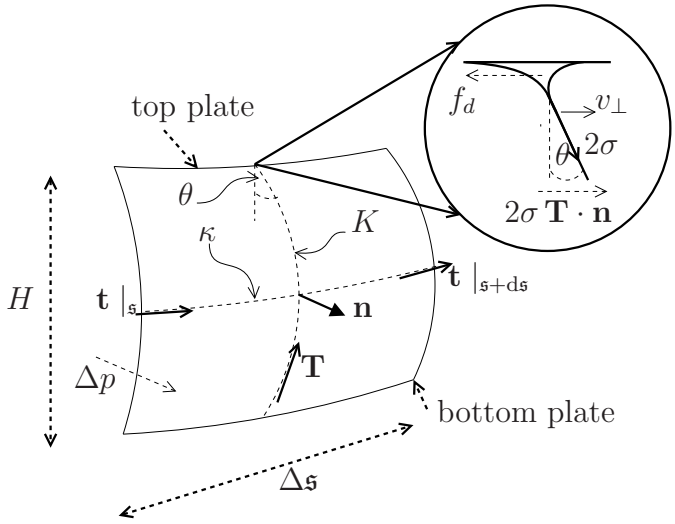

Figure 2.3: A segment $\Delta\mathfrak{s} \ll L$ of a film moving in a confined linear channel of width L and a separation H between the plates is considered. The film surface has a curvature κ along the the plates, and a curvature K across them. The film moves at a velocity $v_\perp$ in the normal direction $\mathbf{n}$. The inset shows a force balance between the viscous drag force $\mathcal{C}v_\perp$ and the surface tension.

of film tangents $\mathbf{T}$ and $\mathbf{t}$ in each direction, determines the curvatures K and κ, respectively. In Figure 2.3 the angle θ corresponds to the deviation of the tangent $\mathbf{T}$ with respect to the vertical at the top plate. Now consider a single film moving along a channel of width L, and with a separation between glass plates equal to H (with $H \ll L$) [20]. The film itself now need no longer have any curvature along the plates, but has a curvature K between them. Thus, the film cross-section across the plates is an arc of a circle, and the amount G that it bulges forward (between the plate surface and the centre plane between the plates) is given as obtained in [20] as

$$G = \frac{1}{K}\left(1 - \left(1 - \left(\frac{KH}{2}\right)^2\right)^{1/2}\right). \tag{2.11}$$

From equation (2.11), it is possible to deduce that when the glass plates are viewed perpendicularly (looking down on the top or up at the bottom plate), the film will appear to be a line of thickness G.

Figure 2.3 (see also [19] for a similar figure) shows a portion of length $\Delta\mathfrak{s}$ of film, moving along two plates with a gap H between them. At any point along this segment on either, the top or the bottom plate, the film meets the plates forming a meniscus (also called wet zone or Plateau border), which can be seen in the inset of Figure 2.3. It is in this region that the majority of the dissipation occurs, specifically in the dissipative transition region of the meniscus (see Figure 2.4). This dissipative force can be quantified in terms of the viscous drag force f_d, which acts opposite to the direction of motion. This force can be expressed per unit of length of the meniscus. The thickness and length along the plates of the aforementioned transition region is expressed (relative to H) as a function of the capillary number Ca (to be defined shortly), with an order $Ca^{2/3}$ and $Ca^{1/3}$, respectively [19, 143] (see Figure 2.4). It can be determined then that the shear stress in this region is of order $\mu v_\perp/(Ca^{2/3}H)$, with μ as the dynamic viscosity of the liquid and $v_\perp$ as the speed of film motion in the direction of the film normal. Then, integrating over the extent $Ca^{1/3}H$ along the aforementioned transition region, it can be determined that the drag force per unit length of the meniscus is of order $\mu v_\perp Ca^{-1/3}$. Here capillary number Ca is specifically defined as $Ca = \mu v_\perp/\sigma$, with σ as the surface tension force [119]. The viscous drag force (per length of meniscus) can now be computed as

$$f_d = -\Lambda\sigma Ca^{2/3}\mathbf{e}_x, \tag{2.12}$$

where $\mathbf{e}_x$ is a unit vector in the direction of motion, and Λ corresponds to the dimensionless pre-factor, which depends on the geometry of the channel [119].

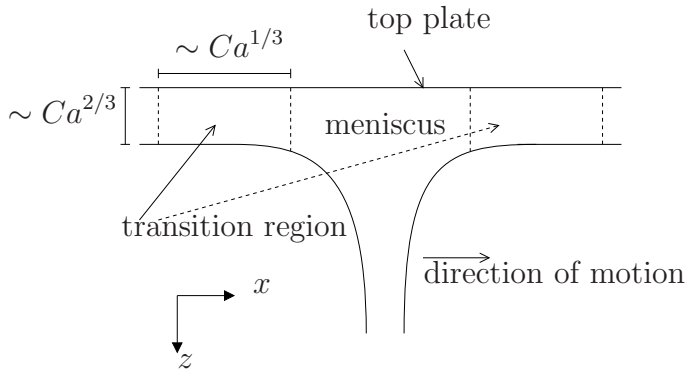

Figure 2.4: Sketch transition region adjacent to a plate in which the viscous drag force is concentrated.

The viscous drag force per unit of length of the meniscus can be now expressed per unit cross-sectional area. We assume a sufficiently small $\Delta\mathfrak{s}$ and a sufficiently small curvature κ (see Figure 2.3) such that $\kappa\,\Delta\mathfrak{s} \ll 1$, and then multiply drag per unit length by the meniscus perimeter $2\Delta\mathfrak{s}$ (wet zone), and then divide by the cross section area $\Delta\mathfrak{s}\,H$. Finally, considering that $\Lambda = 38$ (as was estimated in [119]), it is possible to obtain obtain the drag force per cross-sectional area as $-(76/H)\sigma Ca^{2/3}\mathbf{e}_x$. It is also possible to write the drag force per cross section using a drag coefficient

$$\mathcal{C}v_{\perp}^{a} = \frac{76}{H}\sigma Ca^{2/3}, \tag{2.13}$$

where $\mathcal{C}$ corresponds to the viscous drag coefficient, and a is an exponent (ideally 2/3 but often for convenience taken to equal unity). As we will explain later on, choosing $a = 1$ in a model, makes it far easier to impose constraints on bubble areas, and use them to deduce bubble pressures. A value for the drag coefficient $\mathcal{C}$ can then be estimated under the following conditions. It is considered that the liquid-foam solution is a water surfactant-glycerol mixture (5% glycerol volume) with $\mu = 1.16 \times 10^{-3}\,\mathrm{Pa}\cdot\mathrm{s}$ and $\sigma = 2.7 \times 10^{-2}\,\mathrm{N\,m^{-1}}$, the foam being

generated by the same apparatus used in [19, 119], with an apparent velocity $v = 0.025\,\mathrm{m\,s^{-1}}$ (along the transport channel), with width $L = 9\,\mathrm{mm}$ and thickness $H = 3\,\mathrm{mm}$ (so the gap between the plates is indeed narrow), for which via (2.13), $\mathcal{C} \approx 290\,\mathrm{kg\,m^{-2}\,s^{-1}}$.

We emphasise that we have estimated $\mathcal{C}$ here based on a linear drag law $a = 1$, whereas, as has been proven in [119], the viscous drag force actually has a non-linear dependence with respect to the velocity, which means that the coefficient a in (2.13) is strictly speaking $a \approx 2/3$. The value of drag force per unit velocity however has quite a weak velocity dependence scaling only like $v_\perp^{-1/3}$. To this extent, the foam dynamics can be captured with a reasonable precision taking $a = 1$ as we did in the estimate of drag coefficient $\mathcal{C}$ above, and as has been done already in related works using the viscous froth model [19–21, 23, 24, 31, 33]. A linear drag law is considered moreover since, as alluded to earlier, it also simplifies in imposing bubble area constraints and computing bubble pressures [19].

2.2.2 Foam structures in a confined system

Quasi-two-dimensional foams are confined not only across the thickness of the bubble monolayer or plate-to-plate separation (earlier denoted H) but also across the width of the confining channel (earlier denoted L). This confinement across the width can govern the foam structure that is realised. Non-Newtonian behaviour has been exhibited by the foam structures as they flow, transitioning between different structural configurations as flow proceeds, yielding a non-linear relation between driving pressures and migration velocities [65, 119, 124]. As was demonstrated by [4], for a given driving pressure, the velocity at which the liquid-foam flows through a confined plates geometry (Hele-Shaw cell), depends upon how the bubbles are arranged topologically, exhibiting discontinuities in the resulting velocities at the transition between the different topological structures

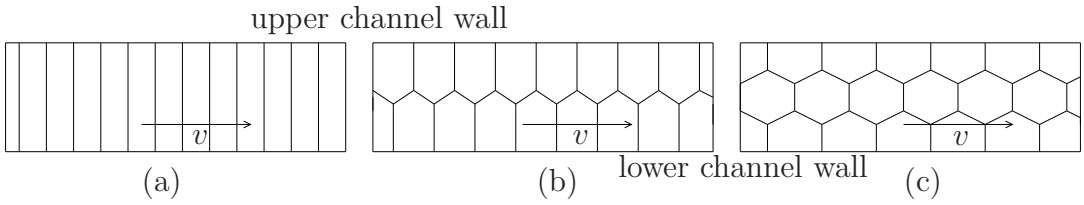

Figure 2.5: Foam flow structures moving at a velocity v through a confined linear channel. Here the systems are viewed normal to the confining plates (so they appear as two-dimensional systems) and what appear as upper and lower channel walls in this two-dimensional view are actually sidewalls of the original three-dimensional channel. In such systems, foam films are in general one-dimensional curves, but in all these special cases they reduce to straight lines. (a) Bamboo structure. (b) Staircase structure. (c) Double staircase structure.

such as bamboo, staircase, and double staircase structures (see Figure 2.5).

The reason that these different velocities result is because, depending upon how the films are oriented spatially, how long they are and how fast they are moving, they experience differing amounts of viscous drag. The velocity in each structure in Figure 2.5 is then set by the requirement that viscous drag force must be balanced by the driving pressure force. How the bubbles prefer to arrange within the system and the drag per unit velocity they thereby experience, depends on the ratio between bubble size and channel size (i.e. channel width). The single staircase structure (also called hexa-one) shown in Figure 2.5(b) (and likewise the double staircase (also called hexa-two) in Figure 2.5(c)) correspond in principle to an arbitrarily long train of bubbles moving along the channel (i.e. infinite staircases). Hexa-three, hexa-four, etc., structures, have also been obtained in lab scale simulations [124]. Under these circumstances, and assuming monodispersity, bubbles have the exact same shape no matter how far along the staircase they are. For a channel of width L, the size of a bubble in a staircase such as Figure 2.5(b) (measured from one of the channel walls to the farthest point of that bubble away from that wall) is always at least $L/2$ [21, 33, 144]. On the other hand, when the channel width is such that $L \leq 2\sqrt{A/\pi}$ (with A as the

monodisperse bubble areas), a bamboo foam is more likely to be obtained [4]. In contrast, for $L \geq 2\sqrt{A/\pi}$ bubbles might pack in a staircase or double staircase depending on the operational condition of the microfluidic device along which bubbles are flowing [4, 127]. Nevertheless all above mentioned structures, once they are originally set up, and provided they consist of arbitrarily large numbers of bubbles in a train moving along a perfectly straight channel, manage to migrate without deforming. Bubbles thereby leave the channel in the same order in which they entered it, meaning there are no bubble neighbour exchanges, or so-called $T1$ topological transformations [21].

What was discovered by [32] however is that when the channel is curved, such transformations become possible again. They entail that a film shrinks until it becomes zero length. Two bubbles formerly in contact, then lose contact with one another, and different bubbles contact each other in their place (see section 1.1.4). The precise order of occurrence of the $T1$ transformations is not known a priori [144]. Indeed whether or not they even occur at all depends upon on how rapidly the system is moving: a threshold velocity associated with a threshold imposed driving pressure is needed before they occur. Therefore, key questions of interest, in a flowing foam system, are to predict at which velocities and at which driving pressures $T1$s occur, and how the bubble areas influence their occurrence [24]. When flow is rapid, even simple cases are found to exhibit complex dynamics [19, 33, 144, 145]. What must change between a slow moving system (no $T1$s present) and a faster moving one (with $T1$s) is the amount of viscous drag that is present. A model to predict the onset of $T1$s must therefore incorporate viscous drag in some fashion. As has been proven in [119], the viscous drag force has a non-linear dependence with respect to the velocity. However, in this work we consider for simplicity a linear drag law, with a drag coefficient denoted $\mathcal{C}$: this still manages to capture the key physics, i.e. $T1$ transformations

only occurring after a threshold. We also consider a comparatively dry foam in which film lengths greatly exceed the size of the vertices at which three films meet. Drag therefore must be assigned to film elements rather than to vertices or to film endpoints. Assumptions like these have been used in a number of prior studies [20, 21, 23, 24, 31, 33, 119] and they lead to a simple viscous froth model that we discuss next.

2.2.3 Viscous froth model

The viscous froth model was originally formulated as a generalization of two models, known as the ideal soap froth and ideal grain growth models, which can be derived from it under particular limiting conditions [21, 146]. This model was originally conceived in the dry limit, although under certain condition can also be used for wet foams [21], albeit the focus of the present thesis is on dry systems. The viscous froth model combines and balances the pressure difference across the films with the net surface tension force, which depends on the local curvature, converting any mismatch between them into film motion, from where viscous drag force arises [19] (see Figure 2.6). Mathematically, the viscous froth model can be derived by considering a non-straight moving foam film confined between two glass plates, with any segment of this film then being as introduced back in Figure 2.3. A force balance between the pressure difference across the film Δp and the surface tension forces (acting along and across the plates, coupled with film curvature) can be performed starting from Figure 2.3. Here we summarize the derivation of the model from [19].

First, the driving force associated with pressure across a small (infinitesimal) elemental area of film $H\,\mathrm{d}\mathfrak{s}$ can be computed as $\Delta p\,H\,\mathrm{d}\mathfrak{s}$, with Δp as the upstream minus the downstream pressure. Second, as shown in Figure 2.3 the delimited region may be curved along the direction of movement κ and also across the plates

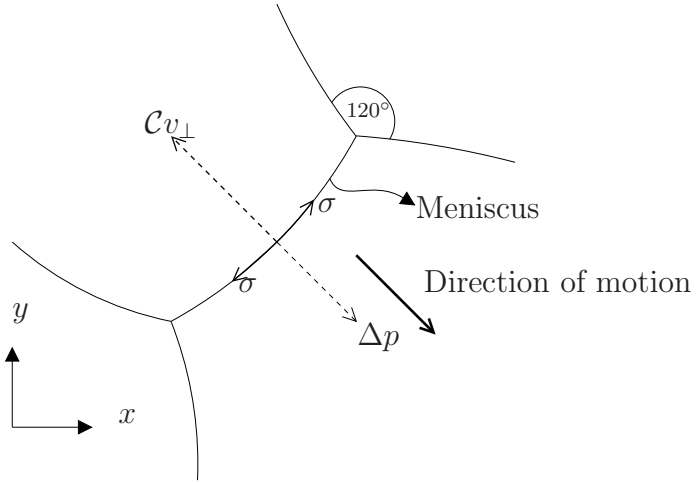

Figure 2.6: Two-dimensional force balance across a moving curved film. The pressure difference across the film is Δp, while $\mathcal{C}$ corresponds to the viscous drag coefficient (associated with a moving meniscus) and $v_\perp$ is the velocity in the normal direction. Also σ corresponds to the surface tension (film tension is twice this). The films meet its neighbours subtending an angle of $2\pi/3$ (or 120°).

K, and the curvatures can be computed as spatial change of the tangents $\mathbf{t}$ and $\mathbf{T}$, respectively. If seen from downstream, $\kappa < 0$ here if the film is concave, and $\kappa > 0$ if convex. The surface tension force balance per length on the sides of a film segment (of extent $\Delta\mathfrak{s}$ as drawn in Figure 2.3), when written in terms of the tangent $\mathbf{t}$, can be expressed as $(2\sigma H\,\mathbf{t}\;|_{\mathfrak{s}+\Delta\mathfrak{s}} - 2\sigma H\,\mathbf{t}\;|_{\mathfrak{s}})/\Delta\mathfrak{s}$, which in the limit when $\Delta\mathfrak{s} \to 0$ corresponds to $2\sigma H\,\mathrm{d}\mathbf{t}/\mathrm{d}\mathfrak{s}$. Geometrically $\mathrm{d}\mathbf{t}/\mathrm{d}\mathfrak{s} = -\kappa\mathbf{n}$, from which it is deduced that, for an infinitesimal element $\mathrm{d}\mathfrak{s}$, the net surface tension force in the normal direction (due to curvature along the plates) is $-2\sigma\kappa H\,\mathrm{d}\mathfrak{s}$. Third, at the top and bottom plates, the surface tension forces are $2\sigma\,\mathbf{T}\cdot\mathbf{n}$ (top) and $-2\sigma\,\mathbf{T}\cdot\mathbf{n}$ (bottom), respectively (see inset of Figure 2.3). Our convention is that $\mathbf{T}\cdot\mathbf{n} < 0$ at the top and $\mathbf{T}\cdot\mathbf{n} > 0$ at the bottom, so these represent forces (in the negative direction) of the meniscus on the film, the forces of the film on the meniscus being in the positive direction and opposite and equal to these. Force balance on the meniscus (zero net force there) then results when these tensions

are summed with the viscous drag forces at each the plates $-\mathcal{C}v_\perp\,(H/2)\,\mathrm{d}\mathfrak{s}$. Note that $\mathcal{C}$ here corresponds to the overall drag coefficient across the plates [19], the sum of the drag force on both plates being $-\mathcal{C}v_\perp\,H\,\mathrm{d}\mathfrak{s}$. It follows that the tension that the menisci place on the film balances the total drag force on the menisci, and so in the film force balance, we can eliminate the former in favour of the latter.

The sum of all the aforementioned forces on the film must be equal to zero, therefore it is possible to deduce that

$$0 = \Delta p\,H\mathrm{d}\mathfrak{s} - 2\sigma\kappa H\mathrm{d}\mathfrak{s} - \mathcal{C}v_\perp H\mathrm{d}\mathfrak{s}, \tag{2.14}$$

which divided by the surface area $H\mathrm{d}\mathfrak{s}$ results in

$$\mathcal{C}v_\perp = \Delta p - 2\sigma\kappa. \tag{2.15}$$

Equation 2.15 corresponds to the dimensional form of the viscous froth model, with a linear viscous drag law ($a = 1$). In this work the viscous froth model will be used in its dimensionless form, for which $v_\perp$ is rescaled by the velocity $2\sigma/(L\mathcal{C}) \approx 0.002\,\mathrm{m\,s^{-1}}$, Δp by the pressure $2\sigma/L \approx 6\,\mathrm{N\,m^{-2}}$, the curvature κ by $1/L \approx 111.1\,\mathrm{m^{-1}}$ and finally the time scale by $L^2\mathcal{C}/(2\sigma) \approx 0.43\,\mathrm{s}$. Here we have used estimates of σ, $\mathcal{C}$, L and H given earlier in section 2.2.1. Now the dimensionless viscous froth model can be written as (for compactness of notation using the same symbols for dimensional and dimensionless variables)

$$v_\perp = \Delta p - \kappa. \tag{2.16}$$

The left-hand side of the equation (2.16) represents the linear viscous drag force, and the right-hand side represents the driving forces, which can only be in balance for a static film (in accordance with Laplace's law). Static foams are governed

by the ideal soap froth model $\Delta p = \kappa$ in dimensionless form [21, 147].
From equation (2.16) we can deduce that the pressure-driven growth model (addressed in section 2.1.4) can be recovered, under the assumption that the effect of the curvature (or in a dimensional formulation, the surface tension-curvature term) is negligible with respect to the pressure ($\kappa \ll \Delta p$ in equation (2.16)). Thus there is a close analogy between pressure-driven growth and the viscous froth. Recall also (see section 2.1.4 also [80]) that incorporating a (weak) surface tension curvature term within pressure-driven growth was a method (albeit a computationally expensive one) of stabilising the mathematical behaviour of pressure-driven growth by avoiding the formation of sharp concave corners and/or spurious loops. One way of making the pressure-driven growth model stable, and prevent the formation of kink or corners, is therefore to convert it to a viscous froth with weak surface tension.

Yet another limit of interest occurs in the viscous froth model when the effect of the pressure difference across the surface is neglected. In that case normal velocity matches curvature and the ideal grain growth model can be obtained [146, 148, 149]. This model was originally formulated in the context of boundary growth in metals [149], in which the pressures across the cells are no longer relevant. The motion of interfaces is then driven solely by local curvature. Thus static foams, pressure-driven growth and curvature-driven growth are all special cases of the viscous froth. Having introduced the model we now go on to consider implications for bubble areas.

2.2.3.1 Bubble areas

The so-called ideal soap froth model only considers foam evolution as consequence of the gas diffusion across the films owing to the pressure difference. The area of the bubbles changes gradually, but apart from that, bubbles are in equilibrium

satisfying Laplace's law. This process for two-dimensional foams is governed by the von Neumann's law [21], which (in dimensional form) established that the area variation over time obeys

$$\frac{\mathrm{d}A}{\mathrm{d}t} = \frac{2\pi}{3}\sigma\varrho(\eta - 6), \tag{2.17}$$

where η is the number of sides of the bubble, σ is the surface tension (film tension being twice this), ϱ corresponds to the gas permeability constant (rate of transfer of bubble area per pressure per unit film length), A is the bubble area, and t is the time. From equation (2.17) it can be proven that the area of a bubble with six edges $\eta = 6$ will remain constant until a topological transformation occurs and it either gains or loses an edge. Gas diffusion can cause neighbouring bubbles to grow or shrink, and these are what then drive topological transformations for the ideal soap froth. The most common topological transformation is a $T1$ or bubble neighbour exchange in which some bubbles gain edges and others lose them [21]. On the other hand, if the gas diffusion across the film is neglected ($\sigma\varrho \to 0$), such that $\mathrm{d}A/\mathrm{d}t \to 0$, there will be no growth or shrinkage for any bubble on time scales of interest and hence no diffusively driven $T1$s. The only "$T1$" topological transformations that then take place then arise from putting an external stress on the foam, a point we will return to shortly.

A similar expression to that given above can be deduced for the grain growth model, the expression then being known as the Mullins' law [21]. This establishes that

$$\frac{\mathrm{d}A}{\mathrm{d}t} = \frac{2\pi}{3}\frac{\sigma}{\mathcal{C}}(\eta - 6). \tag{2.18}$$

Here 2σ now denotes the tension at the grain boundary, $\mathcal{C}$ is a drag coefficient and η is number of sides. Both equations (2.17) and (2.18) were formulated by considering a polygon-like cells comprised of a number η of curved edges (boundaries)

dividing a two-dimensional plane, with the boundaries meeting three by three at vertices subtending angles of $2\pi/3$ [149]. If $\eta < 6$ the cell loses area, and if $\eta > 6$ the cell gains area. The area of a cell with $\eta = 6$ remains constant over time.

One of the implications of the viscous froth model is that since it generalises the ideal soap froth model and the grain growth model (reducing to each of these in suitable limits as mentioned earlier), it is also possible to generalize von Neumann's law and Mullins' law, leading to an associated coarsening dynamic equation [21, 146].

A general expression to compute bubble area variations over time can therefore be deduced starting from the viscous froth model (written as given by equation (2.15)). Therefore, considering that the area change of a bubble is equal to the net displacement of its η surrounding films, which locally move with a normal velocity field $v_\perp$, it is possible to deduce that

$$\frac{\mathrm{d}A}{\mathrm{d}t} = \oint v_\perp \,\mathrm{d}\mathfrak{s} = \frac{1}{\mathcal{C}} \oint (\Delta p - 2\sigma\kappa)\,\mathrm{d}\mathfrak{s}, \tag{2.19}$$

where based on the linear viscous drag law assumption ($a = 1$), and since $\mathrm{d}A/\mathrm{d}t = \oint v_\perp \mathrm{d}\mathfrak{s}$ (with $\mathfrak{s}$ being the arc length along the films), the relationship between $\mathrm{d}A/\mathrm{d}t$ and driving forces now is a simple linear equation. The analogous dimensionless form of (2.19), for compactness of notation retaining the same symbols as before, corresponds to

$$\frac{\mathrm{d}A}{\mathrm{d}t} = \oint v_\perp \,\mathrm{d}\mathfrak{s} = \oint (\Delta p - \kappa)\,\mathrm{d}\mathfrak{s}. \tag{2.20}$$

Although this is a coarsening dynamics equation, if the time scales of interest are too short for any significant coarsening to occur, bubble areas are then constrained. The left hand side of equation (2.19) vanishes and it leaves us a linear

system of equations for bubble pressures, the coefficients in the equations being a function of film lengths. Interesting dynamics can still result in this limit but the viscous froth must be subjected to some sort of external forcing. In this case the viscous froth is no longer a model for foam coarsening, but instead a model for foam rheology: this point will be returned to shortly.

On the other hand, from Fick's law [21], which defines the gas permeability as $\varrho = -(\mathrm{d}A/\mathrm{d}t)/(\oint \Delta p \, \mathrm{d}\mathfrak{s})$, and also based on Gauss's theorem for curvature [21], it is possible to express equation (2.19) back in dimensional form as,

$$\frac{\mathrm{d}A}{\mathrm{d}t} = \frac{2\pi}{3}\left(\frac{\sigma\varrho}{1+\mathcal{C}\varrho}\right)(\eta - 6). \tag{2.21}$$

This corresponds to a general equation for foam coarsening dynamics, where by considering two limiting cases $\mathcal{C}\varrho \ll 1$ and $\mathcal{C}\varrho \gg 1$, it is possible to recover the von Neumann's law (for ideal soap froth) and Mullins' law (for grain growth) respectively.

2.2.3.2 Viscous froth as a rheological model

On time scales of interest in foam rheology, little diffusive coarsening tends to take place so the viscous froth model can be solved assuming constant bubble areas. The left hand side of (2.20) now vanishes, and taken over each and every bubble, the equation reduces (with the help of Gauss's theorem) to a linear system that relates bubble pressures to film lengths and number of sides per bubble. Many studies to predict foam rheology as foam flows through confined channels have been already realized by using the viscous froth model in this fashion [21, 32, 119, 150]. This model can capture out-of-equilibrium phenomena, overcoming limitations with previous models which in some cases produce discontinuities and jumps in film configuration as the systems undergo $T1$ topological

transformations (bubbles change their neighbours as alluded to earlier) [19]. Using viscous froth, out-of-equilibrium phenomena can be modelled in systems even comprised of a comparatively large number of bubbles [21]. It is not necessary however to consider very large numbers of bubbles to see interesting behaviour. Even a so-called simple lens system (i.e. a single bubble attached to one side of a channel with a spanning film joining that bubble to the other side of the channel; see Figure 2.7(a) later on) could exhibit interesting behaviour [19].

Although the viscous froth model was first obtained in the dry limit (which is the limit treated in this thesis), it can also be adapted to capture wet foam dynamics. This is what it was achieved in [23], where a simple lens system was studied, but considering wet films. This study proved that as the liquid fraction increases (for a fixed bubble area), in comparison with the dry limit, the migration velocity needed to achieve $T1$ decreases, as an effect of the increment in the drag force. In addition, in [23] it was proven that for the same driving velocity, films can suffer more deformations in wet systems than in the dry limit.

The viscous froth model has also been adapted to study systems with non-uniform surfactant concentration along the films [14]. Gradients of surfactant may appear as the film elements deform (stretching or shrinking) under the action of the viscous froth dynamics, leading to differences in surface tension along films. Based on surface tension gradients, the Marangoni effect [15] begins to act, distributing the surfactant along the films, affecting in turn the surface tension, and therefore the deformation rate of the films. This is what has been studied in [15]. In [15] the motion of a simple lens system along different channels was studied by accounting for variations in the surface tension in terms of the Gibbs-Marangoni parameter (a ratio of the rates associated with Marangoni flow and flow due to the viscous froth dynamics). For large values of the Gibbs-Marangoni number

(leading to large gradients of surface tension) higher driving velocities were required to drive the system to topological transformations, i.e. making the system more stable. We do not consider the complications associated with having finite liquid fraction and/or associated with surface tension gradients here. Instead in Chapter 5 we look at the complications associated with increasing the number of bubbles compared to the simple lens geometry considered by [15, 19, 23].

The viscous froth model has also shown quantitative agreement in experiments of flow of trains of bubbles through curved channels [4, 21, 24] exhibiting $T1$s for high speed flow but not low speed flow, thereby showing a very rich and complex dynamics including in systems comprised of relatively few bubbles. In particular, in [32], the model was applied to a train of twelve equal-sized bubbles in the staircase structure (two bubbles across the walls as in Figure 2.5(b) and several bubbles along the plates) but flowing now, not in a straight channel, but instead through a 180° bend geometry. From [32] it was proven that for arbitrarily low velocities (hence arbitrarily low driving pressures), there was no $T1$ topological transformation. On the other hand, for a high flow rate (hence higher driving pressure), $T1$ topological transformations took place in the curved bend, making the foam structure unstable [32]. Clearly this differs from the situation of an infinite staircase in a straight channel as described earlier.

2.2.3.3 Infinite staircase vs simple lens

The work of [32] raises the issue of whether the topological transformation observed was due to the curvature of the channel or due to the staircase being finite or a mixture of both. One way to address this question is to consider a finite staircase in a straight channel. In [19], the viscous froth model was applied to the motion along a straight channel of a lens bubble attached to one of the channel walls and a spanning film connecting the lens with the opposite

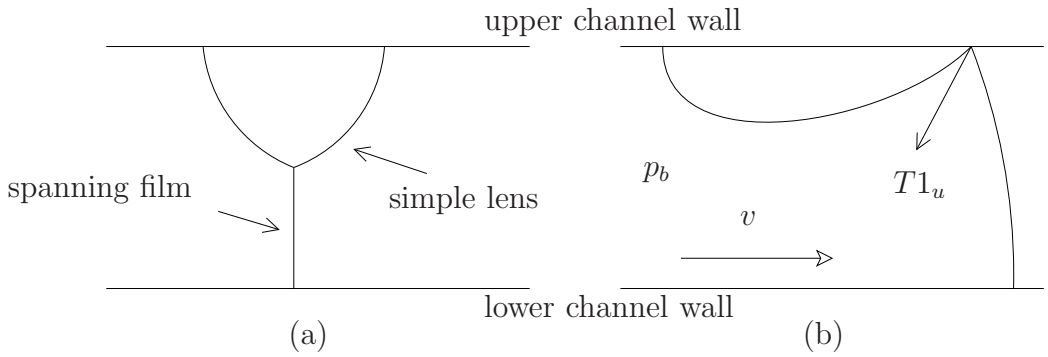

Figure 2.7: (a) Sketch of the simple lens problem studied in [19]. (b) $T1_u$ topological transformation for a structure moving at velocity v due to a back pressure p_b imposed upon it.

channel wall: this is known as the simple lens system (see Figure 2.7(a)). It can be viewed as a drastic truncation of the infinite staircase considered in Figure 2.5(b). From [19], it was found that the lens system exhibits stability when a comparatively low imposed back pressures p_b is placed across the structure. In contrast, for higher applied pressure, the structure tends to undergo a topological transformation despite the channel being entirely straight. The simple lens topological transformation involves a very particular route by which the structure can break up; the vertex moves upwards approaching to the upper channel wall and the film that connects the vertex and a side wall (front film) shrinks to zero, and subsequently the spanning film detaches from the lens bubble, leaving this behind (see Figure 2.7(b)). This topological transformation involving a vertex reaching the upper wall will be called in this study a $T1_u$. This is to distinguish it from a topological transformation involving a collision between two vertices away from a wall, such as was observed in [32], which will be called here a $T1_c$: although this $T1_c$ occurred for the bubble trains in [32], it cannot occur in the simple lens system (since there is only a single vertex away from the wall, hence no other vertex with which to collide). Alternatively, a system comprised of a comparatively large lens bubble (and hence a comparatively short spanning film),

might in principle undergo a $T1_l$, where a vertex reaches the lower channel wall, although this was not observed to occur in the simple lens system either [19].
By slowly (i.e. quasistatically) increasing the imposed back pressure p_b, the simple lens system can be tracked through a sequence of different steady states. These move further and further away from the original equilibrium (Figure 2.7(a)) acquiring higher and higher energies (total film length is a measure of energy here), until at some critical back pressure $p_b = p_b^*$ (p_b^* being a function of bubble area, becoming larger as the lens bubble area becomes smaller [19]), the system reaches a saddle-node bifurcation point, where a new steady solution branch (proven to be unstable for the simple lens, in [19]) meets the original one. All film lengths remain finite at the saddle-node bifurcation point so a $T1_u$ has not yet been reached. At this bifurcation point, it is not possible to keep increasing the steady state system energy by increasing the back pressure. Instead, the new steady solution branch can be tracked by expressing it in terms of a new variable (e.g. a turning angle measured along a film instead of back pressure). The new steady solution branch (albeit unstable) can now be tracked quasistatically to yet higher energies, but with p_b now decreasing as energy increases. Eventually the branch reaches an endpoint at a $T1_u$ topological transformation typically with $p_b < p_b^*$. This second branch however, being unstable, is of limited interest physically. More interesting is to increase p_b slowly along the original solution branch up to the saddle-node bifurcation point p_b^*, and subsequently follow the unsteady state evolution of the system beyond that point once stability is lost. This also results in a $T1_u$ transformation, but the rate at which this is approached [19] is now determined by the internal unsteady state dynamics of the system, irrespective of how slowly the imposed back pressure p_b is increased beyond p_b^*. Conceptually this is distinct from a situation (albeit not actually observed in [19]) in which a $T1_u$ would be reached at some critical p_b^* by following a sequence of steady state solutions branch along an entirely stable solution branch. In that case the system

could remain in a state with a very short film, arbitrarily close to a $T1_u$, for an arbitrarily long time. However, as mentioned, the simple lens was never observed to undergo quasistatic $T1_u$.

By analogy with the infinite staircase discussed earlier, it is conceivable that a truncated staircase with a *finite* number of bubbles, at least for certain choices of bubble sizes, might asymptote towards a fixed geometric structure in the limit of high imposed back pressures, without undergoing any $T1$ (neither a $T1$ reached quasistatically, nor one reached dynamically following loss of stability at a saddle-node bifurcation). As per the infinite staircase then, this fixed geometric structure would be inherently stable, simply migrating faster and faster as back pressure increased. This notwithstanding, such behaviour was never observed in the case of the simple lens, although it is admittedly a very drastic truncation of the infinite staircase [19]. Therefore in order to consider the transition from topological transformations or loss of stability to inherently stable systems, it is necessary to explore the effect of the number of bubbles upon system behaviour. The work in Chapter 5 takes a step towards that by considering a system comprised specifically of three bubbles of various sizes arranged in a staircase structure and flowing along a confined channel. The three-bubble system is deemed to be a next step up in complexity from the simple lens case and, as such, helps to bridge the gap between the simple lens and the infinite staircase. The main focus is to find, as a function of certain chosen bubble areas (bubble sizes), the aforementioned topological transformations and/or saddle-node bifurcation points, or in the absence of such situations, demonstrate inherent stability instead. The above mentioned Chapter 5, constitutes a main results chapter of the thesis as has been stated. We note however that generalisations of the viscous froth model (over and above what is considered in Chapter 5) are possible, and are found in literature (see also section 2.2.3.2 and [14, 15, 23]).

This completes the review of both the pressure-driven growth model and viscous froth model. The main results chapters obtained using these models now follow.

Chapter 3

Foam-liquid front propagation in Eulerian coordinates

This chapter is comprised of a work published in the journal Proceedings of the Royal Society A: Mathematical, Physical and Engineering Sciences, by Carlos Torres-Ulloa, Stefan Berres, and Paul Grassia. The title of the article is "Foam-liquid front propagation in Eulerian coordinates", which was published on the 18th of December 2018, volume 474, number 2220, pages 20180290, DOI `https://doi.org/10.1098/rspa.2018.0290`. In this work the pressure-driven growth model is used to capture the foam-liquid front propagation by using an Eulerian version of the model, which is based on a coupled system of Hamilton-Jacobi equation [116]. All results presented here are reproducible via analytical results detailed in the article and numerical algorithms and analytical methods detailed in this chapter. Supplementary material to this work is also presented in Appendix A. C. Torres-Ulloa carried out the simulation study under S. Berres and P. Grassia's supervision. Drafting of the article was shared between C. Torres-Ulloa, S. Berres and P. Grassia.

Summary: A mathematical model formulated as a system of Hamilton-Jacobi equations describes implicitly the propagation of a foam-liquid front in an oil reservoir, as the zero-level set of the solution variable. The conceptual model is based on the "pressure-driven growth" model in Lagrangian coordinates. The Eulerian mathematical model is solved numerically, where the marching is done via a finite volume scheme with an upwind flux. Periodic reinitialization ensures a more accurate implicit representation of the front. The numerical level set contour values are initially formed to coincide with an early-time asymptotic analytical solution of the pressure-driven growth model. Via the simulation of the Eulerian numerical model, numerical data are obtained from which graphical representations are generated for the location of the propagating front, the angle that the front normal makes with respect to the horizontal, and the front curvature, all of which are compared with the Lagrangian model predictions. By making this comparison, it is possible to confirm the existence of a concavity in the front shape at small times, which physically corresponds to an abrupt reorientation of the front over a limited length scale: much less distance than the front has propagated.

3.1 Introduction

An idealized schematic model that explains the movement of the foam front in the petroleum reservoir was introduced in [64] and [70] (as described in section 2.1). This model is used as a basis for work developed in [80] and herein. A brief description of the Lagrangian formulation of the pressure-driven growth model was already covered in sections 2.1.3 and 2.1.4, in order to understand the physics of the model. As detailed in section 2.1.3, the front is itself corresponds to the finely-textured foam zone, where all resistance to the flow is concentrated.

Recently in [104] it was proposed that an Eulerian model might overcome some of the difficulties with the computational simulation of the Lagrangian model, which requires regridding but without any indication of where to place newly added grid points (see details in section 2.1.4.1). This issue becomes particularly acute when one recognizes that the pressure-driven growth model can exhibit singularities [80], which physically are regions in which the finely-textured foam front reorients significantly over a small distance. Although we choose to employ an Eulerian model in this work, originally pressure-driven growth was formulated as a Lagrangian model (see details in section 2.1.4). Hence previous model formulations have been Lagrangian (following front material points) [80,91,104,112,114]. In a Lagrangian scheme one can never be certain whether a singularity computed numerically is really present in the physical model or is merely an artifact of misplacement of newly added or newly injected Lagrangian grid points. In [104] some preliminary Eulerian data were discussed (and indicated a small concavity in the front shape), but [104] did not describe in detail how those data were obtained. The present chapter provides the details.

A set of asymptotic analytical solutions of the Lagrangian pressure-driven growth model developed in [80], [104] and [114] have shown that over time a gap appears between the top boundary and material points on the front initially near the top boundary, and that is an essential part of the physics (material points slightly below the top boundary move downwards as well as sideways). This situation is described in more detail in Appendix A. To address this issue, a method is sought to describe the front evolution without the need to handle injected Lagrangian points. It is proposed to reformulate the model in Eulerian coordinates, since this type of formulation does not require a continuous monitoring of the material points. Instead it fixes the physical domain and measures how the front evolves through that domain. Eulerian simulation thereby detects jumps or kinks in the

front orientation angle, which are difficult to identify with a Lagrangian model.

The purpose of this current chapter is to show the reformulation of the pressure-driven growth model as an Eulerian one (see section 3.2), to present the numerical implementation of the Eulerian model (which needs to be formulated in terms of two dependent variables rather than just a single one), and to examine Eulerian data in more detail, including a full description of the methodology used to obtain them. The present work is arranged as follows. In section 3.2 the general context of the Eulerian solution is introduced, explaining the mathematical formulation for the pressure-driven growth model, using Eulerian coordinates. Then, in section 3.3 a description is given of the numerical scheme by which the new model was solved. This leads to the results, in section 3.4, where the comparison between the Lagrangian and Eulerian model is made, using the explicit representation for the front at different times and also measuring the curvature and the orientation angle of the front. The conclusions are given in section 3.5.

3.2 Eulerian model

In this section the Eulerian model for foam-liquid front propagation is presented and its connection to a Lagrangian model is shown. The Eulerian model is expressed using the Hamilton-Jacobi equation [151], which in general terms can be written as

$$\Phi_t + \mathcal{H}(\nabla\Phi) = 0, \tag{3.1}$$

where $\Phi = \Phi(\mathbf{x}, t)$, $\mathbf{x} \in \mathbb{R}^m$, and the Hamiltonian $\mathcal{H}$ depends on the gradient $\nabla\Phi$. The front is implicitly represented as a zero-level set where $\Phi = 0$. To simulate the propagation of the implicit representation for propagation fronts, we make use of the Level Set Method [152], an established robust technique to simulate the evolution of curves. The method can be used to solve problems that involve the

movement of curves and boundaries, for example the propagation of fire fronts [153], surface reconstruction [154], and also to predict the deformation patterns of multi-layered materials [155]. The method evolves a function $\Phi = \Phi(\mathbf{x}, t)$ with special focus on a manifold of co-dimension one (i.e. a surface in a three-dimensional domain and a curve in a two-dimensional domain), which is implicitly described as a zero-level set where $\Phi = 0$. These manifolds propagate in a normal direction with a specified velocity [156]. We adopt a sign convention in which the direction of front propagation is taken to be in the $+\nabla\Phi$ direction, rather than in the $-\nabla\Phi$ direction. The Eulerian model developed in this paper has however some special features over and above a "standard" level set technique, and these features are described below.

3.2.1 Eulerian model derivation

Equations are taken in dimensionless form throughout. The Eulerian model uses the front propagation velocity $\mathbf{U} = (u, v) = \dot{\mathbf{x}}$ such that $\mathrm{d}x/\mathrm{d}t = u$ and $\mathrm{d}y/\mathrm{d}t = v$. Here u and v are propagation velocities in x and y direction, respectively. The Eulerian model is formulated by a Hamilton-Jacobi equation as follows

$$\frac{\partial \Phi}{\partial t} + u\frac{\partial \Phi}{\partial x} + v\frac{\partial \Phi}{\partial y} = 0, \tag{3.2}$$

where the front is expressed implicitly as zero-level set of the solution variable $\Phi = \Phi(x, y, t)$, which depends on time and two spatial dimensions. It takes positive values on the right side of the front, ($\Phi > 0$), a zone which (in the surfactant-alternating gas foam improved oil recovery system as considered here) corresponds to the liquid, and it takes negative values on the left side, ($\Phi < 0$), a zone which corresponds to the foamed gas, see Figure 3.1. The time evolution of Φ is determined in the two space dimensions by the corresponding front propagation velocity $\mathbf{U}$ with components u and v. The velocities correspond to those

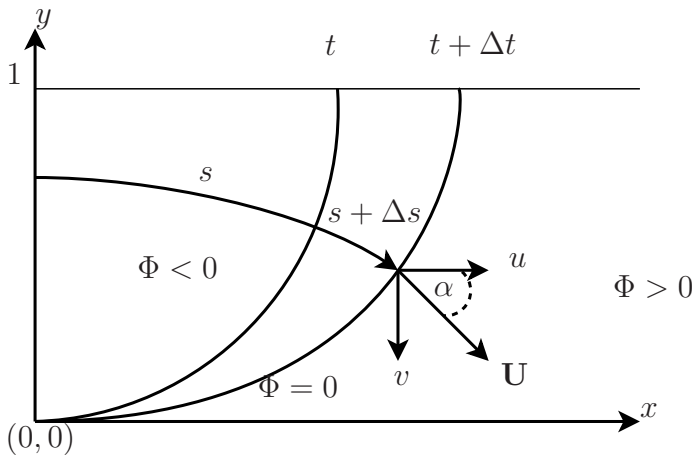

Figure 3.1: Dimensionless Eulerian model solution domain, with $x \in [0, \infty)$, $y \in [0, 1]$ and $t \in [0, \infty)$, showing also dependent variables Φ and s.

established in the Lagrangian model (equations 2.5):

$$\mathbf{U} = \begin{pmatrix} u \\ v \end{pmatrix} = \frac{y}{s}\mathbf{n}. \tag{3.3}$$

For the Eulerian model the normal $\mathbf{n}$ of the propagating front is determined as [157]

$$\mathbf{n} = \frac{\nabla\Phi}{|\nabla\Phi|} = \frac{1}{\sqrt{\Phi_x^2 + \Phi_y^2}} \begin{pmatrix} \Phi_x \\ \Phi_y \end{pmatrix}, \tag{3.4}$$

where the notation $|\cdot|$ corresponds to the Euclidean norm. The complication in this model, compared to a conventional Hamilton-Jacobi system is that $\mathbf{U}$ depends on the path length s (viz. equations (2.7) and (2.8) as given in section 2.1.4). Hence the equation (3.2) is insufficient as it gives an evolution equation solely for Φ; in fact, it is necessary to obtain an evolution equation for s also. The length of the trajectory s evolves similarly to Φ as it convects the same way. It is still possible to determine Lagrangian particle paths, even given an Eulerian field, so the concept of path length or distance travelled by each material point retains its meaning. During the convection s increases according to the travelled path,

incrementing at a rate $|\mathbf{U}| = \sqrt{u^2 + v^2} \equiv y/s$, according to equation (2.9) given in section 2.1.4. Therefore, the time evolution of s is described by a Hamilton-Jacobi equation with a source term as

$$\frac{\partial s}{\partial t} + u\frac{\partial s}{\partial x} + v\frac{\partial s}{\partial y} = \frac{y}{s}, \tag{3.5}$$

where the source term models the increment of the trajectory length. Although s can be computed globally, only values of s in the neighbourhood of $\Phi = 0$ level set are required. With the goal of simplifying the equations, we apply the definition of the front normal as a gradient (3.4) to the definition of the velocity (3.3), which in turn is substituted into the transport equation (3.2) giving

$$\Phi_t + \frac{y}{s}|\nabla\Phi| = 0. \tag{3.6}$$

For the evolution of s given by the equation (3.5), we have (again substituting from (3.3))

$$s_t + \frac{y}{s}\left(\frac{\nabla\Phi\cdot\nabla s}{|\nabla\Phi|} - 1\right) = 0. \tag{3.7}$$

Generalizing, the system composed for equations (3.6) and (3.7), has the structure

$$\Phi_t + \mathcal{H}(y, s, \nabla\Phi) = 0, \tag{3.8}$$

$$s_t + \mathcal{G}(y, s, \nabla s, \nabla\Phi) = 0, \tag{3.9}$$

where both equations, (3.8) and (3.9), have to be solved in a coupled way, with $\mathcal{H}$ and $\mathcal{G}$ as the respective Hamiltonians,

$$\mathcal{H} = \frac{y}{s}|\nabla\Phi|, \tag{3.10}$$

$$\mathcal{G} = \frac{y}{s}\left(\frac{\nabla\Phi\cdot\nabla s}{|\nabla\Phi|} - 1\right). \tag{3.11}$$

The boundary conditions of the coupled system (3.8)–(3.9) are

$$\Phi(t, x, y = 1) = x - \sqrt{2t}, \quad s(t, x, y = 1) = \sqrt{2t}, \tag{3.12}$$

as was established in [64] and [70], noting that the evolution of the front at the top, i.e. at $y = 1$ is described by $x = \sqrt{2t}$. On the other hand, at $x = 0$, $s = 0$, and $\Phi = -\sqrt{2yt}$. Since we are ultimately interested only in how the zero-level set propagates, the choice of boundary conditions is non-unique, but the choices indicated here have the advantage of keeping Φ on the boundary relatively close to being distance from the zero-level set. Finally, as the model considers first-order equations, we need only one boundary condition per spatial dimension (that applies to both equations (3.8) and (3.9)), whilst information propagates from the top ($y = 1$) downwards and from the left ($x = 0$) rightwards. The initial conditions of the coupled system (3.8)–(3.9) are

$$\Phi(t = \varepsilon^2/2, x, y) = x - \sqrt{y\varepsilon^2}, \quad s(t = \varepsilon^2/2, x, y) = \sqrt{y\varepsilon^2}, \tag{3.13}$$

where $\varepsilon \ll 1$. The value of ε is fixed for simulation purposes equal to just a few times the grid spacing (in section 3.4). A finite ε avoids the need to consider times all the way down to $t = 0$ (at which velocities are theoretically infinite). The term $\sqrt{y\varepsilon^2}$ in the initial condition (3.13) arises from an early-time analytical solution, called the Velde solution, which is a good approximation for the front shape at early times ($t \ll 1$) [70, 80, 114]. We start with a small but non-zero ε which keeps s non-zero within the denominators of (3.6)–(3.7). This establishes that at time $t = \varepsilon^2/2$ the zero-level set is situated just slightly shifted from the y axis. Intuitively results should be insensitive to ε, since both equations (3.13) already incorporate an early time asymptotic behaviour of the system. Concluding, the Eulerian model to solve consists of the equation system (3.8)–(3.9) together, with the corresponding initial and boundary conditions.

3.3 Numerical scheme

In this section the numerical method to solve the presented mathematical model in the form of a strongly coupled system of Hamilton-Jacobi equations is outlined. We remark that in the present work a full description is given of the methodology used to obtain some preliminary Eulerian results already presented by [104]. The numerical methods were *not* themselves presented in [104]. In order to obtain a numerical solution of the mathematical model and a computational simulation of the foam-liquid displacement process, first a discrete approximation of the equations (3.8) and (3.9) is needed. A finite volume scheme is used, applying an upwind flux according to [158]. This section continues as follows: first in section 3.3.1 the spatial discretization is described, in section 3.3.2 the numerical flux for Φ and s is given, in section 3.3.3 the reinitialization is introduced and how it is used in the numerical simulation is described, and finally in section 3.3.4 it is explained how the orientation angle α and curvature κ are measured for the propagation front.

3.3.1 Spatial discretization

For the spatial discretization the domain in the x and y direction is divided, for simplicity, into N_x and N_y elements of equal width $\triangle x$ and $\triangle y$, respectively. Also, the domain is enlarged on all sides of the rectangle. In the x direction it is incremented by $\triangle x/2$ on each side, and in the y direction by $\triangle y/2$ on each side. This is done so that the corners of the domain are included as the centre of the corresponding volume elements generated. For illustration see Figure 3.2, where X denotes the maximum distance at which the position of the front is required, and the points $(0,0)$, $(0,1)$, $(X,0)$ and $(X,1)$ are centre nodes of their surrounding volume elements.

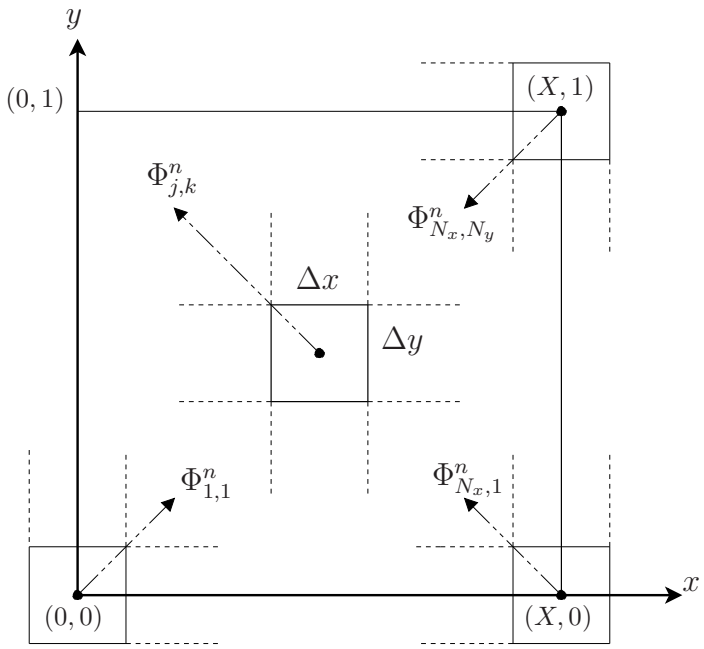

Figure 3.2: Spatial discretization over the domain $y \in [0, 1]$ and $x \in [0, X]$, where X is the maximum distance at which the position of the front is required. N_x and N_y are the number of partitions in x and y direction respectively: partitioned into equal sized areas ($\Delta x = \Delta y$). Here $j \in \{1, ..., N_x\}$ and $k \in \{1, ..., N_y\}$ are the coordinates of the node, associated with a value of $\Phi^n_{j,k}$ at the time t^n.

3.3.2 Numerical flux

In order to solve the governing equations in the form of a two-dimensional system of two strongly coupled Hamilton-Jacobi equations, we use a coupled finite volume scheme, with an upwind flux, the flux being the numerical approximation of equations (3.10) and (3.11) [158]. According to the scheme, in time step t^n, the variable is reconstructed by a piecewise polynomial and evolved to time step t^{n+1}. For the stepwise numerical solution one assumes that the discrete approximation in the nodes (j,k) at time $t = t^n$ is given by $\Phi^n_{j,k} \approx \Phi(x_j, y_k, t^n)$. To evolve the solution at these points to time $t = t^{n+1}$ one utilizes a fully upwind version of the numerical flux of [158], which establishes that Φ and s evolve at a rate

$$\frac{\mathrm{d}}{\mathrm{d}t}\,\Phi_{j,k}(t) = \mathcal{H}(y, s, \Phi_x^-, \Phi_y^+), \qquad \frac{\mathrm{d}}{\mathrm{d}t}\,s_{j,k}(t) = \mathcal{G}(y, s, \Phi_x^-, \Phi_y^+, s_x^-, s_y^+), \tag{3.14}$$

respectively, where $\mathcal{H}$ and $\mathcal{G}$ are given by equations (3.10) and (3.11), and where Φ_x^-, Φ_y^+, s_x^- and s_y^+ are the derivatives x and y in a given direction relative to the referred volume. We only need Φ_x^-, Φ_y^+, s_x^- and s_y^+ since for the specific curve shape as indicated in Figure 3.1 we expect $\Phi_x > 0$ and $\Phi_y < 0$, which implies that $\partial\mathcal{H}/\partial\Phi_x \geq 0$ and $\partial\mathcal{H}/\partial\Phi_y \leq 0$, and analogously for s, $\partial\mathcal{G}/\partial s_x \geq 0$ and $\partial\mathcal{G}/\partial s_y \leq 0$. This indicates that the numerical flux is entirely upwind. Even though the upwind flux holds for the specific front shapes to be considered in the present work, a general numerical flux (see Appendix A.3) is needed in order to deal adequately with model extensions including heterogeneities and anisotropies [158]. In each time step, both equations for Φ and s are evolved simultaneously. Which equation (Φ or s) is treated first is irrelevant, because in order to obtain $\Phi^{n+1}_{j,k}$ and $s^{n+1}_{j,k}$, in each case, the data for $\Phi^n_{j,k}$ and $s^n_{j,k}$ are only used once. To calculate Φ_x^-, Φ_y^+, s_x^- and s_y^+ we suppose that we have approximated Φ at time $t = t^n$ for all nodes. Then, we carry out a piecewise quadratic interpolation

in both spatial dimensions, from which subsequently we obtain the expressions for the derivatives (see Appendix A.3). For the temporal discretization of Φ and s we use the Euler method,

$$\frac{\mathrm{d}}{\mathrm{d}t}\Phi_{j,k}(t) \approx \frac{\Phi_{j,k}^{n+1} - \Phi_{j,k}^{n}}{\triangle t}, \qquad \frac{\mathrm{d}}{\mathrm{d}t}s_{j,k}(t) \approx \frac{s_{j,k}^{n+1} - s_{j,k}^{n}}{\triangle t}. \tag{3.15}$$

To ensure numerical stability in the evolution of the equations according to [159] one sets

$$\triangle t < \frac{\min(\triangle x, \triangle y)}{\max\{|a_{j,k}^{-}|, |b_{j,k}^{+}|\}}, \tag{3.16}$$

where $a_{j,k}^{-}$ and $b_{j,k}^{+}$ are the local propagation velocities in the x and y direction respectively (see Appendix A.3). The time step size is adapted according to the evolution speeds of s and Φ by setting the Courant-Friedrichs-Levy (CFL) number to 0.475, following [158].

3.3.3 Reinitialization

In the calculations of the Level Set Method, usually the discrete representation of the level set function develops non-smoothness during its evolution, since numerical errors increase. This impacts the structure of the solution and finally destroys the stability of the scheme [156]. To correct this, a numerical strategy is introduced, which is known as reinitialization. It restores the regularity of Φ and stabilizes its time evolution. The reinitialization is done after each time step. Then the degraded solution Φ is converted into a distance function, see [152]. This distance function measures the distance to the zero-level set such that its absolute value corresponds to this distance, and its sign is retained. One method to realize the reinitialization is to solve the evolution equation obtained in [156], namely

$$\frac{\partial \Phi}{\partial t'} = \mathrm{sign}(\Phi)(1 - |\nabla \Phi|), \tag{3.17}$$

where t' is an "artificial" time, sign(Φ) is a sign function which takes the value 1 in the region where $\Phi > 0$, -1 where $\Phi < 0$, and 0 on the interface $\Phi = 0$ level set. Smooth behaviour of Φ is not guaranteed, since the interface itself is computed numerically [156]. In this work, the method suggested in [160] is used, where equation (3.17) is solved, but the numerically smoothed version of the sign function

$$\text{sign}(\Phi) = \Phi(\Phi^2 + |\nabla\Phi|^2(\triangle x)^2)^{-1/2}, \tag{3.18}$$

is used. Note that the equation (3.18) works reliably for a square spatial partition, i.e. $\triangle x = \triangle y$, that corresponds (for most of the calculations to be considered here) to the case of the present solution. During the application of the reinitialization using this equation, the value of sign(Φ) needs to be constantly updated during the evolution of Φ, that evolves in time until a steady state is reached, typically in two artificial time steps (t') if the reinitialization is executed in each time step (t). The reinitialization helps to obtain a notably smoother shape of the front and in particular for the front curvature.

3.3.4 Calculation of front orientation angle α and curvature κ

As was mentioned before, the Eulerian and Lagrangian model results can be compared via the orientation angle and the curvature along the front, in addition to comparing the front location. The angle α is the angle measured between the normal $\mathbf{n}$ of the front and the horizontal straight line parallel to x axis and the curvature κ is a spatial derivative of this. To compute the orientation angle at all points of a front for a given time t, first, an explicit representation $(x_i, y_i),\ i \in \{1, ..., N_y\}$ of points on the front is obtained from the implicit representation by the curves of level zero by a linear interpolation of the data of Φ. From these

points on the front the angle is approximated as

$$\alpha_i = \arctan\left(\frac{x_i - x_{i+1}}{y_i - y_{i+1}}\right), \qquad i \in \{1, ..., N_y - 1\}.$$

Once the orientation angle α for each point on the front is calculated, the curvature can be estimated as (see also equation (A.13) in Appendix A.2)

$$\kappa_i = \frac{\alpha_{i+1} - \alpha_i}{\sqrt{(x_i - x_{i+1})^2 + (y_i - y_{i+1})^2}} \qquad i \in \{1, ..., N_y - 1\}.$$

Another way to obtain the curvature, which is used in this work following [156], is to calculate it in terms of Φ by the function

$$\kappa = \frac{\Phi_{yy}\Phi_x^2 - 2\Phi_x\Phi_y\Phi_{xy} + \Phi_{xx}\Phi_y^2}{(\Phi_x^2 + \Phi_y^2)^{(3/2)}}. \tag{3.19}$$

Both α and κ are calculated numerically for grids of various different resolutions. The results are shown in the next section.

3.4 Results

In this section, results of the computational simulation of the Eulerian model of the system of equations (3.8) and (3.9) are presented in comparison to the (Lagrangian) pressure-driven growth model. Specifically the front shape, the front orientation angle α and the curvature κ are shown compared with the analytical solutions of [80] and [104]. First in section 3.4.1 we present the numerical results of the front shape, in section 3.4.2 the front orientation angle α is shown revealing the presence of a concave corner or kink, in section 3.4.3 the computation of the curvature κ is shown, and finally in section 3.4.4 the numerical representation for the movement of the kink through the front is given as a function of the time.

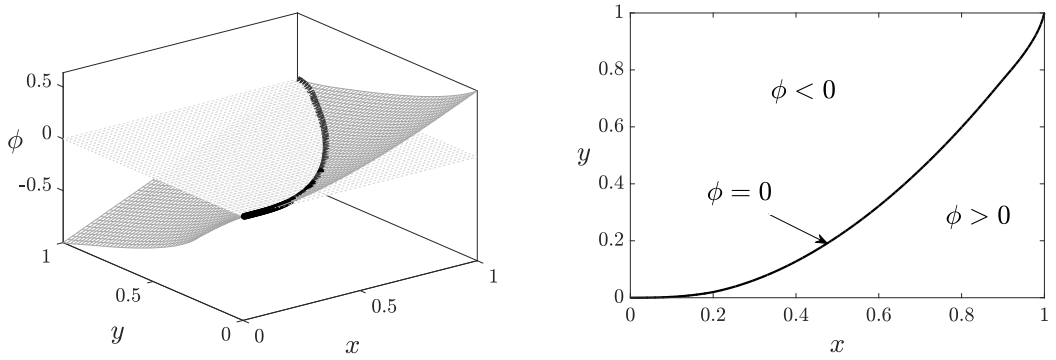

(a) (b)

Figure 3.3: Foam-liquid front at evolution time $t = 0.5$ over the domain $0 \leq x \leq 1$, $0 \leq y \leq 1$. (a) Intersection of surface Φ with plane xy. (b) Contour line of zero-level set $\Phi = 0$.

3.4.1 Front shape

The front shape obtained by the computational simulation of the Eulerian model given by the system of two Hamilton-Jacobi equations (3.8) and (3.9) is shown in Figures 3.3 and 3.4. The simulations are realized with a $N_x = N_y = 200$ grid. In Figure 3.3(a) the values of solution Φ at time $t = 0.5$, over the domain $(x, y) \in [0, 1]^2$ are shown, and the intersection of Φ with the xy plane, which represents the propagating foam-liquid front, where $\Phi = 0$, is highlighted. An explicit representation of the front is shown in Figure 3.3(b), where the values of Φ for the zero-level set and on both sides are indicated. In Figure 3.4 one can see that the numerical solutions of the Eulerian model are visually similar to the results of the (Lagrangian) pressure-driven growth model, independently of the time.

The model has been set up using an early asymptotic solution (as was established by the equation (3.13)), in such a way that ε should have hardly any bearing on the results. In order to verify the limited effect of ε in the front shape, we have calculated the front position for $\varepsilon \in [10^{-2}, 10^{-3}, 10^{-4}]$ from time $t = \varepsilon^2/2$ to time $t = \hat{\varepsilon}^2/2$ (with $\hat{\varepsilon} = 10^{-1}$). The front displacement error (averaged over the length of the front) compared with the known asymptotic analytical solution at time

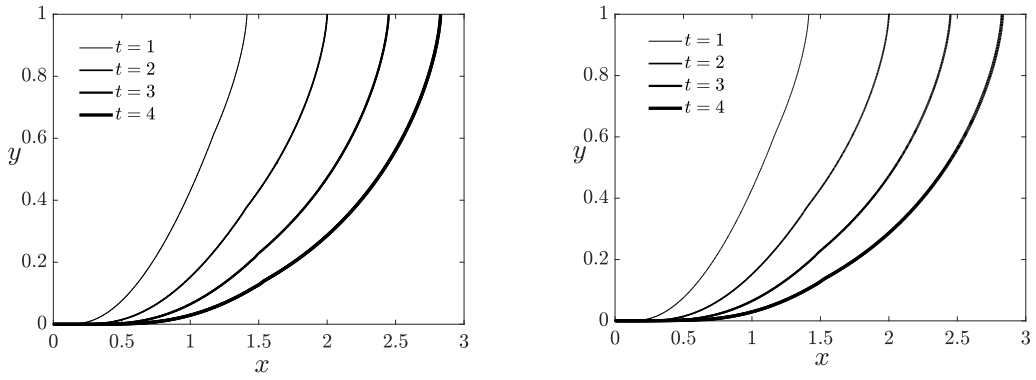

(a) (b)

Figure 3.4: Front position on domain $(x, y) \in [0, 3] \times [0, 1]$. (a) Lagrangian model, (b) Eulerian model.

$t = \hat{\varepsilon}^2/2$, for each ε studied, is equal to 7.49×10^{-4}, 8.01×10^{-4} and 8.05×10^{-4}, which, given that the top of the front has already displaced by $\hat{\varepsilon}$, implies a good agreement at early times and consequently at later time also. It was also found, measuring the absolute error, that the order of convergence (respect to spatial refinement) of the solution is approximately equal to 2, which is in concordance with the numerical method used [158].

As was mentioned before, at the top of the front ($y = 1$) the orientation angle $\alpha = 0$, however, it turns out that immediately below the top it grows like square root of distance from the top [80]. As a result, the angle can be quite significant even at relatively small distance below the top. This can be difficult to appreciate in Figure 3.3(b), but it becomes clear when measuring the front orientation angle α (as will be discussed in section 3.4.2).

Specifically in Figure 3.4 the data obtained with the (Lagrangian) algorithm and numerical parameter values in [80] are compared with those of the computational simulation using the Eulerian model for times $t \in \{1, 2, 3, 4\}$. The agreement seen between data from the original Lagrangian model (Figure 3.4(a)) and the Eulerian

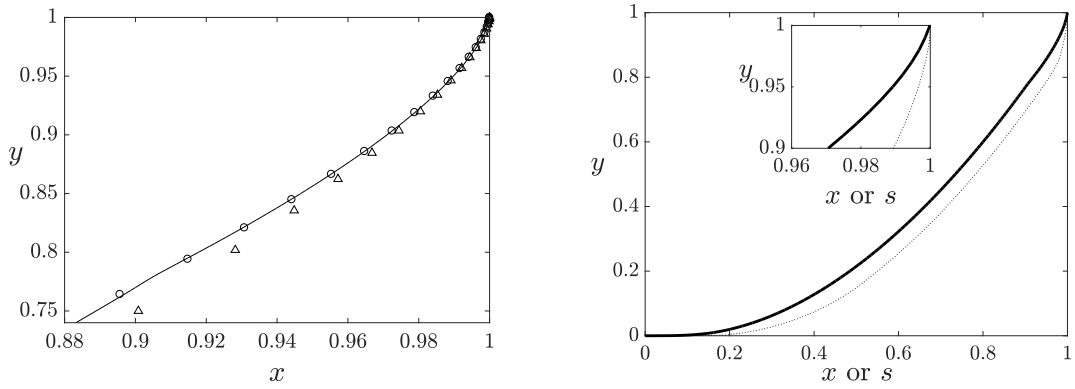

Figure 3.5: (a) Zoom on domain $(x, y) \in [0.88, 1] \times [0.74, 1]$ for $t = 0.5$. Solid line: Numerical results by solving Hamilton-Jacobi equation system. "△": Analytical solution from [104], taking $c = 1$ (see Appendix A.2). "○": Analytical solution from [104], taking $c = 0.75$ (see Appendix A.2). (b) Position of foam-liquid front and trajectory length at $t = 0.5$ over domain $(x, y) \in [0, 1]^2$, calculated with a $N_x = N_y = 200$ grid. Dotted line: length of trajectory s. Solid line: Front position.

model (Figure 3.4(b)) proves that the Eulerian model is being computed correctly. In Figure 3.5(a) the numerical solution for the Hamilton-Jacobi equation system is plotted for the points near to the top boundary. This is done in order to make a comparison between the Eulerian model and an approximate analytical similarity solution, developed in [104]. This similarity solution depends on a parameter c, defined such that $2c - 1$ is the ratio between $\mathrm{d}s/\mathrm{d}y$ and $\mathrm{d}x/\mathrm{d}y$. Since s is approximately equal to x near the top, it might be thought naively that $c = 1$. However this ignores the fact that both $\mathrm{d}s/\mathrm{d}y$ and $\mathrm{d}x/\mathrm{d}y$ are equal to zero at the top. When the problem is formulated correctly, it is possible to obtain that $c = 0.75$ right at the top, and moreover (using an integro-differential approach presented in [104]) the value of c remains effectively constant over the entire upper region of the front (see sections 2.1.4 and 2.1.4.2 for a description of the upper region), moving downwards from the top. The form of those similarity

expressions can be found in Appendix A.2 and as seen in Figure 3.5(a), the case $c = 0.75$ gives an excellent fit. To corroborate this, in Figure 3.5(b) the position of points x on the front is compared to the length of trajectory s, i.e. for given value of y (and for a given value of t) the magnitude of x and s is shown. For all material points the trajectory length s is greater than the front displacement x because points move both downwards and sideways. Even at the top $y \approx 1$, where $s \approx x$, we observe that $\mathrm{d}s/\mathrm{d}y$ is less than $\mathrm{d}x/\mathrm{d}y$, as was deduced in [104]. Since the ratio between $\mathrm{d}s/\mathrm{d}y$ and $\mathrm{d}x/\mathrm{d}y$ equals $2c - 1$, it is clear that c is less than 1 near the top.

3.4.2 Front orientation angle α

For a more stringent comparison between our Eulerian numerical data and predictions of the early-time asymptotic theories, the orientation angle and the curvature are measured. Note that the front orientation angle is zero at the top of the front ($y = 1$) at all times, and approaches $\pi/2$ at the bottom of the front ($y = 0$) at least in the limit of long times. Figure 3.6 (solid line) shows the Eulerian data of the orientation angle α at time $t = 0.5$ over the domain $[0, 1] \times [0, 1]$ with a grid $N_x = N_y = 400$. The front shapes presented in section 3.4.1 are continuous and can be resolved with relatively few grid point ($N_x = N_y = 200$ grid in the case), whereas for derivative quantities like the front orientation angle α and curvature κ (which exhibit discontinuities) a refined grid is necessary to resolve the location of the kink (Figure 3.7 shows the effect of having a low resolution in such a case). In Figure 3.6, a kink or discontinuity in the front orientation angle α around location $y \approx 0.78$ can be seen at this time ($t = 0.5$). This situation has already been discussed in [104]. It corresponds to the foam front reorienting itself on a small distance comparable with the thickness of the finely-textured foam front (rather than comparable with the much longer length scale over which the front has propagated). The kink or discontinuity in α arises due to an incompatibility

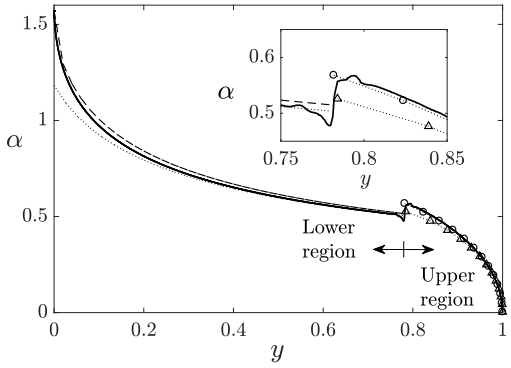

Figure 3.6: Front orientation angle α of the numerical Eulerian model (solid line, with $N_x = N_y = 400$ grid) vs analytical solutions for $t = 0.5$ on domain $(x, y) \in [0, 1]^2$. For the lower region the improved Velde solution, equation (A.3) (dotted line) and the Velde solution (dashed line) are plotted. In the upper region, two analytical expressions from [104] are plotted: ("△") $c = 1$ and ("○") $c = 0.75$ (see Appendix A.1 and A.2).

between material points which have continuously been on the foam front since time zero (which are unaware of the top boundary condition) and material points which have been newly injected from the top boundary since time zero (and which are influenced by the top boundary condition). This corresponds to a concave corner in the x versus y representation of the front albeit one that is not easy to recognize in Figure 3.5. Following section 2.1.4, we refer to the points above the concave corner as the "upper" region and points below it as the "lower" region. Approximate analytical formulae (see Appendix A.1 and A.2) are available to describe each region. Figure 3.8 shows good agreement between numerical and analytical results in each case.

Even though the angle α is sufficient to show how similar the new Eulerian solution is to the Lagrangian representation of the front considered by [104] and also sufficient to show the appearance of a kink in the angle (strong evidence of a concave corner as per [104]), in order to obtain an even more stringent test of

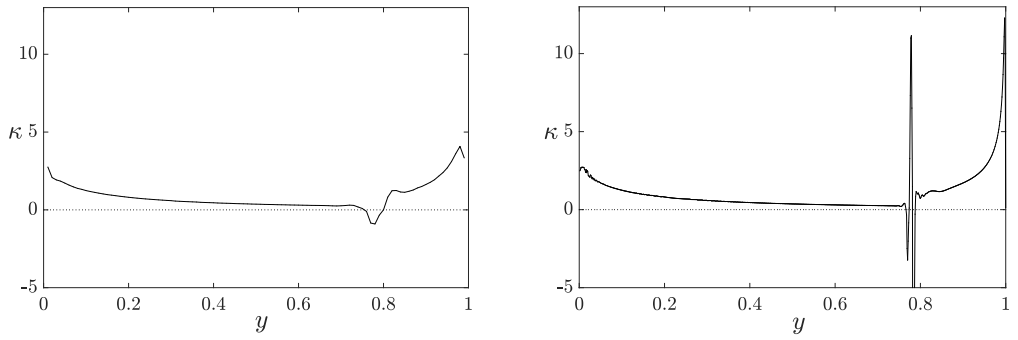

(a) (b)

Figure 3.7: Curvature κ for two different grid refinement levels at the time $t = 0.5$. (a) $N_x = N_y = 100$ and (b) $N_x = N_y = 800$.

the Eulerian formulation the curvature is measured in the next subsection.

3.4.3 Front curvature κ

Owing to the jump or kink in the angle, we expect the curvature to be large and negative at the kink point (specifically to scale inversely with the grid spacing in our numerical scheme). There may also be some numerical diffusivity [161], causing points near the kink to be affected as well. In Figure 3.7 the numerical values of the curvature obtained by the Eulerian numerical simulation of the front propagation is shown for $t = 0.5$ with grid partitions $N_x = N_y = 100$ (Figure 3.7(a)) and $N_x = N_y = 800$ (Figure 3.7(b)) over the domain $(x, y) \in [0, 1]^2$. Unsurprisingly the curvature computed at the kink itself becomes more significant if the grid is refined. Moreover, oscillations in the values of curvature κ appear close by the kink, but these are numerical artifacts. What is of more interest here however is how the curvature computed via equation (3.19) changes away from and on the approach to the kink. As can be seen in Figures 3.7 and 3.8 the curvature is largest near the top and bottom of the domain, but decreases on the approach to the kink. Because of its location (in an otherwise comparatively

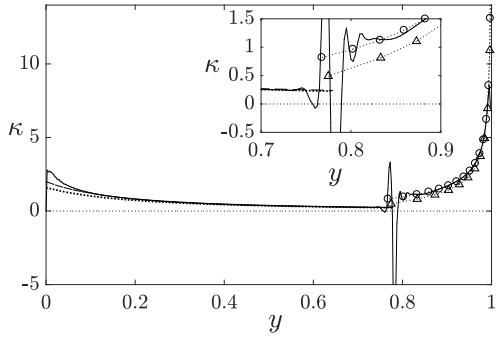

Figure 3.8: Front curvature κ of the numerical Eulerian model (solid line, with $N_x = N_y = 400$ grid points) vs analytical solutions for $t = 0.5$ on domain $(x, y) \in [0, 1]^2$. For the lower region, equation (A.4) (dotted line) and the Velde solution (dashed line) are plotted. In the upper region, two analytical expressions deduced from [104] are plotted: ("△") $c = 1$ and ("○") $c = 0.75$ (see equation (A.14) in Appendix A.2).

low curvature region), the behaviour at the kink could be misinterpreted, for the Lagrangian method, as a consequence of possible misplacement of material points. Under such circumstances, a convex front shape can be switched to a concave one merely by very small point misplacements. The Eulerian model (which does not require that the material points be tracked) does not suffer from this disadvantage, and moreover in Figure 3.8 is seen to agree with approximate analytic curvature predictions (see Appendix A.1 and A.2).

3.4.4 Kink position as function of time

In Figures 3.6, 3.7 and 3.8, it was possible to examine the location of the kink or discontinuity (identified as the steepest part locally on the α versus y curve) with different numbers of grid points over the same domain at the same time, and this situation was also compared with some analytical expressions for the front itself, in both the lower region and the upper region. The interesting aspect here is to analyse how the location of the kink evolves with time. This fact was already

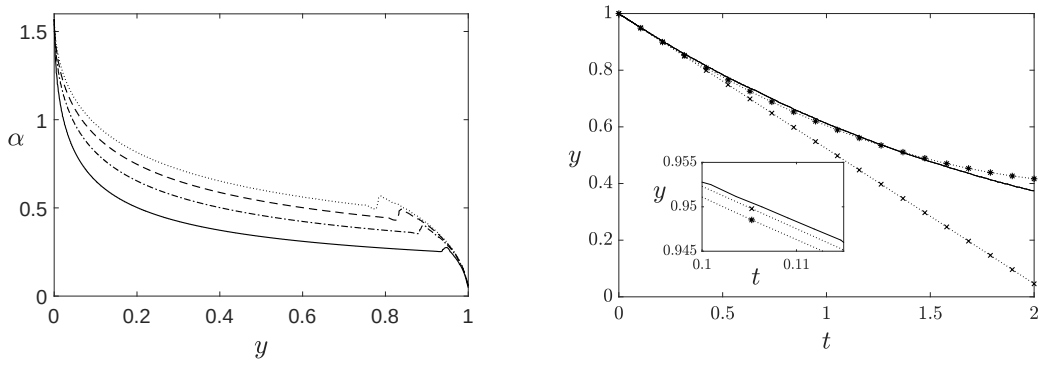

Figure 3.9: (a) Orientation angle α for different times, over the domain $(x, y) \in [0, 1] \times [0, 1]$ with $N_x = N_y = 400$. Dotted line: $t = 0.5$, dashed line: $t = 0.375$, dot-dashed line: $t = 0.25$, solid line: $t = 0.125$. (b) Kink position y as a function of the time t (over the domain $(x, y) \in [0, 2] \times [0, 1]$) for the Eulerian data (solid line, grid of $N_x = 800$ and $N_y = 400$) and the position y of material points initially just beneath the top determined by the equation (A.2), with initial vertical location $y_0 \to 1$ ("$*$"), and equation $y = 1 - 0.954t/2$ ("$\times$") discussed in [104].

mentioned in [104], where it was established that the location of the kink would be at $y = 1 - 0.954t/2 + O(t^2)$. This was predicted via a similarity solution, but not validated against numerical data.

Numerical data are presented here in Figure 3.9. Specifically 3.9(a) examines how the front orientation angle α as a function of height y evolves over time. In Figure 3.9(b) it is shown how the kink moves in the y direction (solid line) as a function of time, the kink position heuristically being detected as the position of the steepest positive derivative of the angle. In the Lagrangian picture, as points are injected from the top, it is thought that the concavity is a result of the collision of those injected points with those originally along the y-axis (see Figure A.1). The movement of the kink through y over the time can be fit to a quadratic function of order t^2 with the form of $y = 1 + a_1 t + a_2 t^2$, where the parameters a_1 and a_2 were found through interpolation. The fitted parameters after interpolation within the

interval $t \in [0, 2]$ over the domain $(x, y) \in [0, 2] \times [0, 1]$ are $a_1 = -0.4635$ and $a_2 = 0.0784$, which vary only very slightly from equation (A.2) (see Appendix A.1) that was obtained by tracking a material point initially at the top of the lower region. We see that, for much of the evolution, the predicted location of the kink according to the curve fit is actually very slightly below what is predicted by equation (A.2) which gives the location of the material point initially at the top of the front. This is the opposite of what was found in [104] via a first-order theory in time, which predicted the location of the concave corner or kink via a linear equation $y = 1 - 0.954t/2$, which is higher up that the material point initially at the top given by $y = 1 - t/2$ at first order (see equation (A.1)). Equation (A.2) is however itself just an asymptotic expansion of a Lagrangian model (albeit now to second-order not first-order in time). The zoomed inset in Figure 3.9(b), at early time $t \approx 0.1$, shows the prediction of (A.2) being below the first-order prediction for the kink location, but the numerical kink location is above either of them. Whether the location of the kink is above or below the location of the uppermost material point initially on the front is inconclusive, but what is clear is that these two locations are close to one another and they can only be distinguished numerically using a high resolution grid.

3.5 Conclusions

We have simulated the shape of a foam-liquid front evolving via pressure-driven growth but using an Eulerian model. The simulation results of the Eulerian model are largely similar to the Lagrangian results of [80]. Good agreement, not only between Eulerian and Lagrangian numerical solutions, but also between Eulerian results and an asymptotic analytical solution from [104] were found. These results mutually validate all these various methods, in particular those with respect to front orientation angle and front curvature, see Figures 3.4, 3.6 and 3.8.

With the developed computational code, systems of Hamilton-Jacobi equations are solved. As a guideline for spatial discretization and explicit time discretization by the Eulerian method as a reference the work of [158] was taken. In the Eulerian model the front representation is determined implicitly as a zero-level set. This implicit representation liberates us from the necessity to inject material points explicitly onto the front from the top, as would be required by the simulation of the Lagrangian model, making the Lagrangian model susceptible to errors in the event that those newly injected points are wrongly placed.

Though the Eulerian solution is implicit, expressing the front position as the zero-level set of the solution variable Φ, one can obtain an explicit representation of the location of the front for each time instant. From the data obtained by the numerical solution of the Eulerian model, one can detect a jump or kink in the front orientation angle. This gives evidence of the existence of a sharp concavity in the front (when seen from downstream), which is evident when measuring the curvature along the front: it becomes large and negative at the kink. Although the existence of such concavity was predicted before, via an analytical Lagrangian solution obtained at early times, its predicted location was not guaranteed at later times. By knowing the existence and location of the concave corner we can be certain that the predictions of the Lagrangian numerical solution are not just numerical artifacts coming from a misplacement of new injected material points. Physically this concavity indicates that the front has reoriented itself over a small distance, in relation to the distance over which it has propagated. Mathematically this concavity can be interpreted as a consequence of the information from the top boundary condition ($\Phi(x, y = 1, t) = x - \sqrt{2t}$) propagating into the solution domain and being distinct from that associated with points originally on the front.

From the Eulerian calculations, it can be confirmed that the concavity is close to height $y \approx 1 - 0.4635t + 0.0784t^2$, for $t \leq 2$. This equation predicts a location that is very close to the vertical position of a material point originating on the y-axis immediately below the top boundary. It is then possible to demonstrate that the concave corner not only migrates downwards on the front, but also slows down as it migrates. This is perhaps unsurprising due to the depth-dependent speed related to the net driving pressure, such that at certain depth the front must eventually stop propagating. This however would happen at later times than what any Lagrangian analytical solution would be able to predict. As alluded to above, the concavity actually occurs at the point at which material points coming from the top boundary manage to arrive, assuming they are injected early on in the evolution. Since we have analytical approximations (see Appendix A.1–A.2 and also Appendix B.1 for details) to the both zones of the front (points originally on the front and newly injected ones) it is possible to estimate where they join [104]. There are however different scenarios in which they can join. Material points in the upper region are injected onto the front and subsequently consumed by the kink some time later as [104] showed. In the lower region the situation is less clear cut. If the material point that was initially at the top of the lower region remains lower down than the kink, then material points are being extracted from the kink (as happens at early times in Figure 3.9(b)). On the other hand if that material point initially at the top of the lower region is predicted to move higher up than the kink (as happens later on in Figure 3.9(b)), material points are then being consumed. One of the issues with the analytic material point location and numerical kink location being so close together in Figure 3.9(b) is that it is difficult to distinguish the two situations of points being extracted and points being consumed. One of the challenges is that we have a second order analytical estimate for the material point location (see equation (A.2) in Appendix A.1) but only a first order analytical estimate for the kink location obtained in [104].

It is possible then that obtaining an improved analytical estimate for the kink location might help to clarify the situation. This is studied in Chapter 4.

Chapter 4

Second-order accurate solution of foam front propagation in improved oil recovery

This chapter is comprised of a work published in the journal Proceedings of the Royal Society A: Mathematical, Physical and Engineering Sciences, by Carlos Torres-Ulloa and Paul Grassia. The title of the article is "Breakdown of similarity solutions: a perturbation approach for front propagation during foam-improved oil recovery", which was published on the 20th of January 2021, volume 477, number 2245, pages 20200691, DOI = `https://doi.org/10.1098/rspa.2020.0691`. In this work the pressure-driven growth model is used to capture the foam-liquid front propagation analytically with second-order of accuracy, which is based on first-order similarity equations [117]. Supplementary material to this work is also presented in Appendix B. This is also available at `https://royalsocietypublishing.org/doi/suppl/10.1098/rspa.2020.0691`. All results presented here are analytically reproducible, as detailed this chapter. C. Torres-Ulloa carried out the study under P. Grassia's supervision. Drafting of the article was shared between C. Torres-Ulloa and P. Grassia.

Chapter 4. Second-order accurate solution of foam front propagation in improved oil recovery

Summary: The pressure-driven growth model has been employed to study a propagating foam front in the foam improved oil recovery process. A leading-order similarity solution of the model proves the existence of a concave corner on the front, which initially migrates downwards at a well defined speed that differs from the speed of front material points. At later times however, it remains unclear how the concave corner moves and interacts with points on the front either side of it, specifically whether material points are extracted from the corner or consumed by it. To address these questions, an order t correction to the similarity solution is proposed (t here being time), perturbing the aforementioned first-order (i.e. leading-order) similarity solution. However the perturbation is challenging to develop, owing to the nature of the first-order solution, which exhibits strong spatio-temporal non-uniformities. The second-order solution (incorporating the aforementioned order t correction) solution indicates that the corner's vertical velocity component decreases as the front migrates, and that points initially extracted from the front are subsequently consumed by it. Overall, the perturbation approach developed herein demonstrates how early-time similarity solutions exhibiting strong spatio-temporal non-uniformities break down as time proceeds.

4.1 Introduction

The pressure-driven growth model is used to predict the shape of a propagating foam front in the context of foam improved oil recovery (foam IOR): see details in section 2.1.3. Even when a homogeneous and isotropic reservoir is considered, a first-order Lagrangian analytical solution of the model predicts a concave corner on the front, which starts at the top boundary, and then as time proceeds propagates downwards [104]. This was discussed in detail in section 2.1.4.1. This corner is also called a "matching point" since it is where we must match two regions mentioned in section 2.1.4.2 that divide the front vertically: the "lower

region" incorporating material points originally on the front, and the "upper region" consisting of newly injected points (see Figure A.1 for details). The upper region starts off being of arbitrarily small extent, but grows over time (the lower region shrinks to compensate). Likewise initially the front reorients by an arbitrarily small angle in the upper region (albeit with arbitrarily large curvature), but the amount it reorients grows over time (whereas curvature falls). Specifically it was shown by [104] that the upper region is of vertical extent relative to the maximum penetration depth of the front of order t (t here being the dimensionless time) and it reorients through an angle of order $\sqrt{t}$, making curvature become order $1/\sqrt{t}$. The corner meanwhile arises due to an incompatibility between the upper and lower regions as section 2.1.4.2 explains.

In Chapter 3 [116], the shape of a propagating foam front was obtained by using an Eulerian formulation of the pressure-driven growth model (see also section 2.1.4 for details). The shape of the front was obtained numerically by solving a coupled system of Hamilton–Jacobi equations [158], where the foam front was given implicitly, as the zero-level set [156] of the solution variable. In the Eulerian method it is not necessary to deal explicitly with the aforementioned incompatibility between the positioning of newly injected material points (upper region) and material points already on the front (lower region), since material points are not tracked at all, by contrast with what is required in a Lagrangian method (see section 2.1.4.1 for details). Nonetheless a concave corner or kink still arises, as determined in [104]. This kink was then tracked via an Eulerian scheme in Chapter 3, and its position at early times was found to be consistent with the Lagrangian estimates from [104]. However, at later times the Eulerian solution predicts that the velocity at which the kink or concave corner moves downwards on the front decreases over time, contrary to the constant speed predicted in [104]. Nevertheless, numerical artifacts may appear in the Eulerian solution, since we

can only ever capture the concave corner to within the numerical grid resolution. This then motivates a return to a Lagrangian approach, to search for an improved analytical approximation which will be free of such artifacts.

4.1.1 Concave corner and spatio-temporal non-uniformities

The position of the kink/corner can be tracked over time (see e.g. section 4.4), in terms of "similarity variables" at early times [104]. Early time here means small compared to characteristic time scale identified in [80] which is used to make the system dimensionless (see section 2.1.4 for details). Small time therefore means the top of the front has displaced horizontally by much less than the depth over which the front displaces overall.

Both above and below the corner, it is possible to capture the shape of the front analytically for small times $t \ll 1$, by using equations (2.7) and (2.8), as given in section 2.1.4, and generating approximate solution. By approximating these equations it is possible to track the trajectory of the point that was originally at the top of the front ($y = 1$ when $t = 0$). In particular for the vertical coordinate y, this can be done at first-order (order t) and also at second-order (order t^2) (assuming this point has not been consumed by the concave corner) [80, 104]. Horizontally this point lags an order $t^{3/2}$ distance behind the top of the front (which is always at location $x = \sqrt{2\,t}$ in our dimensionless system, see section 2.1.4). The trajectory of this material point which was initially at $y = 1$ gives an indication where the concave corner (or kink) may be, but not the exact location, since we are tracking a material point near the concave corner, not the corner itself. As already mentioned, what was found by [80, 104] is that the second-order correction for the vertical y location material points originally on the front predicts the material points to move down more slowly than the first-order approximation predicts. Extending this analysis to material points initially

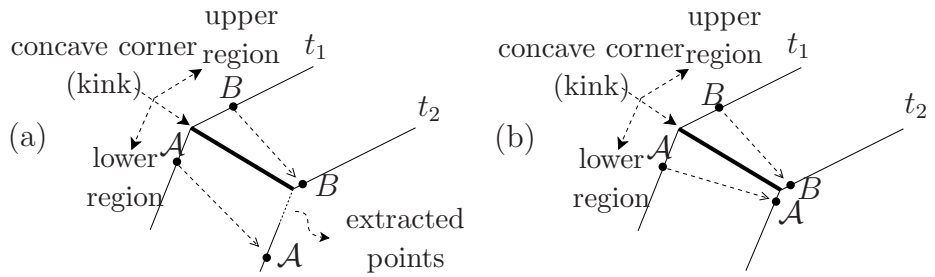

Figure 4.1: Possible trajectories of material points in the neighbourhood of the kink or concave corner. (a) Points between the fixed material point $\mathcal{A}$ and the kink, move away from it, opening a gap between times t_1 and t_2. This gap is filled by points extracted from the kink. Points between the fixed material point B and the kink, are consumed between times t_1 and t_2. (b) An alternative scenario where points between fixed material points $\mathcal{A}$ and B, and the kink/corner are consumed over a time interval between t_1 and t_2.

at $y \leq 1$, a solution is obtained for the lower region [104], to be discussed in section 4.2. In the upper region, front material points are tracked also, but this presents more of a challenge requiring, as previously mentioned, a similarity solution to be revised (see section 4.3). As mentioned before, using the similarity solution a first-order (order t) approximation to the location of the concave corner or kink was found [104]. However, as time proceeds, the first-order similarity solution deviates from a numerical and therefore more exact solution presented in Chapter 3 [116]. This first-order solution showed the corner moving downwards (at very early times) more slowly than the second-order approximation to the material point initially at the top of the lower region, which meant that new material points were being extracted from the kink or corner to populate the lower region (see Figure 4.1(a)). Nevertheless, given that the second-order approximation to the point initially at the top of the lower region indicates that material point's vertical motion slows down over time, eventually it is overtaken by the first-order approximation to the corner or kink: material points in the lower region are now being consumed by the kink, not extracted from it (see Figure 4.1(b)). In this context, extracting material points implies physically that the

zone of finely-textured foam would need to thin slightly (at least temporarily), whereas consuming/destroying such points implies that this region must thicken a little (again at least temporarily). These are just temporary effects, since away from the corner, a local balance between microscale foam generation and foam destruction mechanisms quickly restores the thickness of the finely-textured zone to its previous value (i.e. front thickness proportional to front displacement as mentioned above) on time scales much shorter than the total time for which the front propagates [108]. It is not clear however, whether this prediction of material points being extracted/consumed is the actual behaviour or merely an artifact of having a second-order approximation for one quantity (the material point) and a first-order approximation for the other (the corner). The aim of this chapter then is to obtain the second-order approximation to the corner or kink location by improving upon the first-order similarity solution in the upper region. The question we address then is whether a transition is still seen between the scenario of Figure 4.1(a) and that of Figure 4.1(b) when a consistent second-order approximation is used. Obtaining a second-order solution in the upper region is however challenging, more so than obtaining second-order solutions in the lower region was [104]. Indeed, given that the first-order solution is a similarity solution, the generic mathematical challenge we focus on here is exploring how that similarity solution breaks down at second-order. Significant spatio-temporal non-uniformities arise in the first-order similarity solution for the upper region which are already complicated to handle: a snapshot of the front shape at a fixed very early time will have very sharp curvature, whereas a material point on the front released at very early time will have rapid temporal changes in its vertical velocity component [104]. Hence, we have to perturb the upper region about a solution that evolves over arbitrarily small spatial distances at arbitrarily small times: this then is where the challenge lies. There is also a question concerning for which set of times a second-order solution might be valid given that in [104],

although the first-order solution was obtained formally for dimensionless time $t \ll 1$, it managed to describe the front shape reasonably well even for values of t up to order unity, as was determined by comparison with numerical results from an Eulerian model [116]. Hence we expect the second-order solution should also be valid over a similar time domain.

To summarise, this work expands upon the methodology used in [104], to obtain a second-order accurate solution to track the trajectory of the injected material points for $t \ll 1$, again, in terms of similarity variables in the upper region, but with small perturbations breaking the similarity. This proves challenging to do, because of the strong spatio-temporal non-uniformities associated with the similarity solution. The perturbed solution will be used to find the intersection or matching point between the lower and the upper region of the front (the concave corner or kink), consistently through to second-order. The solution will then be interrogated in an effort to establish which scenario (Figure 4.1(a) or 4.1(b)) is realised as time progresses, noting that the scenario of Figure 4.1(a) is necessarily realized at arbitrarily small times. The rest of this work is laid out as follows. In sections 4.2, 4.3 and 4.4 we review the existing methodology derived by [104], the extension to that methodology appearing from section 4.5 onwards. The second-order solution will be expressed, as before, in terms of similarity variables, but admitting small perturbations at small times $t \ll 1$ that break the similarity (see section 4.5). Then, in sections 4.6 and 4.7, using this new solution we will proceed to track the position of the concave corner with an accuracy of second-order in time t. Finally, in section 4.8, we will use the second-order solution to compute the shape of the upper region of the front, in comparison with the previous solution given in [104]. Conclusions are offered in section 4.9.

4.2 Front propagation in the lower region

This section reviews the theory for the lower region presented in [104]. The key result we derive is equation (4.9), which describes the shape of the lower region. Readers familiar with the derivations from [104] may want to skip directly to section 4.3. To determine the front lower region shape, we solve equations (2.7), (2.8), and (2.10) for $t \ll 1$. For small times the front is close to being a vertical line, the angle α being very small along it. So, we can estimate $\cos(\alpha) \approx 1$, via a leading-order Taylor expansion. Moreover, we can also approximate the trajectory as $s \approx x$. Hence, we can compute equation (2.7) as $\mathrm{d}x/\mathrm{d}t \approx y/x$. Then, after integration, we obtain that $x \approx \sqrt{2yt}$, which is known as the Velde solution [80, 104]. A higher-order solution known as the improved Velde solution was also given in [104], establishing that

$$x \approx \sqrt{2yt + t^2/6}. \tag{4.1}$$

This solution recognises that historically points have been higher up (and hence faster moving) than their current y location indicates. As a result they have moved further than the Velde solution indicates, i.e. the x location computed by equation (4.1) is bigger than $x \approx \sqrt{2yt}$. Up till this point, we have the Velde solution of order $t^{1/2}$ and the improved Velde solution with a correction of order $t^{3/2}$, giving the x displacement of the lower region of the front. We can also obtain an order t solution to compute the vertical location y of the points in the lower region (corresponding to a first-order solution). This solution can be derived for small times $t \ll 1$, starting from equation (2.8), with $s \approx \sqrt{2yt}$ and $\sin(\alpha) \approx \alpha \approx \tan(\alpha) \equiv \mathrm{d}x/\mathrm{d}y \approx \sqrt{t/(2y)}$, via the Velde solution. As long as α is small, the curvature of the front $\mathrm{d}\alpha/\mathrm{d}\mathcal{S}$ (with $\mathcal{S}$ being measured down along the front as in Figure 2.2) can then be approximated by $|\mathrm{d}\alpha/\mathrm{d}y| \approx t^{1/2}y^{-3/2}/(2\sqrt{2})$, so is likewise a small quantity when $t \ll 1$. Using (4.1) in place of the Velde

solution only perturbs this curvature slightly. This modest curvature in the lower region is a contrast from the order $1/\sqrt{t}$ curvature that turns out to be present in the upper region. Here we have adopted (as introduced in section 2.1.4) the notation of [104], where $\mathrm{d}/\mathrm{d}y$ denotes a derivative along a front comprised of various material points at fixed t, whereas $\mathrm{d}/\mathrm{d}t$ denotes a time derivative following a specified material point. Then, integrating equation (2.8), we determine

$$y \approx y_0 - t/2, \tag{4.2}$$

where y_0 is the initial position of a material point originally anywhere below the top $y_0 \leq 1$. Therefore, for the point initially at the top of the lower region ($y_0 = 1$), we can compute

$$y_{\mathrm{1st,lower}} \approx 1 - t/2, \tag{4.3}$$

as its first-order approximated location over time. Considering that, at first-order, all material points in the lower region migrate downwards with vertical velocity component of $-1/2$, new material points must be injected in order to fill the gap between the $y_0 = 1$ point and the top of the reservoir (which in our dimensionless system is at $y = 1$). Hence, we can define a rescaled form for the vertical coordinate of the points, as

$$\zeta = 2(1 - y)/t, \tag{4.4}$$

where ζ represents a ratio of distances, that between the top of the reservoir and any arbitrary point y on the front, divided by the vertical distance through which the material point initially at the top of the front has displaced. Here at leading order, ζ takes values from $\zeta = 0$ at the top of the reservoir ($y = 1$), to $\zeta = 1$ for the topmost original material point of the lower region, with $\zeta > 1$ for points even lower down. However, a direct computation of the concave corner (or

matching point between the lower and upper regions) found it actually occurs at $\zeta = \zeta_{\text{cross}} < 1$ ($\zeta_{\text{cross}} \approx 0.954$, based on a much more complex integro-differential equation, changing to roughly $\zeta_{\text{cross}} \approx 0.94$ for a simpler but approximate differential equation approach), as shown in [104]. The subscript "cross" denotes the point at which upper and lower regions cross over one another, i.e. the corner or matching point we seek. Since the material point originally at the top of the front is now slightly lower down in y (slightly higher in ζ) than the kink or concave corner is, new material points have been extracted from the kink to fill the lower region (see e.g. Figure 4.1(a)). In addition, at any given y, we can define ξ as the horizontal displacement of the front, back from the leading edge at the top of the front $\sqrt{2t}$, given by

$$\xi = \sqrt{2t} - x. \tag{4.5}$$

We can also express ξ geometrically, as

$$\xi = \int_y^1 (\mathrm{d}x/\mathrm{d}y)\,\mathrm{d}y = \int_y^1 \tan(\alpha)\,\mathrm{d}y. \tag{4.6}$$

We cannot yet use equation (4.6) to determine ξ exactly, since it extends all the way into the upper region, for which α versus y is still unspecified. However, we can still use it to estimate the order of magnitude of ξ, under the assumption that α (albeit not curvature approximated here by $|\mathrm{d}\alpha/\mathrm{d}y|$) has similar order of magnitude moving between the upper and lower regions. For small times $t \ll 1$, since $\alpha \approx \sqrt{t/(2y)}$ via the Velde solution (with $\alpha = \mathrm{atan}(\mathrm{d}x/\mathrm{d}y) \approx \mathrm{d}x/\mathrm{d}y$), we define Ξ as, the rescaled in time horizontal displacement [104], via

$$\Xi = \xi/t^{3/2}, \tag{4.7}$$

which recognises that ξ is an order $t^{3/2}$ quantity, since we are integrating an order $\sqrt{t}$ quantity over an order t distance in the y direction close to $y = 1$ (see equation

(4.4)). Furthermore, we can express the lower region of the front, corresponding to $\zeta \geq \zeta_{\text{cross}}$, in terms of ζ and Ξ, by first substituting equation (4.1) into equation (4.5), to obtain

$$\xi = \frac{2t - x^2}{\sqrt{2t} + x} \approx \frac{2t - 2yt - t^2/6}{\sqrt{2t} + x}, \tag{4.8}$$

and then specifically near the top of the domain where $x \approx \sqrt{2t}$, we can obtain after introducing equations (4.4) and (4.7), that

$$\Xi \approx \frac{\zeta - 1/6}{2\sqrt{2}}, \quad \text{if} \quad \zeta \geq \zeta_{\text{cross}}, \tag{4.9}$$

where, $\zeta \geq \zeta_{\text{cross}}$ here requires

$$y \leq y_{\text{cross}} \equiv 1 - (t/2)\zeta_{\text{cross}}, \tag{4.10}$$

which implies that (4.9) is a solution describing specifically the lower region up to the matching point or concave corner at location y_{cross} as defined by equation (4.10). The utility of equation (4.9) is that it gives a Ξ versus ζ relation for the lower region, and if we can also obtain a Ξ versus ζ relation for the upper region, we can find where the two regions intersect, and hence determine ζ_{cross}. This is what [104] achieved, by expressing the upper region in terms of a similarity equation (see section 4.3 and also, in Appendix B, section B.1 along with section B.2). Note that equation (4.9) is a leading-order solution for Ξ, accurate to order $t^{3/2}$. Later on in section 4.5, we introduce equation (4.22), which corresponds to an order $t^{5/2}$ accurate solution for the lower region, close to the concave corner, improving upon equations (4.1) and (4.9) (see also details in Appendix B section B.3). Geometrically, equation (4.1) is a parabola, and (4.9) represents a tangent to that parabola at $y = 1 - t/2$ or equivalently at $\zeta = 1$, the geometrical distance between the parabola and its tangent being negligible at the current order of approximation. Having this approximation for the front lower region, it

is possible to obtain a more accurate (second-order) estimate of the trajectory y as a function of time t for material points in the lower region, as an improvement over and above equation (4.2). As was proven in [104], such points move obeying

$$y \approx y_0 - t/2 + 5\,t^2/(48\,y_0), \tag{4.11}$$

where $y_0 \leq 1$ is initial location of the points when $t = 0$ (see also Appendix A.1). Equation (4.11) is a perturbation of (4.2) indicating that when $t \ll 1$ all points move downwards with the same leading-order velocity, and moreover velocity changes away from this leading-order value only gradually with time. So, assuming that the $y_0 = 1$ point (the point originally at the top of the front), has not been consumed yet by the concave corner, so its location can still be tracked, and assuming it remains reasonably close to the concave corner itself (to the extent that the aforementioned value of $\zeta_{\text{cross}} \approx 0.94$, is relatively close to unity), we have an indication of where the junction between the upper and the lower region might be using equation (4.11). Indeed, we can compute the approximate vertical location of the topmost original material point in the lower region as

$$y_{\text{2nd,lower}} \approx 1 - t/2 + 5\,t^2/48 \approx 1 - 0.5\,t + 0.1042\,t^2. \tag{4.12}$$

In summary, we have a first-order estimate of the kink location y_{cross}, given by equation (4.10), and a second-order estimate $y_{\text{2nd,lower}}$ (equation (4.12)) for a material point that improves upon equation (4.3) and that we postulate, is close to the kink location, although without definitive proof. The reason that the estimate $y_{\text{2nd,lower}}$ was so readily obtained is that the lower region is comparatively uniform in space and time when $t \ll 1$, i.e. low curvatures of the front and weak perturbations away from a leading-order material point velocity. Our objective now is to obtain a second-order correction to the equation for y_{cross}. Before achieving that however we need to switch over focus to the upper region. As

we will see, analysing the upper region proves to be challenging due to strong spatio-temporal non-uniformities that are present there.

4.3 First-order location of the upper region's material points

In this section we review the methodology employed in [104], to determine the first-order solution for the shape of the upper region of the front, in order to determine how it might match with the lower region. The key results we derive are equations (4.15)–(4.17), which describe the shape of the upper region of the front, parametrically, in terms of a parameter $\mathcal{T}$, which represents the fraction of time that an injected point has been on the front. We start by introducing similarity equations in the upper region, and then based on these, we develop an order time t solution to compute the vertical y movement of the points of the front's upper region, along with an order $t^{3/2}$ expression for the x displacement. Readers familiar with the derivations from [104], may prefer to skip directly to section 4.4. Higher-order corrections are considered later on in section 4.5.

4.3.1 Introducing similarity variables

As [104] showed, if at any given small instant in time ($t \ll 1$), the location and orientation of a material element (treated as a set of closely spaced collinear material points) is identified relative to the overall extent of the upper region and overall amount that the upper region reorients (both of which happen to be arbitrarily small when $t \ll 1$), then it should be possible to collapse together the front shapes in the upper region at different instants of time into a self-similar

form. Hence, we can express the front orientation angle α of the upper region, as

$$\alpha = \sqrt{t/2}\,\mathcal{A}(\zeta), \tag{4.13}$$

where $\mathcal{A}$ is a function of the variable ζ defined earlier [104] (see also section B.1 in Appendix B, which specifies the function implicitly as $\zeta = \zeta(\mathcal{A})$). If t is small here, α is likewise small. On the other hand, using (4.4) and (4.13), curvature $\mathrm{d}\alpha/\mathrm{d}\mathcal{S}$ which is approximately $|\mathrm{d}\alpha/\mathrm{d}y|$ becomes $(t/2)^{-1/2}\,\mathrm{d}\mathcal{A}/\mathrm{d}\zeta$, and hence is large when t is small. Note also that $\sqrt{t/2}$ is, at leading order, the amount that a material element reorients at the top of the lower region. This leading-order estimate is obtained via the Velde solution, since we are looking at small times $t \ll 1$ close to $y \approx 1$. Knowing the top of the lower region reorients to $\alpha \approx \sqrt{t/2}$, if we compare this with equation (4.13) for the upper region, any value of $\mathcal{A}(\zeta)$ greater than unity at the bottom of the upper region thereby implies a concave kink. Moreover, the front meets the top perpendicularly, as the boundary condition at $y = 1$ requires that the angle $\alpha = 0$ there. This then implies that $\mathcal{A}$ varies from 0 at the top, to some value $\mathcal{A}_{\text{cross}}$ at the cross-over or matching point, estimated to be at $\zeta = \zeta_{\text{cross}}$. We know from [104], that ζ_{cross} is slightly less than unity, so at leading order, the kink or concave corner moves down slightly more slowly than material points originally at the top of the lower region. Moreover [104] showed that $\mathcal{A}_{\text{cross}} \approx 1.18$ roughly, which is slightly greater than unity, so the upper region reorients more than the lower region does. As mentioned earlier, that is what produces the kink or corner.

4.3.2 First-order upper region representation in terms of $\mathcal{T}$

Since points originally on the front $y_0 \leq 1$ move downward (as we demonstrated in section 4.2), material points must be injected from the top onto the front [80], in order to have a continuous solution over time. For the upper region, we define

t_{inj}, as the time at which a material point has been injected. For a fixed time t, we require that $t_{\text{inj}} \in (0, t]$. As in [104], we can define a coordinate $\mathcal{T}$ such that $1 - \mathcal{T}$ is the ratio between t_{inj} and t, as

$$\mathcal{T} = 1 - t_{\text{inj}}/t. \tag{4.14}$$

We can express the front location (coordinates ζ and Ξ) in terms of $\mathcal{T}$ instead of $\mathcal{A}$ (contrast section B.1 in Appendix B). Here $\mathcal{T}$ can be varied by fixing t and varying t_{inj} (thereby looking at a collection of different material points) or alternatively by fixing t_{inj} and varying t (following the trajectory of an individual material point): both ways of varying $\mathcal{T}$ turn out to be useful later on. If t_{inj} is significantly smaller than t, the points injected tend to be already close to the concave corner, implying that $\mathcal{T} \to \mathcal{T}_{\text{cross}}$. Here, $\mathcal{T}_{\text{cross}} < 1$ (as obtained via an integro-differential equation solution), typically $\mathcal{T}_{\text{cross}} \approx 0.948$ [104]; or alternatively $\mathcal{T}_{\text{cross}} \approx 0.9431$ for the simpler differential equation approach to be employed here, see section 7.4.3 in [104]), corresponds to the maximum value of $\mathcal{T}$, which is reached at the concave corner. Points with t_{inj} smaller than $(1 - \mathcal{T}_{\text{cross}})t$ have already been consumed by the concave corner, so are no longer part of the propagating front (see Figure 4.1). By contrast, if $t_{\text{inj}} \to t$, the material points are near to the top, which implies that $\zeta \ll 1$, $\mathcal{A} \ll 1$, $\Xi \ll 1$ and $\mathcal{T} \ll 1$. To date, we have presented a first-order theory of the upper region as per [104]. The second-order theory to be presented from section 4.5 onwards, is most naturally expressed in terms of the variable $\mathcal{T}$ defined by equation (4.14), rather than in terms of $\mathcal{A}$ as is presented in section B.1 in Appendix B. Before tackling the second-order theory therefore, we need to recast the theory for the upper region in terms of $\mathcal{T}$, and then explain how to identify the matching point between the lower and upper region. As mentioned previously, at small times $t \ll 1$, we can collapse together the front shapes at different times, expressing the shape in terms of similarity

variables $\mathcal{A}$, ζ and Ξ, instead of α, y and ξ. In particular, assuming that the upper region of the front consists of a set of material points, each one injected at a different time $t_{\text{inj}} \in (0, t]$, we can compute the front shape for a fixed time t in terms of $\mathcal{T}$, varying it between 0 up to some $\mathcal{T}_{\text{cross}}$. It follows from [104] that

$$\mathcal{A} \approx \mathcal{A}_0 \equiv \frac{1-(1-\mathcal{T})^c}{c}, \tag{4.15}$$

where $2c-1$ is the assumed constant invariant ratio between $\mathrm{d}s/\mathrm{d}y$ and $\mathrm{d}x/\mathrm{d}y$, over the upper region [104] (see section B.1 in Appendix B). Substituting into equation (B.2) we deduce

$$\zeta \approx \zeta_0 \equiv \frac{1-c\mathcal{T}-(1-\mathcal{T})^c}{c(1-c)}. \tag{4.16}$$

Equations (4.15)–(4.16) have been expressed in the form $\mathcal{A}_0(\mathcal{T})$ and $\zeta_0(\mathcal{T})$ to highlight that they are leading-order expressions which may need to be corrected as time increases. It can be readily checked that $\mathrm{d}\zeta/\mathrm{d}\mathcal{A} \equiv (\mathrm{d}\zeta/\mathrm{d}\mathcal{T})/(\mathrm{d}\mathcal{A}/\mathrm{d}\mathcal{T})$, when computed at leading order via equations (4.15)–(4.16), is compatible with equation (B.1) (the original form given by [104]). We also obtain a leading-order expression for the rescaled horizontal displacement of the upper region $\Xi = (2\sqrt{2})^{-1}\int_0^\zeta \mathcal{A}\,\mathrm{d}\zeta$ in the form $\Xi \approx \Xi_0(\mathcal{T})$, by substituting from equations (4.15)–(4.16) to give

$$\Xi \approx \Xi_0 \equiv \frac{2c((1-\mathcal{T})^c - c - 1)\mathcal{T} + (1+c)(1-\mathcal{T})^{2c} - 2(2c+1)(1-\mathcal{T})^c + 3c + 1}{4\sqrt{2}c^2(1-c^2)}. \tag{4.17}$$

Taken together (4.16) and (4.17), both in terms of $\mathcal{T}$, give a parametric representation of the upper region of the front, with the same order of accuracy in time as the lower region as computed by equation (4.9), i.e. order $t^{3/2}$ in ξ and order t in y. Therefore, we can determine in terms of $\mathcal{T}$, the matching point between the

lower and the upper region of the front. This is how [104] proceeded to obtain $\mathcal{T}_{\text{cross}}$, and the details will be discussed in the next section.

4.4 First-order matching point between upper and lower region

Now we review the methodology used in [104] to determine the first-order vertical location of the concave corner over time. Reviewing this enables us subsequently to extend that methodology to second-order in section 4.5. The key first-order results are shown in Figure 4.2. A snapshot of the shape of the front is plotted in Figure 4.2(a), and in Figure 4.2(b), the trajectory of the concave corner at leading order is plotted, in comparison with the first-order approximated trajectory of material points in the upper and lower region. Having consulted Figures 4.2(a)–(b), some readers may prefer to skip to section 4.5, in which the methodology is extended to higher-order solutions. Our immediate objective via Figure 4.2, is to obtain the first-order matching point between the lower and upper region of the front (namely the concave corner). We proceed by plotting both regions, using equation (4.9) for the lower region, and equations (4.16)–(4.17) for the upper region, identifying the intersection or matching point (see Figure 4.2(a)). We decide to plot $-\Xi$ vs $-\zeta$, since it has the same orientation as x versus y. Assuming $c = 3/4$ (the value given by [104], see Appendix B section B.1 for details), the matching point between these two regions turns out to be $\zeta_{\text{cross}} \approx 0.9397$ and $\Xi_{\text{cross}} \approx 0.2733$, and is obtained at $\mathcal{T}_{\text{cross}} \approx 0.9431$ (see Figure 4.2(a)). This same result was previously obtained in [104] albeit expressed not in terms of $\mathcal{T}$ but rather in terms of $\mathcal{A}$ (equations (B.2)–(B.3)), with the corner found at $\mathcal{A}_{\text{cross}} \approx 1.18$ roughly. Given the value of ζ_{cross}, we can compute via equation (4.10)

$$y_{\text{1st,cross}} = 1 - 0.4698\, t, \tag{4.18}$$

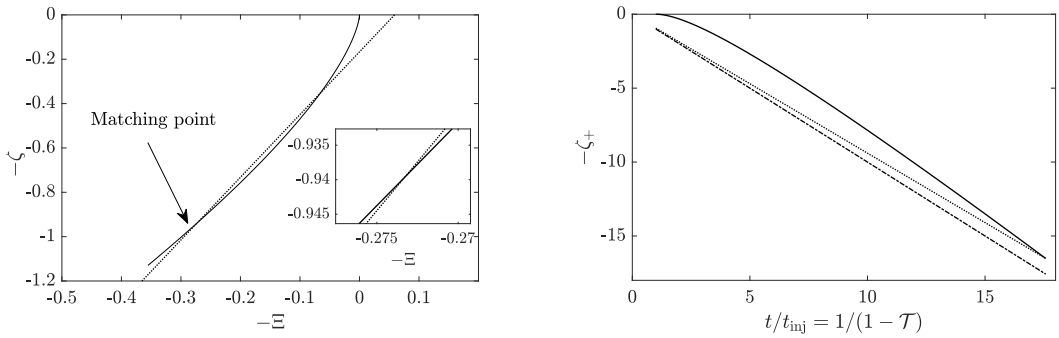

(a) (b)

Figure 4.2: (a) Matching point between the lower (dotted line) and the upper (solid line) region of the front. Here, $-\zeta$ is the rescaled vertical y location of the front and $-\Xi$ is the rescaled horizontal displacement of the front behind the leading edge at the top. (b) Rescaled $-\zeta_+(\mathcal{T})$ location (see in Appendix B section B.2 for additional details) versus a rescaled time defined as $t/t_{\rm inj} = 1/(1-\mathcal{T})$ with $0 \le \mathcal{T} \le \mathcal{T}_{\rm cross} \approx 0.9431$. Solid curve: trajectory of a material point in the upper region. Dotted line: trajectory of the concave corner itself. Dashed-dotted line: trajectory of the topmost material point originally at the top of the front at time $t = 0$.

as the first-order vertical location of the concave corner (the cross-over or matching point between the upper and the lower region of the front). Here we employ the notation $y_{\rm 1st,cross}$ (instead of simply $y_{\rm cross}$ used earlier) to emphasise that this is a first-order solution. In the rest of the section we explore some consequences and concepts that follow from having found the first-order matching point. These will be generalized to second-order in later sections of the paper. Further details can be found in Appendix B section B.2 which based on the value of $\mathcal{T}_{\rm cross}$ defines $t_{\rm inj(min)}(t)$ (the earliest injected point still surviving on the front at time t) and $t_{\rm max}(t_{\rm inj})$ (the maximum time out to which a point injected at $t_{\rm inj}$ survives). Appendix B section B.2 also presents another rescaling of the y coordinate $\zeta_+ = (1-y)/(t_{\rm inj}/2) = \zeta/(1-\mathcal{T})$ which is relevant to Figure 4.2(b). Whilst the variable ζ is useful for representing the shape of the front at fixed t, the variable ζ_+ is more useful for representing the trajectory of a material point with fixed $t_{\rm inj}$. Indeed, for a fixed $t_{\rm inj}$ (and hence fixed material point), plotting

ζ_+ vs $1/(1-\mathcal{T})$ (with $1/(1-\mathcal{T}) = t/t_{\text{inj}}$ via equation (4.14)) is just a rescaling of y vs t. In Figure 4.2(b) the solid curve represents the trajectory $-\zeta_+$ of a material point moving through the upper region as $-\zeta(\mathcal{T})/(1-\mathcal{T})$, with $\zeta(\mathcal{T}) \equiv \zeta_0(\mathcal{T})$ at leading order as given by equation (4.16). The dotted line shows the $-\zeta_+$ position of the concave corner itself, namely $-\zeta_{\text{cross}}/(1-\mathcal{T})$, with $\zeta_{\text{cross}} \approx 0.9397$. The solid curve and the dotted line coincide only when $\mathcal{T} = \mathcal{T}_{\text{cross}} \approx 0.9431$. The dash-dotted line shows the trajectory in terms of $-\zeta_+$ of a point in the lower region that was originally at the top of the front, as $-1/(1-\mathcal{T})$. Note that the solid curve in Figure 4.2(b) is not a straight line, which implies non-uniform motion. The fact that this is not a straight line in Figure 4.2(b) indicates that, in the upper region, material point motion always varies with time even in the limit of very small t_{inj} and hence very small t: this is one of the challenges of tracking material points in the upper region.

4.5 Second-order correction to front shape

To date all we have done is review the first-order findings of [104], recast in terms of a more convenient variable set. Now we extend those findings to obtain a second-order accurate solution in time to compute the upper and lower region of the front. Key results we obtain are equations (4.23)–(4.25), from which we can track upper region material points on the front, and equation (4.26), for which we can compute the corresponding location of points in the lower region. Some details are relegated to Appendix B.

4.5.1 Second-order location of the upper region's material points

Although we parameterise the system in terms of $\mathcal{T}$ here, if we recall that ζ and Ξ could also be expressed readily in terms of $\mathcal{A}$ (see equations (B.2) and (B.3),

in Appendix B respectively), it is useful to begin by computing a second-order expression for the front orientation angle $\mathcal{A}$, for a small but finite time t (see Appendix B, section B.4.1 for details of how this is achieved). It is reasonable to expand $\mathcal{A}$ as

$$\mathcal{A}(\mathcal{T}, t) \approx \mathcal{A}_0(\mathcal{T}) + t\,\mathcal{A}_1(\mathcal{T}), \tag{4.19}$$

in order to determine the effect of an order t correction upon the rescaled front orientation angle $\mathcal{A}$ (which corresponds to an order $t^{3/2}$ correction for α, see equation (4.13)). Equation (4.19) breaks the similarity solution, depending as it does on both $\mathcal{T}$ and t, not merely on $\mathcal{T}$. Consistently, we can expand the rescaled vertical (see Appendix B, section B.4.2 for details), and horizontal (see Appendix B, section B.4.3 for details) location of the upper region's material points respectively, in the form of

$$\zeta(\mathcal{T}, t) \approx \zeta_0(\mathcal{T}) + t\,\zeta_1(\mathcal{T}), \tag{4.20}$$

$$\Xi(\mathcal{T}, t) \approx \Xi_0(\mathcal{T}) + t\,\Xi_1(\mathcal{T}). \tag{4.21}$$

Here, $\mathcal{A}_0$, ζ_0 and Ξ_0 from section 4.3, and $\mathcal{A}_1$, ζ_1 and Ξ_1 obtained in Appendix B section B.4, turn out to be well defined quantities in terms of $\mathcal{T}$. In addition, since ζ is related to y via equation (4.4) and Ξ is related to ξ via equation (4.7), and hence to x via equation (4.5), it follows that equations (4.20) and (4.21) are order t^2 and $t^{5/2}$ accurate expressions, in y and x respectively. To use these expressions to find the matching point between both regions of the front, we must also calculate, with a consistent order of accuracy, the shape of the lower region.

4.5.2 Second-order correction to lower region front shape

We now present an extension of the equation (4.9), used to compute the lower region of the front. Note that the equation (4.9), has been derived via an order

$t^{3/2}$ accurate solution in the x direction (given by equation (4.1); also known as the improved Velde solution), and an order t accurate solution in the y direction (given by equation (4.2)). We need however, to incorporate the order t^2 effect, in the vertical, which is given by equation (4.11), along with an order $t^{5/2}$ correction to compute the x location of material points, to achieve the same order of accuracy as is computed for the upper region via equation (4.20) and (4.21). The required expression is (see Appendix B section B.3)

$$\Xi \approx \frac{1}{2\sqrt{2}}\left(\zeta - \frac{1}{6} + \frac{t}{8}\left(\zeta^2 - \frac{\zeta}{3} + \frac{107}{540}\right)\right), \quad \text{if} \quad \zeta \geq \zeta_{\text{cross}}, \tag{4.22}$$

which represents a parabola, as it includes a second-order term in ζ. This is applicable specifically near the top of the lower region ($\zeta \geq \zeta_{\text{cross}}$ but not $\zeta \gg 1$). Here, we see how a self-similar solution (given by equation (4.9) involving only Ξ and ζ), valid for early times, is broken as a higher-order correction in time is introduced. According to equation (4.22), for any specified ζ, the order t correction term for Ξ is positive, so on a graph such as Figure 4.2(a), which plots coordinates $(-\zeta,-\Xi)$, we obtain a point to the left of the $t \to 0$ limit (dotted line in Figure 4.2(a)).

4.5.3 Rescaled location of the upper region's material points

The form of equations (4.19), (4.20), (4.21) (upper region), and (4.22) (lower region), indicates that in the limit $t \to 0$, the upper region can be expressed in similarity form via variables ζ and Ξ, in which for the upper region in particular, only the ratio $t_{\text{inj}}/t \equiv 1 - \mathcal{T}$ was relevant. Nevertheless, for small but finite t, the similarity solution is broken as alluded to earlier, and both values t_{inj} and t are needed. To explore how the similarity solution becomes broken, we can either select a given t and find the front shape ζ vs Ξ at that time, or alternatively we can select a given t_{inj} and find how a material point injected at time t_{inj}

moves and reorients. This latter approach is easier since the governing equations for pressure-driven growth are expressed in Lagrangian form. A rescaling of the variables is now convenient. We define ζ_+ and Ξ_+, as the rescaled $1-y$ and $\sqrt{2t}-x$ front location, rescaling respectively, by amounts depending solely on the now fixed t_{inj} (respectively by $t_{\text{inj}}/2$ and $t_{\text{inj}}^{3/2}$), and we track a material point trajectory parametrically, by varying $\mathcal{T}$ from 0 up to $\mathcal{T}_{\text{cross}}$ (the matching point between the lower and upper region). Consistently, we define $\mathcal{A}_+$ as the rescaled front orientation angle α, rescaled by $\sqrt{t_{\text{inj}}/2}$. Using definitions analogous to equations (4.4), (4.7), and (4.13), but with t_{inj} in place of t, and relating $\mathcal{A}_+$, ζ_+ and Ξ_+ back to $\mathcal{A}$, ζ and Ξ, we compute via equations (4.19)–(4.21)

$$\mathcal{A}_+ \approx \frac{\mathcal{A}_0(\mathcal{T})}{\sqrt{1-\mathcal{T}}} + t\,\frac{\mathcal{A}_1(\mathcal{T})}{\sqrt{1-\mathcal{T}}} \equiv \mathcal{A}_{+,0}(\mathcal{T}) + t_{\text{inj}}\frac{\mathcal{A}_1(\mathcal{T})}{(1-\mathcal{T})^{3/2}} = \mathcal{A}_{+,0}(\mathcal{T}) + t_{\text{inj}}\,\mathcal{A}_{+,1}(\mathcal{T}), \tag{4.23}$$

$$\zeta_+ \approx \frac{\zeta_0(\mathcal{T})}{1-\mathcal{T}} + t\,\frac{\zeta_1(\mathcal{T})}{1-\mathcal{T}} \equiv \zeta_{+,0}(\mathcal{T}) + t_{\text{inj}}\frac{\zeta_1(\mathcal{T})}{(1-\mathcal{T})^{2}} = \zeta_{+,0}(\mathcal{T}) + t_{\text{inj}}\,\zeta_{+,1}(\mathcal{T}), \tag{4.24}$$

$$\Xi_+ \approx \frac{\Xi_0(\mathcal{T})}{(1-\mathcal{T})^{3/2}} + t\,\frac{\Xi_1(\mathcal{T})}{(1-\mathcal{T})^{3/2}} \equiv \Xi_{+,0}(\mathcal{T}) + t_{\text{inj}}\frac{\Xi_1(\mathcal{T})}{(1-\mathcal{T})^{5/2}} = \Xi_{+,0}(\mathcal{T}) + t_{\text{inj}}\,\Xi_{+,1}(\mathcal{T}), \tag{4.25}$$

where t has been replaced by $t_{\text{inj}}/(1-\mathcal{T})$ (as follows from equation (4.14)). Hence, if we can determine how the front shape is perturbed at any given $t \ll 1$ (given by equations (4.19)–(4.21)), we can also determine how the trajectory of a material point is perturbed at any given t_{inj}, i.e, for different choices of $t_{\text{inj}} \ll 1$, we have different solutions of Ξ_+ and ζ_+ versus $\mathcal{T}$, which correspond to the actual geometric path that a fixed injected material point takes (at least to second-order accuracy) to reach the concave corner (the intersection with the lower region).

4.5.4 Rescaled location of the lower region's material points

To find where material points injected in the upper region from time t_{inj} intersect the lower region, we convert (4.22) (applicable near the top of the lower region) into $\Xi_+ \equiv \Xi/(1-\mathcal{T})^{3/2}$ vs $\zeta_+ \equiv \zeta/(1-\mathcal{T})$ format. At any given time $t = t_{\text{inj}}/(1-\mathcal{T})$, it follows via equation (4.22)

$$\Xi_+ \approx \frac{(1-\mathcal{T})^{-3/2}}{2\sqrt{2}}\left(\zeta_+(1-\mathcal{T}) - \frac{1}{6} + \frac{t_{\text{inj}}}{8}\left(\zeta_+^2(1-\mathcal{T}) - \frac{\zeta_+}{3} + \frac{107}{540(1-\mathcal{T})}\right)\right) \tag{4.26}$$

where, given any t_{inj}, our challenge is to find a $\mathcal{T}$ value (and hence a time t) at which equations (4.24) and (4.25) intersect equation (4.26). Therefore, equations (4.24) and (4.25) give a locus ζ_+ and Ξ_+ swept out by a material point in the upper region, and equation (4.26) gives the Ξ_+ that would be on the lower region at that same ζ_+. The upper and lower region only meet when, at the same ζ_+, they also have the same Ξ_+. This then gives the matching or cross-over $\zeta_{+\text{cross}}$ and $\Xi_{+\text{cross}}$ point: for additional details see section B.6 in Appendix B. Despite the similarity between equations (4.22) and (4.26), note the subtle difference in the way we use them. With equation (4.22) it is convenient to fix t, and consider how Ξ varies with ζ at that fixed t. With equation (4.26), however, we vary t (by varying $\mathcal{T}$ at given t_{inj}), and select a particular ζ_+ (depending on $\mathcal{T}$ and hence on t), considering how Ξ_+ then varies. Therefore, tracking different t_{inj} gives different cross-over points $\zeta_{+\text{cross}}$ and $\Xi_{+\text{cross}}$, which can be expressed in a form giving the ζ_{cross} and Ξ_{cross} location of the concave corner over time t: see section 4.6 and also Appendix B section B.7 for details. After using equation (4.26) in the way described above to locate the matching point, there turns out to be an alternative way in which this equation can be used. Given the $\mathcal{T}$ and ζ_+ values at the matching point, respectively $\mathcal{T}_{\text{cross}}$ and $\zeta_{+\text{cross}}$, it is possible to find, for any given t_{inj}, corresponding values of t and y at the matching point. For these specific t and y values, equation (4.11) can then be used to identify a y_0 value (i.e.

a material point in the lower region, labelled by its initial location on the front) which coincides at the concave corner with the given upper region material point labelled by t_{inj}. It turns out (see section B.8 in Appendix B) that the required y_0 only differs from unity by order t_{inj} amounts, so it is more useful to define a quantity $\mathfrak{z}_0 = 1 - y_0$ and hence a quantity Z_0

$$Z_0 \equiv \frac{1 - y_0}{t_{\text{inj}}/2} = \frac{\mathfrak{z}_0}{t_{\text{inj}}/2}. \tag{4.27}$$

Once y_0 or equivalently Z_0 is known for any given t_{inj}, then at all times t up the matching point, equation (4.11) can now be rescaled into ζ_+ vs $\mathcal{T}$ coordinates (see section B.8 in Appendix B for details), giving the trajectory followed by the lower region material point, generally having (at any given time t or equivalently at any given $\mathcal{T}$) a ζ_+ different from the upper region material point (except at the matching point). Substituting the lower region ζ_+ into equation (4.26) and varying $\mathcal{T}$ gives the trajectory followed over time by this material point in terms of ζ_+ vs Ξ_+, which can be compared with the trajectory for the upper region material point described by equations (4.24)–(4.25). Trajectories of both points can be followed over time, and at the matching point, they coincide. Before equation (4.26) can be used in this particular fashion however, first the matching point itself must be found.

4.6 Perturbed location of the concave corner

In this section we present the perturbation analysis to track the location of the concave corner with second-order accuracy in time. The key result is equation (4.34), giving the vertical location of the concave corner over time. This is what we contrast, in section 4.7, with the first-order solution for the corner given by equation (4.18). The analysis proceeds as follows. Given a set of small but

finite t_{inj} values here, we can obtain different $\mathcal{T}_{\text{cross}}$ values, with which we can determine the variation in location of the concave corner over time. In the limit when $t_{\text{inj}} \to 0$, the value we seek is the aforementioned $\mathcal{T}_{\text{cross}} \approx 0.9431$ (which we now denote $\mathcal{T}_{\text{cross,0}}$). More generally however, varying t_{inj}, will cause $\mathcal{T}_{\text{cross}}$ (obtained as per the procedure discussed in section 4.5.4) to vary also. In the limit of sufficiently small t_{inj}, we can approximate this variation via

$$\mathcal{T}_{\text{cross}} \approx \mathcal{T}_{\text{cross,0}} + t_{\text{inj}}\mathcal{T}_{\text{cross,1}} \approx \mathcal{T}_{\text{cross,0}} + (1 - \mathcal{T}_{\text{cross,0}})\mathcal{T}_{\text{cross,1}}\, t. \tag{4.28}$$

Here, as mentioned above, $\mathcal{T}_{\text{cross,0}}$ is the lowest order approximation found previously, and $\mathcal{T}_{\text{cross,1}}$ is a next order correction to be determined. Knowing $\mathcal{T}_{\text{cross}}$, we can also define additional quantities t_{max} and $t_{\text{inj(min)}}$ (mentioned in section 4.4 and defined in Appendix B section B.2). Substituting (4.28) into equation (B.5) and Taylor expanding, we deduce that the maximum time $t = t_{\text{max}}$ for which a material point injected at t_{inj} could survive would be

$$t_{\text{max}} \equiv \frac{t_{\text{inj}}}{(1 - \mathcal{T}_{\text{cross}})} \approx \frac{t_{\text{inj}}}{1 - \mathcal{T}_{\text{cross,0}}} + \frac{t_{\text{inj}}^2 \mathcal{T}_{\text{cross,1}}}{(1 - \mathcal{T}_{\text{cross,0}})^2}, \tag{4.29}$$

Moreover, at the cross-over point, the earliest injected material point still surviving at time t has $t_{\text{inj}} = t_{\text{inj(min)}}$ with, according to equations (4.28) and (B.4)

$$t_{\text{inj(min)}} \equiv (1 - \mathcal{T}_{\text{cross}})t \approx (1 - \mathcal{T}_{\text{cross,0}})\, t - (1 - \mathcal{T}_{\text{cross,0}})\mathcal{T}_{\text{cross,1}}\, t^2. \tag{4.30}$$

Although the discussion of sections 4.5.3–4.5.4 focussed on functions used for tracking loci of material points, i.e. fixed t_{inj}, having the value of $t_{\text{inj(min)}}$ can also be useful. Knowing $t_{\text{inj(min)}}$ makes it possible to reconstruct the shape of the upper region (fixed t), by selecting a set of injected points t_{inj} in the domain $t_{\text{inj(min)}} \leq t_{\text{inj}} \leq t$. Then, computing $\mathcal{T} = 1 - t_{\text{inj}}/t$ for each one, and computing Ξ and ζ (given by equations (4.21) and (4.20), respectively) for each $\mathcal{T}$ at the

given time t, we can reconstruct the front shape. Thus, we can convert between material point trajectories and front shapes. This will be explored further in section 4.8. Once we know the values of $\mathcal{T}_{\text{cross},0}$ and $\mathcal{T}_{\text{cross},1}$, we can determine the perturbed value of $\mathcal{A}_+$ at the concave corner (denoted $\mathcal{A}_{+\text{cross}}$) by using equation (4.23), as

$$\mathcal{A}_{+\text{cross}} \approx \mathcal{A}_{+,0}(\mathcal{T}_{\text{cross},0} + t_{\text{inj}}\mathcal{T}_{\text{cross},1}) + t_{\text{inj}}\,\mathcal{A}_{+,1}(\mathcal{T}_{\text{cross},0} + t_{\text{inj}}\mathcal{T}_{\text{cross},1}), \tag{4.31}$$

which upon expanding for sufficiently small t_{inj} gives

$$\begin{aligned}\mathcal{A}_{+\text{cross}} &\approx \mathcal{A}_{+,0}(\mathcal{T}_{\text{cross},0}) + t_{\text{inj}}\left(\mathcal{T}_{\text{cross},1}\mathcal{A}'_{+,0}(\mathcal{T}_{\text{cross},0}) + \mathcal{A}_{+,1}(\mathcal{T}_{\text{cross},0})\right)\\ &\equiv \mathcal{A}_{+\text{cross},0} + t_{\text{inj}}\mathcal{A}_{+\text{cross},1},\end{aligned} \tag{4.32}$$

where $\mathcal{A}'_{+,0}$ denotes the function $\mathrm{d}\mathcal{A}_{+,0}/\mathrm{d}\mathcal{T}$ (which is obtained via equations (4.15) and (4.23)). There are analogous expressions for ζ_+ and Ξ_+ at the concave corner (denoted $\zeta_{+\text{cross}}$ and $\Xi_{+\text{cross}}$): the formulae are given in equations (B.40)–(B.42) in Appendix B section B.7. There are also analogous expressions, but expanded in terms of t rather than in terms of t_{inj}. These provide the cross-over values of $\mathcal{A}$, ζ and Ξ, denoted $\mathcal{A}_{\text{cross}}$, ζ_{cross} and Ξ_{cross}: see equations (B.44)–(B.46) in Appendix B. Various ways to estimate the location of the concave corner, in an effort to improve upon the first-order estimate $y_{\text{1st,cross}}$ already given in equation (4.18), now present themselves. Based on the definition of $\zeta_+ \equiv (1-y)/(t_{\text{inj}}/2)$, we can obtain, by tracking the vertical location of a given injected material point t_{inj} over time up to its intersection with the concave corner, an estimate of the y location of the corner. We denote this by $y^{\text{inter}}_{\text{cross}}$, i.e. the value of the matching point determined by this intersection, and it turns out to be

$$y^{\text{inter}}_{\text{cross}} = 1 - (t_{\text{inj}}/2)\,\zeta_{+\text{cross}}(t_{\text{inj}}). \tag{4.33}$$

Here $\zeta_{+\text{cross}}(t_{\text{inj}})$ is obtained as already mentioned by tracking t_{inj} on the upper region using equations (4.24)–(4.25), until its location coincides with the lower region given by equation (4.26). The value of $\zeta_{+\text{cross}}(t_{\text{inj}})$ determined here will not agree perfectly with the expression obtained via a small t_{inj} expansion for $\zeta_{+\text{cross}}$ (see equation (B.41) in Appendix B), although agreement should be good when t_{inj} is sufficiently small. We can combine this expression for $y_{\text{cross}}^{\text{inter}}$ vs t_{inj} with an expression for time at cross-over $t = t_{\text{inj}}/(1 - \mathcal{T}_{\text{cross}})$ vs t_{inj}, this latter expression again not agreeing perfectly with the Taylor expanded form given in (4.29). Despite these small discrepancies, a parametric representation of the cross-over y vs time t can now be obtained by varying t_{inj}. A slightly different estimate for the second-order vertical location of the concave corner over time t, can be obtained by combining equation (4.10) with a small t expansion for ζ_{cross} in equation (B.45), obtaining

$$y_{\text{2nd,cross}} \approx 1 - (t/2)\,\zeta_{\text{cross},0} - (t^2/2)\,\zeta_{\text{cross},1}. \tag{4.34}$$

In the limit of sufficiently small t, this should agree with what (4.33) predicts, but is rather simpler to evaluate. Provided we can determine $\zeta_{\text{cross},1}$ (the value of $\zeta_{\text{cross},0}$ being already known from literature [104]; see also Table 4.1 later on), we can estimate the second-order position of the concave corner over time. Predictions for how second-order effects perturb not only the concave corner but also material point trajectories are discussed in the next section.

4.7 Second-order matching between upper and lower region

In this section, we determine the effect of selecting a small but finite time upon the evolution of the upper region of the front, and how the matching point between

the lower and the upper region moves with time. Recall that we are working with second-order accuracy in time, in the sense that we have included an order t^2 correction (newly derived here for the upper region, but already given by [104] in the case of the lower region) to compute vertical location y, and an order $t^{5/2}$ expression in time (newly derived in the present work) to compute the horizontal position x or ξ of a material point, with a consistent order of accuracy in time for both, upper and lower region. After suitable rescaling, this is given by equations (4.20) and (4.21) for the upper region, and equation (4.22) for the lower region. In order to measure the concave corner location over time, we use equations (4.25) and (4.24) to compute the (Ξ_+, ζ_+) location of the upper region's material points, which is done by fixing t_{inj} (following the trajectory of a specific material point), and then tracking (parametrically in terms of $\mathcal{T}$) the locus swept out by the material point, up to the matching point with the lower region, with a (Ξ_+, ζ_+) location given by equation (4.26). To find the intersection where the two regions meet (see the discussion in section 4.5.4), it is sufficient to focus on a point in the lower region with the same ζ_+ value as the material point in the upper region, and determine the corresponding Ξ_+ value via (4.26). This is what is plotted in Figure B.2 in section B.6 in Appendix B. When the location of the matching point is found however, we can identify which specific material point from the lower region (identified by the value of Z_0 via equation (4.27)) happens to be present there (again see the discussion in section 4.5.4 and details in section B.8). Then trajectories of both upper and lower region material points can be tracked until their intersection. This is what is plotted here in Figure 4.3. The curves are close to overlapping along almost all the trajectory, although they only actually intersect at the matching point $(\Xi_{+\text{cross}}, \zeta_{+\text{cross}})$. In Figure 4.3, we see that the matching point is slightly sensitive to t_{inj}. Increasing t_{inj} causes it to shift the left (i.e. larger Ξ_+) and also slightly downwards (larger ζ_+). We also note Figure 4.3 that values of Z_0 are negative (see more explanation in

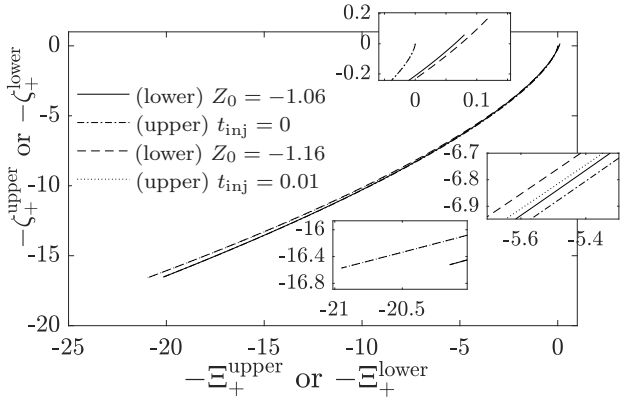

Figure 4.3: Trajectory of fixed material points labelled by $t_{\rm inj}$ in the upper region, and fixed material points labelled by $Z_0 \equiv (1-y_0)/(t_{\rm inj}/2)$ in the lower region in terms of rescaled vertical and horizontal distances ζ_+ and Ξ_+. Dash-dotted line for upper region $t_{\rm inj} = 0$ vs solid line for lower region $Z_0 \approx -1.06$ (see section B.8 in Appendix B for explanation of how to determine this Z_0 value). Dotted line for $t_{\rm inj} = 0.01$ vs dashed line for $Z_0 \approx -1.16$.

Appendix B section B.8). This implies y_0 values in excess of unity, i.e. points not actually present on the front initially, but which instead are extracted from the corner into the lower region as the system evolves. Although Figure 4.3 only shows two $t_{\rm inj}$ values ($t_{\rm inj} \to 0$ and $t_{\rm inj} = 0.01$) we have repeated the calculations for a number of $t_{\rm inj}$ values in the domain $t_{\rm inj} \in [0, 0.01]$, determining in each case the $\mathcal{T}$ value, namely $\mathcal{T}_{\rm cross}$, at which these points meet the concave corner (see Figure 4.4) and hence the maximum survival time $t_{\rm max}(t_{\rm inj})$, which is also estimated at least for $t_{\rm inj} \ll 1$ by equation (4.29) (see Figure 4.5). We can also compute $\mathcal{A}_+$, ζ_+, and Ξ_+ at the concave corner (see Figures 4.6(a)–(c)), and then (by employing equations (4.23)–(4.25)), $\mathcal{A}$, ζ, and Ξ values there (see Figures 4.6(d)–(f)). These expressions plotted in Figure 4.6 break similarity by allowing separate dependence on $t_{\rm inj}$ and t, rather than holding all values fixed at the matching point. At sufficiently small $t_{\rm inj}$ and/or t we expect variation in all the above mentioned quantities to be linear in $t_{\rm inj}$ and/or t, as established by equations (B.40)–(B.42) and (B.44)–(B.46), respectively (as given in Appendix B section B.7). Here, we achieve this by focussing firstly on exceedingly small

$\mathcal{T}_{\text{cross},0}$	$\mathcal{T}_{\text{cross},1}$	$\mathcal{A}_{+\text{cross},0}$	$\mathcal{A}_{+\text{cross},1}$	$\zeta_{+\text{cross},0}$	$\zeta_{+\text{cross},1}$	$\Xi_{+\text{cross},0}$	$\Xi_{+\text{cross},1}$
0.9431	0.4608	4.94	16.11	16.52	81.64	20.15	211.28
		$\mathcal{A}_{\text{cross},0}$	$\mathcal{A}_{\text{cross},1}$	$\zeta_{\text{cross},0}$	$\zeta_{\text{cross},1}$	$\Xi_{\text{cross},0}$	$\Xi_{\text{cross},1}$
		1.1784	−0.0528	0.9397	−0.1686	0.2733	−0.0257

Table 4.1: Parameters for equations (4.28), (B.40)–(B.42), (B.44)–(B.46) (given in section B.7 in Appendix B), and (4.34).

times $t_{\text{inj}} \in [0, 0.0001]$, thereby obtaining parameters for equations (4.28), (B.40)–(B.42), (B.44)–(B.46) and subsequently for (4.34), i.e. we obtain firstly $\mathcal{T}_{\text{cross},0}$ and $\mathcal{T}_{\text{cross},1}$ using data for $t_{\text{inj}} \in [0, 0.0001]$, from which we compute $\mathcal{A}_{+\text{cross},0}$, $\mathcal{A}_{+\text{cross},1}$, $\zeta_{+\text{cross},0}$, $\zeta_{+\text{cross},1}$, $\Xi_{+\text{cross},0}$ and $\Xi_{+\text{cross},1}$, and subsequently $\mathcal{A}_{\text{cross},0}$, $\mathcal{A}_{\text{cross},1}$, $\zeta_{\text{cross},0}$, $\zeta_{\text{cross},1}$, $\Xi_{\text{cross},0}$ and $\Xi_{\text{cross},1}$. These values are summarized in Table 4.1. Note that although $\mathcal{A}_{\text{cross},0}$, $\zeta_{\text{cross},0}$ and $\Xi_{\text{cross},0}$, can be straightforwardly expressed in terms of $\mathcal{A}_{+\text{cross},0}$, $\zeta_{+\text{cross},0}$ and $\Xi_{+\text{cross},0}$ and $\mathcal{T}_{\text{cross},0}$ (see equations (4.23)–(4.25)), the relations for $\mathcal{A}_{\text{cross},1}$, $\zeta_{\text{cross},1}$ and $\Xi_{\text{cross},1}$ in equations (B.44)–(B.46), are rather more complex, and these quantities can even have opposite sign from $\mathcal{A}_{+\text{cross},1}$, $\zeta_{+\text{cross},1}$ and $\Xi_{+\text{cross},1}$ in equations (B.40)–(B.42), as in fact is obtained here (see Table 4.1). How such sign changes can arise is discussed in section B.7. The above mentioned sign changes have the following implication. In a view such as Figure 4.3, $-\Xi_+$ vs $-\zeta_+$, which compares trajectories of material points released at different t_{inj}, we have already seen that increasing t_{inj} drives the concave corner to the left and downwards, with the leftward shift being particularly noticeable due to the large $\Xi_{+\text{cross},1}$ value in Table 4.1. On the other hand, since $\zeta_{\text{cross},1}$ and $\Xi_{\text{cross},1}$ are negative, snapshots of the instantaneous front shape at various times t, using now $-\zeta$ vs $-\Xi$ coordinates in a view similar to Figure 4.2(a), would show the corner shifting upwards and to the right, the upward shift being dominant owing to $\Xi_{\text{cross},1}$ in Table 4.1 being very small. In addition, the negative value of $\mathcal{A}_{\text{cross},1}$ implies that the kink in front orientation angle at the concave corner is less than first-order theory predicts, but since $\mathcal{A}_{\text{cross},1}$, like $\Xi_{\text{cross},1}$, is numerically

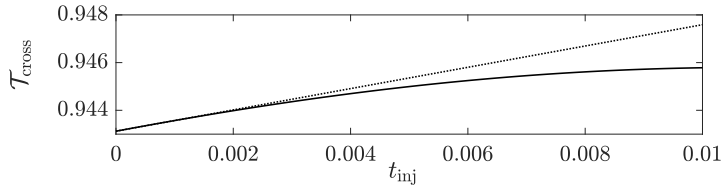

Figure 4.4: $\mathcal{T}_{\text{cross}}$ as a function of t_{inj}. Solid line: Value $\mathcal{T}_{\text{cross}}$ of the matching point tracked up to time $t_{\text{inj}} = 0.01$. Dotted line: linear approximation obtained from data up to time $t_{\text{inj}} = 0.0001$, with $\mathcal{T}_{\text{cross}} \approx \mathcal{T}_{\text{cross},0} + t_{\text{inj}}\mathcal{T}_{\text{cross},1}$ and for $\mathcal{T}_{\text{cross},0} \approx 0.9431$ and $\mathcal{T}_{\text{cross},1} \approx 0.4608$.

small in Table 4.1, the shift in kink angle is likewise small, compared with the vertical shift of the corner. The fact that fixing t produces a vertical shift in the corner location, whereas fixing t_{inj} produces a horizontal shift, indicates how the similarity solution breaks down, i.e. the solution no longer depends solely on the ratio t_{inj}/t. We now return to consider t_{inj} values in the domain, $t_{\text{inj}} \in [0, 0.01]$, instead of the much narrower domain $t_{\text{inj}} \in [0, 0.0001]$ used to obtain the data of Table 4.1. In Figure 4.4 we see $\mathcal{T}_{\text{cross}}$ as a function of t_{inj}, and it is clear that only for small times ($t_{\text{inj}} \leq 0.002$) we can consider the relation for $\mathcal{T}_{\text{cross}}$ to be a linear function well approximated by $\mathcal{T}_{\text{cross}} \approx \mathcal{T}_{\text{cross},0} + t_{\text{inj}}\mathcal{T}_{\text{cross},1}$ (given by equation (4.28)), with values of $\mathcal{T}_{\text{cross},0}$ and $\mathcal{T}_{\text{cross},1}$ given by Table 4.1. Nonetheless, at least on the domain of Figure 4.4, we found that as t_{inj} increases, the matching point $\mathcal{T}_{\text{cross}}$ still manages to increase albeit deviating from equation (4.28). The values of $\mathcal{T}_{\text{cross}}$ now affect the behaviour of a number of other quantities ($t_{\max}$, $t_{\text{inj(min)}}$ as well as $\mathcal{A}_{+\text{cross}}$, $\zeta_{+\text{cross}}$, $\Xi_{+\text{cross}}$, $\mathcal{A}_{\text{cross}}$, ζ_{cross}, and Ξ_{cross}) as we explain below, with an impact in turn on the corner's vertical y coordinate location (as we go on to explain).

4.7.1 Values of $t_{\max}$ vs t_{inj} and $t_{\text{inj(min)}}$ vs t

As has been indicated already in sections 4.4 and 4.6, for a given fixed t_{inj} we can calculate the maximum survival times $t_{\max}(t_{\text{inj}})$ (time at which the injected point

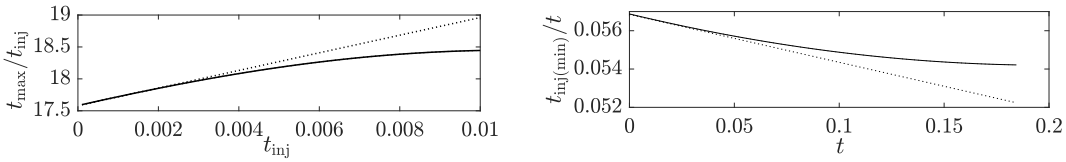

(a) (b)

Figure 4.5: (a) Maximum survival time, for a given injected material point. Solid line: $t_{\max}/t_{\inj}$ vs $t_{\inj}$, given by equation (B.5) (as given in Appendix B). Dotted line: approximation given by equation (4.35). (b) Minimum injection time of all surviving material points as a function of time. Solid line: $t_{\inj(\min)}/t$ vs t, given by equation (B.4). Dotted line: approximation given by equation (4.36).

$t_{\inj}$ reaches the concave corner). This is obtained by equation (B.5) (as given in Appendix B) and/or via an expansion (4.29), and is what Figure 4.5(a) shows. Equivalently (see Figure 4.5(b)) for a given t we can determine the injection time $t_{\inj(\min)}$ of the earliest injected point still surviving (see equation (4.30)). From the data in Figure 4.4 and Table 4.1, specifically via the linear approximation of $\mathcal{T}_{\text{cross}}$ in (4.28), we evaluate equations (4.29) and (4.30), as

$$t_{\max}/t_{\inj} \approx 17.57 + 142.33\, t_{\inj}, \tag{4.35}$$

$$t_{\inj(\min)}/t \approx 0.0569 - 0.0262\, t, \tag{4.36}$$

which are also plotted in Figures 4.5(a) and (b), respectively. Overall, equations (4.35) and (4.36) represent, at least for small time, good approximations to $t_{\max}$ and $t_{\inj(\min)}$. Note in particular that $t_{\inj(\min)}/t \equiv 1 - \mathcal{T}_{\text{cross}}$ (see equation (B.4) in Appendix B) so the data in Figure 4.5(b) mirror those in Figure 4.4.

4.7.2 Values of $\mathcal{A}_{+\text{cross}}$, $\zeta_{+\text{cross}}$, $\Xi_{+\text{cross}}$, $\mathcal{A}_{\text{cross}}$, ζ_{cross}, and Ξ_{cross}

Using $\mathcal{T}_{\text{cross}}$ obtained from Figure 4.4 we can also determine evolution of the orientation and position of the concave corner over time, by evaluating either equations (4.23)–(4.25) or equations (4.19)–(4.21) setting also $t = t_{\max}(t_{\inj})$ via

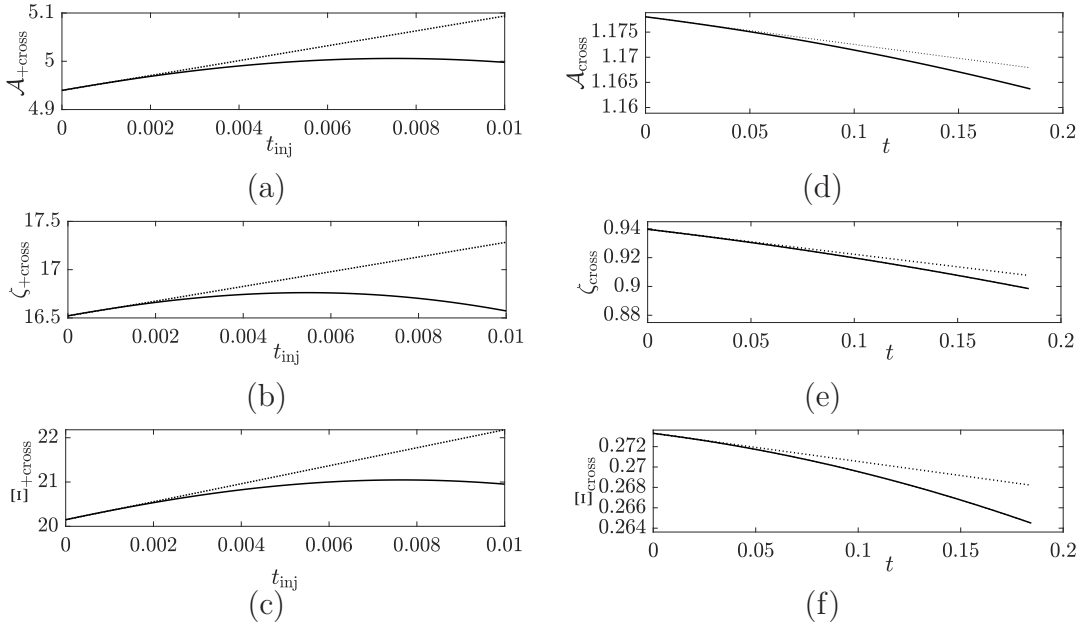

Figure 4.6: Values of variables at the matching point over time t_{inj} or t. Different computations of (a) $\mathcal{A}_{+\text{cross}}$, (b) $\zeta_{+\text{cross}}$, and (c) $\Xi_{+\text{cross}}$ for $t_{\text{inj}} \leq 0.01$. These are obtained respectively by equations (4.23)–(4.25) evaluated at $\mathcal{T}_{\text{cross}}$ (solid lines), and by equations (B.40)–(B.42) (dotted lines), with parameters as shown in Table 4.1. (d) $\mathcal{A}_{\text{cross}}$, (e) ζ_{cross} and (f) Ξ_{cross}, for $t = t_{\max}(t_{\text{inj}}) = t_{\text{inj}}/(1 - \mathcal{T}_{\text{cross}})$, with $t_{\text{inj}} \leq 0.01$, which are obtained respectively by equations (4.19)–(4.21) evaluated at $\mathcal{T}_{\text{cross}}$ (solid lines), and by equations (B.44)–(B.46) (dotted lines), with parameters as shown in Table 4.1.

Figure 4.5(a). The behaviour is as follows (see Figure 4.6). In Figures 4.6(a)–(c) we see how $\mathcal{A}_{+\text{cross}}$, $\zeta_{+\text{cross}}$ and $\Xi_{+\text{cross}}$ (i.e. values at the concave corner), respectively, increase at early times as t_{inj} increases, and then, at slightly larger t_{inj}, are predicted to decrease. In contrast, in Figures 4.6(d)–(f), we see $\mathcal{A}_{\text{cross}}$, ζ_{cross} and Ξ_{cross}, respectively, decrease as time t increases. The implications of these findings for ζ_{cross} in particular are discussed next.

4.7.3 Data for corner's vertical location

As can be seen in Figure 4.6(e), ζ_{cross} decreases with increasing t, which has an important implication: the vertical location of the concave corner is higher up

in y than was predicted at leading order. Using equation (4.34) for the vertical location of the concave corner over time, along with data from Table 4.1 fed into equation (B.45) we can deduce

$$y_{\text{2nd,cross}} \approx 1 - 0.4698t + 0.0843\,t^2. \tag{4.37}$$

This is plotted in Figure 4.7, representing an improvement over and above the formula $y_{\text{1st,cross}}$ given by equation (4.18) (also plotted in Figure 4.7). In this same figure we also show (obtained parametrically by varying t_{inj}) data computed for $y^{\text{inter}}_{\text{cross}} = 1 - (t_{\text{inj}}/2)\zeta_{+\text{cross}}$, as given by equation (4.33), vs $t = t_{\max} \equiv t_{\text{inj}}/(1-\mathcal{T}_{\text{cross}}(t_{\text{inj}}))$ as given by equation (B.5) in Appendix B. That this parametric expression for $y^{\text{inter}}_{\text{cross}}$ vs t must agree well with equation (4.37) for sufficiently small t follows from the two curves as seen in Figure 4.6(e) initially having the same slope. As t increases though (albeit well beyond the domain plotted in Figure 4.6(e)) considerable deviation sets in between $y^{\text{inter}}_{\text{cross}}$ and $y_{\text{2nd,cross}}$, and this is what we see in Figure 4.7. This is mainly associated with the $\zeta_{+\text{cross}}$ data obtained within equation (4.33) falling well below the predictions of a small t_{inj} expansion given by equation (B.41), ultimately leading to $y^{\text{inter}}_{\text{cross}}$ data exceeding $y_{\text{2nd,cross}}$. Moreover, we plot an Eulerian predicted position of the concave corner, a numerical result given in Chapter 3, section 3.4.4 [116], as

$$y_{\text{Eulerian}} = 1 - 0.4635t + 0.0784t^2, \tag{4.38}$$

obtained via interpolation of numerical data, fitted over a domain $t \in [0, 2]$, in a space domain $x \in [0, 2]$, $y \in [0, 1]$, where the grid size for the solution variable in the numerical Eulerian method was $\Delta x = \Delta y = 2.5 \times 10^{-3}$, with the time step Δt set via the Courant-Friedrichs-Lewy condition (CFL) [156] (see section 3.3 for details). Over the domain in Figure 4.7 these Eulerian data are evidently close to $y_{\text{2nd,cross}}$ data but further away from the data for $y^{\text{inter}}_{\text{cross}}$. We have also

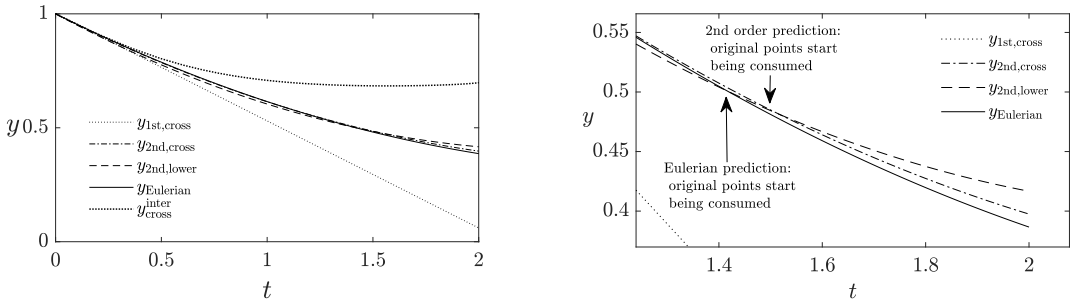

(a) (b)

Figure 4.7: Vertical y position of the concave corner as a function of time t. (a) Dotted line: first-order solution $y_{\text{1st,cross}}$ given by equation (4.18). Dash-dotted line: second-order solution $y_{\text{2nd,cross}}$ given by equation (4.37). Dashed line: Solution for a material point originally at the top of the lower region $y_{\text{2nd,lower}}$, see equation (4.12). Solid line: Eulerian numerical solution y_{Eulerian}, see equation (4.38). Dense-dotted line: Solution $y^{\text{inter}}_{\text{cross}}$ given by equation (4.33). (b) Zoomed view of (a) at later times.

plotted the trajectory of the topmost point of the lower region $y_{\text{2nd,lower}}$ given by equation (4.12), via a second-order approximation (see Figure 4.7). By comparing $y_{\text{2nd,lower}}$ with the position of the concave corner obtained via our $y_{\text{2nd,cross}}$ we can determine that not only are material points from the upper region being consumed by the concave corner (which follows because $t_{\text{inj(min)}} = (1 - \mathcal{T}_{\text{cross}})t$ is an increasing function of time), but also that material points must initially be extracted from the concave corner in order to populate the lower region, as early on $y_{\text{2nd,lower}}$ is below $y_{\text{2nd,cross}}$. This however only appears to happen until a certain time after which points of the lower region start being consumed by the concave corner. Indeed at a certain time $y_{\text{2nd,lower}}$ intersects the concave corner (see Figure 4.7(b)): all extracted points have now been consumed. So, initially new points are extracted into the lower region, then those same points are consumed, after which the points originally present in the lower region start being consumed.

We have currently several different methods to estimate the position of the concave corner, hence different estimates of when $y_{\text{2nd,lower}}$ and the concave corner

might coincide. Via the first-order analytical solution for the corner $y_{\text{1st,cross}}$, compared to $y_{\text{2nd,lower}}$, we could determine that originally present points start being consumed by the concave corner from time $t \approx 0.289$ at $y \approx 0.864$, although this result is likely to be unreliable employing as it does $y_{\text{1st,cross}}$. Meanwhile the point $y_{\text{cross}}^{\text{inter}}$ never coincides with $y_{\text{2nd,lower}}$ for any $t > 0$. However, the second-order solution for the corner $y_{\text{2nd,cross}}$ coincides with $y_{\text{2nd,lower}}$ at time $t \approx 1.518$ at $y \approx 0.481$. On the other hand, using the corner location as predicted via the Eulerian method, we determine that material points originally present in the lower region start being consumed by the concave corner at time $t \approx 1.416$ at $y \approx 0.501$ (see Figure 4.7(b)). At the comparatively large times considered here, there is difference among the various predictions. The difference is unsurprising, since our first and second-order analytical solutions are formally small time expansions, so we do not expect them to be valid all the way up to $t = 2$. To quantify deviations between the Eulerian data and the various other solutions that we have derived, we measure the root-mean-square (rms) error with respect to the Eulerian data, up to $t = 2$. The rms error between y_{Eulerian} and $y_{\text{1st,cross}}$ turned out to be 0.1473, between y_{Eulerian} and $y_{\text{cross}}^{\text{inter}}$ it was 0.1518, and between y_{Eulerian} and $y_{\text{2nd,cross}}$ it was 0.0039. This proves that the second-order solution given by equation (4.37) gives a much better estimate for the concave corner position over time than the first-order solution does, as expected. In addition, the rms difference between y_{Eulerian} and $y_{\text{2nd,lower}}$ was found to be 0.0118, which is larger than the error between y_{Eulerian} and $y_{\text{2nd,cross}}$. The difference between y_{Eulerian} and $y_{\text{2nd,cross}}$ must come from either higher-order corrections in time (and hence not captured equations (4.19)–(4.21) nor by $y_{\text{2nd,cross}}$) or else truncation error in the numerical scheme used to obtain y_{Eulerian}. Since the difference between y_{Eulerian} and $y_{\text{2nd,lower}}$ is however larger than this, we assert that the difference between $y_{\text{2nd,lower}}$ and the location of the concave corner is genuine and not solely due to error in our second-order expansion. Thus, we confirm that we are actually

extracting material points to populate the lower region at early times, but later on, we consume those extracted points again. However, doubt is still present, regarding the exact time at which material points originally present on the front start being consumed, as our estimates require extrapolation out of the $t \ll 1$ domain where second-order solutions formally apply. In summary, we found that our second-order predicted location of the concave corner fits the Eulerian data reasonably well, at both, small times $t \ll 1$ and also up to times of order unity. Nevertheless, for points away from the concave corner, we have not yet demonstrated whether the position of the Lagrangian material points forming the upper region fit front shape predictions from the Eulerian numerical data. This will be considered in the next section.

4.8 Second-order front shape at later times

In order to check reliability of our second-order results, we compute for a given time $t = 1$, the front shape $(-\Xi, -\zeta)$ (see Figure 4.8(a)), as a collection of material points with different t_{inj} all at the same t, specifically $t = 1$. Thus, we fix t and vary t_{inj} from $t_{\text{inj(min)}}$ to t, by varying $\mathcal{T}$, from 0 up to $\mathcal{T}_{\text{cross}}$. We plot $(-\Xi, -\zeta)$ at both first-order (equations (4.16)–(4.17)) and second-order (equations (4.20)–(4.21)) comparing results with the numerical Eulerian data. When $t = 1$, the first-order theory predicts $t_{\text{inj(min)}} = 1 - \mathcal{T}_{\text{cross},0} \approx 0.0569$ whereas the second-order procedure (i.e. tracking (4.24)–(4.25) until they match with (4.26)) requires $t_{\text{inj(min)}} \approx 0.0997$ to achieve matching at $t = 1$. This is already outside the domain $t_{\text{inj}} \in [0, 0.01]$ analysed in section 4.7, and likewise outside the domain in which we can apply equation (4.36) to estimate t_{inj} given t. A value $t_{\text{inj(min)}} \approx 0.0997$ when $t = 1$ implies $\mathcal{T}_{\text{cross}} \approx 0.9003$ in order for equations (4.24)–(4.25) and (4.26) to match, which is actually less than the value of $\mathcal{T}_{\text{cross},0}$. It follows that $\mathcal{T}_{\text{cross}}$ initially increases as t_{inj} increases (as per Figure 4.4) but for

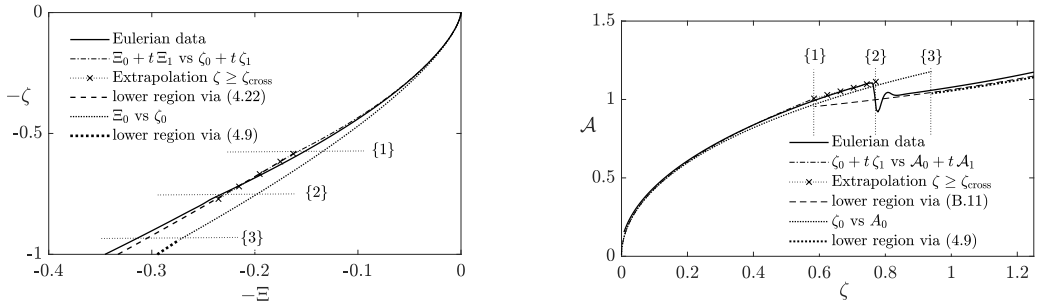

(a) (b)

Figure 4.8: First and second-order solution, for upper and lower region, compared with Eulerian data at time $t = 1$. Horizontal and vertical lines labelled with $\{1\}$, $\{2\}$ and $\{3\}$ specify the matching point between regions. (a) Rescaled front shape $(-\Xi, -\zeta)$. (b) Rescaled front orientation angle $\mathcal{A}$ against rescaled vertical coordinate ζ.

large t_{inj} it starts to decrease. In addition to front shape data $(-\Xi,-\zeta)$ as plotted in Figure 4.8(a), we also show, in Figure 4.8(b), the orientation angle $\mathcal{A}$ versus ζ. For the upper region, this is given parametrically, in terms of $\mathcal{A}_0(\mathcal{T})$ and $\zeta_0(\mathcal{T})$ (at first-order), and $\mathcal{A}(\mathcal{T}, t)$ and $\zeta(\mathcal{T}, t)$ (at second-order), via equations (4.15), (4.16), (4.19) and (4.20). We also plot the lower region angle $\mathcal{A}(t)$ vs $\zeta(t)$, which is determined either using equation (4.1) (accurate to order $t^{3/2}$ in x) or else via (B.11) (in Appendix B; accurate to order $t^{5/2}$ in x) coupled with equation (4.11). The upper and lower region predictions are compared with Eulerian data, although in Figure 4.8(b), these display oscillations in the neighbourhood of the concave corner, which are just numerical artifacts [116].

In Figure 4.8(a), we see how the self-similar nature of ζ and Ξ, present at early times, is broken at a finite time $t = 1$. Here, we also appreciate how the upper region given by equations (4.20) and (4.21), intersects the lower region given by equation (4.22), at $\zeta(\mathcal{T}_{\text{cross}}, t = 1) \approx 0.5839$ and $\Xi(\mathcal{T}_{\text{cross}}, t = 1) \approx 0.1627$, with $\mathcal{T}_{\text{cross}} \approx 0.9003$ (horizontal line labelled by $\{1\}$ in Figure 4.8(a)). This point corresponds to a y value of $y_{\text{cross}}^{\text{inter}}$ at $t = 1$ (see Figure 4.7). Nevertheless, we

extend the second-order solution via a linear extrapolation up to the point where equation (B.45) would predict the location of the concave corner (see section B.9 in Appendix B for details), suggesting instead $\zeta_{\text{cross}}(t=1) \approx 0.7711$ (horizontal line labelled by {2} in Figure 4.8(a)). This now corresponds to a y value of $y_{\text{2nd,cross}}$ at $t=1$ (see Figure 4.7). Here also we see that our current second-order solution for ζ vs Ξ is closer to the Eulerian data, than the first-order solution is. Indeed the dotted curve, corresponding to the upper region via a first-order approximation ($\zeta_0(\mathcal{T})$, $\Xi_0(\mathcal{T})$), finishes even further away, with $\zeta_{\text{cross},0} \approx 0.9397$ and $\Xi_{\text{cross},0} \approx 0.2733$ (values quoted in Table 4.1; see horizontal line labelled by {3} in Figure 4.8(a) corresponding to $y_{\text{1st,cross}}$ in Figure 4.7), intercepting the lower region predicted by (4.18) (thick-dotted line). In addition, we see that the lower region (given by second-order equation (4.22) at least for parts of the lower region near the concave corner), is relatively close to the Eulerian solution, more so than first-order equation (4.9). In Figure 4.8(b), we show the orientation angle $\mathcal{A}$ vs ζ, highlighting, as in Figure 4.8(a), the second-order matching point, which occurs at $\zeta(\mathcal{T}_{\text{cross}}) \approx 0.5839$ with $\mathcal{A}(\mathcal{T}_{\text{cross}}) \approx 1.0063$ and with $\mathcal{T}_{\text{cross}} \approx 0.9003$ (vertical line labelled {1} in Figure 4.8(b), corresponding to $y^{\text{inter}}_{\text{cross}}$). This data is extrapolated up to the concave corner location predicted by equation (B.45) (vertical line labelled {2} in Figure 4.8(b), corresponding to $y_{\text{2nd,cross}}$), which gives $\zeta_{\text{cross}}(t=1) \approx 0.7711$, and a corresponding value of $\mathcal{A} \approx 1.1131$ (note that this value is slightly different from that predicted by extrapolation of equation (B.44), which gives $\mathcal{A}_{\text{cross}}(t=1) \approx 1.1259$). We also show the intersection between the two regions via the first-order solution (vertical line labelled {3} in Figure 4.8(b), corresponding to $y_{\text{1st,cross}}$, see section 4.3.2 for details). The value of $\mathcal{A}(\mathcal{T}_{\text{cross}}) \approx 1.0063$ (labelled by {1}) in Figure 4.8(b) is curious. This is so close to unity that the orientation of the upper and lower region are nearly parallel, making it possible in Figure 4.8(a) to extrapolate the solution of the upper region, and still remain close to the lower region. In a near parallel case like that it is

difficult to pinpoint exactly where the intersection between these regions occurs. This may help to explain why the Eulerian prediction seems to give the concave corner (with a sudden decrease of $\mathcal{A}$ in Figure 4.8(b)) at a different ζ value, closer to the point labelled {2} than {1}: we already know from Figure 4.7 that $y_{\mathrm{2nd,cross}}$ fits y_{Eulerian} better than $y_{\mathrm{cross}}^{\mathrm{inter}}$ does. Despite the subtleties, from Figure 4.8(a) and (b), we see that the current second-order solution fits the Eulerian data better than the first-order solution does, giving good agreement even up to times of order unity.

4.9 Conclusions

We have considered a dimensionless form of the pressure-driven growth model used to predict the foam front propagation in an oil reservoir. The front has been captured as the region of finely-textured foam of very low mobility, where injected gas meets reservoir liquid. The foam front is represented as a curve of negligible thickness, which propagates through the porous medium due to the pressure difference across it, and at the same time is retarded by dissipation. The focus here was on early time behaviour, such that the distance the front has propagated horizontally is less than the maximum vertical depth through which it can displace, albeit some of the results we present are extrapolated beyond that regime. As was shown in previous studies [104, 116], and also in Chapter 3, the foam front can be divided vertically into two regions (lower and upper) that intersect in a concave corner. In this study we have obtained a second-order solution in time, to track the trajectory of the material points of the upper region of the front, up to the aforementioned concave corner or matching point between both regions. Obtaining the second-order solution in the upper region was particularly challenging owing to strong spatio-temporal non-uniformities that are present there. Our approach was to start with solutions in terms of dimensionless similarity

solutions, but then at second-order include corrections showing how those similarity solutions break down. This obtained an approximation accurate to order $t^{5/2}$ for the horizontal x location of the material points of the upper region of the front, and an order t^2 accurate approximation for their vertical y location, in each case, with the same order at which the lower region has been computed. At any specified time t, a second-order solution predicted the vertical location of the concave corner higher up than the first-order solution, but very close to the prediction of an independently obtained Eulerian prediction obtained in Chapter 3. Based on the second-order solutions we can determine that the speed at which the concave corner or kink moves downwards decreases over time, although as it moves down on the front its velocity decreases (due to the net driving pressure also decreasing with depth). Eventually of course it will reach a depth at which driving pressure is balanced by hydrostatic pressure, and the downward motion will then cease. We have also proven that initially material points are extracted from the concave corner to populate the lower region, since the topmost point originally present on the front at time $t = 0$ initially moves down faster than the concave corner does, as predicted via the first and/or second-order solution obtained in this study. Later on, due to second-order effects in time, with the downward motion of such material points slowing down over time, the lower region material points originally on the front eventually reach the concave corner, which must therefore have consumed any previously extracted material points. Therefore, we can assert that all points extracted into the lower region are eventually consumed, however, based on the different approximations that we use, we can actually have different predictions for exactly when this occurs. The issue is that the time we are trying to identify is already sufficiently long that there might be some uncertainty whether expanding in time as far as a second-order solution remains adequate or whether yet a higher-order correction is required, which will be challenging in view of strong spatio-temporal non-uniformities present in the

upper region. Nevertheless, with the new solutions we were also able to compute the shape of the upper region of the front, which fitted the Eulerian data even up to times of order unity. Therefore, the second-order analytical solution frees us of having to obtain computationally expensive numerical simulations in order to determine accurately the shape of the front at a specific time, which is relevant for real field applications.

Chapter 5

Foam flow in confined straight channels

This chapter is comprised of a work submitted to the journal Physical Review E, by Carlos Torres-Ulloa and Paul Grassia. The title of the article is "Viscous froth model applied to the motion of two-dimensional bubbles in a channel: The three-bubble case", which was submitted in late December 2020. In this work the viscous froth model is used to study the rheology of a system comprised of three bubbles as they flow in a confined straight channel. Supplementary material to this work is also presented in Appendix C.

Summary: The viscous froth model can be used to predict rheological behaviour of a two-dimensional liquid-foam system comprised of a number of bubbles confined between two glass plates. The model incorporates three physical phenomena: namely the viscous drag force, the pressure difference across foam films, and the surface tension acting along them, converting any mismatch between the pressure forces and film curvature to film motion. In the so-called infinite staircase structure, the system does not undergo topological bubble neighbour exchange transformations, for any imposed driving back pressure, bubbles then flowing out of the channel of transport in the same order in which they entered it. In contrast, in a simple single bubble staircase or so-called lens system, for higher imposed back pressures, topological transformations do occur, helping to relax the system. The case studied here, i.e. the three-bubble case, bridges between the dynamics seen in the infinite staircase and simple staircase/lens. Steady state three-bubble solutions are obtained for a range of bubble sizes and imposed back pressures. As an imposed back pressure increases quasistatically from equilibrium, systems undergo either topological transformations, reach saddle-node bifurcation points, or asymptote to an inherently stable structure which ceases to change as the back pressure is further increased.

5.1 Introduction

A two-dimensional foam system comprised by three bubbles attached together is studied in this chapter by using the viscous froth model, particularly as the system flows along a straight channels in a truncated staircase configuration. Although, other studies have been carried out for more bubbles, these considered the complication of non-straight channels [21,24], which may affect the dynamics. What still remains unclear in literature though, even for a straight channel, is how the staircase system would behave as a function of the number of bubbles.

Two limiting cases are of special interest for this chapter. These are the so-called simple lens problem, which consists at equilibrium (in a two-dimensional view) of a single bubble lens attached to an upper channel wall and a spanning film connecting it with the lower channel wall [19] (see Figure 2.7 in section 2.2.3.3), and the infinite staircase structure [144] (see Figure 2.5(b) in section 2.2.2). While the simple lens has been characterized as undergoing topological transformation as the system driving velocity increases [19], the infinite staircase remains stable (not suffering any topological change) up to arbitrarily large driving velocities. This work therefore aims to interpolate between the simple lens case and the infinite staircase structure, by studying as mentioned above a system comprised of three bubbles in a staircase configuration starting from equilibrium; when seen in a two-dimensional view (see Figure 5.1) two symmetric (i.e. equal area) bubbles are attached to an upper channel wall, and a spanning bubble (possibly of different size) connects them to the lower channel wall. This system is considered here in the dry limit, so Plateau's rules applied.

As is known from literature [19], when the simple lens moves at an increasing velocity v driven via an increasing imposed back pressure p_b, is expected to deform leading to topological transformations and/or loss of stability (at a saddle-node bifurcation point, see section 2.2.3.3). However, for a large number of bubbles $N \gg 1$ arranged in a staircase, the system is expected to remain in the stable state without any $T1$ event [144] (indeed without even any geometric distortion of the structure), no matter how large a pressure is used to drive it. One of the aims of this chapter is to establish whether the three-bubble system $N = 3$ behaves more akin to the simple lens, or more akin to the infinite staircase, or perhaps whether it can exhibit either type of behaviour depending on the particular bubble sizes considered. The methodology considered here is an entirely steady state one, i.e. the imposed back pressure p_b (or in the event that a saddle-node bifurcation is

encountered, some other variable imposed in lieu) is varied quasistatically, and changes in the resulting steadily propagating three-bubble structure are tracked through parameter space. This methodology is adequate to establish for which parameter sets $T1$s occur, and to classify the various types of $T1$ that are found ($T1_c$, $T1_u$ or $T1_l$ as mentioned earlier). However an unsteady state approach (not considered here) would of course be required to examine how the system evolves following any $T1$.

The rest of this work is structured as follows. In section 5.2 we introduce a three-bubble symmetric system, as aforementioned, symmetric in the sense that the first and third bubbles have equal size. Here it is also shown how the structure is set up in equilibrium. In section 5.3 we apply the viscous froth model to obtain necessary conditions for the existence of an inherently stable migration structure out of equilibrium, at arbitrarily large driving pressure. In section 5.4 we introduce the methodology by which steady state solutions (i.e. solutions for a steadily propagating but out-of-equilibrium three-bubble system) are obtained for an arbitrary imposed back pressure. This includes a discussion of the method by which the solutions are tracked to a topological transformation. Finally in section 5.5, we present the steady state solution results. Conclusions are offered in section 5.6. Additional details of equations, results and numerical methods are relegated to Appendix C, as specified through this paper.

5.2 Three-bubble symmetric system

The system under study in this work is formed of three two-dimensional bubbles flowing through a straight channel of width L, with two of these attached to the upper channel wall (bubbles $\mathcal{B}_1$ and $\mathcal{B}_3$, symmetric as they have the same size) and one bubble $\mathcal{B}_2$ (possibly with a different size) attached to the lower

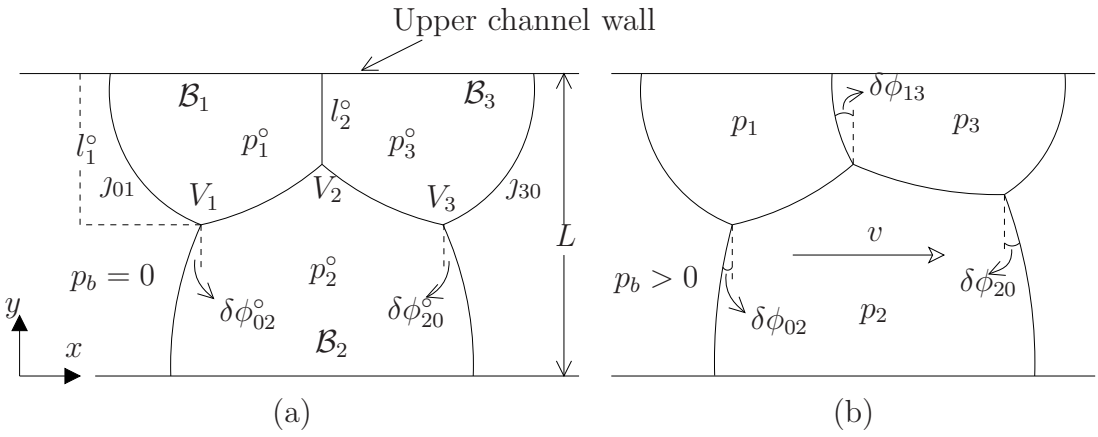

Figure 5.1: (a) Equilibrium system for channel of dimensionless width $L = 1$. (b) The system is set in motion, travelling at an unknown migration velocity v, as a consequence of an imposed back pressure $p_b > 0$. The film $\jmath_{13}$ turns through an unknown angle $\delta\phi_{13}$. Moreover $\delta\phi_{02}$ and $\delta\phi_{20}$ are no longer opposite and equal.

channel wall (see Figure 5.1(a)). In the dimensionless form of the model, as used in this work, $L = 1$. This three-bubble structure is a generalisation of the simple lens (see Figure 2.7), which had only a single bubble. Note that we consider an odd number of bubbles here, since in the simple lens case interesting behaviour stemmed from the fact that unequal numbers of films attached to the upper and lower walls. Like the simple lens, the three-bubble structure is also a truncated case of the infinite staircase (see Figure 2.5(b)), albeit not quite so drastic a truncation. It is comprised of seven films denoted by $\jmath_{ij}$, where the subscript $[i, j] \in \{0, 1, 2, 3\}$ indicates the bubbles that each film divides (see Figure 5.1(a)), such that $[i, j] \equiv 0$ outside the structure. In addition, we use the superscript "$\circ$" to denote variables in the equilibrium. In the equilibrium state, the pressure of the spanning bubble $\mathcal{B}_2$ corresponds to p_2°, the pressures of the symmetric bubbles $\mathcal{B}_1$ and $\mathcal{B}_3$ are $p_1^\circ = p_3^\circ$, and the imposed back pressure p_b satisfies $p_b = 0$. The distance between the top of the channel and the vertex V_1 and V_3 is l_1°, and between the top of the channel and the vertex V_2 is l_2°. Films $\jmath_{01}$, $\jmath_{02}$ and $\jmath_{12}$ join at the vertex V_1, and the films $\jmath_{12}$, $\jmath_{13}$ and $\jmath_{23}$ join at the vertex V_2, while the films $\jmath_{23}$, $\jmath_{30}$ and $\jmath_{20}$ join at the vertex V_3. Finally, the film $\jmath_{12}$ connects the

vertices V_1 and V_2, and the film $\jmath_{23}$ connects the vertices V_2 and V_3. Every film forms an angle of $\pi/2$ with the respective wall of the channel and an angle $2\pi/3$ with other films. The length of the films in equilibrium are $\mathcal{L}^\circ_{01} = \mathcal{L}^\circ_{30}$, $\mathcal{L}^\circ_{12} = \mathcal{L}^\circ_{23}$ and $\mathcal{L}^\circ_{02} = \mathcal{L}^\circ_{20}$. Film $\jmath_{13}$ is flat at equilibrium and the angles through which the films $\jmath_{02}$ and $\jmath_{20}$ turn are $\delta\phi^\circ_{02} = -\delta\phi^\circ_{20}$. It turns out that turning angles on all other films in the equilibrium state can be determined once $\delta\phi^\circ_{02}$ and $\delta\phi^\circ_{20}$ are known. In what follows we will consider systems both in equilibrium and systems that are steadily moving, but out-of-equilibrium (see Figure 5.1(b)). In section 5.2.1 we give further details of the geometry of the three-bubble system. Then, in section 5.2.2 we introduce the system's governing equations. In section 5.2.3 we determine the equilibrium structure (further detail in section C.1 in Appendix C). Finally in section 5.2.4 we describe the conditions to achieve a topological transformation for the three-bubble system. Understanding all of this geometrical and topological information turns out to be relevant to the body of results that we present later on in section 5.5.

5.2.1 Configuration of the three-bubble symmetric system

In the (stationary) equilibrium (see Figure 5.1(a)) and (steadily moving) out-of-equilibrium structure (see Figure 5.1(b)), the films join three by three at the respective vertices subtending an angle of $2\pi/3$ and join at an angle of $\pi/2$ with respect to the channel side walls. How much a film is oriented at each point is measured with respect to the vertical in the anticlockwise direction as an angle $\phi_{ij}(\mathfrak{s}_{ij})$ (see Figure 5.1(b) and 5.2(c)), where $\mathfrak{s}_{ij}$ corresponds to the distance measured along a film from a wall or vertex up to a total length per film $\mathcal{L}_{ij}$, with the direction in which $\mathfrak{s}_{ij}$ is measured to be specified shortly. The orientation angle at the start of each film is expressed as $\phi_{ij}(\mathfrak{s}_{ij} = 0) \equiv \phi_{ij,0}$, and the orientation

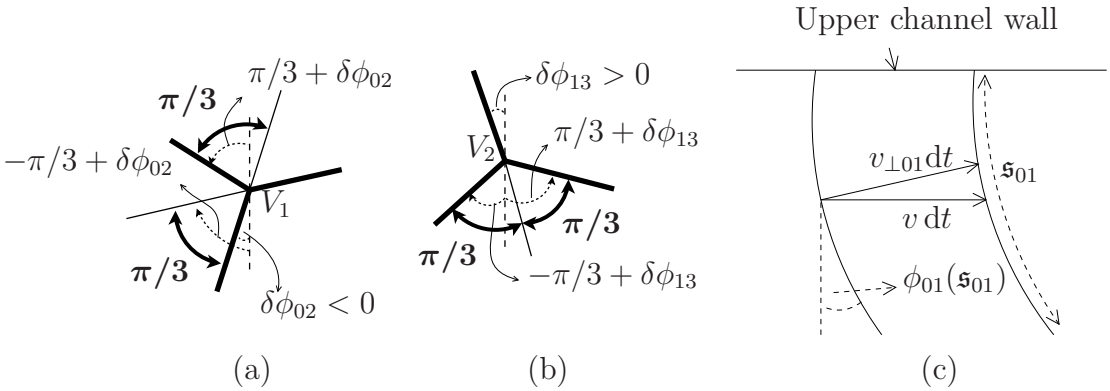

Figure 5.2: Angle measurement convention. In (a) and (b), the inset shows zoomed views near V_1 and V_2, respectively, for each film meeting at the vertex. Here, orientation angles are measured in the anticlockwise direction starting from the vertical (dash line) to the film (thick solid line). (c) View of film $\jmath_{01}$ which is attached to the upper channel wall. At a distance $\mathfrak{s}_{01}$ measured along it, an element of the film has an orientation angle $\phi_{01}(\mathfrak{s}_{01})$ with respect to the vertical. In a time step $\mathrm{d}t$, the element moves a distance $v_\perp \mathrm{d}t$ in the normal direction and an apparent distance $v\,\mathrm{d}t = v_{\perp 01}\mathrm{d}t/\cos(\phi_{01})$ along the channel.

angles at the ends of films as $\phi_{ij}(\mathfrak{s}_{ij} = \mathcal{L}_{ij}) = \phi_{ij,\mathcal{L}}$. Hence, the total turning angle of each film $\jmath_{ij}$ is then expressed as $\delta\phi_{ij} \equiv \phi_{ij,\mathcal{L}} - \phi_{ij,0}$ (with $[i,j] \in [0,1,2,3]$). In this work, we consider that for films connected with the upper channel wall, $\mathfrak{s}_{ij}$ grows downwards, where the initial orientation angle at this point is equal to $\phi_{ij,0} \equiv 0$. Films $\jmath_{12}$ and $\jmath_{23}$, are also considered to have $\mathfrak{s}_{ij}$ growing downwards, so they start at vertex V_2 (with $\mathfrak{s}_{ij} = 0$), where their initial orientation angles are expressed in terms of $\delta\phi_{13}$, as specified in Table 5.1. In contrast, for films connected with the lower channel wall, $\mathfrak{s}_{ij}$ is considered to grow upwards, where their initial orientation angle corresponds to $\phi_{ij,0} \equiv 0$. In this work we specify bubble areas by fixing the vertical distance (measured down from the upper channel wall) of the vertices V_1 and V_2 in equilibrium (see section 5.2.3, and further details in section C.1 in Appendix C). These distances are denoted l_1° and l_2°, respectively. Note that in equilibrium, vertex V_3 is at the same vertical location as vertex V_1 on symmetry grounds. In addition, we can readily express either for equilibrium and

Film	from	to	$\phi_{ij,0}$	$\phi_{ij,\mathcal{L}}$	$\delta\phi_{ij}$
$\jmath_{02}$	Lower channel wall	vertex V_1	0	$\delta\phi_{02}$	$\delta\phi_{02}$
$\jmath_{13}$	Upper channel wall	vertex V_2	0	$\delta\phi_{13}$	$\delta\phi_{13}$
$\jmath_{20}$	Lower channel wall	vertex V_3	0	$\delta\phi_{20}$	$\delta\phi_{20}$
$\jmath_{01}$	Upper channel wall	vertex V_1	0	$\pi/3+\delta\phi_{02}$	$\pi/3+\delta\phi_{02}$
$\jmath_{12}$	vertex V_2	vertex V_1	$-\pi/3+\delta\phi_{13}$	$-\pi/3+\delta\phi_{02}$	$\delta\phi_{02}-\delta\phi_{13}$
$\jmath_{23}$	vertex V_2	vertex V_3	$\pi/3+\delta\phi_{13}$	$\pi/3+\delta\phi_{20}$	$\delta\phi_{20}-\delta\phi_{13}$
$\jmath_{30}$	Upper channel wall	vertex V_3	0	$-\pi/3+\delta\phi_{20}$	$-\pi/3+\delta\phi_{20}$

Table 5.1: Orientation angles $\phi_{ij}(\mathfrak{s}_{ij})$ for every film, from $\mathfrak{s}_{ij}=0$ up to $\mathfrak{s}_{ij}=\mathcal{L}_{ij}$. Applying rules on vertex meeting angles, the initial and final orientation angles are expressed in terms of three total turning angles $\delta\phi_{13}$, $\delta\phi_{02}$, and $\delta\phi_{20}$, respectively.

out-of-equilibrium systems, final orientation angles at the ends of films $\jmath_{01}$ and $\jmath_{12}$ (at vertex V_1), denoted $\phi_{01,\mathcal{L}}$ and $\phi_{12,\mathcal{L}}$, in terms of $\delta\phi_{02}$, and for films $\jmath_{23}$ and $\jmath_{30}$ (at vertex V_3), denoted $\phi_{23,\mathcal{L}}$ and $\phi_{30,\mathcal{L}}$, in terms of $\delta\phi_{20}$. This is what we have summarized in Table 5.1. Only three of the total turning angles, namely $\delta\phi_{02}$, $\delta\phi_{13}$ and $\delta\phi_{20}$, are treated as being independent. This follows since, by applying rules on vertex meeting angles, we can deduce that $\delta\phi_{01}=\phi_{01,\mathcal{L}}\equiv\delta\phi_{02}+\pi/3$, $\delta\phi_{12}=\delta\phi_{02}-\delta\phi_{13}$, $\delta\phi_{23}=\delta\phi_{20}-\delta\phi_{13}$, and $\delta\phi_{30}=\phi_{30,\mathcal{L}}\equiv\delta\phi_{20}-\pi/3$.

When the system is set in motion (by imposing an external force) for a given imposed back pressure p_b, we need to obtain in addition the aforementioned turning angles, film lengths, pressures, and the migration velocity v (see Figure 5.1(b)). Therefore, to define a system we have to determine 19 unknown variables, namely 7 turning angles $\delta\phi_{ij}$ (measured from the end to the start of each film), 7 film lengths $\mathcal{L}_{ij}$, 3 bubble pressures p_i, the imposed back pressure p_b, and migration velocity v. In this work we propose two different ways of parametrizing film coordinates. The first one is in terms of film orientation angles ϕ_{ij} (varying between $\phi_{ij,0}$ and $\phi_{ij,\mathcal{L}}$), and the second is in terms of distances measured along films $\mathfrak{s}_{ij}$ (varying between 0 and $\mathcal{L}_{ij}$). Using either way of parametrizing, there are a set of well-defined constraints that must be satisfied.

If coordinates are computed in terms of orientation angles (see section C.2.1 in Appendix C), we can reduce the number of independent variables as follows. Since film lengths can be computed readily in terms of turning angles along films and vice versa, as explained in section C.2.2 in Appendix C, we can reduce the number of unknown independent variables to 12. Furthermore, by applying rules on vertex meeting angles, specifically at vertices V_1 and V_3, turning angles $\delta\phi_{ij}$ can be expressed in terms of the three turning angles treated as independent, namely $\delta\phi_{13}$, $\delta\phi_{02}$, and $\delta\phi_{20}$, thereby reducing the number of unknown variables to 8. No further variables can be eliminated by imposing rules on meeting angles at vertex V_2, because vertex V_2 is already negotiated both when reaching vertex V_1 via films $\jmath_{13}$ and $\jmath_{12}$, and likewise when reaching vertex V_3 via films $\jmath_{13}$ and $\jmath_{23}$. For any given set of 8 independent variables as identified above, when computing film coordinates in terms of orientation angles ϕ_{ij}, the system must satisfy 3 area constraints (one constraint per bubble), plus 4 constraints on the y position, 2 at V_1 and 2 at V_3. This is explained further in section 5.4.3. No additional constraints arise from the y position at V_2, since this vertex is already negotiated when reaching V_1 and V_3 via $\jmath_{12}$ or $\jmath_{13}$. Thus we have 8 independent variables and 7 constraints. One of the variables remains therefore free to be selected as a control variable, and imposing a value for it then determines all the other variables. Typically we select a back pressure p_b (as in Figure 5.1) to be the control variable, although as we will see later on, alternative choices are possible. By contrast, if film coordinates are computed not in terms of orientation angle ϕ_{ij} but rather in terms of distances along films $\mathfrak{s}_{ij}$ (see section C.2.3 in Appendix C), the number of independent variables can be reduced from 19 to just 12, by computing film turning angles in terms of film length: this is already explained in section C.2.2. In that section what is obtained are distances along films $\mathfrak{s}_{ij}$ as a function of the orientation angles ϕ_{ij} and vice versa, from which it is possible to relate film lengths $\mathcal{L}_{ij}$ to film turning angles $\delta\phi_{ij}$. In all cases, we have to

consider 3 constraints on bubble areas. In addition there are 4 constraints on angles, consistently with Table 5.1, 2 constraints at V_1 and 2 at V_3. There are also 4 constraints on y values at vertices, 2 at V_1 and 2 at V_3. This is explained further in section 5.4.4. In each case no additional constraints arise from vertex V_2, since the orientation angles at vertices V_1 and V_3 as well as the y coordinates there, already depend on negotiating vertex V_2. With 12 independent variables and 11 constraints in total, one of the variables (typically p_b, but other choices are possible) is retained as a control variable.

To summarise, depending on whether we parametrize the system in terms of orientation angles or in terms of distances measured along films, we have different numbers of independent variables and constraints to consider. However in both cases there is one more variable than constraint, meaning that one of the variables can be set as a control. These constraints meanwhile are formulated by applying the viscous froth model to determine the shape of each film, in terms of pressure difference across films Δp_{ij} and migration velocity v (see section 5.2.2). Once these film shapes are established, and film endpoints are specified (in terms of either $\delta\phi_{ij}$ or $\boldsymbol{\mathcal{L}}_{ij}$), then enclosed bubble areas, coordinate locations of vertices, and (if needed) orientation angles at film endpoints can all be determined. The constraints are therefore merely expressed as functions (albeit complicated non-linear functions) of the system variables.

We recall that we seek to find, for a given system, not only how it evolves as p_b increases, but also whether a topological transformation i.e. bubble rearrangement occurs. As the three-bubble structure we consider here is rather more complicated geometrically than the simple lens considered by [19], the set of possible topological transformations it can undergo is likewise more complicated. We consider that a $T1_c$ topological transformation will take place when the length of film $\jmath_{12}$

tends to 0, implying the collision between the film vertices V_1 and V_2, and that $\delta\phi_{12} \to 0$. On the other hand, a $T1_u$ topological transformation takes place when the length of film $\jmath_{30}$ tends to 0, implying that the vertex V_3 has reached the upper channel side wall, with $\delta\phi_{30} \to 0$. Meanwhile a $T1_{l1}$ topological transformation happens when the length of film $\jmath_{02}$ goes to 0, implying that the vertex V_1 has reached the lower channel side wall, with $\delta\phi_{02} \to 0$. In addition, a $T1_{l3}$ topological transformation happens when the length of film $\jmath_{20}$ goes to 0, implying that the vertex V_3 has reached the lower channel side wall, with $\delta\phi_{20} \to 0$. Yet another possibility to consider is that the system reaches a saddle-node bifurcation (further details in section 5.2.4), or reaches an inherently stable structure without undergoing any $T1$ whatsoever even for arbitrary large migration velocity (further details in section 5.3). Under such circumstances, by analogy with an infinite staircase, the system should eventually approach a limiting state that does not suffer any further deformation as p_b increases. This is what we discuss in section 5.3. First however we present the model and governing equations (section 5.2.2), discuss the equilibrium structure (section 5.2.3), and impose conditions on the out-of-equilibrium topological transformations (section 5.2.4).

5.2.2 Model and governing equations for steady state solution

In this section we recall the methodology used in [19], to obtain the equations governing the steady state film coordinates of the system. Readers familiar with this procedure from [19], may prefer to skip directly to section 5.2.3. Equation (4.35) corresponds to the dimensional form of the viscous froth model, with a linear viscous drag law. We assume typical parameter values $L = 9\,\mathrm{mm}$, $\sigma = 27 \times 10^{-3}\,\mathrm{N\,m^{-1}}$, and $\mathcal{C} = 290\,\mathrm{kg\,m^{-2}\,s^{-1}}$, the latter having been given by [19]. In this work the viscous froth model will be used in its dimensionless form, for

which $v_\perp$ is rescaled by the velocity $2\sigma/(L\mathcal{C}) \approx 0.002\,\mathrm{m\,s^{-1}}$ using the scales given earlier, Δp by the pressure $2\sigma/L \approx 6\,\mathrm{N\,m^{-2}}$, the curvature κ by $1/L \approx 111\,\mathrm{m^{-1}}$ and finally the time scale by $L^2\mathcal{C}/(2\sigma) = 0.43\,\mathrm{s}$. Thus the dimensionless viscous froth model applied to the motion of a local film element can be written as

$$v_{\perp ij} = \Delta p_{ij} - \kappa_{ij}. \tag{5.1}$$

Here $v_{\perp ij}$ is the normal velocity, and Δp_{ij} the pressure difference, both measured in the left to right direction. The curvature term depends on our sign convention. If $\mathfrak{s}_{ij}$ is measured downwards, we define $\kappa_{ij} = -\mathrm{d}\phi_{ij}/\mathrm{d}\mathfrak{s}_{ij}$; when $\mathfrak{s}_{ij}$ is measured upwards, we define instead $\kappa_{ij} = \mathrm{d}\phi_{ij}/\mathrm{d}\mathfrak{s}_{ij}$. With this convention, seen from downstream, convex films are always positively curved and concave films are always negatively curved. In either case, the left-hand side of the equation (5.1) represents the linear viscous drag force, and the right-hand side represents the driving forces, which can only be in balance for a static film (following Laplace's law).

If the system is at steady state, then in a small time interval $\mathrm{d}t$, all points in the structure have a uniform apparent displacement $v\,\mathrm{d}t$. However the structure's apparent horizontal displacement is also related to the turning angle and the normal velocity by $v_{\perp ij}\mathrm{d}t/\cos(\phi_{ij})$. Hence, the left hand side of (5.1) can be expressed as $v_{\perp ij} = v\,\cos(\phi_{ij})$. Using the aforementioned definition for the curvature κ_{ij}, velocity $v_{\perp ij}$, and the pressure difference across films Δp_{ij}, equation (5.1) can be expressed in terms of the orientation angle ϕ_{ij} as

$$\frac{\mathrm{d}\mathfrak{s}_{ij}}{\mathrm{d}\phi_{ij}} = \pm\frac{1}{\Delta p_{ij} - v\,\cos(\phi_{ij})}, \tag{5.2}$$

with the sign "$\pm$" set as $-$ for films where $\mathfrak{s}_{ij}$ is measured from the upper to the lower channel wall direction, and as $+$ for films where $\mathfrak{s}_{ij}$ is measured from the

lower to the upper channel wall direction. Knowing the range of angles covered by each film, equation (5.2) can be integrated to obtain film length $\mathcal{L}_{ij}$ (see section C.2.2 in Appendix C). Additionally, a film element of length $\mathrm{d}\mathfrak{s}_{ij}$ along the film which has turned through an angle ϕ_{ij}, with respect to the vertical can be represented in Cartesian coordinates as $(\mathrm{d}x_{ij}, \mathrm{d}y_{ij})$ where

$$\mathrm{d}x_{ij}/\mathrm{d}\mathfrak{s}_{ij} = \sin(\phi_{ij}), \tag{5.3}$$

$$\mathrm{d}y_{ij}/\mathrm{d}\mathfrak{s}_{ij} = -\cos(\phi_{ij}), \tag{5.4}$$

if $\mathfrak{s}_{ij}$ is measured downward (as is the case in Figure 5.2(c)), and

$$\mathrm{d}x_{ij}/\mathrm{d}\mathfrak{s}_{ij} = -\sin(\phi_{ij}), \tag{5.5}$$

$$\mathrm{d}y_{ij}/\mathrm{d}\mathfrak{s}_{ij} = \cos(\phi_{ij}), \tag{5.6}$$

if $\mathfrak{s}_{ij}$ is measured upward. In both cases ϕ_{ij} is measured in the anticlockwise from the vertical. Then equation (5.2) can be re-expressed, for both cases ($\mathfrak{s}_{ij}$ measured upwards, and $\mathfrak{s}_{ij}$ measured downwards), as

$$\frac{\mathrm{d}x_{ij}}{\mathrm{d}\phi_{ij}} = \frac{-\sin(\phi_{ij})}{\Delta p_{ij} - v\cos(\phi_{ij})}, \tag{5.7}$$

$$\frac{\mathrm{d}y_{ij}}{\mathrm{d}\phi_{ij}} = \frac{\cos(\phi_{ij})}{\Delta p_{ij} - v\cos(\phi_{ij})}. \tag{5.8}$$

Equations (5.7), and (5.8) can be integrated with $v = 0$ to determine the equilibrium structure (see section 5.2.3 to follow), or with $v > 0$ to determine the film coordinates when the structure is set in motion. This latter case with $v > 0$ is rather more complicated to integrate, so discussion of it is deferred until section 5.4.

5.2.3 Equilibrium structure

When the imposed back pressure $p_b = 0$, the structure is at equilibrium with $v = 0$ and $\delta\phi_{13} = 0$. Although our main interest in the present work will be in moving structures with p_b, v and $\delta\phi_{13}$ all being non-zero, understanding the equilibrium structure is important for the following reasons. Firstly we use two equilibrium length scales l_1° and l_2° (discussed in more detail below) as surrogates for bubble areas, so it is necessary to understand how they do in fact relate to bubble areas. Secondly varying the values of l_1° and l_2° affects all the length scales in the structure, including the lengths of all the films. Since $T1$ transformations in out-of-equilibrium structures involve films shrinking away to zero, identifying films which are already particularly short in the equilibrium structure gives an indication of the types of $T1$ to which a system is most likely to be susceptible. These points are discussed below, with additional detail in section C.1 in Appendix C.

Here equilibrium variables are denoted with the superscript "$\circ$". The variables that define the shape of the structure are then bubble pressures p_1°, p_2°, p_3° (with $p_1^\circ = p_3^\circ$ on symmetry grounds since bubble areas A_1 and A_3 are equal), and the total turning angles $\delta\phi_{02}^\circ$ and $\delta\phi_{20}^\circ$ (with $\delta\phi_{02}^\circ = -\delta\phi_{20}^\circ$ on symmetry grounds). All these variables can be determined by fixing two parameters that we denote l_1° and l_2°. Here as indicated in Figure 5.1(a), l_1° is the vertical distance between the upper channel wall to both vertex V_1 and V_3 (on symmetry grounds), and l_2° (which is always less than l_1°) is the distance from the upper channel wall to vertex V_2. At equilibrium moreover, film lengths $\mathcal{L}_{ij}^\circ$ are determined by energy minimization. Laplace's law then applies, implying that all films except film $\jmath_{13}$ (which is entirely flat with length $\mathcal{L}_{13}^\circ = l_2^\circ$), are arcs of circles with uniform curvature. The x_{ij} and y_{ij} coordinates for each film can be computed by integrating equations (5.7), (5.8) for $v = 0$, as determined in section C.1 in Appendix C. Then by imposing meeting

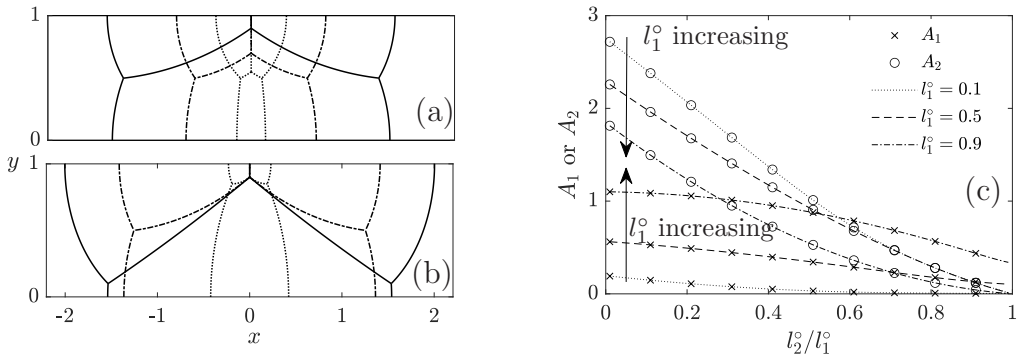

Figure 5.3: (a) Equilibrium structures for a fixed $l_1^\circ = 0.5$ and three different l_2°. Solid line: $l_2^\circ/l_1^\circ = 0.1$. Dot-dashed line: $l_2^\circ/l_1^\circ = 0.3$. Dotted line: $l_2^\circ/l_1^\circ = 0.45$. (b) Equilibrium structures for a fixed $l_2^\circ = 0.1$ and three different l_1°. Solid line: $l_1^\circ = 0.9$. Dot-dashed line: $l_1^\circ = 0.5$. Dotted line: $l_1^\circ = 0.15$. (c) Polydisperse bubble areas for three fixed values of l_1° and various values of $l_2^\circ/l_1^\circ \in [0, 1]$.

rules upon the y coordinates at vertices, the bubble pressures p_1° and p_2°, and total turning angle $\delta\phi_{02}^\circ$, can be obtained as functions of l_1° and l_2°. Since at equilibrium films are arcs of circles, bubble areas $A_1 = A_3$ and A_2 can be calculated directly in terms of p_1°, p_2°, and $\delta\phi_{02}^\circ$, and therefore can be also computed in terms of l_1° and l_2°, albeit via quite complex non-linear equations. These are given by equations (C.9) and (C.10) in section C.1 in Appendix C.

Figure 5.3 shows how the shape of the equilibrium structure changes as a function of either l_2° at fixed l_1° (Figure 5.3(a)) or l_1° at fixed l_2° (Figure 5.3(b)). In Figure 5.3(c), we plot bubble areas for polydisperse systems (polydisperse in the sense that $A_1 = A_3 \neq A_2$), considering three fixed values of l_1° and various values of $l_2^\circ/l_1^\circ \in (0, 1)$. As we see, for small l_1°, bubble area A_2 is almost always bigger than bubble area A_1 except when l_2°/l_1° is exceedingly close to unity. On the other hand for large l_1°, a large l_2°/l_1° value gives bubble area A_2 much smaller than A_1. We can also deduce that for $l_1^\circ \to 1$ and $l_2^\circ \to 0$, the maximum allowed area of bubble $\mathcal{B}_1$ corresponds to $A_1 = A_3 = 1.2755$ (with $A_2 = 1.7321$).

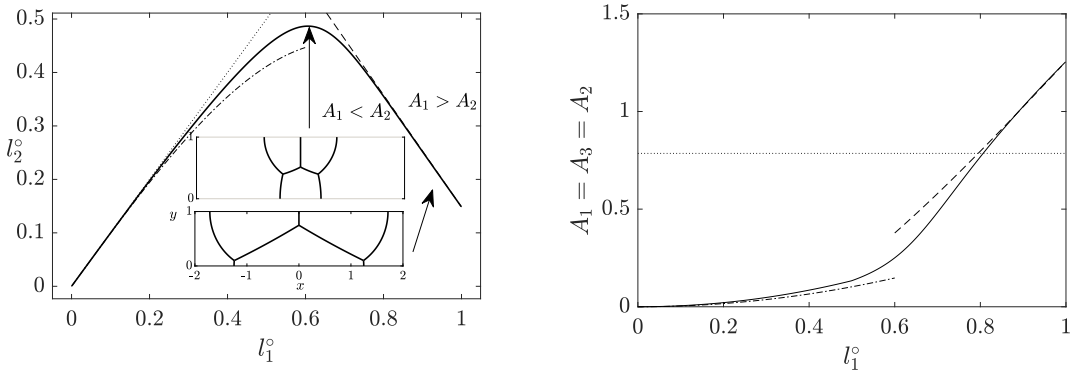

(a) (b)

Figure 5.4: (a) Structures for l_1° and l_2° for which the areas $A_1 = A_2$ (i.e. monodisperse system). Solid line: l_1° versus l_2° for equal areas (with $A_1 > A_2$ above the solid line and $A_1 < A_2$ below it). Dottted line: $l_1^\circ = l_2^\circ$. Dash-dotted line shows $l_2^\circ \approx l_1^\circ - (2\pi/(3\sqrt{3}) - 1/2){l_1^\circ}^3$ obtained in the limit of small $l_1^\circ \to 0$ and $l_2^\circ \to l_1^\circ$ (see equation (C.24) in section C.1.4.1 in Appendix C). Dashed line shows $l_2^\circ \approx (6 - 2\sqrt[4]{3}\sqrt{\pi})/9 + (((14\sqrt[4]{3}\sqrt{\pi} + 15)\pi + 51\sqrt[4]{27}\sqrt{\pi})/(108\pi))(1 - l_1^\circ) \approx 0.1483 + 1.0486\,(1 - l_1^\circ)$ obtained in the limit of $l_1^\circ \to 1$ (see equation (C.30) in section C.1.4 in Appendix C). The inset figures show the monodisperse structure for two different combinations of l_1° and l_2°. (b) Monodisperse bubble areas $A_1 = A_3 = A_2$ for values of $l_1^\circ \in [0, 1]$ with different values of l_2° as given in (a).

For $l_1^\circ \to 0$ and $l_2^\circ/l_1^\circ \to 0$, we obtain that the area of bubble $\mathcal{B}_2$ corresponds to $A_2 = 2.8868$ (with $A_1 = A_3 = 0.1208$). In this $l_1^\circ \to 0$ limit though particularly when as l_2°/l_1° exceeds $1/2$, the area of bubbles $A_1 = A_3$ might become really small (see Appendix C section C.1.4 for details). Meanwhile the solid line in Figure 5.4(a) corresponds to the values of l_1° and l_2° where the sizes of the bubbles are equal $A_1 = A_2 = A_3$, i.e. the system is monodisperse. A monodisperse scenario is of particular interest as it could be easily reproducible experimentally using the same apparatus described in [119]. Points above the solid line have $A_1 > A_2$ and points below it have $A_1 < A_2$. In addition, the dotted line on Figure 5.4(a) shows the maximum allowed value of l_2°, i.e. the line $l_2^\circ = l_1^\circ$. Note that when $l_1^\circ \ll 1$ the monodisperse case approaches close to this dotted line. In Figure 5.4(a) therefore, small values of l_1° with l_2° nearly the same as l_1°, is

able to give small monodisperse bubbles, albeit in real processes, bubbles this small are unlikely to pack in a staircase structure with just two bubbles across the width of the channel. Indeed for $l_1^\circ \ll 1$ it is possible to demonstrate that monodispersity requires $l_2^\circ \approx l_1^\circ - (2\pi/(3\sqrt{3}) - 1/2)l_1^{\circ 3}$ (see dash-dotted line in Figure 5.4(a)) (see section C.1.4 in Appendix C for details). However as alluded to above, this relation is of limited interest since bubbles this small (relative to the channel) would be unlikely to pack in the way indicated, such that bubble $\mathcal{B}_2$ is now highly elongated. More likely to pack in a staircase are monodisperse systems with large bubbles $l_1^\circ \to 1$ for which it turns out l_2° is relatively small, i.e. $l_2^\circ \approx (6 - 2\sqrt[4]{3}\sqrt{\pi})/9 + (((14\sqrt[4]{3}\sqrt{\pi} + 15)\pi + 51\sqrt[4]{27}\sqrt{\pi})/(108\pi))(1 - l_1^\circ) \approx 0.1483 + 1.0486\,(1 - l_1^\circ)$, as given by equation (C.30) in section C.1.4 in Appendix C (see also dashed line in Figure 5.4(a)).

In Figure 5.4(b) we show for a wide range of values of $l_1^\circ \in (0, 1)$ the area of monodisperse bubbles, where bigger bubbles are obtained for larger values of l_1°. However for monodisperse systems with large values of l_1° and relatively small values of l_2° (corresponding to big bubbles), even though a staircase is admitted, the system might prefer to pack in the so-called bamboo structure [4] (just a single bubble across the entire channel width as in Figure 2.5(a)), instead of the staircase structure indicated in the inset of Figure 5.4(a). Based on work of [4] (as mentioned in section 2.2.2), if $L \leq 2\sqrt{A/\pi}$ systems tend to prefer to pack in a bamboo structure, so we can determine that the corresponding critical area becomes $A_{\text{crit}} = \pi/4$ (for dimensionless $L = 1$) (see straight line in Figure 5.4(b)). Based on Figure 5.4(b) intermediate values of l_1° tend therefore to be of most interest in monodisperse systems, since they are most likely to adopt a single staircase configuration [4, 127]. As Figure 5.4(a) shows monodisperse structures with intermediate l_1°, have larger l_2° values than either the $l_1^\circ \ll 1$ or $l_1^\circ \to 1$ monodisperse cases. In order to consider a broad range of behaviours in

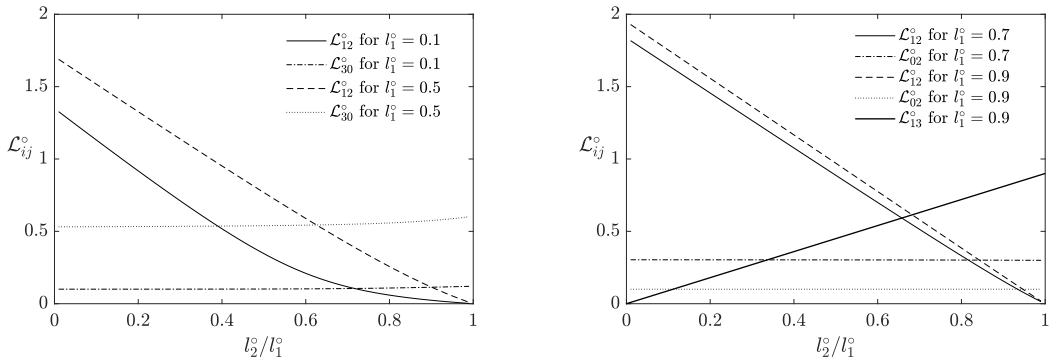

Figure 5.5: Film lengths $\mathcal{L}^\circ_{ij}$ in equilibrium, for three fixed l°_1 values and $l^\circ_2/l^\circ_1 \in [0.01, 0.99]$. (a) For $l^\circ_1 = 0.1$ and for $l^\circ_1 = 0.5$ we compute $\mathcal{L}^\circ_{12}$ and $\mathcal{L}^\circ_{30}$, and (b) for $l^\circ_1 = 0.7$ and for $l^\circ_1 = 0.9$ we compute $\mathcal{L}^\circ_{12}$ and $\mathcal{L}^\circ_{02}$.

what follows however, in the rest of this work we will tend to focus on values of $l^\circ_1 \in [0.01, 0.99]$ and $l^\circ_2/l^\circ_1 \in [0.01, 0.99]$.

Once we have computed an equilibrium state, we know values of bubble pressures p°_i, film turning angles $\delta\phi^\circ_{ij}$ and also film lengths $\mathcal{L}^\circ_{ij}$. Values of film length $\mathcal{L}^\circ_{ij}$ are of particular interest for the following reason. Although we are considering the equilibrium state here, later on in this work we will consider driving the system to an out-of-equilibrium state up to the point of a $T1$ topological transformation, at which a film shrinks away to zero length. We have already mentioned (see section 5.2.1) that four types of $T1$ are possible, $T1_c$ (corresponding to shrinking of film $\jmath_{12}$), $T1_u$ (corresponding to shrinking of film $\jmath_{30}$), $T1_{l1}$ (corresponding to shrinking of film $\jmath_{02}$), and $T1_{l3}$ (corresponding to shrinking of film $\jmath_{20}$). We can therefore estimate based on the shortest film *in the equilibrium state*, to which type of topological transformation a particular system *might* be most susceptible.

In Figure 5.5(a), for a small $l^\circ_1 = 0.1$ we compute $\mathcal{L}^\circ_{12}$ and $\mathcal{L}^\circ_{30}$ as functions of l°_2/l°_1. This shows $\mathcal{L}^\circ_{30}$ being the smaller of the two for most l°_2/l°_1 values ($T1_u$ more likely), but being the larger of the two when l°_2/l°_1 is close to unity ($T1_c$

more likely). Likewise for $l_1^\circ = 0.5$, we show that $\mathcal{L}_{30}^\circ < \mathcal{L}_{12}^\circ$ for small l_2°/l_1°, but $\mathcal{L}_{30}^\circ > \mathcal{L}_{12}^\circ$ for larger l_2°/l_1°. In Figure 5.5(b), for $l_1^\circ = 0.7$ and $l_1^\circ = 0.9$ we compute $\mathcal{L}_{12}^\circ$ and $\mathcal{L}_{02}^\circ$ (which is also equal to $\mathcal{L}_{20}^\circ$) vs l_2°/l_1°. For small l_2°/l_1°, the value of $\mathcal{L}_{02}^\circ$ is smaller ($T1_{l1}$ and/or $T1_{l3}$ are more likely). For large l_2°/l_1° though, the value of $\mathcal{L}_{12}^\circ$ decreases ($T1_c$ is more likely). Note that analysis of equilibrium film lengths gives an *indication* of which type of $T1$ is more likely, but not a definitive proof, since what matters for $T1$ is how the $\mathcal{L}_{ij}$ values evolve away from equilibrium. This will be discussed in more detail in section 5.5.

5.2.4 Conditions to achieve a topological transformation

Our aim in the first instance is to introduce slow quasistatic increases in imposed back pressure p_b to evolve the system through a sequence of steady states that move increasingly far from equilibrium as p_b increases. We anticipate however that for sufficiently high imposed back pressures a steady state structure with the topology indicated in Figure 5.1(b) might not exist in all cases. This could happen when certain films in the structure shrink down to zero length implying a $T1_c$, $T1_u$, $T1_{l1}$ or $T1_{l3}$ topological transformation (see Figure 5.6) which then causes the structure to break up.

Nevertheless for a slowly (i.e. quasistatically) increasing back pressure p_b imposed on a system, there are two conceptually distinct ways in which each of these $T1$ transformations can occur. First, a particular film might quasistatically shrink to zero length as an imposed back pressure p_b increases towards some critical pressure p_b^*, leading then directly to $T1$ transformation. In this situation, films can be maintained with an arbitrarily small length for an arbitrarily long time, as long as the rate of increase of p_b is low. Alternatively (as for the simple lens system in [19]) systems can reach the end of a solution branch at a saddle-node bifurcation, such that beyond a certain critical pressure p_b^* steady state solutions

cease to exist, even though all films still have a finite length at p_b^*. Again as for the simple lens [19], the rate of any subsequent evolution would be determined by the internal dynamics of the system, not by the rate at which an externally imposed pressure is changed. Once p_b attains p_b^*, typically the internal dynamics might drive the system to a $T1$ but (as described in section 2.2.3.3 for the simple lens) this happens at a rate determined by the system itself: on the approach to $T1$, films can no longer be kept arbitrarily short for arbitrarily long times.

This saddle-node scenario implies the existence of a new steady state solution branch (typically unstable), which meets the original branch at the saddle-node bifurcation. Since p_b cannot be increased beyond p_b^* at steady state, in order to track this new steady solution branch away from the saddle-node bifurcation, we need to select a new control variable, usually (as in the case of [19]) a total turning angle $\delta\phi_{ij}$. As we track the new steady state solution branch, the value of p_b (which is now a response variable) is found to decrease. Similarly, the migration velocity v, and possibly the pressures p_1, p_2, and p_3 also, are expected to decrease, by an amount dependent upon the decrease in p_b. This was already seen in [19] for the simple lens. The expectation is that the new branch can be followed all the way to a $T1$ topological transformation, albeit with the value of p_b at the $T1$ in question, now denoted $p_{b,T1}$, smaller than the aforementioned p_b^*. Tracking the new branch via a steady state methodology is straightforward to do, although we cannot preclude encountering yet another saddle-node bifurcation, implying yet another solution branch to be followed requiring yet another change of control variable. Even though the new steady solution branch itself may be dynamically unstable (hence difficult to reach from an *unsteady* state), locating and tracking it through the domain $p_b \leq p_b^*$ can still be worthwhile. By demonstrating that it joins up with the original stable solution, we prove the existence of the saddle-node bifurcation, verifying in turn that for $p_b > p_b^*$ there is no longer a corresponding steady state solution.

What happens to this saddle-node system when p_b is increased from a value slightly below p_b^* to a value slightly above it, is now a question of physical interest. That is however an inherently dynamic question that we cannot address with the steady state methodology to be employed here. Given the lack of steady state solutions in that domain, we anticipate, that the system would eventually evolve towards a $T1_c$, $T1_u$, $T1_{l1}$ or $T1_{l3}$ transformation (again see Figure 5.6), albeit as we have already explained, these should now become dynamic events, with their own internal rate of evolution being unrelated to how slowly increases in p_b are imposed externally. Regardless of whether the $T1$ is realised quasistatically or dynamically, a $T1_c$ happens when the film length $\mathcal{L}_{12} \to 0$ i.e. the vertices V_1 and V_2 collide, and consequently $\delta\phi_{02} \to \delta\phi_{13}$ (see Figure 5.6(a)) or equivalently $\delta\phi_{12} \to 0$ (see Table 5.1). Meanwhile a $T1_u$ happens when $\mathcal{L}_{30} \to 0$ i.e. the vertex V_3 reaches the upper channel wall, and $\delta\phi_{30} \to 0$ (see Figure 5.6(b)) (or equivalently $\delta\phi_{20} \to \pi/3$, see Table 5.1) . When a $T1_{l1}$ takes place $\mathcal{L}_{02} \to 0$ i.e. vertex V_1 goes to the lower channel wall, also implying that $\delta\phi_{02} \to 0$ (see Figure 5.6(c)). On the other hand a $T1_{l3}$ takes place when $\mathcal{L}_{20} \to 0$ i.e. vertex V_3 goes to the lower channel wall, also implying that $\delta\phi_{20} \to 0$ (see Figure 5.6(d)). Specifically in the case of a $T1_{l1}$, having $\delta\phi_{02} \to 0$ does not always imply a $T1_{l1}$, since for some given p_b, that film $\jmath_{02}$ might have finite length but simply become flat between changing from being concave to convex (seen from downstream), a situation that we will see later on does in fact occur.

Thus, when film coordinates are parametrized in terms of orientation angle ϕ_{ij} (as was done by [19]; see also section 5.4.1, and also further details in Appendix C section C.2.1) we refer in this work to a $T1^{\phi}_{c,p_b}$, $T1^{\phi}_{u,p_b}$, $T1^{\phi}_{l1,p_b}$, and $T1^{\phi}_{l3,p_b}$, if the system reaches a topological transformation by quasistatically increasing p_b. In that case p_b^* is the back pressure at which the $T1$ happens. Meanwhile $T1^{\phi}_{c,\delta\phi_{ij}}$,

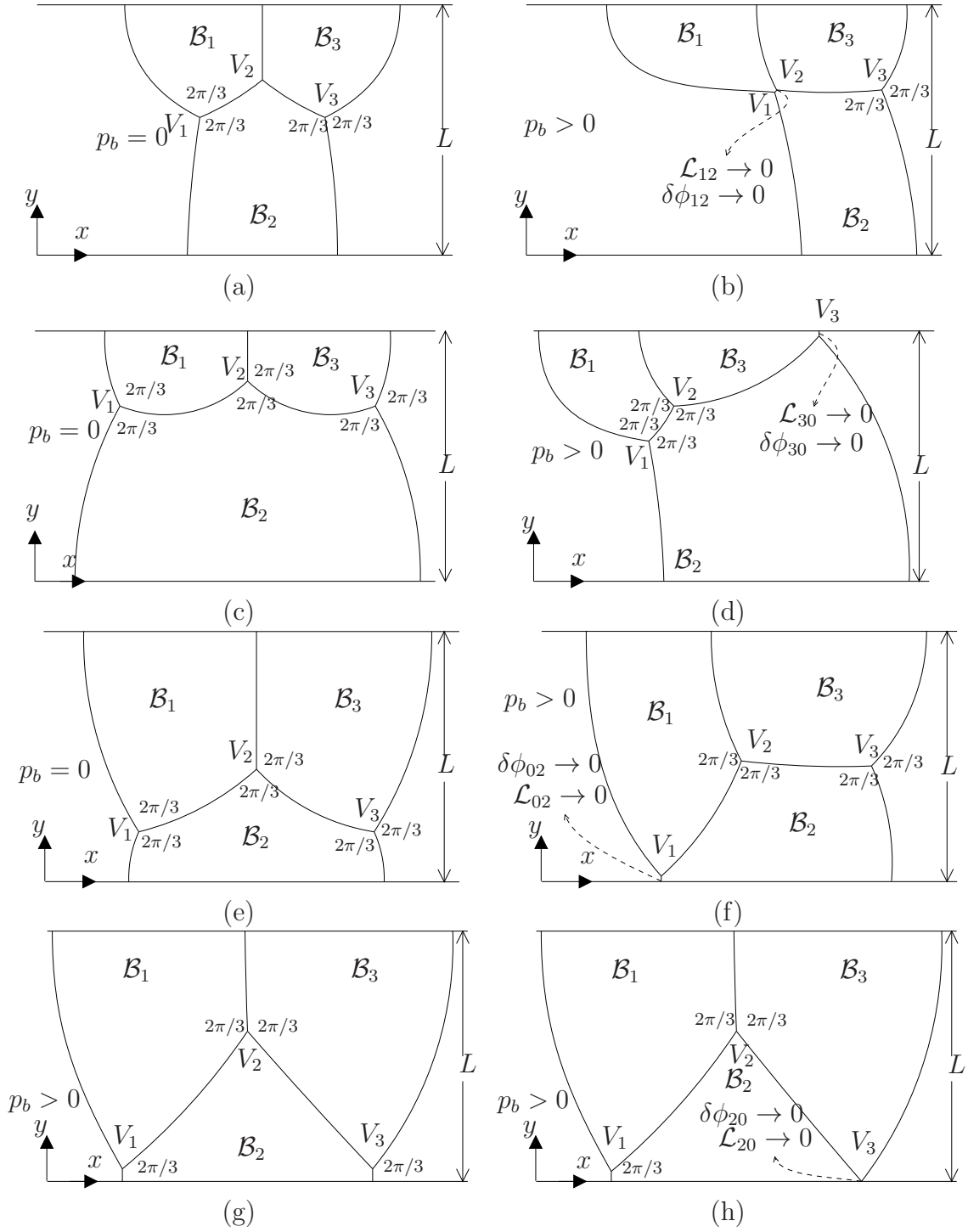

Figure 5.6: Three-bubble system topological transformations sketches. In (a), (c), (e), (g) we show the equilibrium structure for systems with different bubble area distributions. In (b), (d), (f), (h) we show the sketch of the respective topological transformation.

$T1^{\phi}_{u,\delta\phi_{ij}}$, $T1^{\phi}_{l1,\delta\phi_{ij}}$, and $T1^{\phi}_{l3,\delta\phi_{ij}}$, are used to denote topological transformations found on a new solution branch, which we track following a change of control variable at a saddle-node bifurcation. Here $\delta\phi_{ij}$ is the new control variable, and typically it is chosen as the particular turning angle that is driven quasistatically to zero as the new solution branch approaches the topological transformation. Thus we would select $\delta\phi_{12}$ on the approach to a $T1_c$, $\delta\phi_{30}$ for a $T1_u$, $\delta\phi_{02}$ for a $T1_{l1}$ and $\delta\phi_{20}$ for a $T1_{l3}$. In any of these cases, at the $T1$ itself, generally $p_b = p_{b,T1} < p_b^*$, since p_b^* corresponds now to the aforementioned saddle-node bifurcation not to the topological transformation itself. An additional scenario might also be found, in which p_b starts increasing again immediately before a $T1$, after first having decreased when we switched to a different control variable. Such cases will be denoted as, e.g. $T1^{\phi}_{u,\delta\phi_{30},p_b}$ if $\delta\phi_{30}$ is used a control variable, or as $T1^{\phi}_{l1,\delta\phi_{02},p_b}$ if $\delta\phi_{02}$ is used instead.

Note however (as already mentioned in section 5.2.1) we also have the option of parametrizing film coordinates by distance along films $\mathfrak{s}_{ij}$, rather than in terms of film orientation angle ϕ_{ij}, the conversion between $\mathfrak{s}_{ij}$ and ϕ_{ij} being provided by equation (5.2) (see also section 5.4.2, and further details in Appendix C section C.2.2). This can be convenient to do if large segments of particular films turn out to be nearly straight, meaning they have nearly the same ϕ_{ij} but very different $\mathfrak{s}_{ij}$. The respective topological transformations are now denoted as $T1^{s}_{c,p_b}$, $T1^{s}_{u,p_b}$, $T1^{s}_{l1,p_b}$ and $T1^{s}_{l3,p_b}$, if they are reached by quasistatically increasing p_b. They are denoted as $T1^{s}_{c,\mathcal{L}_{ij}}$, $T1^{s}_{u,\mathcal{L}_{ij}}$, $T1^{s}_{l1,\mathcal{L}_{ij}}$, and $T1^{s}_{l3,\mathcal{L}_{ij}}$ if a change of control variable is required and the topological transformation is now reached by quasistatically decreasing one of the film lengths. Here $\mathcal{L}_{ij}$ is the specific film length that approaches zero at the topological transformation, typically $\mathcal{L}_{12}$, $\mathcal{L}_{30}$, $\mathcal{L}_{02}$ or $\mathcal{L}_{20}$ in the case of $T1_c$, $T1_u$, $T1_{l1}$ or $T1_{l3}$ respectively. The methodology for how we track the steady state solution along the stable and, if necessary, the unstable

solution branches up to the topological transformation is explained in section 5.4. In summary, in this work we focus on steady state systems increasing back pressure p_b quasistatically up to some critical value p_b^*, with some (albeit not all) cases then requiring a switch of control variable at that point, selecting either a film turning angle $\delta\phi_{ij}$ or a film length $\mathcal{L}_{ij}$ depending on how the system is parametrized. In all the above mentioned systems, topological transformations if they happen at all, are observed to occur in only four distinct ways, namely $T1_c$, $T1_u$, $T1_{l1}$, or $T1_{l3}$, corresponding to vanishing of films $\jmath_{12}$, $\jmath_{30}$, $\jmath_{02}$ and $\jmath_{20}$. Which one of these transformations occurs depends on the bubble areas $A_1 = A_3$ and A_2, which are defined by fixing in the equilibrium state l_1° and l_2°. Nevertheless, it turns out that an alternative scenario can arise, namely that as p_b is increased a given system might reach an inherently stable structure, which does not suffer any further deformation as p_b increases. This is described in section 5.3.

5.3 Inherently stable structure

Here we study a type of steady state solution for a three-bubble system that does not change geometrically as the imposed back pressure p_b increases even up to arbitrarily high levels. Instead the three-bubble structure propagates faster and faster as p_b increases, whilst its geometry does not change (as also happens for an infinite staircase in Figure 2.5(b)). Key results we deduce are equations (5.9), (5.10) and (5.11)–(5.13), which are used to predict bubble pressures, orientation angles, and bubble areas, respectively, when migration velocity $v \to \infty$ and hence back pressure $p_b \to \infty$ also.

As demonstrated in [19], in the high velocity limit, films that are convex (when viewed from downstream) leave the channel wall at right angles, and are exceedingly flat along most of their length, only curving very sharply in the neighbour-

hood of vertices away from channel walls. Meanwhile as found in [144], films that are concave (viewed from downstream) leave walls at a right angle, curve very sharply near the walls, but then become very flat moving downstream. Both of these results actually follow from equation (5.1). Via that equation, it is possible to deduce that for concave films ($\kappa_{ij} < 0$ according to the sign convention in section 5.2.2), the largest magnitude of curvature $|\kappa_{ij}|$ corresponds to the smallest magnitude of ϕ_{ij}. In contrast for convex films ($\kappa_{ij} > 0$) the largest magnitude of curvature should correspond to largest magnitude of ϕ_{ij}. According to equation (5.1), large curvatures arise when normal velocity $v_{\perp ij}$ and pressure difference Δp_{ij} are large but out of balance. Since films can only turn through finite angles, large curvatures $\kappa_{ij} = \pm \mathrm{d}\phi_{ij}/\mathrm{d}\mathfrak{s}_{ij}$ are necessarily confined to small distances. In both cases then (convex or concave), all curvature is confined in a small region at the upstream end of the film, with moreover the size of this region becoming smaller as the velocity grows. The analysis below relies on films being sufficiently long to ensure that the curved region accounts for just a small portion of the film, with the rest of the film being flat; it therefore relies on bubbles being comparatively large, as larger bubbles tend also to have longer films.

5.3.1 Structure with almost flat films

Consider now a foam structure composed of three bubbles of some arbitrary size, travelling in a steady state configuration at a high velocity along a straight channel, as shown in Figure 5.7. Here by applying equation (5.1) to the convex film $\jmath_{20}$ we can deduce that $p_2 = v$, similarly for film $\jmath_{30}$ that $p_3 = v$. It follows that film $\jmath_{23}$ has negligible pressure difference across it, so (if it is also straight along most of its length) it must be horizontal, with a turning angle along its length of $\delta\phi_{23} = 0$. It also follows that $\delta\phi_{20} = -\delta\phi_{30} = \pi/6$ (see Figure 5.7). In addition, consideration of film $\jmath_{02}$ now tells that $p_b - p_2 = v$, from which it follows that $v = p_b/2$. Film $\jmath_{12}$ meanwhile has curvature zero at its downstream end

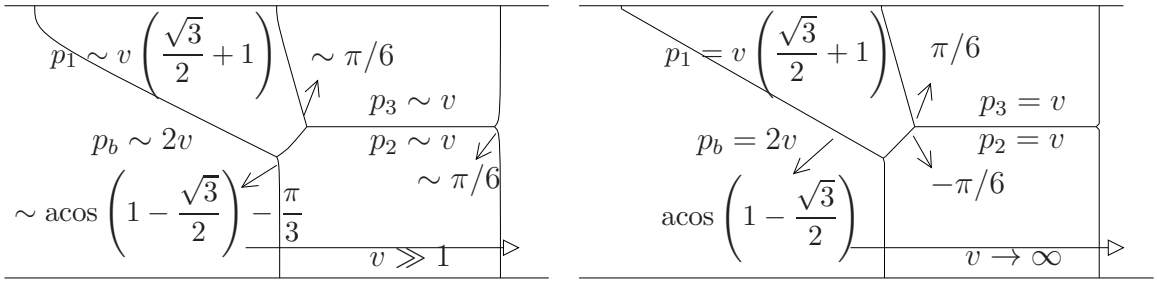

Figure 5.7: Three-bubble system travelling along a straight channel in a high migration velocity limit. Here bubbles $\mathcal{B}_1$ and $\mathcal{B}_3$ adjoin the upper channel wall, while bubble $\mathcal{B}_2$ adjoins the lower channel wall. (a) Migration velocity $v \gg 1$. Here films are flat over most of their length. Turning angles are indicated as follows $\delta\phi_{02} \to \operatorname{acos}(1-\sqrt{3}/2) - \pi/3$, and $\delta\phi_{13} \sim \delta\phi_{20} \to \pi/6$. (b) Migration velocity $v \to \infty$. Here films are entirely flat, with all the curvature focused arbitrarily close to the vertices if film orientation is convex, and arbitrarily close to the channel walls if film orientation is concave, the sense of the curvature being as seen from the downstream direction.

(its downstream orientation angle $\phi_{12,0}$ must be $-\pi/6$ in order to meet $\jmath_{23}$ at the required angle), but curvature on $\jmath_{12}$ grows moving upstream on the approach to vertex V_1, where it meets films $\jmath_{02}$ and $\jmath_{01}$. The orientation of film $\jmath_{13}$ now follows from a requirement that it meets $\jmath_{23}$ at the correct angle. Specifically film $\jmath_{13}$ now must turn through an angle of $\delta\phi_{13} = \pi/6$ (with the curvature being confined near the wall), from which we can deduce p_1. The normal velocity on the straight part of this film is $v_{\perp 13} = v\cos(\delta\phi_{13}) = \sqrt{3}v/2$ and the pressure difference across it is $p_1 - p_3$ where we already know $p_3 = v$. Hence

$$p_1 = \left(\frac{\sqrt{3}}{2}+1\right)v. \tag{5.9}$$

The pressure difference $p_b - p_1$ across film $\jmath_{01}$ now becomes $(1-\sqrt{3}/2)v$. Since along film $\jmath_{01}$, curvature $\kappa_{01} \to 0$ away from the wall, we determine the maximum

turning angle for this film as

$$\delta\phi_{01} = \text{acos}\left(1 - \frac{\sqrt{3}}{2}\right) \approx 1.4364. \tag{5.10}$$

Using equation (5.10) we can deduce orientation angles of films $\jmath_{02}$ and $\jmath_{12}$, consistently with what is given in Table 5.1. We find that $\delta\phi_{02} = \delta\phi_{01} - \pi/3 \approx 0.3892$, and that $\delta\phi_{12} = \delta\phi_{01} - \pi/2 \approx -0.1344$.

Once we know the film orientations and total turning angles, we can compute bubble areas, just by giving the length of films $\jmath_{12}$, $\jmath_{23}$, and $\jmath_{30}$, from which we can go on to find constraints upon bubble areas that might reach the inherently stable migrating structure, proceeding as follows. First we compute bubble areas for the structure in Figure 5.7(b) in terms of $\mathcal{L}_{12}$, $\mathcal{L}_{23}$ and $\mathcal{L}_{30}$ recognising that all bubbles are now polygonal in shape. The result is as follows

$$\begin{aligned} A_1 = \frac{(\mathcal{L}_{30} + \mathcal{L}_{12}\cos(\phi_{12,0}))^2}{2}\tan(\delta\phi_{01}) + (\mathcal{L}_{30} + \mathcal{L}_{12}\cos(\phi_{12,0}))\mathcal{L}_{12}\sin(|\phi_{12,0}|) \\ -\frac{\mathcal{L}_{30}^2}{2}\tan(\delta\phi_{13}) - \frac{\mathcal{L}_{12}^2}{2}\sin(|\phi_{12,0}|)\cos(\phi_{12,0}), \end{aligned} \tag{5.11}$$

where this equation recognises that the area of bubble A_1 corresponds to a triangle of height $\mathcal{L}_{30} + \mathcal{L}_{12}\cos(\phi_{12,0})$ and base $\tan(\delta\phi_{01})$ times that height, plus a rectangle of the same height and a width of $\mathcal{L}_{12}\sin(|\phi_{12,0}|)$, minus a triangular chunk belonging to bubble $\mathcal{B}_3$ of height $\mathcal{L}_{30}$ and base $\tan(\delta\phi_{01})$ times this, minus another triangular chunk belonging to bubble $\mathcal{B}_2$ of size $\mathcal{L}_{12}^2\sin(|\phi_{12,0}|)\cos(\phi_{12,0})/2$. The area of bubble $\mathcal{B}_2$ can be computed as

$$A_2 = (1 - \mathcal{L}_{30})(\mathcal{L}_{23} + \mathcal{L}_{12}\sin(|\phi_{12,0}|)) - \frac{\mathcal{L}_{12}^2}{2}\sin(|\phi_{12,0}|)\cos(\phi_{12,0}), \tag{5.12}$$

where the area A_2 here corresponds to a rectangle of size $(1 - \mathcal{L}_{30})\mathcal{L}_{23}$, plus an

additional rectangle of height $(1 - \mathcal{L}_{30})$ and width $\mathcal{L}_{12}\sin(|\phi_{12,0}|)$, less a small triangle which is of size $\mathcal{L}_{12}^2\sin(|\phi_{12,0}|)\cos(\phi_{12,0})/2$. Finally the area of bubble $\mathcal{B}_3$ is determined as

$$A_3 = \mathcal{L}_{23}\mathcal{L}_{30} + \frac{\mathcal{L}_{30}^2}{2}\tan(\delta\phi_{13}), \tag{5.13}$$

which corresponds to a rectangle of size $\mathcal{L}_{30}\mathcal{L}_{23}$, plus a triangle of height $\mathcal{L}_{30}$ and base $\tan(\delta\phi_{13})$ times this. Specifying the value of A_1, A_2 and A_3 (with $A_1 = A_3$ in our system), then defines the values $\mathcal{L}_{12}$, $\mathcal{L}_{23}$, $\mathcal{L}_{30}$. As discussed in section 5.2.3, our technique for fixing the areas actually involves fixing parameters l_1° and l_2° (which are distances from the upper channel walls to vertices in the equilibrium state). The values of $A_1 \equiv A_3$ and A_2 on the left hand sides of (5.11)–(5.13) are then complicated nonlinear functions of l_1° and l_2° (see Appendix C section C.1 for details). Hence solving equations (5.11)–(5.13) will give $\mathcal{L}_{12}$, $\mathcal{L}_{23}$, $\mathcal{L}_{30}$ as functions of l_1° and l_2°. Constraints can now be placed on the bubble areas as discussed in the next section.

5.3.2 Constraints upon the flat film state

We note that (at least as sketched in Figure 5.7) the shortest edge in the system is $\mathcal{L}_{12}$. It seems then that a likely reason why an inherently stable structure might not be found would be due to equations (5.11)–(5.13) predicting $\mathcal{L}_{12} \to 0$ for certain combinations of A_1 and A_2. If we impose the condition $\mathcal{L}_{12} \to 0$ on the above equations, and treat A_1 as a free parameter, then the value of A_2 (and likewise of $\mathcal{L}_{23}$ and of $\mathcal{L}_{30}$) is fixed for any specified A_1. This represents a minimum A_2 for the inherently stable state to exist for any given A_1 (see solid line in Figure 5.8). These results can also be presented in terms of l_1° and l_2° and what we find is that for any given l_1° there is a maximum l_2° at which the inherently stable state can exist. This is shown later in Figure 5.10(b), in section 5.5.1. On the other hand, there is an alternative way in principle that the structure

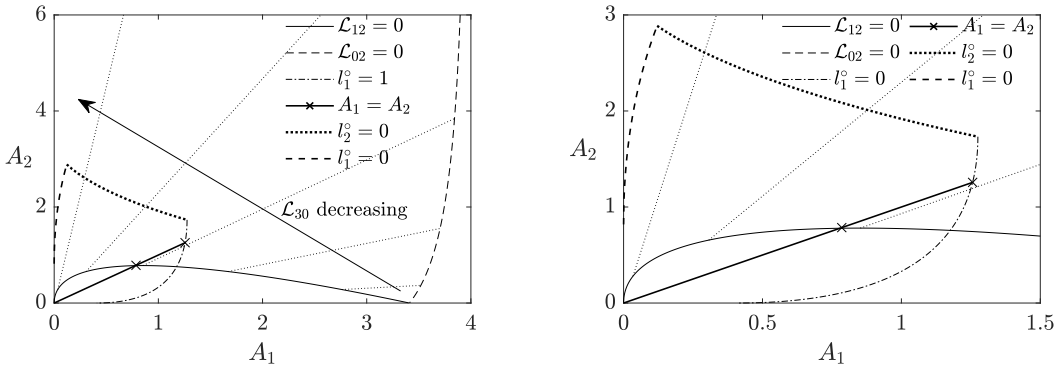

Figure 5.8: (a) A_2 vs A_1 relations in the inherently stable state. (b) Zoomed view of (a). Solid and dashed lines, respectively, show the limit as either $\mathcal{L}_{12} \to 0$ or $\mathcal{L}_{02} \to 0$. The thin dotted lines meanwhile denote the relationship between A_1 and A_2 for a fixed value of $\mathcal{L}_{30}$, with $\mathcal{L}_{30}$ decreasing from bottom right to top left ($\mathcal{L}_{30} = 0.9$, 0.7, 0.5, 0.3 and 0.1). Also shown is the A_1 vs A_2 relation for an equilibrium system in the limit $l_1^\circ \to 1$, but with variable l_2° (dash-dotted curve), the A_1 vs A_2 relation for an equilibrium system in the limit $l_2^\circ \to 0$ with variable l_1° (bold dotted curve), and the A_1 vs A_2 relation for an equilibrium system in the limit $l_1^\circ \to 0$ with variable $\overset{\circ}{2}/l_1^\circ$ (bold dashed curve): see Appendix C section C.1.4 for details. In addition we show a monodisperse line $A_1 = A_2$.

sketched in Figure 5.7(b) can break up. This is for the length $\mathcal{L}_{02}$ to approach zero, which requires $\mathcal{L}_{30} + \mathcal{L}_{12}\cos(\phi_{12,0}) \to 1$ (see dashed line in Figure 5.8). We have analysed this case, and (see dashed line towards the right of Figure 5.8(a)) yet again there turns out to be a minimum A_2 for any A_1. However we are now dealing with A_1 values that are rather larger than previously. In fact it is possible to demonstrate that the bubbles need to be so large for the $\mathcal{L}_{02} \to 0$ limiting condition to apply that it would not be possible to stack them in a staircase structure at equilibrium in the first place. This can be seen as follows. The domain of permitted A_1 and A_2 values to achieve an equilibrium structure is marked off in the bottom left hand corner of Figure 5.8(a) (see also Appendix C section C.1.4). The domain is delineated here by the dashed curve $l_1^\circ \to 0$ (see Appendix C section C.1.4.1), with variable $l_2^\circ/l_1^\circ < 1/2$), by the dash-dotted curve $l_1^\circ \to 1$ (see Appendix C section C.1.4.2), with variable l_2°, and by the bold dotted curve $l_2^\circ \to 0$ (see Appendix C section C.1.4.3), with variable l_1°. The $l_1^\circ \to 1$ curve can be considered to give a maximum A_1 to achieve an equilibrium staircase for a given selected A_2. Meanwhile the $l_1^\circ \to 0$ and $l_2^\circ \to 0$ curves can be considered to give a maximum A_2 to achieve an equilibrium staircase for a selected A_1.
Outside of this zone marked off in Figure 5.8(a) there would be no equilibrium staircase structure present that we could subsequently drive out of equilibrium by imposing a back pressure. The limiting case $\mathcal{L}_{02} \to 0$ of the inherently stable structure (dashed line to the right of Figure 5.8(a)) does not therefore need to be considered any further as it corresponds to A_1 values well outside the zone in question. It is only the limiting case $\mathcal{L}_{12} \to 0$ of the inherently stable structure that is of concern here. In fact it is only a fairly small domain of A_2 vs A_1 values (see the zoomed view in Figure 5.8(b)) which are compatible both with having an inherently stable state with $\mathcal{L}_{12} > 0$ (the region above the solid line) and with having originated from an equilibrium staircase structure.

In Figure 5.8 one way of mapping out the permitted domain of A_1 and A_2 for an inherently stable state to exist is to select, in the first instance, a fixed value of $\mathcal{L}_{30}$, which is a convenient parameter to use since $\mathcal{L}_{30}$ values cover a known domain $\mathcal{L}_{30} \in [0, 1]$. For each chosen $\mathcal{L}_{30}$, we then map out a locus of A_1 and A_2 values by varying $\mathcal{L}_{12}$. A number of these loci are shown in Figure 5.8(a) by thin dotted curves, which turn out to be very nearly straight lines on that figure. When $\mathcal{L}_{12} \to 0$ the thin dotted curve intersects the solid curve, and when $\mathcal{L}_{12} \to (1-\mathcal{L}_{30})/\cos(\phi_{12,0})$ (which implies $\mathcal{L}_{02} \to 0$) it intersects the dashed curve over to the right of Figure 5.8(a). Of course this latter intersection is well outside the domain of states which form a staircase at equilibrium. For any chosen $\mathcal{L}_{30}$ therefore, there will be on each thin dotted line a maximum $\mathcal{L}_{12}$ (strictly less than $(1 - \mathcal{L}_{30})/\cos(\phi_{12,0})$, with the value of $\phi_{12,0}$ given in section 5.3.1) forming a staircase at equilibrium. The equations for these thin dotted lines are given in Appendix C, section C.3.1.

In the limit of $\mathcal{L}_{12} \to 0$ we can determine by equating (5.11) and (5.13) that

$$\mathcal{L}_{23} \approx \mathcal{L}_{30} \left((1/2) \tan(\delta\phi_{01}) - \tan(\delta\phi_{13}) \right), \tag{5.14}$$

which leads in turn to

$$A_1 = A_3 \approx (1/2) \left(\tan(\delta\phi_{01}) - \tan(\delta\phi_{13}) \right) \mathcal{L}_{30}^2 \tag{5.15}$$

and

$$A_2 \approx (1 - \mathcal{L}_{30}) \mathcal{L}_{30} ((1/2) \tan(\delta\phi_{01}) - \tan(\delta\phi_{13})). \tag{5.16}$$

Values of $\delta\phi_{01}$ and $\delta\phi_{13}$ are known (see section 5.3.1) and we can then deduce that for monodispersity $\mathcal{L}_{30} \approx ((1/2) \tan(\delta\phi_{01}) - \tan(\delta\phi_{13}))/(\tan(\delta\phi_{01}) - (3/2) \tan(\delta\phi_{13})) \approx 0.4779$. This leads to $A_1 = A_2 = A_3 \approx 0.7787$.

For comparison, on Figure 5.8(b) we also show via a thick solid line the values

$A_1 = A_2$ giving a monodisperse system. For monodisperse systems at least, the data plotted here prove that the inherently stable state is only possible for comparatively large bubbles, specifically for values of $A_1 = A_2$ bigger than 0.7787, and less than about 1.2565 (note that this lies on the dash-dotted curve $l_1^\circ \to 1$). The former value is surprisingly close to $\pi/4$ (the bubble area at which a circular bubble has diameter equal to the channel width, and so may prefer a bamboo structure over a staircase), while the latter corresponds to $l_1^\circ \to 1$ as we have said, along with $l_2^\circ \approx 0.1483$ (monodisperse bubbles any larger than this could not form an equilibrium staircase at all).

In summary Figure 5.8 (in particular the zoomed view in Figure 5.8(b)) identifies a permitted domain corresponding straight films moving in the high velocity limit. However, since for slower migration velocities films are curved, some systems might undergo topological transformation before reaching the inherently stable structure. Therefore not all the possible configurations allowed in Figure 5.8(b) necessarily reach the inherently stable state. In general then Figure 5.8(b) gives the necessary but not sufficient conditions for the inherently stable state to exist. In the cases for which the systems satisfy the necessary condition to reach the inherently stable structure, we can also compute their energy. This corresponds to the maximum energy that such a system will reach which exceeds the energy it had at equilibrium: see section C.3.2 in Appendix C for details.

5.4 Steady state solution methodology

In this section, we describe the methodology employed to determine the steady state migration solution of a moving system. The methodology described here is based on the work developed in [19] to simulate the motion of a simple lens system (see Figure 2.7) in a straight confined channel, and is applied here to simulate

the motion of three bubbles (see Figure 5.1), using a similar operational methodology. Readers already familiar with that methodology may wish to skip directly to results in section 5.5, but in what follows we highlight some of the features of the methodology, especially those that are particular to the three-bubble case as opposed to the simple lens. Fuller details can be found in Appendix C section C.2.

Starting from an equilibrium structure, the system can be deformed by applying an external force, typically by increasing p_b, which drives the structure out-of-equilibrium propagating at an a priori unknown steady migration velocity v. Hence, for a moving system with well-defined bubble areas set up in equilibrium by fixing l_1° and l_2°, we increase p_b quasistatically. If a steady state exists, typically for p_b less than some maximum allowed p_b^*, we seek to find a configuration, such that the vertex meeting rules, and also the area constraints are satisfied. Under those circumstances, to determine the x, y coordinates of the films, we must integrate the equations given in section 5.2.2, the integrated expressions being explained further in sections 5.4.1 and 5.4.2. These coordinates can be obtained by parametrizing film coordinates in terms of orientation angles ϕ_{ij} or distances along films $\mathfrak{s}_{ij}$. Both forms are discussed in detail in section C.2 in Appendix C. Film coordinates in terms of $\mathfrak{s}_{ij}$ are particularly useful since as the migration velocity increases, long films tend to become flat (see section 5.3). Hence almost the same orientation angle ϕ_{ij} can be found at many different locations along the film, but the different locations all have different $\mathfrak{s}_{ij}$. Regardless of the parametrization chosen, the state of the system is now fixed via constraint equations. The constraint equations that apply are deduced in sections 5.4.3 and 5.4.4, respectively.

In the case of parametrizing films in terms of orientation angle ϕ_{ij}, the set of variables that govern the state of the system are as mentioned in section 5.2.1:

the total turning angles ($\delta\phi_{02}$, $\delta\phi_{13}$, and $\delta\phi_{20}$), bubble pressures (p_1, p_2, and p_3), and migration velocity (v). All of these can be considered as response variables for a given imposed back pressure p_b, which is specified as the control variable at least on the stable solution branch. So there are 7 values to find in order to determine the shape of the moving system. However, as alluded to above, for systems in which films become flat, it is no longer feasible to compute film coordinates in terms of orientation angles. We consider that a film has become flat when the value of $|\kappa_{ij}|$ at any point along it falls below a threshold value typically $|\kappa_{ij}| < 10^{-7}$. There is no risk of confusing this with a film shape containing an inflection, i.e. a change of sign of κ_{ij} at just a single isolated point, since inflections turn out to be precluded for steadily propagating films. Films that are deemed flat according to the above criterion (excluding of course the equilibrium state for which $\kappa_{13} \equiv 0$ on symmetry grounds, but which is easily handled via the methodology of section 5.2.3) are then parametrized in terms of their distance measured along them $\mathfrak{s}_{ij}$. In this case, as section 5.2.1 states, the system state is given by 11 response variables, these being the 7 film lengths $\mathcal{L}_{ij}$, the 3 bubble pressures (p_1, p_2, and p_3), and the migration velocity (v). Again, all of these are given as a function of the imposed control variable p_b, at least on the stable solution branch. Regardless of how the films are parametrized, the system must satisfy the vertex meeting rules (for y coordinates and, where applicable as per Table 5.1, for vertex meeting angles also), plus bubble area constraints.

5.4.1 Film coordinates in terms of ϕ_{ij}

The process of obtaining equations that describe the film shape in terms of orientation angle ϕ_{ij} for a three-bubble system in motion generalizes what was already done for the viscous froth lens studied in [33]. The equations, which are closed-form analytical expressions albeit quite complex ones, are obtained in Appendix

C section C.2, and are written here generically as

$$x_{ij} = x_{ij}(x_{ij,0}, \phi_{ij,0}, a_{ij}, v, \phi_{ij}), \tag{5.17}$$

$$y_{ij} = y_{ij}(y_{ij,0}, \phi_{ij,0}, a_{ij}, v, \phi_{ij}), \tag{5.18}$$

with $x_{ij,0}$, $y_{ij,0}$ being coordinate locations at the start of the film at $\phi_{ij} = \phi_{ij,0}$, and with a_{ij} as the mobility parameter defined as $a_{ij} = v/\Delta p_{ij}$. Note that we obtain two slightly different forms of the generic equation (C.35), one for $|a_{ij}| < 1$ and other for $|a_{ij}| > 1$, as given in section C.2.1 in Appendix C. These equations for the coordinates will be inserted into constraint equations on y coordinates of vertices, and on bubble areas.

5.4.2 Film coordinates in terms of $\mathfrak{s}_{ij}$

If we switch to parametrizing film coordinates in terms of distance measured along a film, the equations we require are described in detail in section C.2.3 in Appendix C. The equations we deduce are now given as a function of $\mathfrak{s}_{ij}$, but again with $a_{ij} = v/\Delta p_{ij}$. Hence we obtain generic equations for x_{ij} and y_{ij} in the form of

$$x_{ij} = x_{ij}(x_{ij,0}, \phi_{ij,0}, a_{ij}, v, \mathfrak{s}_{ij}), \tag{5.19}$$

$$y_{ij} = y_{ij}(y_{ij,0}, \phi_{ij,0}, a_{ij}, v, \mathfrak{s}_{ij}). \tag{5.20}$$

On different films, different expressions may be used in terms of a_{ij} and $\mathfrak{s}_{ij}$ (depending whether $|a_{ij}| < 1$ or $|a_{ij}| > 1$ and depending whether $\mathfrak{s}_{ij}$ is measured upwards or downwards). These are given in section C.2.3 in Appendix C. Using equations (C.42)–(C.43), we can easily obtain film coordinates x_{ij} and y_{ij} as a function of distance along a film $\mathfrak{s}_{ij}$, and these relationships can be still used even at high velocities when the films become asymptotically flat as in section 5.3. Again, these equations for the coordinates will be inserted into constraint equa-

tions on y coordinate of vertices, on meeting angles, and on bubble areas. Where the constraints come from has already been discussed in physical terms in section 5.2.1, but in what follows we present the constraint equations themselves.

5.4.3 Constraint equations in terms of turning angle $\delta\phi_{ij}$

Since the films must meet at their respective vertices, we can obtain two sets of two constraint equations, respectively at V_1 and V_3

$$y_{02}(\delta\phi_{02}) = y_{01}(\pi/3 + \delta\phi_{02}) = y_{12}(-\pi/3 + \delta\phi_{02}), \tag{5.21}$$

$$y_{20}(\delta\phi_{20}) = y_{23}(\pi/3 + \delta\phi_{20}) = y_{30}(-\pi/3 + \delta\phi_{20}), \tag{5.22}$$

where the arguments of each of the y_{ij} here are $\phi_{ij,\mathcal{L}}$ as specified in Table 5.1. Note that equations (5.21) and (5.22) fix V_1 and V_3, and (as already mentioned in section 5.2.1) a separate equation for V_2 is not needed since the locations that are specified for $y_{12}(\delta\phi_{02} - \pi/3)$ and $y_{23}(\delta\phi_{20} + \pi/3)$ at V_1 and V_3 in the above equations, already depend upon the location of $y_{13}(\delta\phi_{13})$ at vertex V_2.

As the bubbles change shape, no variation in their areas is possible, these areas being obtained by fixing l_1° and l_2° in equilibrium, which then fixes $A_1 = A_3$ and A_2. The area constraints can be written in terms of x and y coordinates of films, taking into account each film bounding the bubble. Given that the system is comprised of three bubbles, we define three area constraints as follows,

$$A_1 = \int_0^{\delta\phi_{01}} (1 - y_{01}) \frac{\mathrm{d}x_{01}}{\mathrm{d}\phi_{01}} \mathrm{d}\phi_{01} + \int_{\phi_{12,\mathcal{L}}}^{\phi_{12,0}} (1 - y_{12}) \frac{\mathrm{d}x_{12}}{\mathrm{d}\phi_{12}} \mathrm{d}\phi_{12} + \int_{\delta\phi_{13}}^{0} (1 - y_{13}) \frac{\mathrm{d}x_{13}}{\mathrm{d}\phi_{13}} \mathrm{d}\phi_{13}, \tag{5.23}$$

$$A_2 = \int_0^{\delta\phi_{02}} y_{02} \frac{\mathrm{d}x_{02}}{\mathrm{d}\phi_{02}} \mathrm{d}\phi_{02} + \int_{\phi_{12,\mathcal{L}}}^{\phi_{12,0}} y_{12} \frac{\mathrm{d}x_{12}}{\mathrm{d}\phi_{12}} \mathrm{d}\phi_{12} + \int_{\phi_{23,0}}^{\phi_{23,\mathcal{L}}} y_{23} \frac{\mathrm{d}x_{23}}{\mathrm{d}\phi_{23}} \mathrm{d}\phi_{23} + \int_{\delta\phi_{20}}^{0} y_{20} \frac{\mathrm{d}x_{20}}{\mathrm{d}\phi_{20}} \mathrm{d}\phi_{20}, \tag{5.24}$$

$$A_3 = \int_0^{\delta\phi_{13}} (1 - y_{13}) \frac{\mathrm{d}x_{13}}{\mathrm{d}\phi_{13}} \mathrm{d}\phi_{13} + \int_{\phi_{23,0}}^{\phi_{23,\mathcal{L}}} (1 - y_{23}) \frac{\mathrm{d}x_{23}}{\mathrm{d}\phi_{23}} \mathrm{d}\phi_{23} + \int_{\delta\phi_{30}}^{0} (1 - y_{30}) \frac{\mathrm{d}x_{30}}{\mathrm{d}\phi_{30}} \mathrm{d}\phi_{30}. \tag{5.25}$$

Here a number of the integration limits $\delta\phi_{01}$, $\phi_{12,0}$, $\phi_{12,\mathcal{L}}$, $\phi_{23,0}$, $\phi_{23,\mathcal{L}}$, and $\delta\phi_{30}$, can be re-expressed in terms of just three turning angles, namely $\delta\phi_{02}$, $\delta\phi_{13}$, and $\delta\phi_{20}$ respectively, as summarized in Table 5.1. The equation system (5.21)–(5.25) has 7 equations and 8 unknown variables, listed as p_b, v, p_1, p_2, p_3, $\delta\phi_{02}$, $\delta\phi_{13}$ and $\delta\phi_{20}$. The variables' values in the equilibrium structure, by construction, meet the constraints (5.21)–(5.25) provided $p_b = 0$. However a small perturbation in p_b away from zero, would cause a violation of the constraint equations, unless all the other variables also change. Perturbing in powers of p_b leads to a weakly-driven migration solution (see section C.4 in Appendix C). Once we have determined all system variables, for a small change in the control variable p_b away from equilibrium, we can keep increasing p_b in small steps, until either topological transformation takes place, the system loses stability in a saddle-node bifurcation, or the inherently stable configuration is reached (albeit the alternative methodology to be discussed in section 5.4.4 is better equipped for the inherently stable case).

As mentioned earlier (see sections 5.2.1 and 5.2.4), it may also be expedient at some point to switch p_b from being a control variable to a response variable, using one of the other variables, e.g. a film total turning angle, as the new control variable. It is in fact be essential to do this in the neighbourhood of a saddle-node bifurcation, since p_b would then have reached a maximum, and so could not be increased any further without loss of the steady state. The methodology for selecting the new control variable in such cases is described in section 5.4.5.

5.4.4 Constraint equations in terms of film lengths $\mathcal{L}_{ij}$

When film coordinates are computed in terms of distances along films $\mathfrak{s}_{ij}$, with $0 \leq \mathfrak{s}_{ij} \leq \mathcal{L}_{ij}$, we can readily impose constraints based on vertex meeting rules. Considering that at vertex V_1 and at vertex V_3 the $y_{ij}(\mathcal{L}_{ij})$ values of films meeting

at these points have to be equal, we deduce that

$$y_{01}(\mathcal{L}_{01}) = y_{12}(\mathcal{L}_{12}) = y_{02}(\mathcal{L}_{02}), \tag{5.26}$$

$$y_{23}(\mathcal{L}_{23}) = y_{30}(\mathcal{L}_{30}) = y_{20}(\mathcal{L}_{20}). \tag{5.27}$$

In addition, the orientation angle $\phi_{ij}(\mathcal{L}_{ij})$ at each vertex must satisfy

$$\phi_{01}(\mathcal{L}_{01}) - \frac{\pi}{3} = \phi_{02}(\mathcal{L}_{02}) = \phi_{12}(\mathcal{L}_{12}) + \frac{\pi}{3}, \tag{5.28}$$

$$\phi_{23}(\mathcal{L}_{23}) - \frac{\pi}{3} = \phi_{20}(\mathcal{L}_{20}) = \phi_{30}(\mathcal{L}_{30}) + \frac{\pi}{3}, \tag{5.29}$$

consistently with what is shown in Table 5.1. Equations (5.26) and (5.27) are computed by using equation (C.43) (along with formulae given in section C.2.3 in Appendix C), while (5.28) and (5.29) are computed by equation (C.40) and (C.41) as given in Appendix C section C.2.2. Note that equations (5.26)–(5.29) fix V_1 and V_3, and as was the case in section 5.4.3, a separate equation for V_2 is not needed. On the other hand, again as before, we compute bubble areas for a steadily moving system albeit now in terms of $\mathfrak{s}_{ij}$, as

$$A_1 = \int_0^{\mathcal{L}_{01}} (1 - y_{01}) \frac{\mathrm{d}x_{01}}{\mathrm{d}\mathfrak{s}_{01}} \mathrm{d}\mathfrak{s}_{01} + \int_{\mathcal{L}_{12}}^0 (1 - y_{12}) \frac{\mathrm{d}x_{12}}{\mathrm{d}\mathfrak{s}_{12}} \mathrm{d}\mathfrak{s}_{12} + \int_{\mathcal{L}_{13}}^0 (1 - y_{13}) \frac{\mathrm{d}x_{13}}{\mathrm{d}\mathfrak{s}_{13}} \mathrm{d}\mathfrak{s}_{13}, \tag{5.30}$$

$$A_2 = \int_0^{\mathcal{L}_{02}} y_{02} \frac{\mathrm{d}x_{02}}{\mathrm{d}\mathfrak{s}_{02}} \mathrm{d}\mathfrak{s}_{02} + \int_{\mathcal{L}_{12}}^0 y_{12} \frac{\mathrm{d}x_{12}}{\mathrm{d}\mathfrak{s}_{12}} \mathrm{d}\mathfrak{s}_{12} + \int_0^{\mathcal{L}_{23}} y_{23} \frac{\mathrm{d}x_{23}}{\mathrm{d}\mathfrak{s}_{23}} \mathrm{d}\mathfrak{s}_{23} + \int_{\mathcal{L}_{20}}^0 y_{20} \frac{\mathrm{d}x_{20}}{\mathrm{d}\mathfrak{s}_{20}} \mathrm{d}\mathfrak{s}_{20}, \tag{5.31}$$

$$A_3 = \int_0^{\mathcal{L}_{13}} (1 - y_{13}) \frac{\mathrm{d}x_{13}}{\mathrm{d}\mathfrak{s}_{13}} \mathrm{d}\mathfrak{s}_{13} + \int_0^{\mathcal{L}_{23}} (1 - y_{23}) \frac{\mathrm{d}x_{23}}{\mathrm{d}\mathfrak{s}_{23}} \mathrm{d}\mathfrak{s}_{23} + \int_{\mathcal{L}_{30}}^0 (1 - y_{30}) \frac{\mathrm{d}x_{30}}{\mathrm{d}\mathfrak{s}_{30}} \mathrm{d}\mathfrak{s}_{30}. \tag{5.32}$$

The equation system (5.26)–(5.32) has 11 equations and 12 unknown variables, listed as p_b, v, p_1, p_2, p_3, $\mathcal{L}_{01}$, $\mathcal{L}_{02}$, $\mathcal{L}_{12}$, $\mathcal{L}_{13}$, $\mathcal{L}_{23}$, $\mathcal{L}_{30}$, and $\mathcal{L}_{20}$. The variable values in the equilibrium structure, by construction, meet the constraints (5.26)–(5.32) provided $p_b = 0$. Again perturbation solutions can be obtained for small non-zero

imposed p_b, and thereafter solutions can be tracked by taking small steps in p_b. Indeed for a small change in p_b away from equilibrium, we can convert values of response variables obtained via the weakly-driven migration solution in terms of film orientation angles (see section C.4 in Appendix C) to film length with the help of equations (C.38) and (C.39), from which the approximated values of all 12 out-of-equilibrium system variables can be obtained. Then, we can keep increasing p_b in small steps, until either a topological transformation take place, the system loses stability (at a saddle-node bifurcation), or an inherently stable state is reached. Again for systems that exhibit a saddle-node bifurcation we need in particular to switch the control variable from p_b to a new variable. The criteria for selecting the new control variable are explained in the following section.

5.4.5 Setting new control variables

As explained in section 5.2 (see e.g. section 5.2.4), as p_b is increased, the system might reach the end of a steady solution branch at some maximum allowed back pressure, but without necessarily reaching any topological transformation quasistatically. This implies the existence of a different solution branch (typically unstable), meeting the original one at a saddle-node bifurcation with $p_b = p_b^*$. To move beyond this saddle-node bifurcation and track the new solution branch, we can no longer use p_b as a control variable, since it has ceased increasing. Instead we must switch one of the erstwhile response variables to become a new control variable. Typically we choose one of the total turning angles $\delta\phi_{ij}$ in the case of parametrizing the system in terms of orientation angle ϕ_{ij}, or one of the film lengths $\mathcal{L}_{ij}$ in the case of parametrizing in terms $\mathfrak{s}_{ij}$. The reason that these turning angles and/or film lengths are sensible choices is that our aim is to follow the new solution branch up to $T1$, occurring now at some $p_{b,T1}$ which is less than p_b^*: the turning angle and length of one particular film necessarily vanish at the $T1$ itself. As already mentioned in section 5.2.4, we want however to ensure that

we select the control variable belonging to the "correct" film, i.e. to the film that eventually disappears at $T1$. A strategy for determining which film to select is presented below.

In the case of computing film coordinates in terms of ϕ_{ij}, we augment our system of variables by introducing turning angles $\delta\phi_{ij}$ for all 7 films, instead of just the 3 turning angles $\delta\phi_{13}$, $\delta\phi_{02}$ and $\delta\phi_{20}$ we have been working with to date. Of course this also requires introducing 4 additional equations relating the various $\delta\phi_{ij}$ to one another, but these are very simple relations easily obtained via Table 5.1. In fact the very simplicity of these relations is why it was possible to eliminate 4 of the original 7 values of $\delta\phi_{ij}$ in the first place. The numerical method should now select either $\delta\phi_{12}$, $\delta\phi_{30}$, $\delta\phi_{02}$, or $\delta\phi_{20}$ as the new control variable, since these are the particular angles that go to zero respectively as the system approaches a $T1_c$, $T1_u$, $T1_{l1}$, or $T1_{l3}$ transformation. We moreover select whichever of these four turning angles has lowest magnitude since that identifies the type of $T1$ to which the system is currently most susceptible. However, if the magnitude of the smallest of the four is actually increasing on the approach to the saddle-node bifurcation point, one of the remaining three with the next lowest magnitude is then chosen. We then step away from the saddle-node bifurcation point by imposing small step decreases in the magnitude of whichever $\delta\phi_{ij}$ is currently the control variable. Values of $\delta\phi_{12}$, $\delta\phi_{30}$, $\delta\phi_{02}$ and $\delta\phi_{20}$ are evaluated on each iteration step, and the choice of the control variable is reassessed such that whichever of these turning angles has the smallest magnitude at each step (provided the magnitude is also decreasing) is selected as the control variable. The choice of control variable might thereby change, but the procedure ensures that the turning angle that goes to zero is always eventually selected as the control variable, at least on the final approach to any $T1$. We thereby reach either a $T1^{\phi}_{c,\delta\phi_{12}}$, a $T1^{\phi}_{u,\delta\phi_{30}}$, $T1^{\phi}_{l1,\delta\phi_{02}}$ or a $T1^{\phi}_{l3,\delta\phi_{20}}$, the superscript indicating film coordinates parametrized by

ϕ_{ij} and the subscript indicating the new control variable that has now replaced p_b.

If film coordinates are parametrized in terms of distances along films $\mathfrak{s}_{ij}$, the numerical method sets as the new control variable either $\mathcal{L}_{12}$, $\mathcal{L}_{30}$, $\mathcal{L}_{02}$ or $\mathcal{L}_{20}$, i.e. one of the film lengths that goes to zero when the system approaches one of the respective topological transformations. In each iteration step, the film length with the lowest magnitude is typically chosen. As before, if at the saddle-node bifurcation point the smallest of these is increasing, one of the remaining options is selected, again the one with the next lowest magnitude. This is reassessed in each iteration step such that the $\mathcal{L}_{ij}$ that eventually goes to zero, triggering a topological transformation, is ultimately chosen. Therefore, in the notation we have established, the system undergoes either a $T1^s_{c,\mathcal{L}_{12}}$, $T1^s_{u,\mathcal{L}_{30}}$, $T1^s_{l1,\mathcal{L}_{02}}$ or $T1^s_{l3,\mathcal{L}_{20}}$ transformation, as distinct from a topological transformation that is reached on a single solution branch solely by increasing p_b without any saddle-node bifurcation being present.

In summary, in cases for which saddle-node bifurcations are present at some maximum $p_b = p_b^*$, we have established a procedure by which we can switch robustly from one steady solution branch to another. Although the second branch is expected to be unstable (hence not readily achieved in experiment), by tracking it away from p_b^* and showing that p_b decreases along it, we demonstrate (as already mentioned in section 5.2.4) that there is a well-defined critical p_b^* beyond which steady state solutions really do indeed cease to exist. This is worthwhile since it clearly distinguishes the saddle-node bifurcation situation from an alternative situation in which steady solutions are still present with increasing p_b but there is just some issue with a numerical scheme merely failing to find them. A numerical scheme could fail for instance because of the way we parametrize films: indeed films that become nearly flat as p_b increases are not readily parametrized in terms

of orientation angle, and distance along films is a better parameter choice.

5.4.6 Numerical method

In equilibrium, the system variables by construction satisfy the vertex meeting rules and area constraints, regardless of whether parametrization is in terms of orientation angle ϕ_{ij} (equations (5.21)–(5.25)), or distance along films $\mathfrak{s}_{ij}$ (equations (5.26)–(5.32)). However, we start off here by parametrizing in terms of orientation angle. Hence, once the equilibrium structure is set up with $p_b = 0$, which is done by fixing l_1° and l_2°, an initial perturbation away from equilibrium can be obtained using the weakly-driven migration solution (see section C.4 in Appendix C). This is done for an initial step change of control variable (p_b in the first instance) from the equilibrium by an amount $\varepsilon = 10^{-2}$. Using the weakly-driven solution as a starting point, the extent to which the constraints are violated is reduced by employing Newton-Raphson minimization, adjusting all variable values so as to ensure that the constraint violations are reduced to within an error of order 10^{-7} or less. Once this is achieved, we can be confident that we have found a steady state solution.

After correcting the weakly-driven velocity limit solution, we introduced additional step changes in the control variable (p_b initially) in steps of $\varepsilon = 0.01$, using the converged solution from one step as an initial guess for the next. If at any iteration step, the value of $|\kappa_{ij}| = |\Delta p_{ij} - v\cos(\phi_{ij})|$ of any film at any point is such that $|\kappa_{ij}| < 10^{-7}$, we consider switching from parametrizing in terms of ϕ_{ij} to $\mathfrak{s}_{ij}$. Independently of how we parametrize, if at any iteration step the Newton-Raphson algorithm fails to find the corresponding steady state solution, the system variables are taken back to the last, known to be correct, values. Then, the step size is reduced to half of its original value, i.e. $\varepsilon = 0.005$. This procedure is repeated until a steady state solution can actually be found for a sufficiently

small step size. Nevertheless, when $\varepsilon < 10^{-6}$, we assume that no further steady state solution can be found for the currently selected control variable. This might imply that we have reached a topological transformation, which we interrogate by examining film lengths: if a film length has shrunk below $\varepsilon < 10^{-6}$, then it is considered that a topological transformation has taken place. On the other hand, if $\varepsilon < 10^{-6}$ and all film lengths are $\mathcal{L}_{ij} > 10^{-6}$, this implies that we have reached a saddle-node bifurcation. In such cases we switch control variable using the criteria explained in section 5.4.5. An additional scenario is that in which for any step change $\varepsilon > 10^{-6}$ the lengths of all films are bigger than 10^{-6}, and the orientation angles $\delta\phi_{ij}$ converge to the predicted values for the inherently stable system (see section 5.3 for details). Convergence is assumed when the difference of each angle with respect to the predicted ones is less than 10^{-6}. In this case we consider that the system has reached the inherently stable configuration. On the other hand, in the case of reaching a saddle-node bifurcation point, we change the control variable, repeating the procedure again with a step size $\varepsilon = 0.01$, although noting that whereas on the original solution branch we stepped upwards in p_b on the new solution branch, we might be stepping downwards in the new control variable (we are specifically trying to reduce the magnitude of our chosen $\delta\phi_{ij}$ or $\mathcal{L}_{ij}$).

5.5 Steady state out-of-equilibrium results

In this section we present the steady state solution results for systems driven out-of-equilibrium for a wide range of l_1° and l_2°, i.e. we consider bubbles with a variety of different sizes (see Tables C.1 and C.2 in section C.1 in Appendix C to relate l_1° and l_2° to bubble areas). We find the shapes of the bubbles as they migrate through a confined channel, spanning the range from low to high imposed driving pressures. We start by studying the effect of having different

values of l_1° and l_2° upon the different possible topological transformations that the three-bubble system might reach. This is discussed in section 5.5.1. Then in section 5.5.2 we compare for a selected set of systems, the maximum or critical imposed back pressure with the pressure at which the system actually attains topological transformation. In section 5.5.3 we show examples in which we change control variables in order to track the steady state solution along a second solution branch. Along this particular branch, the imposed back pressure p_b changes, and typically decreases as the topological transformation is approached. Subsequently, in section 5.5.4 we study the system geometry as an inherently stable configuration is approached. Finally in section 5.5.5 the three-bubble system is compared with the simple lens system, by computing in each case, the imposed back pressure vs migration velocity. Additional information concerning how individual bubble pressures and system energy change as the imposed back pressure increases have been relegated to Appendix C section C.5.1 and section C.5.2, respectively. In addition more information about imposed back pressures needed to attain topological transformation is found in sections C.5.3–C.5.4.

As these are steady state computations, what matters is to establish under which conditions steadily migrating structures are admitted and for which conditions topological transformations take place (but not what happens after those transformations). We explore how film turning angles, film lengths, bubble pressures, and migration velocity change as the structures deform out-of-equilibrium. In Figure 5.9 we can see, as an example, the case of a structure characterized in equilibrium by fixing $l_1^\circ = 0.5$ and $l_2^\circ = 0.3$. The resulting shape of the migrating structure is shown for three different imposed back pressures p_b. As the structure deforms away from equilibrium, films either grow or shorten. The majority of films grow in length, leading to an increment in the system energy (sum of lengths over all the films). However the film lengths $\mathcal{L}_{12}$ and $\mathcal{L}_{30}$ shrink, leading

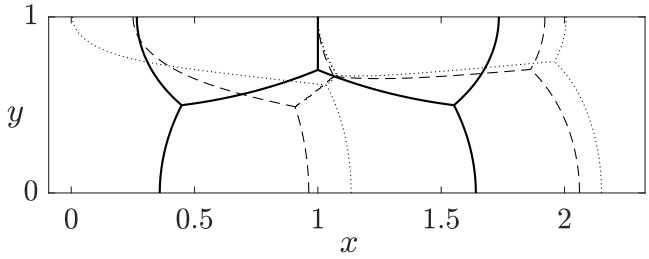

Figure 5.9: Steady state simulation for a fixed $l_1^\circ = 0.5$ and $l_2^\circ = 0.3$ in the equilibrium, and three arbitrary imposed back pressures. Solid line: $p_b = 0$. Dashed line: $p_b = 9.7037$. Dotted line: $p_b = 14.7037$. The energies (i.e. sum of lengths of all the films) are respectively 3.5849, 3.8116, and 4.1315 so increase with p_b, even though some individual films shorten.

in the cases in which $\mathcal{L}_{12}$ and $\mathcal{L}_{30}$ shrink away to zero to either a $T1_c$ or $T1_u$ topological transformation respectively (see discussion in section 5.2.4). In Figure 5.9, the length of film $\jmath_{02}$, namely $\mathcal{L}_{02}$, shrinks at first, but at higher p_b grows again. The minimum of $\mathcal{L}_{02}$ turns out to happen roughly around a p_b value at which the film becomes entirely flat ($\delta\phi_{02} = 0$), with the film then switching from concave to convex seen from downstream. Different combinations of l_1° and l_2° can however be found at which the length $\mathcal{L}_{02}$ or $\mathcal{L}_{20}$ shrink all the way to zero, leading to a $T1_{l1}$ or $T1_{l3}$ topological transformation, respectively.

5.5.1 Type of topological transformation for different l_1° and l_2° values

To determine for which values of l_1° and l_2° the structure undergoes either a $T1_c$, $T1_u$, $T1_{l1}$ or $T1_{l3}$ topological transformation, steady state solutions are obtained for a wide range of values of $l_1^\circ \in [0.01, 0.02, 0.03, ..., 0.99]$ and $l_2^\circ/l_1^\circ \in [0.01, 0.02, 0.03, ..., 0.99]$. For each system we start off parametrizing the films in terms of orientation angles ϕ_{ij}, and using p_b as control variable. However the system may reach a saddle-node bifurcation at the end of a stable solution branch,

and in order to track the steady state solution up to a topological transformation, we then need to switch the control variable, as specified in section 5.4.5. On the other hand, if (for large p_b) films become very flat, it is recommended (see section 5.4.6) to switch from parametrizing in terms of orientation angle ϕ_{ij} to parametrizing in terms of distance along films $\mathfrak{s}_{ij}$. The domain in which we have to switch to parametrizing in terms of $\mathfrak{s}_{ij}$ is that for large values of l_1° and small to moderate values of l_2°/l_1°. By contrast, the current scheme (parametrized in terms of ϕ_{ij}) has no issues dealing with small values of l_1°. In the small l_1° regime, systems undergo either $T1_u$ or $T1_c$ topological transformations, with $T1_u$ being favoured for small l_2°/l_1° (area A_2 much larger than areas $A_1 = A_3$ which are small) and $T1_c$ being favoured for larger values of l_2°/l_1° (less disparity between A_2 and $A_1 = A_3$ with all areas being comparatively small). This then is what we show in Figures 5.10 and 5.11.

In an effort to identify to which type of $T1$ a given system might be most susceptible, it is interesting (as mentioned in section 5.2.3) to ask whether any of the above mentioned films are already quite short *in the equilibrium state*. Accordingly we examine the corresponding equilibrium film lengths $\mathcal{L}_{12}^\circ$, $\mathcal{L}_{30}^\circ$ and $\mathcal{L}_{02}^\circ = \mathcal{L}_{20}^\circ$ for a variety of bubble sizes, i.e. a variety of l_1° and l_2°. This is what Figure 5.10(a) shows. What we see is that large l_2°/l_1° shows $\mathcal{L}_{12}^\circ$ is the smallest film length (suggesting susceptibility to $T1_c$), small l_1° (but without very large l_2°/l_1°) shows $\mathcal{L}_{30}^\circ$ is the smallest length (susceptibility to $T1_u$), and for large l_1° (again without very large l_2°/l_1°) $\mathcal{L}_{02}^\circ = \mathcal{L}_{20}^\circ$ is the shortest length (the system might be susceptible to either T_{l1} or T_{l3}). Although Figure 5.10(a) gives an indication as to which type of $T1$ a system might be susceptible, we emphasise that this is not a definitive proof. The data in Figure 5.10(a) are based entirely on the equilibrium state, and a film that starts off quite short at equilibrium, might actually grow rather than shrink as we depart from equilibrium.

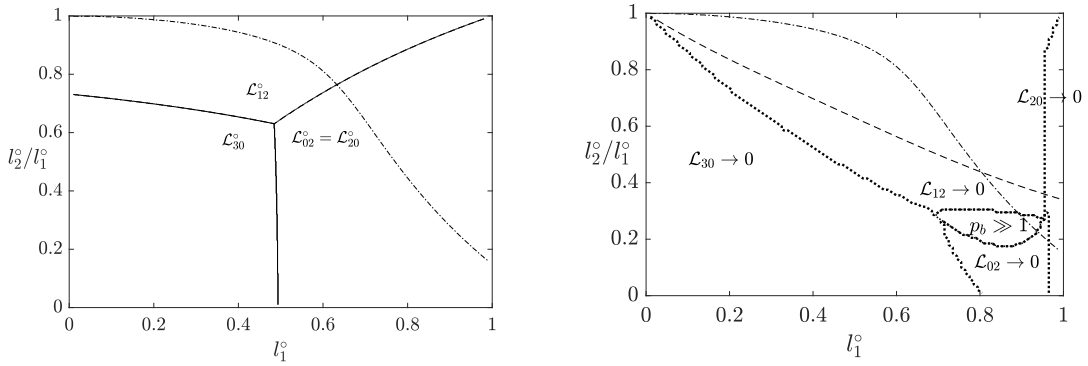

Figure 5.10: (a) Phase diagram dividing the studied values of l_1° and l_2°/l_1° in equilibrium in three regions, each region showing which film length $\mathcal{L}_{ij}^\circ$ is the shortest one. The dash-dotted line corresponds to the values of l_1° and l_2°/l_1° for which the structure is monodisperse (all bubbles of the same size). Above the dash-dotted line the area of bubbles $A_1 = A_3 > A_2$, and below it $A_1 = A_3 < A_2$. (b) Topological transformation phase diagram for systems set up at equilibrium with $l_1^\circ \in [0.01, 0.99]$ vs $l_2^\circ/l_1^\circ \in [0.01, 0.99]$. The dash-dotted line is as per (a).

Figure 5.10(b) shows which type of topological transformation $T1$ the different systems *actually* undergo as a function of l_1° and l_2°/l_1°. Here we show this by specifying in each case which one of the film lengths $\mathcal{L}_{ij}$ shrinks all the way down to zero, although for the purposes of this figure we make no distinction between a $T1$ reached on a stable steady state branch (by increasing p_b) and a $T1$ reached on an unstable branch that we switch onto after a saddle-node bifurcation. The different regions on Figure 5.10(b) are divided by dotted lines. There is a reasonable correlation between the regions marked out in Figure 5.10(a) (i.e. which film length $\mathcal{L}_{ij}^\circ$ is shortest) and those marked out in Figure 5.10(b) (i.e. which film length $\mathcal{L}_{ij}$ ultimately vanishes at $T1$). However the region in Figure 5.10(b) in which $T1_c$ events occur (i.e. vanishing $\mathcal{L}_{12}$) is rather larger than Figure 5.10(a) might suggest. Likewise the region in Figure 5.10(b) in which either $T1_{l1}$ or $T1_{l3}$ events occur (i.e. vanishing $\mathcal{L}_{02}$ or $\mathcal{L}_{20}$) is much smaller than Figure 5.10(a) sug-

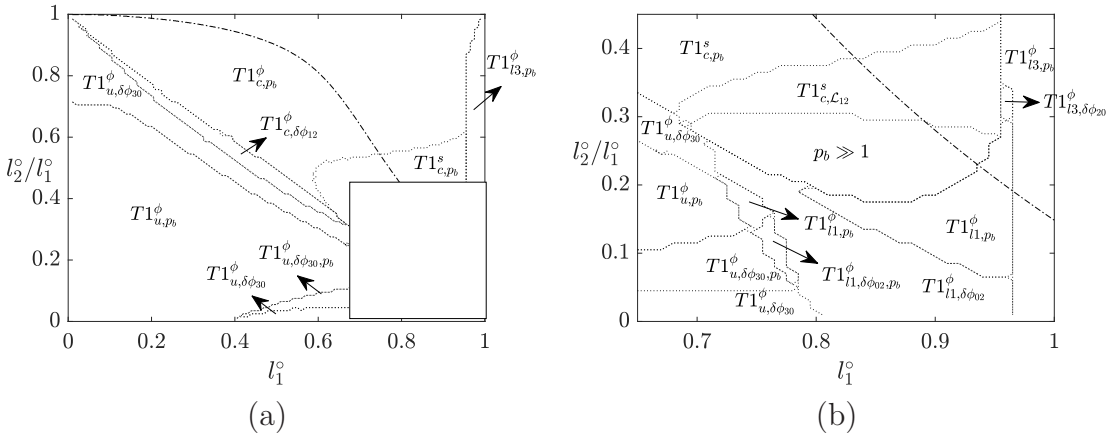

Figure 5.11: (a) Detailed phase diagram for different values (in equilibrium) of l_1° and l_2°/l_1°. Here we show whether the systems reach a topological transformation, either a $T1_c$, $T1_u$, $T1_{l1}$ or a $T1_{l3}$, or reach the inherently stable migrating structure. (b) Zoom in of (a).

gests. Monodisperse cases (the dash-dotted line plotted on Figure 5.10(a) and (b)) tend to correspond to $T1_c$, i.e. $\mathcal{L}_{12} \to 0$, although the monodisperse line also penetrates the region in which films become exceedingly flat without $T1$ occurring (i.e. the inherently stable region labelled in Figure 5.10(b) by $p_b \gg 1$). For yet larger l_1°, the monodisperse case also penetrates the region where the system undergoes $T1_{l1}$ ($\mathcal{L}_{02} \to 0$) or $T1_{l3}$ ($\mathcal{L}_{20} \to 0$).

In Figure 5.10(b) we also indicate the necessary condition derived in section 5.3.2 for systems to admit an inherently stable state. This is shown by a dashed line, with the entire region underneath the dashed line meeting the necessary condition. The information presented here is the same as that presented in Figure 5.8 just expressed in terms of l_1° and l_2°/l_1° rather than in terms of A_1 and A_2. The region of parameter space within which the inherently stable state is actually found (labelled as $p_b \gg 1$) is however significantly smaller than this.

Figure 5.11 shows in detail which specific type of topological transformation the different systems undergo (if they do so), i.e. whether they approach a $T1$ via a stable or unstable solution branch, and whether the systems were parametrized in terms of ϕ_{ij} or $\mathfrak{s}_{ij}$ at the point of reaching it. Looking at Figure 5.11(a) over a wide range of l_1° and l_2°/l_1° values, we see that to the bottom left of the figure, systems favour $T1^{\phi}_{u,p_b}$, and towards the top right they favour $T1^{\phi}_{c,p_b}$, although on the right hand edge cases with $T1^{\phi}_{l3,p_b}$ are observed. Meanwhile in Figure 5.11(b) (zoom in of the bottom right of Figure 5.11(a)), in some cases we see $T1^{\phi}_{l1,p_b}$ topological transformations. All these transformations subscripted p_b are on an original (believed stable) solution branch which is tracked by monotonically increasing p_b. Topological transformations $T1^{\phi}_{u,\delta\phi_{30}}$ and $T1^{\phi}_{c,\delta\phi_{12}}$ that occur on an unstable solution branch are also found for various combinations of l_1° and l_2°/l_1° in Figure 5.11(a). For the most part, these tend to form "buffer regions" between the $T1^{\phi}_{u,p_b}$ and $T1^{\phi}_{c,p_b}$ regions. In Figure 5.11(b) we also see examples of $T1^{\phi}_{l1,\delta\phi_{02}}$ and $T1^{\phi}_{l3,\delta\phi_{02}}$. As we have mentioned, tracking these sorts of transformations (subscripted $\delta\phi_{ij}$) involves p_b reaching a maximum and decreasing again after a saddle-node bifurcation.

In certain cases, a second saddle-node bifurcation is reached when the steady state solution is tracked in terms of $\delta\phi_{30}$ and $\delta\phi_{02}$. On this new solution branch p_b starts increasing again, just before reaching a topological change. This behaviour for p_b proves the existence of a *second* saddle-node bifurcation. Thus the value of p_b increases on an original solution branch, then decreases after a new control variable is selected to negotiate a saddle-node bifurcation, but finally p_b starts increasing again after a second saddle-node bifurcation, immediately before the $T1$. Such cases are denoted $T1^{\phi}_{u,\delta\phi_{30},p_b}$ and $T1^{\phi}_{l1,\delta\phi_{02},p_b}$ topological transformations. Whether the solution branch between the second saddle-node bifurcation and the eventual $T1$ might be stable or unstable, is not a question we can interrogate with our current steady state solution methodology.

Whilst saddle-node bifurcations were ubiquitous in the simple lens [19], for the three-bubble case in Figure 5.11 they occupy a comparatively small fraction of the l_1° vs l_2°/l_1° phase space. As alluded to earlier, for the most part, they form "buffer regions" separating the various $T1^{\phi}_{u,p_b}$, $T1^{\phi}_{c,p_b}$, $T1^{\phi}_{l1,p_b}$ and $T1^{\phi}_{l3,p_b}$ regions from one another: in "buffer regions" like these, competition between different types of $T1$ might be expected.

Also as mentioned in sections 5.4.2, 5.4.4 and 5.4.6 there are certain instances in which we switch from parametrizing the system in terms of orientation angle ϕ_{ij} to parametrizing in terms of distance along a film $\mathfrak{s}_{ij}$. The trigger for this change in parameterization is when curvature $|\kappa_{ij}|$ on at least parts of films becomes small, meaning that different positions on the film have nearly the same ϕ_{ij}, albeit different $\mathfrak{s}_{ij}$. This is most likely an issue in systems that have comparatively large bubbles and hence comparatively long films enclosing them, corresponding to cases for which l_1° is large and l_2°/l_1° is small to moderate. This is exactly the region in Figure 5.11 where the change in parametrization occurs. What we see for instance in Figure 5.11(a) is a region of $T1^{s}_{c,p_b}$ topological transformations and zooming into Figure 5.11(b) we see $T1^{s}_{c,\mathcal{L}_{12}}$ transformations also. Physically a $T1^{s}_{c,p_b}$ is no different from a $T1^{\phi}_{c,p_b}$: they both involve monotonic increases in p_b up to a $T1$, but have merely been computed by parametrizing in different ways. Likewise, despite the different computational approach, physically there is no difference between $T1^{s}_{c,\mathcal{L}_{12}}$ and $T1^{\phi}_{c,\delta\phi_{12}}$. Both involve p_b increasing up to a saddle-node bifurcation on one solution branch, and meeting a new (typically unstable) branch along which p_b then decreases.

Additionally Figure 5.11(b) reveals, in the same way that Figure 5.10(b) did, that some systems also reach the inherently stable structure (labelled here as

$p_b \gg 1$), where no further deformation in the structure can be seen. A change in parametrization from ϕ_{ij} to $\mathfrak{s}_{ij}$ is always triggered in this case, since approaching the inherently stable state, curvatures fall as films become asymptotically flat. Film orientations and film lengths then approach limiting values, while internal bubble pressures and migration velocity keep increasing at a constant rate as the imposed back pressure increases. Although details are not discussed here, we have checked (see section C.5.1–C.5.2) that computed values of the above mentioned quantities match with the predicted values given in section 5.3.1. As we already saw in the context of Figure 5.10(b), just a fraction of all the possible combinations of l_1° and l_2°/l_1° that would meet the necessary condition for inherent stability are ultimately seen to achieve that state. In Figure 5.11(b), the domain of inherently stable solutions lies lower down in l_2°/l_1° value than the region of $T1^s_{c,p_b}$ topological transformations, with the $T1^s_{c,\mathcal{L}_{12}}$ region forming a "buffer" between the two. Other parameter regimes despite meeting the aforementioned necessary condition, e.g. those with small values of l_1°, undergo topological transformation (typically $T1_u$) and never reach the inherently stable state. Moreover systems having large l_1° and rather small l_2°/l_1° lead, as Figure 5.11(b) shows, to various types of $T1_l$ transformation, e.g. $T1^\phi_{l1,p_b}$, $T1^\phi_{l1,\delta\phi_{02}}$ or $T1^\phi_{l3,p_b}$.

In summary, we have determined for which values of l_1° and l_2° the systems undergo either $T1_c$, $T1_u$, $T1_{l1}$ or $T1_{l3}$ (reached either quasistatically by increasing the imposed back pressure, or else by passing through a saddle-node bifurcation), or reach the inherently stable migrating structure. In the following sections we show how, as the imposed back pressure p_b is increased, the response variables change as the system approaches the different topological transformations discussed above. On the other hand, when we encounter a saddle-node bifurcation, we need to change control variables from p_b to $\delta\phi_{ij}$ (or to $\mathcal{L}_{ij}$ depending how films are parametrized). The value of p_b is now expected to decrease, and we

want to demonstrate that explicitly. This then is what we discuss in the next few sections.

5.5.2 Critical imposed back pressure p_b^* and $T1$ back pressure $p_{b,T1}$

As we have already discussed, the critical imposed back pressure p_b^* corresponds to the maximum allowed pressure for which a steady state solution exists. At this point, either the system achieves a topological transformation, or else reaches the end of the current steady solution branch at a saddle-node bifurcation point. In the latter case, we can track the steady state solution onto a second branch by using a different control variable: a turning angle $\delta\phi_{ij}$ (or one of the $\mathcal{L}_{ij}$ values), allowing us to follow what is now an unstable solution branch all the way to a topological transformation, which occurs at some $p_{b,T1}$ less than p_b^*. Here we show for six fixed values of $l_1^\circ \in [0.3, 0.5, 0.7, 0.78, 0.9, 0.97]$ and a wide range of values of $l_2^\circ/l_1^\circ \in [0.01, 0.99]$, the maximum imposed back pressure p_b^* for each system, comparing these values with the pressure $p_{b,T1}$ at which the systems undergo topological transformation with $p_{b,T1} \leq p_b^*$. This is what we see in Figure 5.12. The systems that survive out to largest p_b^* tend to be those with large l_1° and small to moderate l_2°/l_1°, some of these cases being inherently stable (hence having arbitrarily large p_b^*, indicated by zones between vertical dashed lines in Figure 5.12). The data presented in Figure 5.12 are interesting to compare and contrast with results in [19] for the simple lens. When the lens bubble was small, the simple lens system was found to be particularly "rigid" or particularly "strong", requiring a very large imposed pressure to deform significantly away from the equilibrium structure but eventually reaching a $T1_u$ topological transformation. For the three-bubble system in Figure 5.12(a) meanwhile, in the case $l_1^\circ = 0.3$ say, bubbles $\mathcal{B}_1$ and $\mathcal{B}_3$ have relatively modest area, but particularly when l_2°/l_1°

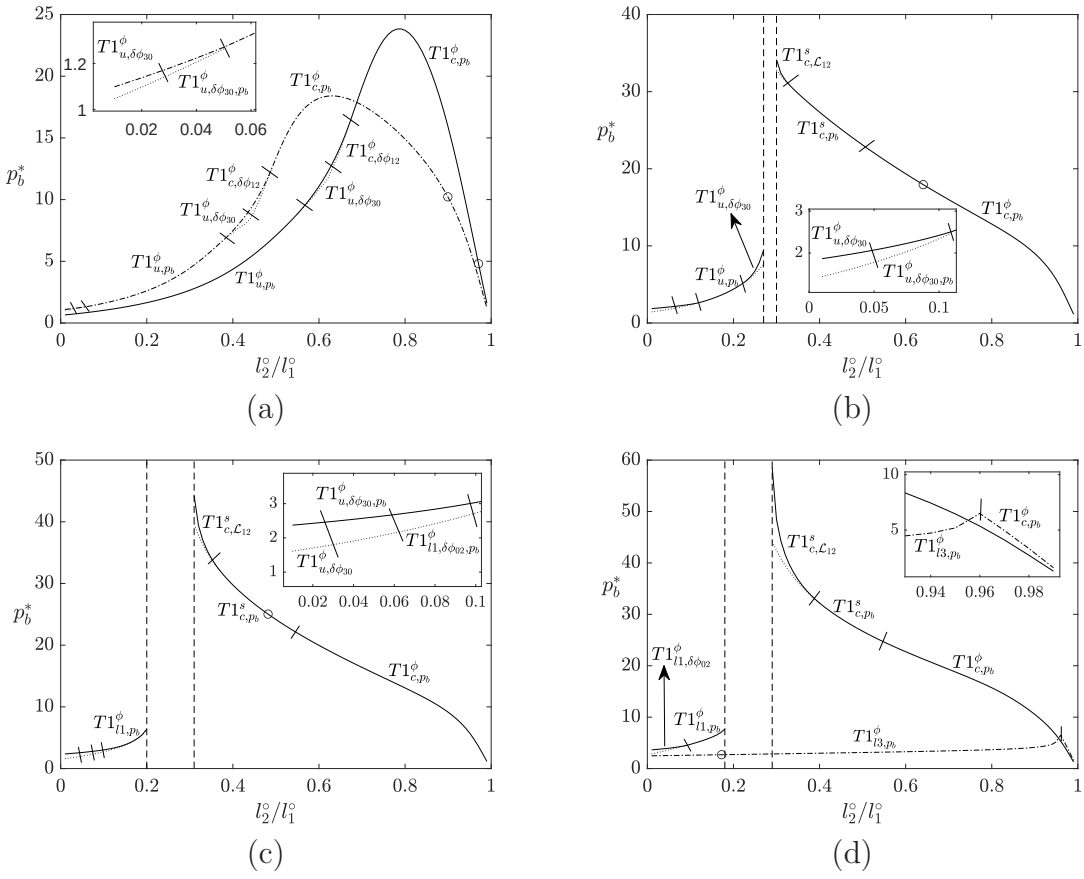

Figure 5.12: Back pressures p_b^* and $p_{b,T1}$, which only differ from one another in the case of a saddle-node bifurcation (where relevant $p_{b,T1}$ are shown with dotted lines). The circle points "$\circ$" corresponds to the values of l_2°/l_1° for which the systems are monodisperse. For each fixed l_1°, the different types of $T1$, as per shown Figure 5.11 are indicated. In (a) we plot data for $l_1^\circ = 0.3$ (solid line), and for $l_1^\circ = 0.5$ (dash-dotted line), in (b) for $l_1^\circ = 0.7$, in (c) for $l_1^\circ = 0.78$, and in (d) for $l_1^\circ = 0.9$ (solid line) and for $l_1^\circ = 0.97$ (dash-dotted line), in each case for $l_2^\circ/l_1^\circ \in [0.01, 0.99]$. In (b), (c), and (d) the region in between the vertical dashed lines encloses the systems that reach the inherently stable structure. Here values of $p_b \gg 1$ are attained.

is small, the area of bubble $\mathcal{B}_2$ is much larger. The implication of having small l_2°/l_1° is that film $\jmath_{13}$ is now so short that the structure (at equilibrium at least) is almost on the point of becoming two individual simple lenses that happen to be side by side. Topological transformation is however realized in the same fashion as for a simple lens, i.e. via a $T1_u$. Nonetheless as section C.5.4 in Appendix C explains however, the three-bubble system can (compared to the simple lens) be much more susceptible to $T1_u$ owing to the geometry of how the vertex that undergoes $T1_u$ is positioned on the bubbles. In the three-bubble system vertex V_3 tends, even at equilibrium, to be positioned quite far towards the right hand end of bubble $\mathcal{B}_3$ making it easy for the bubble and vertex to slip apart.

Increasing l_2°/l_1°, still considering fixed $l_1^\circ = 0.3$, causes the size of bubble $\mathcal{B}_2$ to shrink. For very large l_2°/l_1° (very close to unity) all three bubbles $\mathcal{B}_1$, $\mathcal{B}_2$ and $\mathcal{B}_3$ are quite small area, but unlike the simple lens case, having small bubbles does not impart stability to the three-bubble structure, in the sense that the critical pressure p_b^* actually decreases as l_2°/l_1° increases (assuming l_2°/l_1° is near unity) as Figure 5.12(a) shows. The reason for having a comparatively low p_b^* in this situation is that the three-bubble system undergoes a $T1_c$ topological transformation, i.e. a vertex-vertex collision away from the channel walls. There is no counterpart to this in the simple lens since, for the simple lens, there is only one single vertex away from the walls. As Appendix C section C.5.4 explains, there are ways in which a system with small l_1° can acquire the strength to resist $T1$ in a similar fashion to what is seen for a simple lens [19], but it requires a specific choice of l_2°/l_1°, neither too small nor too close to unity.

Now consider a much larger l_1° (e.g. $l_1^\circ = 0.9$ or $l_1^\circ = 0.97$ as in Figure 5.12(d)) but still with comparatively large l_2°/l_1° approaching unity. In this system, bubbles $\mathcal{B}_1$ and $\mathcal{B}_3$ are comparatively large area, but bubble $\mathcal{B}_2$ is small. Unlike the simple lens though, having this small bubble $\mathcal{B}_2$ present once again does not impart

stability to the system. Again the three-bubble system undergoes topological transformation at comparatively small p_b^* and again the type of transformation that occurs, namely $T1_c$, is unavailable to the simple lens.

Another contrast between the three-bubble system and the simple lens can be seen by considering a three-bubble case in which l_1° is large and l_2°/l_1° is very small. The three-bubble system breaks up via a $T1_{l1}$ or $T1_{l3}$ in this case as Figure 5.12(d) shows: again this happens at a comparatively small p_b^*. That behaviour (a topological transformation at the lower channel wall), is never seen in the simple lens system, even for simple lens which at equilibrium would have a very large lens bubble connected to a very short spanning film, the latter being located near the lower channel wall. Instead, if the simple lens is deformed out of equilibrium, the spanning film lengthens significantly, and the topological transformation always occurs at the upper channel wall [19] rather than at the lower channel wall. In a simple lens of course, the spanning film is relatively free to lengthen, since it is not associated with any bubble area constraint. The three-bubble system is however more constrained: films $\jmath_{02}$ and $\jmath_{20}$ connecting to the lower channel wall both contribute to an area constraint on bubble $\mathcal{B}_2$. Increasing the length of one of these (film $\jmath_{20}$ say) might require the length of the other (film $\jmath_{02}$) to decrease, and that drives a $T1_{l1}$. Alternatively increasing the length of $\jmath_{02}$ might make film $\jmath_{20}$ shorter, leading to $T1_{l3}$. Both types of transformation are seen in Figure 5.12(d) when l_1° is large and l_2°/l_1° is small.

Further details of the types of topological transformations that are possible, and why certain types of transformations are selected for certain limiting values of l_1° and l_2° can be found in sections C.5.3–C.5.4. One of the points discussed there, is that a system with bubbles $\mathcal{B}_1$ and $\mathcal{B}_3$ small, can behave qualitatively differently (in terms of how strong it is to resist $T1$) from a system in which just bubble $\mathcal{B}_2$

is small. The difference is found to be related to the quite different bubble shapes and quite different film curvatures seen when $\mathcal{B}_1$ and $\mathcal{B}_3$ small versus when $\mathcal{B}_2$ is small.

5.5.3 Imposed back pressure p_b vs control variables

Figure 5.12 identified a number of cases that exhibit saddle-node bifurcations such that p_b^* is strictly greater than $p_{b,T1}$. In such cases a new control variable is selected at the bifurcation point, and one convenient way to visualize the system is to plot how p_b varies as a function of that new control variable (or vice versa). The variables that we choose to plot in each case are $\delta\phi_{12}$ if the system reaches a $T1^{\phi}_{c,\delta\phi_{12}}$, $\delta\phi_{30}$ if the system reaches a $T1^{\phi}_{u,\delta\phi_{30}}$, $\delta\phi_{02}$ if the system eventually reaches a $T1^{\phi}_{l1,\delta\phi_{02}}$, and $\delta\phi_{20}$ for if the system reaches a $T1^{\phi}_{l3,\delta\phi_{20}}$. We also plot $\mathcal{L}_{12}$, in the case of a system reaching a $T1^{s}_{c,\mathcal{L}_{12}}$. This is what Figure 5.13 shows. In each case, the new control variable vanishes at the respective $T1$.

In Figure 5.13 in cases that actually exhibit saddle-node bifurcations, we see the expected behaviour, i.e. p_b increasing on one branch, but decreasing on another. However there are some complications, as we can see in Figure 5.13(b). Here for $l_1^\circ = 0.75$ with $l_2^\circ/l_1^\circ = 0.1$ for instance, although p_b does indeed decrease as we move onto the second solution branch, it actually starts increasing again (see inset of Figure 5.13(b)) right near the end of the branch (at which point the magnitude of the control variable $\delta\phi_{30}$ is already very small). The case $l_1^\circ = 0.75$ with $l_2^\circ/l_1^\circ = 0.14$ is more complex still. On this branch (see the inset of Figure 5.13(c)) the selected control variable $\delta\phi_{02}$ initially manages to fall to zero, even though there is no $T1$. Having the value $\delta\phi_{02}$ approach zero is a necessary condition for $T1_{l1}$ but not sufficient, since it also happens that $\delta\phi_{02}$ changes sign when $\jmath_{02}$ switches from being concave to convex. After $\delta\phi_{02}$ changes sign, its magnitude (whilst still remaining exceedingly small) is increasing along the solution branch. In line with the procedure described in section 5.4.5, we therefore temporarily

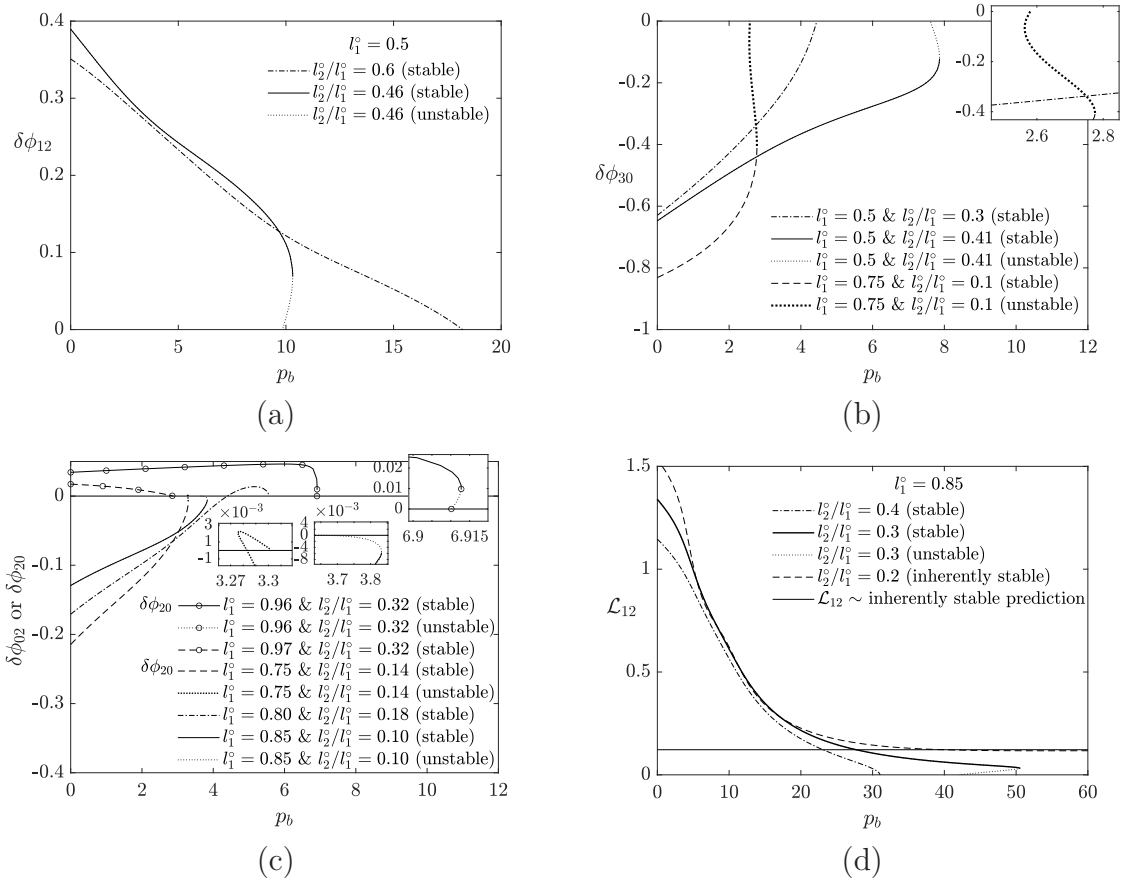

Figure 5.13: Imposed back pressure p_b vs the value of control variables that can be selected to vanish at the point at which topological transformation is reached. In each case the dash-dotted line corresponds to a system that reaches the topological transformation on a stable solution branch (p_b increases monotonically up to the $T1$, implying no need for a change of control variable in such cases). The solid lines correspond to the original stable solution branch for a system that reaches a saddle-node bifurcation (and a change of control variable is applied at that point). The dotted lines correspond to the so-called unstable solution branch, where p_b now starts off decreasing. Additionally, in (d) we plot $\mathcal{L}_{12}$ for a system that reaches the inherently stable configuration, with $\mathcal{L}_{12}$ converging to 0.1220, the predicted value for the particular l_1° and l_2°/l_1° values of the system in question based on the theory presented in section 5.3.1.

switch control variable to one of the other film turning angles. As we continue to track the system, p_b is found to fall to a minimum and starts increasing again. Subsequently $\delta\phi_{02}$ reaches a maximum and starts decreasing, meaning it can be selected as the control variable again. Eventually a $T1_{l1}$ is reached. The case for $l_1^\circ = 0.80$ and $l_2^\circ/l_1^\circ = 0.18$ has similar features, in that $\delta\phi_{02}$ initially exhibits a change of sign without a $T1$ occurring, and then $\delta\phi_{02}$ returns back to zero later on at the $T1_{l1}$ itself. Here though, p_b increases monotonically after the sign change for $\delta\phi_{02}$. Also in Figure 5.13(c) we can see cases in which $\delta\phi_{20}$ approaches zero as the system reaches a $T1_{l3}$. Particularly, in the case of $l_1^\circ = 0.96$, and $l_2^\circ/l_1^\circ = 0.32$, the system reaches a saddle-node bifurcation, with p_b after such point decreasing as the system approaches to a $T1_{l3}$ on a second solution branch. On the other hand, in Figure 5.13(d) we see how a system with $l_1^\circ = 0.85$ and $l_2^\circ/l_1^\circ = 0.2$, reaches an inherently stable structure, with no $T1$ but instead with $\mathcal{L}_{12}$ approaching (for these chosen l_1° and l_2°/l_1° values) a well-defined length of 0.1220. This length can be predicted on the basis of the theory presented in section 5.3.1. In this case the system does not undergo any topological transformation, no matter how large p_b becomes. Further analysis of the approach to the inherently stable state is given in the next section.

5.5.4 Total film turning angles on approach to the inherently stable state

Here we show how the total turning angle of films change as a function of the imposed back pressure p_b, as systems approach the inherently stable structure. In these cases total turning angles eventually reach values that do not change significantly as p_b increases. Since at each vertex total turning angles are related as specified in Table 5.1, here we just focus on $\delta\phi_{02}$, $\delta\phi_{13}$, $\delta\phi_{20}$, these being the total turning angles of the films that connect most directly channel walls

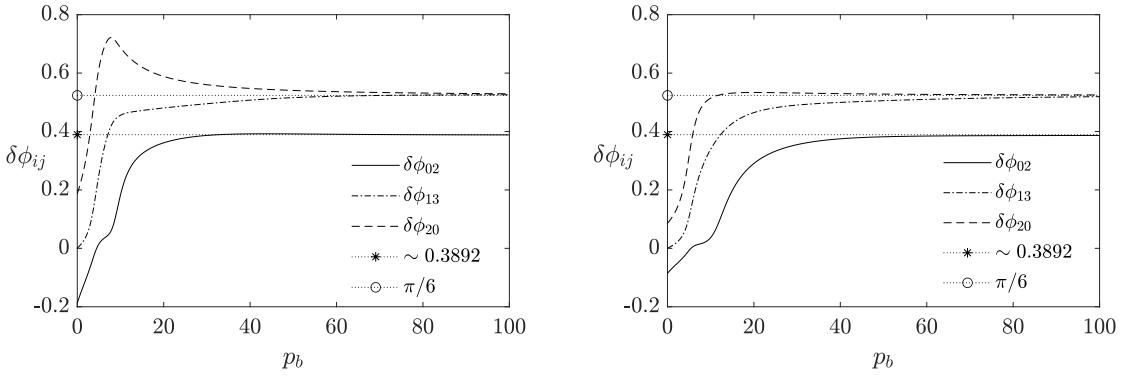

Figure 5.14: Turning angles $\delta\phi_{02}$, $\delta\phi_{13}$ and $\delta\phi_{30}$, vs imposed back pressure p_b. We consider two different values of l_1°, and one value of l_2°/l_1° in each case. As p_b increases, turning angles approximate to values deduced in section 5.3.1, via a prediction for an inherently stable state, specifically. As p_b increases, $\delta\phi_{13}$ and $\delta\phi_{20}$ approach $\pi/6$, and $\delta\phi_{02}$ approaches $\text{acos}(1-\sqrt{3}/2)-\pi/3 \approx 0.3892$. (a) $l_1^\circ = 0.78$ with $l_2^\circ/l_1^\circ = 0.21$. (b) $l_1^\circ = 0.9$ with $l_2^\circ/l_1^\circ = 0.23$.

with respective vertices. As the imposed back pressure is increased more and more, total turning angles $\delta\phi_{13}$ and $\delta\phi_{20}$ approach $\pi/6$, and $\delta\phi_{02}$ approaches $\text{acos}(1-\sqrt{3}/2)-\pi/3 \approx 0.3892$, as obtained in section 5.3.1. This is what we show in Figure 5.14.

5.5.5 Imposed back pressure p_b vs migration velocity v

As was shown in [19], for the simple lens, the driving velocity v is a (weakly) non-linear function of the imposed back pressure p_b, with smaller bubbles reaching higher critical pressures than the larger ones. The velocity was well approximated by $v \approx p_b$ for the simple lens. Here we study for the three-bubble symmetric system how the driving velocity changes as a function of the back pressure, when different systems are considered. Specifically, we computed the driving velocity for $l_1^\circ \in [0.5, 0.7, 0.9]$, in each case with $l_2^\circ/l_1^\circ = 0.5$, up to $p_b = p_b^*$ (see Figure 5.15). We can determine that for the three-bubble system, the migration velocity is

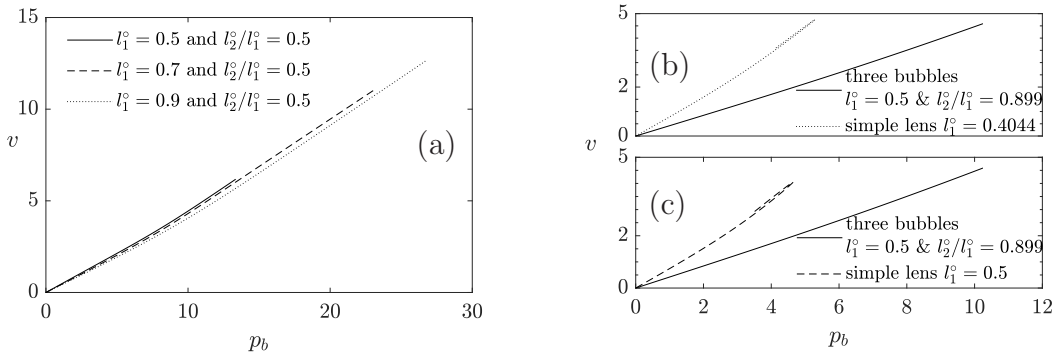

Figure 5.15: Steady state migration velocity v as a function of the imposed back pressure p_b. (a) Different values of $l_1^\circ \in [0.5, 0.7, 0.9]$ for the same value of $l_2^\circ/l_1^\circ = 0.5$ are considered. In (b) and (c) we plot a simple lens vs a three-bubble symmetric case system. Cases are: the three-bubble case with $l_1^\circ = 0.5$ and $l_2^\circ/l_1^\circ = 0.899$ (solid line in (b) and (c)), and the simple lens with $l_1^\circ = 0.4044$ (dotted line in (b)) and with $l_1^\circ = 0.5$ (dashed line in (c)). Bubble areas are $A_1 = A_2 = A_3 = 0.1339$ for the three-bubble system. In the simple lens cases $A_1 = 0.1339$ (for $l_1^\circ = 0.4044$) and $A_1 = 0.2047$ (for $l_1^\circ = 0.5$).

approximately $v \approx p_b/2$. This relation (which is consistent with the predictions in section 5.3.1) comes from the fact that moving across the three-bubble structure, we must cross at least two films. For any chosen l_1°, this relation turns out not to change significantly as we vary l_2°/l_1°, in all the studied cases, the values superposing each other on the scale of Figure 5.15: variation of the v-p_b relation with respect to l_2°/l_1° is exceedingly weak. Some slight variation can be seen when different values of l_1° are considered (at fixed l_2°/l_1°), but even this variation is comparatively weak. Variation seen in Figure 5.15(a) thereby shows the "less weak" of these two weak functions, and for simplicity in each case we plot, just one fixed value of l_2°/l_1°. In Figure 5.15(a), we can see that for increasingly large values of l_1°, the v vs p_b curves have very slightly lower slopes, the system travels at very slightly lower velocity.

In Figure 5.15(b)–(c), we plot for $l_1^\circ = 0.5$ and $l_2^\circ/l_1^\circ = 0.899$ (a monodisperse

three-bubble system) against a similar simple lens structure obtained for the same area (Figure 5.15(b)) and also a simple lens with the same $l_1^\circ = 0.5$ (Figure 5.15(c)). The bubble areas in the three-bubble system are $A_1 = A_2 = A_3 = 0.1339$, whereas the bubble area in the simple lens cases is $A_1 = 0.1339$ with $l_1^\circ = 0.4044$ (dotted line in Figure 5.15(b)), or else is $A_1 = 0.2047$ when $l_1^\circ = 0.5$. Even the latter simple lens case here is not too far away from each area for the three-bubble system. There is a weak l_1° dependence in the v-p_b relation in the simple lens case: larger l_1° gives a slightly smaller v at any given p_b, and moreover larger l_1° means the system only survives out to a smaller p_b (and hence a smaller v). These effects are predicted by [19]. In both the simple lens cases, the systems reach saddle-node bifurcations: switching to a new solution branch causes migration velocity v and pressure p_b to start decreasing before reaching a topological transformation. However, in the simple lens cases plotted here, the "increasing p_b" and "decreasing p_b" solution branches have nearly the same v-p_b relationship, namely $v \approx p_b$. Hence in each case, the data for the two branches (stable and unstable) almost overlay one another, so are only barely visible as separate branches in Figure 5.15(b).

This same behaviour (i.e. increasing and decreasing p_b branches nearly overlaying one another) was seen for the three-bubble system in cases (albeit not plotted here) in situations where it undergoes a saddle-node bifurcation. The present three-bubble system ($l_1^\circ = 0.5$, $l_2^\circ/l_1^\circ = 0.899$) however has no saddle-node bifurcation, but instead attains a $T1_c$ with p_b monotonically increasing. On the other hand for the three-bubble system, the major change that we see is that $v \approx p_b/2$ (instead of $v \approx p_b$ for the simple lens). The factor of $1/2$ follows as mentioned earlier because to traverse the three-bubble structure from left to right we must cross, at the very least, two films (i.e. $\jmath_{02}$ and $\jmath_{20}$ which are both attached to the lower channel wall). Another observation we make is that the three-bubble case

considered here survives out to a higher pressure, but almost the same velocity as the simple lens, regardless of whether we consider a simple lens of the same l_1° or of the same bubble area. This indicates that the particular three-bubble system considered here is at least of "comparable strength" to the simple lens, because even though the three-bubble system survives out to higher back pressures in total (which it manages to achieve merely through having more films that must be crossed from one end of the structure to the other), it still only survives out to comparable velocities (and hence comparable imposed pressure difference per film crossed). This is potentially significant because, as we add yet more bubbles and approach the limit of an infinite staircase, a structure that eventually exhibits topological transformation might only be stable out to a specified imposed pressure difference *per film*. On the other hand, three-bubble systems that reach an inherently stable configuration without topological transformation however (different choices of l_1° and l_2°/l_1° from those plotted here) survive of course out to arbitrarily large imposed pressure per film.

In summary, in the simple lens case, which consists of one bubble attached to a spanning film, the migration velocity approaches $v \approx p_b$, whereas in the three-bubble symmetric case, which consists of two bubbles of equal size plus a spanning bubble (hence two films attached to the lower channel wall), the migration velocity approaches $v \approx p_b/2$. By extension we can deduce that for N bubbles arranged in a staircase structure, the migration velocity should correspond to $v \approx 2p_b/(N+1)$. Nevertheless, we do not know definitively whether in the case when $N \gg 1$, the system always survives out to arbitrarily large p_b per film, effectively reaching arbitrary large velocities v also, or whether it breaks at more modest velocities. Results from the three-bubble system indicated that for certain parameter choices (i.e. certain choices of bubble areas) the structure survived out to arbitrarily large velocities, but other parameter choices only survived out to ve-

locities comparable to those achieved in the single lens. Finally note that velocity v is just one response variable out of several that we can analyse. Other response variables such as bubble pressures and total film energies can be examined, but that discussion is relegated to Appendix C sections C.5.1–C.5.2.

5.6 Conclusions

We have obtained steady state solutions for three-bubble staircase structures (two symmetric, equal area bubbles $\mathcal{B}_1$ and $\mathcal{B}_3$ adjoining one channel wall, and $\mathcal{B}_2$, possibly of different area, adjoining the other). The structure is specified in the equilibrium by a symmetric configuration, which is set by fixing l_1° and l_2°, that correspond to vertex distances from a channel wall with respect to the width of the transport channel. Here small values of l_1° represent small areas for bubbles $\mathcal{B}_1$ and $\mathcal{B}_3$, whereas large values of l_1° imply that bubbles $\mathcal{B}_1$ and $\mathcal{B}_3$ are larger. For values of l_2° exceedingly close to l_1° the size of bubble $\mathcal{B}_2$ is small relative that of bubbles $\mathcal{B}_1$ and $\mathcal{B}_3$. In contrast, for values of $l_2^\circ \ll l_1^\circ$ the size of bubble $\mathcal{B}_2$ tends to be larger than that of $\mathcal{B}_1$ and $\mathcal{B}_3$. For any given l_1°, a monodisperse scenario is found at some point in between these limiting cases for l_2°.

Moving to an out-of-equilibrium state, typically by imposing a driving back pressure on the system, we have determined the shape of the bubbles as these systems migrate through a straight channel, looking at a range of migration velocities from low (i.e. near equilibrium) to high (large deviations from equilibrium, possibly even to the point that the structure breaks up). It is clear that the staircase structure with three bubbles, exhibits more complex and richer dynamics than the simple lens problem [19]. By tracking the steady state solution, different types of topological transformations were found to cause break up of the structure. These were $T1_c$ (vertex-vertex collision), $T1_u$ (transformation at the upper

wall) and $T1_{l1}$ or $T1_{l3}$ (transformation at the lower wall). In the simple lens only the $T1_u$ could occur. More specifically, as the driving back pressure p_b is increased, possible outcomes are:

- A quasistatic $T1_c$ in which vertex V_1 (at the upstream end of the structure) and vertex V_2 (in the middle of the structure) come together and collide as the driving back pressure p_b is gradually increased. This happens for a wide range of l_1° but with comparatively large l_2°/l_1°, hence bubble $\mathcal{B}_2$ smaller than, or of comparable size to bubbles $\mathcal{B}_1$ and $\mathcal{B}_3$.

- A quasistatic $T1_u$ in which vertex V_3 (at the downstream end of the structure) moves to the upper channel wall. This happens again for a range of l_1° but with comparatively small l_2°/l_1°, hence bubble $\mathcal{B}_2$ is rather larger than $\mathcal{B}_1$ and $\mathcal{B}_3$.

- A quasistatic $T1_{l1}$ in which vertex V_1 moves to the lower channel wall. This happens for large l_1° and very small l_2°/l_1°, hence bubbles $\mathcal{B}_1$ and $\mathcal{B}_3$ are large, whilst $\mathcal{B}_2$ is even slightly larger.

- A quasistatic $T1_{l3}$ in which vertex V_3 moves to the lower channel wall. This happens for very large l_1° and a range of l_2°/l_1°, hence bubbles $\mathcal{B}_1$ and $\mathcal{B}_3$ are large, but bubble $\mathcal{B}_2$ could be smaller.

- A saddle-node bifurcation in which the aforementioned $T1_c$, $T1_u$, $T1_{l3}$ and/or $T1_{l1}$ would still occur, but they now occur dynamically rather than quasistatically. In a phase diagram of l_1° vs l_2°/l_1°, these tend to form "buffer" zones separating the various quasistatic $T1_c$, $T1_u$, $T1_{l1}$, $T1_{l3}$ and regions from one another.

- The system does not undergo any break up no matter how large the back pressure is (it reaches an inherently stable state). This tends to happen for

large l_1° and small to moderate l_2°/l_1°, hence areas of all bubbles $\mathcal{B}_1$, $\mathcal{B}_2$ and $\mathcal{B}_3$ tend to be large.

In spite of the different ways that the structure could break, the three-bubble system was found, at least in one particular case we studied, to be of comparable strength to the simple lens. It survived out to higher driving back pressures (which is expected because more films require higher pressure to move them) but it just reaches similar velocities, therefore comparable imposed driving pressure per film. There were exceptions to this however, particularly when one or more bubbles were small. The simple lens is known to be difficult to break in that case, but the three-bubble system breaks much more readily in that case, often via the $T1_c$ route which is not available to a simple lens. Cases when bubbles were particularly large (as opposed to small) admitted yet another behaviour, tending to an inherently stable state, a point which we return to shortly.

In some cases, the aforementioned topological transformations could be induced by tracking a single solution branch increasing imposed back pressure quasistatically (which physically implies a system could be held arbitrarily close to the transformation for an arbitrarily long time) but in other cases they required tracking two distinct solution branches (a situation that was ubiquitous for the simple lens [19]). These two distinct solution branches then meet at a saddle-node bifurcation, as referred to earlier, and were found by tracking solutions firstly by increasing the imposed back pressure, and subsequently by varying a film turning angle, when systems were parametrized in terms of orientation angles, or alternatively varying a particular film length, when systems were parametrized in terms of distances along films. These become the control variables for tracking the second steady state solution branch, whilst imposed back pressure takes the role of a response variable and actually starts to decrease as the new solution branch is tracked.

As obtained for the simple lens case, here we expect that the stable solution branch is the one obtained by using imposed back pressure as control variable. As we approach the back pressure corresponding to the end of that branch, all films retain finite lengths so a topological transformation has not yet occurred. Nonetheless no steady state solutions are permitted for any larger back pressure, so if a larger back pressure were to be imposed, the structure must evolve, presumably towards a topological transformation. As also occurred in the simple lens case, the evolution towards the transformation is expected now to be dynamic rather than quasistatic: the system can no longer be held arbitrarily close to the transformation for an indefinite period. Unsteady state simulation (rather than the steady state methodology used here) is then required to analyse this case.

Dealing with multiple solution branches and associated saddle-node bifurcations, was not the only computational challenge we faced. For a sufficiently high imposed back pressure (hence sufficiently high speed) and for sufficiently large bubbles, films become relatively flat. It is no longer possible to compute the film coordinates in terms of a film orientation angle, since many different points on the film turn through nearly the same angle. It is then expedient to change the system coordinates, and parametrize in terms of distance measured along films instead of film orientation angle. It is only through using that parametrization, that we identified cases (with large l_1° and small to moderate l_2°, i.e. with large bubbles, or more correctly large bubbles relative to channel size) that do not undergo any topological transformation whatsoever, even for an arbitrarily high imposed back pressure, suggesting (as alluded to earlier) the existence of an inherently stable state. In such cases, the three-bubble system can therefore propagate along the channel exceedingly quickly without breaking up. This is particularly relevant in a foam microfluidic system: if one wants to deliver a collection of bubbles (or

equivalently for emulsion microfluidics, a collection droplets) very quickly along a channel, then for a given bubble size, the channel width could be chosen as to ensure that the bubble size to channel size ratio is in the regime for which high velocities can be delivered.

As more bubbles are added to the system, we anticipate this inherently stable situation to become more common for a wider range of bubble sizes, since systems with many bubbles are expected to be able to attain arbitrarily high migration velocities (hence arbitrarily high imposed driving pressure per film), without undergoing any topological transformation. On the other hand, a structure propagating at high speed which does break up via topological transformation, might actually undergo multiple topological transformations, given that we have identified that various different types of transformation (e.g. $T1_c$, $T1_u$, $T1_{l1}$ and $T1_{l3}$ mentioned earlier) are now permitted. In order to determine how a system evolves after a first topological transformation and subsequently how a sequence of multiple transformations would occur, we must compute unsteady state simulations. This will be done in future work.

Chapter 6

Conclusions

The physics of liquid foams have been reviewed in this work, starting from basic concepts such as how foams are created, their geometry, and governing forces, up to a discussion of mathematical models used to predict how foams move and behave under different conditions. However, just a sample of existing models has been reviewed in depth here, particularly those related to the main works presented in chapters 3–5.

Liquid-foam applications have also been discussed, emphasizing processes in which foam flows within porous media, and/or within straight confined channels. Foam flow through porous media is generally studied via macroscale simulation, specifically by using interface motion models such as those, e.g. derived from Darcy's law or a special case thereof, the pressure-driven growth model, which is believed to model the surfactant alternating gas process of foam improved oil recovery reasonably well. Based on the predictions of this model (i.e. how foam fronts sweep through porous oil reservoirs), relevant information can be obtained and used to control and optimize real process operations in foam improved oil recovery processes. This is discussed in chapters 3 and 4. The pressure-driven growth model is based on an underlying fractional-flow theory, which consists of

a one-dimensional model used to determine foam mobility within porous media (and thereby the mobility of the two-dimensional foam front in pressure-driven growth) [64]. Other models to predict foam mobility are also presented and discussed in this thesis, particularly in Chapter 2.

In addition to describing how pressure-driven growth is obtained (in Chapter 2), relevant works available in the literature that apply the model have been analyzed, especially those related to the work presented in chapters 3 and 4, which corresponds to the novel contribution of this work to the literature, as summarised below.

The pressure-driven growth model captures the foam front in a two-dimensional space by a thin curve which represents the region in which a finely-textured foam is being generated, particularly where gas and surfactant solution meet [117]. In literature, this model has been used considering different conditions for the porous media, such as in anisotropic and heterogeneous systems, not just isotropic and homogeneous ones [80, 112]. Studies related with the former scenarios have been reviewed in detail, where the model's versatility has proven to capture, even in these complex scenarios, the various foam front shapes that can occur [112]. On the other hand, despite the apparent simplicity of the latter scenarios, they still exhibit the existence of complexity in the solutions, namely concave corner singularities occurring on the propagating front, as the model is solved either numerically or analytically [116]. When considering isotropic and homogeneous oil reservoirs, early-time Lagrangian numerical solutions for pressure-driven growth were unable to establish unequivocally whether the front was entirely convex [80], although later on, a first-order analytical similarity solution proved the existence of concave corners on the front [104], which was predicted to start at the top of the front and then move downwards at a constant speed. The presence of the concave

corner then was corroborated numerically via using Eulerian coordinates [116], although its location on the front was proved to move (unlike in the case of the analytical similarity solution) at different speeds, specifically with a decreasing downward speed over time (see Chapter 3). This corresponds to one of the main outcomes of this work. Further details can be consulted in Chapter 3. A better understanding of how this concave corner moves down along the propagating front was then achieved by obtaining second-order similarity analytical solution of the model [117]. This solution was achieved by perturbing the aforementioned first-order analytical similarity solution. Performing this perturbation was far from straightforward owing to the strong spatio-temporal non-uniformities that the similarity solution exhibited [117] and techniques needed to be developed that could deal with this. Additional details can be consulted in Chapter 4.

The pressure-driven growth model captures the propagation of a foam front, on the scale of the front as a whole, and does not resolve individual bubbles. However models to predict the foam flow through confined straight channels *on the bubble-scale*, particularly those developed to capture the foam dynamics in two dimensions were also reviewed (see Chapter 2 for details). In particular the viscous froth model was introduced, which can capture flowing foams out of equilibrium. Previous works related to this model were therefore discussed. Using this model a new case, as studied in detail in Chapter 5, was discussed. This corresponds to a three-bubble symmetric staircase structure, consisting of two bubbles stacked across the width of a channel and three bubbles total along its length, and symmetric in the sense that the first and last bubble cover equal area domains. Using the viscous froth model, steady state (but out of equilibrium) solutions were obtained, capturing the shape of the bubbles as the structure moves at different velocities. At high velocity, the structure was however found to be susceptible to breaking up via topological transformations. These could be realised in some

cases by gradual quasistatic increases in velocity, but in other cases it was suggested they could occur suddenly i.e. dynamically. In the latter case, two solution branches were also proven to exist, behaviour already seen in the simple lens system (consisting of just one bubble plus a spanning film) [19]. The two solution branches were shown to meet at a saddle-node bifurcation. It still remains uncertain which solution branch is the stable one (as that requires analysis of unsteady state solutions, not just steady state ones), although previous evidence from the simple lens case suggests that it corresponds to the branch that is obtained by quasisteadily perturbing the system from equilibrium [19]. Nonetheless, as mentioned, this can only be clarified by computing unsteady state simulations. Compared to the simple lens, the set of topological transformations observed for the three-bubble system was far more complex, with many different types of transformation occurring in different parts of parameter space. On the other hand, for a well specified domain of bubble areas, the three-bubble system can also reach an inherently stable structure (avoiding topological transformation), typical of an infinite staircase system (two bubbles across the channel width, and an arbitrary number along it) [144]. This structure can resist topological transformation even for arbitrarily large driving velocity. Thus the three-bubble system exhibits complex behaviour, sometimes akin to a simple lens, and at other times akin to an infinite staircase. Additional, detailed results are available to consult in Chapter 5.

Finally, the solutions and predictions obtained by using these models (pressure-driven growth and viscous froth model), can be used as a pre-assessment tool in real engineering processes (respectively porous media foam flows and microfluidic bubble flows in channels). The solutions/predictions allow to study the effect of changing certain key variables, like injection pressure, liquid saturation, capillary pressure, surfactant concentration, bubble texture, foam mobility and foam col-

lapse (which feed into pressure-driven growth and/or the fractional-flow theory that underlies it) as well as driving pressure, flow velocity, surface tension, viscous drag coefficient, bubble size, and geometry of the channels of transport (which feed into viscous froth), in an effort to improve the process performance. Knowing how these variables influence the system's behaviour is therefore a fundamental part in the development of new technologies, and procedures.

Chapter 7

Future work

The previous chapter considered the overall findings of the thesis both for the pressure-driven growth model and the viscous froth model. In the present chapter some open questions that can be tackled with these models are discussed.

One of the interesting questions to discuss is what happens to pressure-driven growth under a reduction in driving pressure, this situation being quite distinct from the pressure increase already considered by [115]. From [83], we know that under a pressure reduction, parts of the foam front higher up in a reservoir continue moving forwards and downwards, whereas other parts of the front beyond a certain depth start moving backwards and upwards, possibly with a different mobility from the forwards/downwards moving parts. We now also know what mobility to assign to those backward moving parts of the front within a pressure-driven growth model which was the main contribution of [83]. However, it still remains unclear what would happens if the concave corner, which as demonstrated in this work starts at the top and moves downward, as discussed in Chapter 4, starts interacting with any upward moving parts of the front. Yet another alternative scenario is that where the reduction in injection pressure happens only when the concave corner is already quite deep down on the front, so

after pressure reduction, what happens is that it also finds itself moving upwards and backwards. On those backwards moving parts of the front, the sense of what is concave and convex is switched, meaning the erstwhile concave corner is now a convex corner with concave shaped front either side of it. How the corner then propagates and interacts with the concave regions surrounding it is an open question. Indeed the concavities are at risk of shrinking down into corners themselves as is well established for pressure-driven growth [80].

Regarding the work on the viscous froth model, and the possibility of multiple solution branches in the studied three-bubble system (as described in Chapter 5), in order to determine which branch is the stable one, we need to do unsteady state simulations, as already alluded to earlier. This will also establish how the system would evolve after whichever topological transformation occurs first. On the other hand, since the three-bubble system behaves broadly similar to the simple lens [19] (i.e. tends to break up via topological transformation) in much of parameter space, but behaves like an infinite staircase [144] (i.e. resists break up) in a small part of parameter space, an interesting question concerns what happens as more and more bubbles are added. As we add more bubbles though (N-bubble problem), we expect additional complexity to arise, just as the three-bubble system admitted a more complex set of topological transformations than the simple lens did. Nonetheless, as the number of bubbles increases yet further, intuitively we also expect the system to behave like an infinite staircase (i.e. inherently stable with no topological transformation) over more and more of the parameter space, but this needs to be verified by steady and unsteady state simulations. There are implications for microfluidic foam systems in practice. As more bubbles are added to a structure, we might be able to drive systems faster and faster, without any break up of the structure occurring.

Appendix A

Supplementary material: Foam-liquid front in Eulerian coordinates

This appendix consists of the supplementary material of the work presented in Chapter 3: "Foam-liquid front propagation in Eulerian coordinates". Here the deduction of relevant equations used in Chapter 3 is presented (sections A.1–A.2) along with details of numerical schemes (section A.3).

A.1 Asymptotic analytic solution of Lagrangian model

In what follows the early-time analytic solution of the Lagrangian model presented in [70] is recalled. This solution reflects the fact that at the top, for any time ($t > 0$), front orientation angle $\alpha = 0$ and front displacement distance $s = x$ (x here being horizontal coordinate), and for any point on the front at vertical location y, for small times ($t \ll 1$), that $s \approx x$ and $\alpha \approx 0$. On the top, for

$t > 0$, the model (2.7) reduces, after integration, to $x = \sqrt{2t}$, and for any point on the front, for $t \ll 1$ to $x \approx \sqrt{2yt}$, termed the Velde solution by [104]. Using the property that $\sin(\alpha) \approx \mathrm{d}x/\mathrm{d}y$ (for $\mathrm{d}x/\mathrm{d}y \ll 1$) and differentiating $x \approx \sqrt{2yt}$ with respect to y gives $\sin(\alpha) \approx \sqrt{t/2y}$. Putting this in the equation (2.8) gives, after integration,

$$y \approx y_0 - \frac{t}{2}, \tag{A.1}$$

where y_0 is the initial position of a given material point. Equation (A.1) describes material points which originate anywhere below the top $y_0 \leq 1$ and move with a vertical velocity $-1/2$. A higher-order correction was also obtained by [104] still assuming $t \ll 1$

$$y \approx y_0 - \frac{t}{2} + \frac{5t^2}{48y_0}. \tag{A.2}$$

Equation (A.1)−(A.2) have implications for schemes for solving the Lagrangian model numerically (details of such schemes can be found in literature [80]). Owing to (A.1) and (A.2), a gap opens up between the point at the top of the front (which remains on the top boundary for all time) and material points slightly underneath it (those with $y_0 \to 1$) which necessarily drift downwards: in the Lagrangian model, new material points (hereafter called "newly injected points") must continually be injected from the top boundary to fill this gap. Upon leaving the top boundary their downwards velocity component starts off small, but grows over time to ensure that the gap is filled [104]. The gap between the top of the front and the material points that started off immediately below it meanwhile becomes wider and wider over time, such that over time, more and more of the front is comprised of newly injected points (see Figure A.1). Using equation (A.1) it is possible to improve upon the estimate that $x \approx \sqrt{2yt}$, specifically by obtaining the "improved Velde" solution discussed in [104] which established that

Appendix A. Supplementary material: Foam-liquid front in Eulerian coordinates

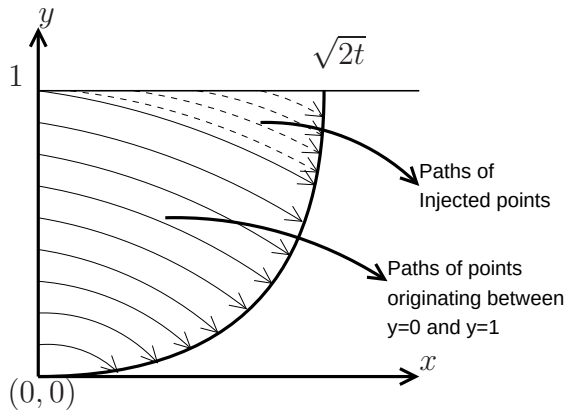

Figure A.1: Distinction between trajectories of points originally at $x = 0$ in $0 \leq y \leq 1$, and points injected at the top $y = 1$ for $x > 0$. In the Lagrangian formulation, to resolve the front shape near the top we need to add new material points to replace those originally on the front that have drifted downwards. However, it is not known a priori where exactly to add them, since the shape of the front itself is unknown.

$x \approx \sqrt{2yt + t^2/6}$. This equation is used in section 3.4 to compare the orientation angle and the curvature of the front in the, so-called, "lower region" of the front [104]. The lower region extends downwards from the position where the original front points and the injected front points meet, whereas the "upper region" extends from this point upwards. Since, using (2.6), $\alpha = \arctan(\mathrm{d}x/\mathrm{d}y)$, it is possible to derive a formula for the curvature in the lower region, the curvature being given by $\kappa = -(\mathrm{d}\alpha/\mathrm{d}y)\cos(\alpha)$ (see also equation (A.13)), so that

$$\alpha \approx \arctan\left(t(2yt + t^2/6)^{-1/2}\right), \tag{A.3}$$

$$\kappa \approx 6^{3/2}\sqrt{t}(12y + 7t)^{-3/2}. \tag{A.4}$$

For the upper region it is possible to obtain, using the similarity equation developed in [104], an analytical approximation of the front position (see Appendix A.2). However the resulting formulae for front orientation angle and curvature are less simple than in (A.3) and (A.4). Nonetheless, the angle and the curvature

can be estimated for both, the "lower" and "upper" region.

A.2 Front shape in the upper region

Using the similarity equations developed in [104] it is possible to obtain a parametric analytical expression for the upper region of the front in terms of $x = x(t, \Xi)$ and $y = y(t, \zeta)$, where Ξ and ζ are the rescaled form of x and y, respectively. Here we recall and extend the results of [104]. If we assume from [104] that

$$\Xi = (\sqrt{2t} - x)t^{-3/2} \equiv \xi t^{-3/2}, \tag{A.5}$$

$$\zeta = 2(1 - y)/t, \tag{A.6}$$

where $t \ll 1$, and also that the orientation angle can be expressed as $\alpha = \sqrt{t/2}\,\mathcal{A}(\zeta)$, then [104] demonstrates

$$\zeta \approx \frac{(1 - c\mathcal{A})^{1/c}}{(1 - c)} - \frac{(1 - c\mathcal{A})}{c(1 - c)} + \frac{1}{c}, \tag{A.7}$$

where, as discussed in Chapter 3 (see section 3.4.1), $2c - 1$ corresponds to the assumed constant ratio between $\mathrm{d}s/\mathrm{d}y$ and $\mathrm{d}x/\mathrm{d}y$ in the upper region [104]. For small times ($t \ll 1$) it is possible to obtain from [104] that

$$\xi \approx -\int_y^1 \left(\alpha + \frac{\alpha^3}{3}\right) \mathrm{d}y. \tag{A.8}$$

If we combine (A.5) and (A.8), using the derivative of (A.6) respect to y ($\mathrm{d}y/\mathrm{d}\zeta = -t/2$), and also with $\alpha = \sqrt{t/2}\,A$ we obtain

$$\Xi = \frac{\xi}{t^{3/2}} \approx -\frac{1}{t^{3/2}}\int_y^1 \left(\alpha + \frac{\alpha^3}{3}\right) \mathrm{d}y = \frac{1}{2\sqrt{2}}\int_0^{\mathcal{A}} \left(\mathcal{A} + \frac{t}{6}\mathcal{A}^3\right) \frac{\mathrm{d}\zeta}{\mathrm{d}\mathcal{A}}\,\mathrm{d}\mathcal{A}, \tag{A.9}$$

where $\mathrm{d}\zeta/\mathrm{d}\mathcal{A}$ can be obtained from (A.7). In order to compare the results obtained in [104] with the Eulerian data obtained here we need to use the same values of c as used in [104], i.e. $c = 1$ and $c = 0.75$. Equation (A.7) is plotted in Figure 3.6, and (A.7) and (A.9) taken together are plotted in Figure 3.5. For $c = 1$ we have via equation (A.7) that (taking the limit when $c \to 1$ of ζ)

$$\zeta = (1 - \mathcal{A}) \log(1 - \mathcal{A}) + \mathcal{A}, \tag{A.10}$$

then differentiating (A.10) respect to $\mathcal{A}$ we can compute, using equation (A.9), that

$$\Xi \approx -\frac{1}{2\sqrt{2}} \int_0^{\mathcal{A}} \log(1 - \mathcal{A}) \left(\mathcal{A} + \frac{t}{6} \mathcal{A}^3 \right) \mathrm{d}\mathcal{A}. \tag{A.11}$$

Now, combining equations (A.5) with (A.10) and (A.6) with (A.11), for each value of $\mathcal{A}$ we can obtain Ξ and ζ, and thus, x and y. The range of $\mathcal{A}$ values is easy to obtain owing to the fact that ζ is the rescaled version of y, i.e. when $\zeta = 1$, $y = 1 - t/2$ (cf. early-time solution (A.1)) and when $\zeta = 0$, $y = 1$. Thus α varies from 0 to $\sqrt{t/2}$ and $\mathcal{A}$ varies from $\mathcal{A} = 0$ ($\zeta = 0$) to $\mathcal{A} = 1$ ($\zeta = 1$) at least in this case $c = 1$ (one of the cases of interest in Figure 3.5).

The same procedure as used to obtain equation (A.11) can to be used in order to obtain the analytical expression for Ξ for values of $c < 1$. As a result we obtain

$$\Xi \approx -\frac{1}{2\sqrt{2}} \int_0^{\mathcal{A}} \left(\frac{(1 - c\mathcal{A})^{1/c} + c\mathcal{A} - 1}{(c - 1)(c\mathcal{A} - 1)} \right) \left(\mathcal{A} + \frac{t}{6} \mathcal{A}^3 \right) \mathrm{d}\mathcal{A}. \tag{A.12}$$

Then, combining equations (A.5) with (A.12) and (A.6) with (A.7), for each value of $\mathcal{A}$ we again obtain Ξ and ζ, and x and y. Here as explained in [104], $\mathcal{A}$ varies from $\mathcal{A} = 0$ to $\mathcal{A} = 1.18$.

Given an expression for α in the upper region (where recall, $\alpha = \sqrt{t/2}\,\mathcal{A}$) it is

possible to obtain an analytical formula for the front curvature using the equation (A.7), then with $\kappa = -\mathrm{d}\alpha/\mathrm{d}S$, where S is the length measured along the front, we obtain

$$\kappa = -\frac{\mathrm{d}\alpha}{\mathrm{d}y}\frac{\mathrm{d}y}{\mathrm{d}S} = -\frac{\mathrm{d}\alpha}{\mathrm{d}y}\cos(\alpha), \tag{A.13}$$

then substituting the similarity solution (A.7) into (A.13) we can deduce that

$$\kappa \approx \left(\frac{2}{t}\sqrt{\frac{t}{2}}\frac{1}{\mathrm{d}\zeta/\mathrm{d}\mathcal{A}}\right)\cos\left(\sqrt{\frac{t}{2}}\mathcal{A}\right) \approx -\left(\frac{\sqrt{2}(c-1)(c\mathcal{A}-1)}{((1-c\mathcal{A})^{1/c}+c\mathcal{A}-1)\sqrt{t}}\right)\left(1-\frac{t\mathcal{A}^2}{4}\right), \tag{A.14}$$

which was plotted in Figure 3.8.

A.3 Semidiscrete central-upwind scheme

Although it turns out that the central-upwind flux numerical scheme that is utilised here is not strictly required in this work (which deals with homogeneous and isotropic systems), it is presented here because this scheme is useful (and essential) in heterogeneous and/or anisotropic systems, which are of physical interest in improved oil recovery [114]. We start from [158]

$$\begin{aligned}\frac{\mathrm{d}}{\mathrm{d}t}\Phi_{j,k}(t) = \; & -\frac{a^-_{j,k}b^-_{j,k}\mathcal{H}^{++} - a^-_{j,k}b^+_{j,k}\mathcal{H}^{+-} - a^+_{j,k}b^-_{j,k}\mathcal{H}^{-+} + a^+_{j,k}b^+_{j,k}\mathcal{H}^{--}}{(a^+_{j,k}-a^-_{j,k})(b^+_{j,k}-b^-_{j,k})} \\ & -\frac{a^+_{j,k}a^-_{j,k}}{a^+_{j,k}-a^-_{j,k}}\Big(\Phi^+_x-\Phi^-_x\Big) - \frac{b^+_{j,k}b^-_{j,k}}{b^+_{j,k}-b^-_{j,k}}\Big(\Phi^+_y-\Phi^-_y\Big),\end{aligned} \tag{A.15}$$

and

$$\begin{aligned}\frac{\mathrm{d}}{\mathrm{d}t}s_{j,k}(t) = \; & -\frac{a^-_{j,k}b^-_{j,k}\mathcal{G}^{++} - a^-_{j,k}b^+_{j,k}\mathcal{G}^{+-} - a^+_{j,k}b^-_{j,k}\mathcal{G}^{-+} + a^+_{j,k}b^+_{j,k}\mathcal{G}^{--}}{(a^+_{j,k}-a^-_{j,k})(b^+_{j,k}-b^-_{j,k})} \\ & -\frac{a^+_{j,k}a^-_{j,k}}{a^+_{j,k}-a^-_{j,k}}\Big(s^+_x-s^-_x\Big) - \frac{b^+_{j,k}b^-_{j,k}}{b^+_{j,k}-b^-_{j,k}}\Big(s^+_y-s^-_y\Big),\end{aligned} \tag{A.16}$$

where $\mathcal{H}^{\triangle\square} := \mathcal{H}(y, s, \Phi_x^{\triangle}, \Phi_y^{\square})$ and $\mathcal{G}^{\triangle\square} := \mathcal{G}(y, s, \Phi_x^{\triangle}, \Phi_y^{\square}, s_x^{\triangle}, s_y^{\square})$ for $\triangle, \square \in \{-, +\}$ (see equation (3.10) and (3.11)). The local propagation velocities $a_{j,k}^{\pm}$ and $b_{j,k}^{\pm}$ are estimated as

$$a_{j,k}^{+} := \max_{\pm}(\mathcal{H}_{\Phi_x}(y, s, \Phi_x^{\pm}, \Phi_y^{\pm}))_+, \qquad a_{j,k}^{-} := \min_{\pm}(\mathcal{H}_{\Phi_x}(y, s, \Phi_x^{\pm}, \Phi_y^{\pm}))_- \tag{A.17}$$

$$b_{j,k}^{+} := \max_{\pm}(\mathcal{H}_{\Phi_y}(y, s, \Phi_x^{\pm}, \Phi_y^{\pm}))_+, \qquad b_{j,k}^{-} := \min_{\pm}(\mathcal{H}_{\Phi_y}(y, s, \Phi_x^{\pm}, \Phi_y^{\pm}))_- \tag{A.18}$$

where $(\cdot)_+ := \max(\cdot, 0)$ and $(\cdot)_- := \min(\cdot, 0)$. The values of $\Phi_x^{\pm}$ are calculated (for any fixed y) using the following interpolating polynomial

$$\tilde{\Phi}(x, t^n) = \Phi_j^n + \frac{(\triangle\Phi)_{j+\frac{1}{2}}^n}{\triangle x}(x - x_j) + \frac{(\triangle\Phi)'_{j+\frac{1}{2}}}{2(\triangle x)^2}(x - x_j)(x - x_{j+1}), \quad x \in [x_j, x_{j+1}], \tag{A.19}$$

where $(\triangle\Phi)_{j+\frac{1}{2}}^n \equiv \Phi_j^n - \Phi_{j+\frac{1}{2}}^n$, $\Phi_{j+\frac{1}{2}}^n = (\Phi_j^n + \Phi_{j+1}^n)/2$ and $(\triangle\Phi)'_{j+\frac{1}{2}}/(\triangle x)^2$ is an approximation of the second derivative of $\Phi_{xx}(x_{j+\frac{1}{2}}, t^n)$. To estimate $(\triangle\Phi)'_{j+\frac{1}{2}}$ we use the minmod limiters

$$(\triangle\Phi)'_{j+\frac{1}{2}} = \text{minmod}\Big(\theta\big[(\triangle\Phi)_{j+\frac{3}{2}}^n - (\triangle\Phi)_{j+\frac{1}{2}}^n\big], \frac{1}{2}\big[(\triangle\Phi)_{j+\frac{3}{2}}^n - (\triangle\Phi)_{j-\frac{1}{2}}^n\big], \theta\big[(\triangle\Phi)_{j+\frac{1}{2}}^n - (\triangle\Phi)_{j-\frac{1}{2}}^n\big]\Big),$$

where $\theta \in [1, 2]$ is a weighting factor, and the multivariable minmod function (for arbitrary arguments w_1, w_2,...) is defined as

$$\text{minmod}(w_1, w_2, ...) = \begin{cases} \min_j\{w_j\} & \text{if } \ w_j > 0 \ \ \forall\ j, \\ \max_j\{w_j\} & \text{if } \ w_j < 0 \ \ \forall\ j, \\ 0 & \text{otherwise.} \end{cases} \tag{A.20}$$

Appendix A. Supplementary material: Foam-liquid front in Eulerian coordinates

In this work a value of $\theta = 1.5$ is used for the minmod weighting factor [158]. Finally from (A.19) one obtains

$$\Phi_x^- = \frac{(\triangle\Phi)^n_{j-\frac{1}{2}}}{\triangle x} \mp \frac{(\triangle\Phi)'_{j-\frac{1}{2}}}{2 \triangle x}.$$

The expressions s_x^- and s_y^+ are obtained in a similar way. For the equations (A.17) and (A.18) we have from the definition of H in equation (3.10) that

$$\mathcal{H}_{\Phi_x} = \frac{y}{s} \frac{\Phi_x}{|\nabla\Phi|}, \qquad \mathcal{H}_{\Phi_y} = \frac{y}{s} \frac{\Phi_y}{|\nabla\Phi|}. \tag{A.21}$$

Moreover, it is easy to show that $(\partial/\partial\Phi_x)\mathcal{H} = (\partial/\partial s_x)\mathcal{G}$ and $(\partial/\partial\Phi_y)\mathcal{H} = (\partial/\partial s_y)\mathcal{G}$, i.e. $\mathcal{H}_{\Phi_x} = \mathcal{G}_{s_x}$ and $\mathcal{H}_{\Phi_y} = \mathcal{G}_{s_y}$, where $\mathcal{H}_{\Phi_x}, \mathcal{H}_{\Phi_y}, \mathcal{G}_{s_x}, \mathcal{G}_{s_y}$ denote partial derivatives (of $\mathcal{H}$ respectively $\mathcal{G}$) with respect to Φ_x, Φ_y, s_x, s_y, respectively. This means that for both equations (3.8) and (3.9), the propagation velocities of the corresponding variable (Φ and s) are the same. For the specific curve shape as indicated in Figure 3.1 we expect $\Phi_x > 0$ and $\Phi_y < 0$, which implies that $\mathcal{H}_{\Phi_x} \geq 0$ and $\mathcal{H}_{\Phi_y} \leq 0$. This indicates that the numerical flux is entirely upwind, since the speeds $a^+_{j,k} = 0$ and $b^-_{j,k} = 0$ in (A.17) vanish. The upwind version of (A.15) and (A.16), where those terms disappear, is (see (3.14))

$$\frac{\mathrm{d}}{\mathrm{d}t}\Phi_{j,k}(t) = \mathcal{H}(y, s, \Phi_x^-, \Phi_y^+), \qquad \frac{\mathrm{d}}{\mathrm{d}t}s_{j,k}(t) = \mathcal{G}(y, s, \Phi_x^-, \Phi_y^+, s_x^-, s_y^+). \tag{A.22}$$

Appendix B

Supplementary material: Foam-liquid front propagation in Lagrangian coordinates

This appendix consists of the supplementary material of the work presented in Chapter 4: "Breakdown of similarity solutions: A perturbation approach for front propagation during foam-improved oil recovery". Here a detailed deduction of the main equations used in Chapter 4 is presented, in addition to further analysis and discussion about the studied phenomena.

Appendix B. Supplementary material: Foam-liquid front propagation in Lagrangian coordinates

Summary: This appendix begins by reviewing and analysing first-order early-time similarity solutions (sections B.1–B.2), specifically in the context of the upper region of a foam front that is propagating during foam improved oil recovery. These first-order solutions, applicable in the limit of early times, were obtained in prior work by [104], and the discussion given below expands upon that in Chapter 4 presented within sections 4.3–4.4. After that, the focus switches to second-order accurate solutions in time. We now consider both the lower (section B.3) and the upper (sections B.4–B.5) regions of a propagating foam front. The analysis for the lower region (section B.3) proves relatively straightforward. However, since strong spatio-temporal non-uniformities are present in the upper region of the front, obtaining second-order solutions there is challenging: the procedure is detailed in section B.4, feeding into the results of section B.5. The key results we deduce are given in sections B.3 and B.5, specifically by equation (B.13) (lower region), and by equations (B.28), (B.37) and (B.39) (upper region). In section B.6, we plot the difference between solutions in the upper and lower regions to identify where these regions match: this expands on the methodology outlined in section 4.5.4 of Chapter 4. Section B.7 gives expressions for front orientation angle, vertical coordinate and horizontal coordinate on time, specifically at the matching point between upper and lower regions: this supports the discussion of sections 4.6–4.7 in Chapter 4. In section B.8 we track material points in the lower region in an analogous fashion to the way we already track material points in the upper region: this corresponds to an alternative methodology also mentioned in section 4.5.4 with data presented in section 4.7. Finally, in section B.9 we obtain a set of equations used to extrapolate the second-order solution to a wider domain, beyond the domain where it was originally obtained: this supports the discussion of section 4.8 in Chapter 4.

Appendix B. Supplementary material: Foam-liquid front propagation in Lagrangian coordinates

B.1 Review of first-order similarity equations

As established in [104], the front upper region can be expressed in terms of a set of similarity variables. These variables as given in Chapter 4 are: $\mathcal{A}$ as the rescaled front orientation angle, ζ as the rescaled vertical front location, and Ξ as the rescaled horizontal front displacement. In [104] it was proven that it is possible to obtain a leading-order expression to define ζ as a function of $\mathcal{A}$, as

$$\mathrm{d}\zeta/\mathrm{d}\mathcal{A} = (1 - (1 - c\mathcal{A})^{1/c-1})/(1 - c), \tag{B.1}$$

which after integrating gives

$$\zeta = ((1 - c) - (1 - c\mathcal{A}) + c(1 - c\mathcal{A})^{1/c})/(c(1 - c)), \tag{B.2}$$

where $2c - 1$ is the constant invariant ratio between $\mathrm{d}s/\mathrm{d}y$ and $\mathrm{d}x/\mathrm{d}y$, over the upper region. As proven in [104], choosing $c = 3/4$ and hence $2c - 1 = 1/2$, gives a suitable approximation for it. In [104] it was demonstrated, via a far more complex integro-differential formulation of the system of equations, that the ratio between $\mathrm{d}s/\mathrm{d}y$ and $\mathrm{d}x/\mathrm{d}y$ in the upper region always lies between 0.5 and 0.51. Hence, treating it as invariant (with assumed value 0.5), despite being an ad hoc approximation, led to negligible error, and had the advantage of producing the simple analytical form, given by equation (B.2).

To determine the horizontal displacement of the upper region of the front, we need to obtain an approximation for Ξ. As in [104], we can take a first-order Taylor expansion of $\tan(\alpha)$ and insert it into equation (4.6) (given in Chapter 4),

in order to obtain for $y \geq 1-(t/2)\zeta_{\text{cross}}$, i.e. $\zeta \leq \zeta_{\text{cross}}$ (upper region), that

$$\Xi \approx \frac{1}{2\sqrt{2}}\int_0^{\zeta} \mathcal{A}\,\mathrm{d}\zeta = \frac{1}{2\sqrt{2}}\int_0^{\mathcal{A}} \mathcal{A}\frac{\mathrm{d}\zeta}{\mathrm{d}\mathcal{A}}\,\mathrm{d}\mathcal{A} = \frac{2(1+\mathcal{A})(1-c\mathcal{A})^{1/c}+\mathcal{A}^2(1+c)-2}{4\sqrt{2}(1-c^2)}, \tag{B.3}$$

where equations (4.4), (4.7), (4.13) (as given in Chapter 4) and (B.1) have been used.

Here we have introduced two similarity equations ((B.2) and (B.3)) to compute the upper region of the front in terms of a rescaled in time front orientation angle $\mathcal{A}$. Therefore, each point on the upper region of the front must have a well defined $\mathcal{A}$ value, which governs on its current ζ and Ξ location. These were the forms of the similarity equations originally obtained by [104]. In section 4.3 of Chapter 4 however we expressed these solutions in terms of an alternative, more convenient variable $\mathcal{T}$ (the fraction of total time that an injected material point has been on the front). The expressions in terms of $\mathcal{T}$ however are equivalent to those written in terms of $\mathcal{A}$.

B.2 Analysing first-order similarity solution

As in [104], we have computed the upper region of the front in terms of $\mathcal{T}$ via a first-order solution (see sections 4.3–4.4 in Chapter 4), up to $\mathcal{T}_{\text{cross}}$, where the matching point between the lower and upper region of the front is located. The lower region at first-order is given in section 4.2 in Chapter 4. At leading order we have obtained that $\mathcal{T}_{\text{cross}} \approx 0.9431$, with $\zeta_{\text{cross}} \approx 0.9397$, and $\Xi_{\text{cross}} \approx 0.2733$. Even on the basis of these first-order results, we can establish a number of useful concepts, which are highlighted below. We can determine for instance, out of all the material points currently on the front, a minimum injected time $t_{\text{inj(min)}}$, which corresponds to the time at which a material point that has reached the

concave corner was injected. This is explained in detail in section B.2.1. On the other hand, there is also a maximum survival time that a material point can remain on the upper region. This is explained in detail in section B.2.2. Then, in section B.2.3 we show how to rescale the vertical coordinated ζ as a function of $\mathcal{T}$, so as to be able to track more readily the location of different injected material points, as explained in section B.2.4. All of these concepts carry over to our second-order analysis so we make extensive use of them in Chapter 4 (see e.g. the results presented in section 4.7 in Chapter 4).

B.2.1 Minimum injected time $t_{\mathrm{inj(min)}}$ as a function of time t

Since $\mathcal{T}_{\mathrm{cross}} < 1$, it follows from equation (4.14) that the point injected at $t_{\mathrm{inj}} = 0$ has been already consumed or destroyed by the concave corner. This then implies that (for any given t) there is a minimum time ($t_{\mathrm{inj(min)}}$) at which a still surviving material point has been injected without yet having been destroyed by the kink, so we can establish that $t_{\mathrm{inj}} \in [t_{\mathrm{inj(min)}}, t]$ defines the full set of material points on the front. At any time t, there must be a material point in the upper region just beside the concave corner, which was injected at a time $t_{\mathrm{inj(min)}}$ significantly less than t, with

$$t_{\mathrm{inj(min)}} = (1 - \mathcal{T}_{\mathrm{cross}})\, t. \tag{B.4}$$

If $\mathcal{T}_{\mathrm{cross}}$ is found via the first-order matching point, we can estimate for any small time t that $t_{\mathrm{inj(min)}} \approx 0.0569\, t$, implying that the points injected before such time have already been consumed by the concave corner. This expression is perturbed when second-order corrections are included (equation (4.36) in Chapter 4).

B.2.2 Maximum survival time t_{max} as a function of time t_{inj}

We can also consider that each injected material point in the front, has a maximum survival time (t_{max} depending on t_{inj}), which is the estimated time that a

material point can survive before reaching the kink or matching point [104] i.e. before being consumed by the concave corner. Note that $t_{\max}(t_{\text{inj}})$ is the inverse of $t_{\text{inj(min)}}(t)$. Hence

$$t_{\max} = t_{\text{inj}}/(1 - \mathcal{T}_{\text{cross}}). \tag{B.5}$$

Note that for $\mathcal{T}_{\text{cross}} \approx 0.9431$ (the leading-order result), it follows $t_{\max} = 17.57 t_{\text{inj}}$. At second-order, equation (4.35) applies instead. By definition, for $t_{\text{inj}} = t_{\text{inj(min)}}$, we find $t_{\max} = t$. Hence, we can then determine that for any given t_{inj}, the domain of t values of interest will be $t_{\text{inj}} \leq t \leq t_{\max}$, and consequently $1 \leq t/t_{\text{inj}} \leq t_{\max}/t_{\text{inj}}$. This is the domain plotted in Figure 4.2(b) in Chapter 4.

B.2.3 Rescaled ζ_+ as a function of $\mathcal{T}$

Since vertical coordinate ζ has been computed for the upper region at leading order in equation (4.16) (as a function of $\mathcal{T}$ up to $\mathcal{T}_{\text{cross}}$), we can calculate at any time t, the position $\zeta(\mathcal{T})$ of the material points injected at different $t_{\text{inj}} \in [t_{\text{inj(min)}}, t]$. However, we can also follow the trajectory of a single material point within the upper region, by fixing t_{inj} and varying $\mathcal{T}$, which corresponds to tracking the point's position over time t. Hence, we define $\zeta_+ = (1-y)/(t_{\text{inj}}/2)$ as the rescaled vertical position of a material point. Here, ζ_+ is a direct measure of $1 - y$, since t_{inj} is fixed for each material point. By contrast, for $\zeta = (1 - y)/(t/2)$ the relationship is less straightforward since both $1 - y$ and t change following the material point. Now consider this material point injected at time t_{inj} which is currently (at some time t, and hence at some $\mathcal{T} = 1 - t_{\text{inj}}/t$) at a vertical location $\zeta_+(\mathcal{T}) \equiv \zeta(\mathcal{T})/(1-\mathcal{T})$. It is of interest to ask where is the location of the concave corner relative to this point. This is always at $\zeta = \zeta_{\text{cross}}$ (for a well defined value of ζ_{cross}, e.g. at leading order $\zeta_{\text{cross}} \approx 0.9397$), and hence at $\zeta_+ = \zeta_{\text{cross}}/(1 - \mathcal{T})$. This gives the instantaneous location of the cross-over point, even though the material point of interest has not yet reached it. Likewise, we can track the posi-

tion of a lower region material point originally (at $t = 0$) at the top of the front, by considering that this point follows a trajectory $\zeta = 1$, which follows from a first-order approximation to the lower region (see equation (4.3)), implying that at first-order $\zeta_+ \equiv 1/(1 - \mathcal{T})$. Thus, we have distinct formulae (plotted at leading order in Figure 4.2(b) in Chapter 4), respectively for a material point in the upper region, for the concave corner or kink, and for a material point in the lower region. Generalisations to these relations at second-order are possible, see e.g. equations (4.24), (B.45) and (B.68).

B.2.4 Using ζ_+ vs $\mathcal{T}$ to compare trajectories

Figure 4.2(b) in Chapter 4, which is a first-order approximation in the limit of arbitrary small t_{inj} and hence arbitrary small t with $t_{\text{inj}} \leq t \leq t_{\text{inj}}/(1 - \mathcal{T}_{\text{cross}})$, shows how a point originally at the top of the lower region $y_0 = 1$ moves downwards with a velocity of $-1/2$ (or equivalently retains $\zeta = 1$ for all time), which is represented in terms of ζ_+ as $1/(1-\mathcal{T})$ (dash-dotted line). Here we see that a gap is present even at $\mathcal{T} = \mathcal{T}_{\text{cross}}$, between this uppermost material point originally on the front, and the final position of the material point injected at t_{inj}, which coincides with the concave corner (specifically when $\mathcal{T} = \mathcal{T}_{\text{cross}}$). The existence of this gap implies that material points must have been extracted from the kink or concave corner to populate the lower region. This however, is a first-order theory, that must be perturbed at second-order. We know the second-order correction to the lower region's material points (equation (4.11)), and we have also mentioned that the point originally at the top of the front moves downwards (considering the second-order effect via equation (4.12)) slower than it would do for the leading-order term in equation (4.3). Nevertheless, this in itself does not tell us if the topmost point originally on the front moves upwards sufficiently (relative to its first-order location) so as to overtake the position of the concave corner. To address this question we need to have a second-order approximation

for the position of the concave corner. Only when that second approximation is available can we determine whether material points in the lower region initially extracted from the kink are subsequently consumed by it. However, given the corner is where the upper and lower regions match, we can only start to answer this question if we also have a second-order approximation to the upper region: this then is what Chapter 4 developed.

In summary, employing the first-order solution we were able to determine the matching point between the upper and the lower region of the front for $t \ll 1$ or equivalently $t_{\text{inj}} \ll 1$, by using similarity variables. We can also verify the existence of the concave corner at the matching point, which was proven by [104]. Since rescaled orientation angle $\mathcal{A}_{\text{cross}}$ in the upper region (see value $\mathcal{A}_{\text{cross},0}$ in Table 4.1) is greater than unity (which is the analogous amount that the lower region reorients near the top at small times), the front not only curves sharply in the upper region, but also undergoes an abrupt reorientation at a concave corner in order to meet the lower region. In the above, we also demonstrated that material points are extracted from the concave corner in order to populate the lower region (at least in the limit of small times), and that material points in the upper region are being destroyed at the matching point. However, even though we are studying an arbitrarily small interval of time $t_{\text{inj}} \leq t \leq t_{\text{inj}}/(1-\mathcal{T}_{\text{cross}}) = t_{\max}$, with $t_{\text{inj}} \ll 1$, the motion of material points (ζ_+ vs t/t_{inj}) in the upper region, as shown in Figure 4.2(b), is non-uniform over this interval. These strong non-uniformities in space and time make it challenging to perturb the upper region to higher-orders of accuracy (in contrast to the lower region in which all points move down uniformly with velocity $-1/2$ at leading order via equation (4.3)). In Chapter 4 (section 4.5 onwards) however, we tackle that challenge to determine how the upper region solution is perturbed as t increases, and thereby obtain a corresponding second-order solution for the location of the matching point, taking

proper account of the spatio-temporal non-uniformities that are present.

B.3 Correction to ξ at order $t^{5/2}$ for lower region front shape

Previous work [104], derived a so-called improved Velde solution for x vs y and t, in the lower region (equation (4.1) in Chapter 4), that was accurate through order $t^{3/2}$ in time. However, in the present work we have points in the upper region placed horizontally to order t accuracy in Ξ, hence order $t^{5/2}$ accuracy in ξ (since $\xi \equiv \Xi\, t^{3/2}$ with $x \equiv \sqrt{2t} - \xi$). We therefore need further improvement in the description of the lower region, to be consistent between both regions. Hence, what we seek for the lower region, is to incorporate an order $t^{5/2}$ correction to the horizontal x location, alongside an order t^2 correction to the vertical location y of the material points, the latter being already available as given by equation (4.11). This is achieved in what follows via an order t correction to the variable Ξ in the lower region. We start by considering the motion of a Lagrangian material point in the x direction, which is given by equation (2.7), as

$$\mathrm{d}x^2/\mathrm{d}t \approx 2\, y(y_0, t)\, \cos(\alpha)\, (x/s), \tag{B.6}$$

where α denotes the orientation angle of the front normal relative to the horizontal, s denotes the path length that a lower region material point has displaced, and y_0 denotes the initial vertical location of a material point in the lower region, which moves to a location $y(y_0, t)$ at time t. At early times near the top of the lower region, we can set $y_0 \equiv 1 - \mathfrak{z}_0$, where it turns out $\mathfrak{z}_0 \ll 1$ for the material points of interest. Here at early times, any value of $\mathfrak{z}_0$ of interest can be treated as a quantity of order t, since via equations (4.4) and (4.11), we can compute

Appendix B. Supplementary material: Foam-liquid front propagation in Lagrangian coordinates

$y \approx 1 - \mathfrak{z}_0 - t/2 + (5t^2)/48$, but also $\zeta \equiv (1-y)/(t/2)$, and hence

$$\mathfrak{z}_0 \approx (\zeta - 1)(t/2) + 5t^2/48. \tag{B.7}$$

Equation (B.7) implies that if we focus attention near the top of the lower region where $\zeta - 1$ is at most order unity, then $\mathfrak{z}_0$ values of interest are at most order t. Within equation (B.6), since α can be expressed geometrically as $\alpha = \mathrm{atan}(\mathrm{d}x/\mathrm{d}y)$, we can obtain via Taylor expansion that $\cos(\alpha) \approx 1 - (1/2)(\mathrm{d}x/\mathrm{d}y)^2 + (3/8)(\mathrm{d}x/\mathrm{d}y)^4$, where $(\mathrm{d}x/\mathrm{d}y)^2$ is computed using the improved Velde solution (given by equation (4.1)), but now written in terms of $\mathfrak{z}_0$ and t, i.e. by using

$$x \approx \sqrt{2t - 2\mathfrak{z}_0 t - 5t^2/6}, \tag{B.8}$$

in which y has been replaced by $y \approx 1 - \mathfrak{z}_0 - t/2$, via first-order approximation, which is given by equation (4.2). Consistent with the current order of expansion, $(\mathrm{d}x/\mathrm{d}y)^4$ is calculated using the Velde solution ($x \approx \sqrt{2yt}$). Then, we compute x/s by considering that $\mathrm{d}s/\mathrm{d}t = \sqrt{(\mathrm{d}x/\mathrm{d}t)^2 + (\mathrm{d}y/\mathrm{d}t)^2}$, which after Taylor expanding to terms of fourth power, gives

$$s \approx x + \frac{1}{2}\int_0^t \frac{(\mathrm{d}y/\mathrm{d}t')^2}{\mathrm{d}x/\mathrm{d}t'}\,\mathrm{d}t' - \frac{1}{8}\int_0^t \frac{(\mathrm{d}y/\mathrm{d}t')^4}{(\mathrm{d}x/\mathrm{d}t')^3}\,\mathrm{d}t', \tag{B.9}$$

with t' here being a dummy integration variable. Here $\mathrm{d}y/\mathrm{d}t'$ is calculated using equation (4.11), $\mathrm{d}x/\mathrm{d}t'$ uses equation (B.8), and $(\mathrm{d}x/\mathrm{d}t')^3$ uses the Velde solution. Hence, we can express equation (B.6), by Taylor expanding out to order t^2 terms (treating $\mathfrak{z}_0$ itself as being order t), as

$$\begin{aligned}\frac{\mathrm{d}x^2}{\mathrm{d}t} &\approx 2\left(1 - \mathfrak{z}_0 - \frac{t}{2} + \frac{5t^2}{48}\right)\left(1 - \frac{t}{4}\left(1 + \mathfrak{z}_0 + \frac{t}{24}\right)\right)\left(1 - \frac{t}{12}\left(1 + \mathfrak{z}_0 + \frac{t}{120}\right)\right) \\ &\approx 2 - 2\mathfrak{z}_0 - \frac{5t}{3} + \frac{101t^2}{180}.\end{aligned} \tag{B.10}$$

Next, integrating (B.10), retaining terms up to third power in time, we deduce

$$x \approx \sqrt{2t - 2\mathfrak{z}_0 t - 5t^2/6 + 101t^3/540}. \tag{B.11}$$

Then, and analogously to equation (4.8), we can obtain

$$\xi = \frac{2t - x^2}{\sqrt{2t} + x} \approx \frac{2\mathfrak{z}_0 t + 5t^2/6 - 101t^3/540}{\sqrt{2t} + \sqrt{2t - 2t\mathfrak{z}_0 - 5t^2/6}}. \tag{B.12}$$

Here, we do not need a high accuracy approximation to x in the denominator, so we have substituted from (B.8). Finally, Taylor expanding in t up to second-order, and introducing equation (B.7), we can compute $\Xi = \xi/t^{3/2}$ as defined by equation (4.7). The resulting equation we obtain is (see equation (4.22) in Chapter 4)

$$\Xi \approx \frac{1}{2\sqrt{2}}\left(\zeta - \frac{1}{6} + \frac{t}{8}\left(\zeta^2 - \frac{\zeta}{3} + \frac{107}{540}\right)\right), \tag{B.13}$$

which represents an improvement upon equation (4.9) including a correction term for small but finite t.

B.4 Order t correction to upper region rescaled variables $\mathcal{A}$, ζ and Ξ

To determine with second-order accuracy, the front orientation angle α, the vertical location y, and horizontal location x of points in the upper region, we need to compute (in terms of the parameter $\mathcal{T}$, i.e. the fraction of time a material point has been on the front) the functions $\mathcal{A}_1(\mathcal{T})$, $\zeta_1(\mathcal{T})$ and $\Xi_1(\mathcal{T})$, respectively. These are required to compute perturbations to rescaled angle $\mathcal{A}$, rescaled vertical coordinate ζ and rescaled horizontal coordinate ξ via equations (4.19)–(4.21) in Chapter 4. The key results we deduce here are equations (B.28), (B.37) and (B.39), which are used to compute $\mathcal{A}_1(\mathcal{T})$, $\zeta_1(\mathcal{T})$ and $\Xi_1(\mathcal{T})$, (see section B.5 to

follow). We compute these actual functional forms by fixing a parameter $c = 3/4$, as was established in section 4.3 in Chapter 4 and in section B.1 following the recommendation of [104]. Results are plotted in Figure B.1 (see section B.5). Note that $\mathcal{A}_1(\mathcal{T})$, $\zeta_1(\mathcal{T})$ and $\Xi_1(\mathcal{T})$ are all negative and become increasingly negative as $\mathcal{T}$ increases. It follows that for a given $\mathcal{T}$, equations (4.19)–(4.21) predict a front shape that reorients less and displaces less vertically and horizontally than the corresponding first-order prediction.

B.4.1 Correction at order t for upper region front reorientation angle $\mathcal{A}(\mathcal{T}, t)$

We start by considering that the variation of the angle α (front normal relative to the horizontal) with time t, of a Lagrangian film element can be quantified in terms of the variation in the normal velocity of the front along an element $\mathcal{S}$ (distance measured along the front itself), as follows

$$\left(\frac{\mathrm{d}\alpha}{\mathrm{d}t}\right)_L = -\frac{\mathrm{d}}{\mathrm{d}\mathcal{S}}\left(\frac{y}{s}\right), \tag{B.14}$$

where y/s is the material point speed given by equation (2.5), and where the subscript L reminds us that we are dealing with a Lagrangian material point. Here $\mathcal{S}$ is specifically distance along the front measured downward (see Figure 2.2 in Chapter 4); this is not to be confused with s which is the material point trajectory. We can differentiate equation (B.14) to obtain

$$\left(\frac{\mathrm{d}\alpha}{\mathrm{d}t}\right)_L = -\frac{1}{s}\frac{\mathrm{d}y}{\mathrm{d}\mathcal{S}} + \frac{y}{s^2}\frac{\mathrm{d}s}{\mathrm{d}y}\frac{\mathrm{d}y}{\mathrm{d}\mathcal{S}} = \frac{\cos(\alpha)}{s}\left(1 - \frac{y}{s}\frac{\mathrm{d}s}{\mathrm{d}y}\right), \tag{B.15}$$

where, $\cos(\alpha) = -\mathrm{d}y/\mathrm{d}\mathcal{S}$ (by geometric definition). We can express s in terms of x by assuming that, in the upper region, the ratio between $\mathrm{d}s/\mathrm{d}y$ and $\mathrm{d}x/\mathrm{d}y$ (these derivatives being measured along the front) can be assumed invariant and

equal to $2c-1$ (the reasons for making this assumption are discussed in section B.1 and justified in [104]). Therefore, imposing a condition (as in Chapter 4) that the leading edge of the front is at location $\sqrt{2t}$ with s and x being equal at that point, we can express (moving down from the leading edge)

$$s \approx \sqrt{2t} - (2c-1)(\sqrt{2t} - x) \approx \sqrt{2t} - (2c-1)\xi, \tag{B.16}$$

where ξ is the horizontal displacement of the front, from the leading edge $\sqrt{2t}$ to a point x on the front, as per equation (4.5). Replacing $\mathrm{d}s/\mathrm{d}y$ by $(2c-1)\mathrm{d}x/\mathrm{d}y$ (the assumed invariant ratio alluded to earlier), we obtain

$$\left(\frac{\mathrm{d}\alpha}{\mathrm{d}t}\right)_L \approx \frac{\cos(\alpha)}{\sqrt{2t} - (2c-1)(\sqrt{2t} - x)} \left(1 - \frac{(2c-1)\,y}{\sqrt{2t} - (2c-1)(\sqrt{2t} - x)} \frac{\mathrm{d}x}{\mathrm{d}y}\right). \tag{B.17}$$

Here, since $\mathrm{d}x/\mathrm{d}y = \tan(\alpha)$ (by geometry), we can approximate $\mathrm{d}x/\mathrm{d}y \approx \alpha + \alpha^3/3$ which is obtained via Taylor expansion in powers of α. We can also Taylor expand $\cos(\alpha)$ in powers of α, and thereby we deduce

$$\left(\frac{\mathrm{d}\alpha}{\mathrm{d}t}\right)_L \approx \frac{1 - \dfrac{\alpha^2}{2}}{\sqrt{2t} - (2c-1)(\sqrt{2t} - x)} \left(1 - \frac{(2c-1)\,y}{\sqrt{2t} - (2c-1)(\sqrt{2t} - x)} \left(\alpha + \frac{\alpha^3}{3}\right)\right). \tag{B.18}$$

Now, introducing $\xi = \sqrt{2t} - x$, along with similarity variables $\alpha = \sqrt{t/2}\,\mathcal{A}$, $\zeta = (1-y)/(t/2)$, and $\xi = t^{3/2}\Xi$, we can determine

$$\left(\frac{\mathrm{d}\alpha}{\mathrm{d}t}\right)_L \approx \frac{1}{\sqrt{2t}} \left(\frac{1 - \dfrac{t\mathcal{A}^2}{4}}{1 - \dfrac{(2c-1)}{\sqrt{2}} t\Xi} \left(1 - \frac{\mathcal{A}}{2}\left(\frac{(2c-1)\left(1 - \dfrac{t}{2}\zeta\right)}{1 - \dfrac{(2c-1)}{\sqrt{2}} t\Xi}\right)\right) \left(1 + \frac{t\mathcal{A}^2}{6}\right) \right). \tag{B.19}$$

We now assume $t \ll 1$, and Taylor expanding each factor in the parentheses in terms of small parameters, we end up with an expression that has a leading-order term plus an order t correction, plus higher-order terms that we neglect. We

obtain

$$\left(\frac{\mathrm{d}\alpha}{\mathrm{d}t}\right)_L \approx \frac{1}{\sqrt{2t}}\left(1-\frac{\mathcal{A}(2c-1)}{2}+t\left(-\frac{\mathcal{A}_0^2}{4}-\frac{\mathcal{A}_0^3(2c-1)}{12}+\frac{(2c-1)\mathcal{A}_0\zeta_0}{4}\right.\right.$$
$$\left.\left.+\left(\frac{2c-1}{\sqrt{2}}-\frac{\mathcal{A}_0(2c-1)^2}{2\sqrt{2}}\right)\Xi_0\right)\right), \tag{B.20}$$

where terms appearing on the right hand side at order t, such as the orientation angle $\mathcal{A}$, the front vertical location ζ and the front horizontal displacement Ξ, have been replaced by leading order expressions $\mathcal{A}_0(\mathcal{T})$, $\zeta_0(\mathcal{T})$ and $\Xi_0(\mathcal{T})$, given by equations (4.15), (4.16) and (4.17), respectively. Thus, we express (B.20) as

$$\left(\frac{\mathrm{d}\alpha}{\mathrm{d}t}\right)_L \approx \frac{1}{\sqrt{2t}}\left(1-\frac{\mathcal{A}(2c-1)}{2}+t\,\Omega(\mathcal{A}_0,\zeta_0,\Xi_0)\right), \tag{B.21}$$

where $\Omega(\mathcal{A}_0,\zeta_0,\Xi_0)$ corresponds to

$$\Omega(\mathcal{A}_0,\zeta_0,\Xi_0) = -\frac{\mathcal{A}_0^2}{4}-\frac{\mathcal{A}_0^3(2c-1)}{12}+\frac{(2c-1)\mathcal{A}_0\zeta_0}{4}+\left(\frac{2c-1}{\sqrt{2}}-\frac{\mathcal{A}_0(2c-1)^2}{2\sqrt{2}}\right)\Xi_0. \tag{B.22}$$

Since $\mathcal{A}_0$, ζ_0 and Ξ_0 are well defined functions of $\mathcal{T}$ (see equations (4.15)–(4.17) in the main text), we can express $\Omega \equiv \Omega(\mathcal{T})$. We can also compute $(\mathrm{d}\alpha/\mathrm{d}t)_L$ as a function of $\mathcal{A}$ and $\mathcal{T}$, by using the similarity equations (4.13) and (4.14). Then, we can express the left side hand of equation (B.21), using equation (4.19), as follows

$$\left(\frac{\mathrm{d}\alpha}{\mathrm{d}t}\right)_L \approx \frac{1}{2\sqrt{2t}}(\mathcal{A}_0+t\,\mathcal{A}_1)+\sqrt{\frac{t}{2}}\left(\left(\frac{\mathrm{d}\mathcal{A}_0}{\mathrm{d}\mathcal{T}}\right)\left(\frac{\mathrm{d}\mathcal{T}}{\mathrm{d}t}\right)_L+\mathcal{A}_1+t\left(\frac{\mathrm{d}\mathcal{A}_1}{\mathrm{d}\mathcal{T}}\right)\left(\frac{\mathrm{d}\mathcal{T}}{\mathrm{d}t}\right)_L\right), \tag{B.23}$$

where since $\mathcal{T} = (1-t_{\mathrm{inj}}/t)$ (which is given by equation (4.14)), we can determine

$$(\mathrm{d}\mathcal{T}/\mathrm{d}t)_L = (1-\mathcal{T})/t. \tag{B.24}$$

Combining equations (B.21) and (B.23), and matching terms at each order of t, we find

$$(1-\mathcal{T})(\mathrm{d}\mathcal{A}_0/\mathrm{d}\mathcal{T}) = 1 - c\mathcal{A}_0, \tag{B.25}$$

and

$$\mathcal{A}_1(1+c) + (1-\mathcal{T})(\mathrm{d}\mathcal{A}_1/\mathrm{d}\mathcal{T}) = \Omega(\mathcal{T}). \tag{B.26}$$

Hence, we can compute

$$\mathcal{A}_0 = (1-(1-\mathcal{T})^c)/c, \tag{B.27}$$

which corresponds to the leading-order front reorientation $\mathcal{A}_0$, obtained in equation (4.15). Moreover, applying the integrating factor $(1-\mathcal{T})^{-(1+c)}$ to equation (B.26), we deduce

$$\mathcal{A}_1 = (1-\mathcal{T})^{1+c}\int_0^{\mathcal{T}} \frac{\Omega(\mathcal{T}')}{(1-\mathcal{T}')^{2+c}}\,\mathrm{d}\mathcal{T}', \tag{B.28}$$

$\mathcal{T}'$ here being a dummy integration variable. Then, after substituting from equation (B.22) and integrating, we obtain an explicit expression for $\mathcal{A}_1 \equiv \mathcal{A}_1(\mathcal{T})$, which is plotted later on in Figure B.1(b) in section B.5. Hence we have obtained the order t correction, to compute the front orientation $\mathcal{A}$. This equation will be used in what follows, to determine the order t term contributing to the vertical location of the upper region's material points.

B.4.2 Correction at order t for upper region front vertical location $\zeta(\mathcal{T}, t)$

We start by considering the velocity of a Lagrangian material point in the y direction, given by equation (2.8) [104]. Then, Taylor expanding $\sin(\alpha)$ in terms

of the small angle α, and rewriting (2.8) we obtain

$$\left(\frac{\mathrm{d}y}{\mathrm{d}t}\right)_L \approx \frac{-(1-(1-y))\left(\alpha-\dfrac{\alpha^3}{6}\right)}{\sqrt{2t}-(\sqrt{2t}-s)} \approx -\frac{\alpha}{\sqrt{2t}}\left(1-(1-y)-\frac{\alpha^2}{6}+\frac{(2c-1)}{\sqrt{2t}}\xi\right), \tag{B.29}$$

where we have substituted equation (B.16) into (B.29), and Taylor expanded. Now introducing the similarity equations (4.4), (4.7) and (4.13), we can express $\alpha = \sqrt{t/2}\,\mathcal{A}$, $\zeta = (1-y)/(t/2)$, and $\xi = t^{3/2}\Xi$, respectively, in order to obtain

$$\zeta + t\left(\frac{\mathrm{d}\zeta}{\mathrm{d}t}\right)_L \approx \mathcal{A}\left(1 - t\frac{\zeta}{2} - t\frac{\mathcal{A}^2}{12} + t\frac{(2c-1)}{\sqrt{2}}\Xi\right), \tag{B.30}$$

where we can approximate the front orientation as $\mathcal{A} \approx \mathcal{A}_0 + t\mathcal{A}_1$, so we can compute

$$\zeta + t\left(\frac{\mathrm{d}\zeta}{\mathrm{d}t}\right)_L \approx \mathcal{A}_0 + t\mathcal{A}_1 - t\frac{\mathcal{A}_0\zeta_0}{2} - t\frac{\mathcal{A}_0^3}{12} + t\frac{(2c-1)}{\sqrt{2}}\mathcal{A}_0\Xi_0. \tag{B.31}$$

In going from equation (B.30) to (B.31), terms appearing on the right side hand at order t, such as the orientation angle $\mathcal{A}$, the front vertical location ζ and the front horizontal displacement Ξ, have been replaced by $\mathcal{A}_0(\mathcal{T})$, $\zeta_0(\mathcal{T})$ and $\Xi_0(\mathcal{T})$, given by equations (4.15), (4.16) and (4.17). Moreover, using equation (4.20), we compute the left hand side of equation (B.31) as follows

$$\zeta + t\,(\mathrm{d}\zeta/\mathrm{d}t)_L \approx \zeta_0 + t\,(\mathrm{d}\zeta_0/\mathrm{d}\mathcal{T})\,(\mathrm{d}\mathcal{T}/\mathrm{d}t)_L + 2t\,\zeta_1 + t^2\,(\mathrm{d}\zeta_1/\mathrm{d}\mathcal{T})\,(\mathrm{d}\mathcal{T}/\mathrm{d}t)_L\,, \tag{B.32}$$

where $(\mathrm{d}\mathcal{T}/\mathrm{d}t)_L$ is given by equation (B.24), in order to obtain

$$\zeta + t\,(\mathrm{d}\zeta/\mathrm{d}t)_L \approx \zeta_0 + (1-\mathcal{T})\,(\mathrm{d}\zeta_0/\mathrm{d}\mathcal{T}) + 2t\,\zeta_1 + t(1-\mathcal{T})\,(\mathrm{d}\zeta_1/\mathrm{d}\mathcal{T})\,. \tag{B.33}$$

Here, $\mathrm{d}\zeta_0/\mathrm{d}\mathcal{T}$ and $\mathrm{d}\zeta_1/\mathrm{d}\mathcal{T}$ are well defined, as ζ_0 and ζ_1 depend only on $\mathcal{T}$. Then, from combining equations (B.31) and(B.33), and matching terms at each order

t, we can deduce that

$$\zeta_0 + (1-\mathcal{T})\,(\mathrm{d}\zeta_0/\mathrm{d}\mathcal{T}) = \mathcal{A}_0, \tag{B.34}$$

and

$$2\zeta_1 + (1-\mathcal{T})\,(\mathrm{d}\zeta_1/\mathrm{d}\mathcal{T}) = \mathcal{A}_1 - \mathcal{A}_0\zeta_0/2 - \mathcal{A}_0^3/12 + (2c-1)\mathcal{A}_0\Xi_0/\sqrt{2}. \tag{B.35}$$

First, we integrate equation (B.34), to obtain

$$\zeta_0 = (1-\mathcal{T})\int_0^{\mathcal{T}} \frac{\mathcal{A}_0(\mathcal{T}')}{(1-\mathcal{T}')^2}\,\mathrm{d}\mathcal{T}' = \frac{1-c\mathcal{T}-(1-\mathcal{T})^c}{c(1-c)}, \tag{B.36}$$

which was obtained previously by equation (4.16). Then in equation (B.35), after applying the integrating factor $(1-\mathcal{T})^{-2}$, we obtain

$$\zeta_1(\mathcal{T}) \approx (1-\mathcal{T})^2 \int_0^{\mathcal{T}} \frac{1}{(1-\mathcal{T}')^3}\left(\mathcal{A}_1 - \frac{\mathcal{A}_0\zeta_0}{2} - \frac{\mathcal{A}_0^3}{12} + \frac{(2c-1)}{\sqrt{2}}\mathcal{A}_0\Xi_0\right)\mathrm{d}\mathcal{T}'. \tag{B.37}$$

Then, since $\mathcal{A}_0$, ζ_0, Ξ_0, and $\mathcal{A}_1$ depend solely on $\mathcal{T}$ (being given by equations (4.15), (4.16), (4.17) and (B.28), respectively), we obtain equation $\zeta_1 \equiv \zeta_1(\mathcal{T})$ which is plotted in Figure B.1 in section B.5.

B.4.3 Correction at order t for upper region front horizontal location $\Xi(\mathcal{T}, t)$

Having obtained an order t correction for $\mathcal{A}(\mathcal{T}, t)$ and $\zeta(\mathcal{T}, t)$, we now compute the order t correction for Ξ, in the form $\Xi(\mathcal{T}, t) \approx \Xi_0(\mathcal{T}) + t\,\Xi_1(\mathcal{T})$. We first combine equations (4.6) and (4.7), and then, Taylor expanding $\tan(\alpha)$, we can obtain $\Xi \approx t^{-3/2}\int_y^1 (\alpha + \alpha^3/3)\,\mathrm{d}y$, where via equation (4.4), we substitute $\mathrm{d}y = -(t/2)\,\mathrm{d}\zeta$ at any given time t, and introducing similarity variable $\alpha = \sqrt{t/2}\,\mathcal{A}$

given by equation (4.13), we deduce

$$\Xi \approx \frac{1}{2\sqrt{2}} \int_0^{\zeta} \left(\mathcal{A} + t\,\frac{\mathcal{A}^3}{6} \right) \mathrm{d}\zeta. \tag{B.38}$$

Then, introducing $\mathcal{A}(\mathcal{T}, t)$, which is given by equation (4.19), and using equation (4.20) to compute $\mathrm{d}\zeta \approx \mathrm{d}\zeta_0 + t\,\mathrm{d}\zeta_1$ (again at a given t), we express (B.38) in terms of $\mathcal{T}$, as

$$\Xi \approx \frac{1}{2\sqrt{2}} \int_0^{\mathcal{T}} \mathcal{A}_0 \frac{\mathrm{d}\zeta_0}{\mathrm{d}\mathcal{T}}\,\mathrm{d}\mathcal{T} + \frac{t}{2\sqrt{2}} \int_0^{\mathcal{T}} \left(\left(\mathcal{A}_1 + \frac{\mathcal{A}_0^3}{6} \right) \frac{\mathrm{d}\zeta_0}{\mathrm{d}\mathcal{T}} + \mathcal{A}_0 \frac{\mathrm{d}\zeta_1}{\mathrm{d}\mathcal{T}} \right) \mathrm{d}\mathcal{T}. \tag{B.39}$$

After integrating, we obtain $\Xi(\mathcal{T}, t) \approx \Xi_0(\mathcal{T}) + t\,\Xi_1(\mathcal{T})$, with $\Xi_1(\mathcal{T})$ as a well defined function in terms of $\mathcal{T}$, which is plotted in Figure B.1(b) along with $\mathcal{A}_1(\mathcal{T})$ and $\zeta_1(\mathcal{T})$. Note, as commented earlier, they are all negative.

B.5 Values of $\mathcal{A}_1(\mathcal{T})$, $\zeta_1(\mathcal{T})$, and $\Xi_1(\mathcal{T})$ for $c = 3/4$

Here we compute $\mathcal{A}_1(\mathcal{T})$, $\zeta_1(\mathcal{T})$, and $\Xi_1(\mathcal{T})$ from equations (B.28), (B.37) and (B.39), respectively, computed in section B.4. The equations are solved in terms of $\mathcal{T}$, for $c = 3/4$. As can be seen in Figure B.1, these variables become increasingly negative as $\mathcal{T}$ increases. This contrasts with the values of $\mathcal{A}_0$, ζ_0 and Ξ_0 obtained in [104], all of which are positive. In summary, the signs of $\mathcal{A}_1(\mathcal{T})$, $\zeta_1(\mathcal{T})$ and $\Xi_1(\mathcal{T})$ indicate via equations (4.19)–(4.21) that, if the front shape is examined for a given $\mathcal{T}$, the effect of having finite t is that film elements have rotated/reoriented less than the leading-order formulae suggest. Likewise film elements are higher up vertically (higher y) and have fallen less far behind the leading edge (they have smaller ξ hence larger x) than the leading-order formulae suggest.

Appendix B. Supplementary material: Foam-liquid front propagation in Lagrangian coordinates

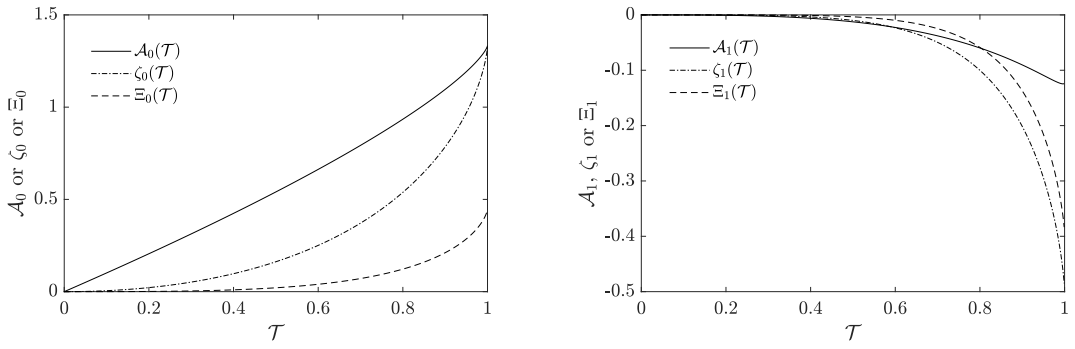

(a) (b)

Figure B.1: Functions appearing in first vs second-order solutions. (a) $\mathcal{A}_0$, ζ_0 and Ξ_0, computed by equations (4.15), (4.16) and (4.17) respectively, as given in Chapter 4. Similar plots can be found in [104]. (b) $\mathcal{A}_1(\mathcal{T})$, $\zeta_1(\mathcal{T})$ and $\Xi_1(\mathcal{T})$, computed from equations (B.28), (B.37) and (B.39), respectively.

B.6 Intersection between upper and lower region in terms of $\mathcal{T}$ for fixed t_{inj}

Here we clarify how the upper region given at second-order by equations (4.24) and (4.25), intersects with the lower region given also at second-order by equation (4.26) (all these equations having been given in Chapter 4). We require to find this intersection, in order to predict where the foam front has a concave corner for any given time t. We can track an injected material point in the upper region at different times t, by fixing an injection time t_{inj} and then varying $\mathcal{T} \equiv 1 - t_{\text{inj}}/t$ in equations (4.24)–(4.25) (upper region), and equation (4.26) (lower region). We then determine for which value of $\mathcal{T}$ both regions intersect. This is what we plot in Figure B.2 for two values of t_{inj}, i.e. $t_{\text{inj}} \to 0$ and $t_{\text{inj}} = 0.01$. By using these equations we found for a set of t values (obtained by varying $\mathcal{T}$ at fixed t_{inj}), a particular ζ_+ value given by equation (4.24) at each $\mathcal{T}$, with a corresponding Ξ_+ value given by either equation (4.25) or (4.26). When for a certain $\mathcal{T}$, the Ξ_+ value coincides in both regions, the intersection occurs (see Figure B.2). Therefore, for a given time t_{inj}, we compute $\zeta_+^{\text{upper}}(\mathcal{T})$ (via equation

Appendix B. Supplementary material: Foam-liquid front propagation in Lagrangian coordinates

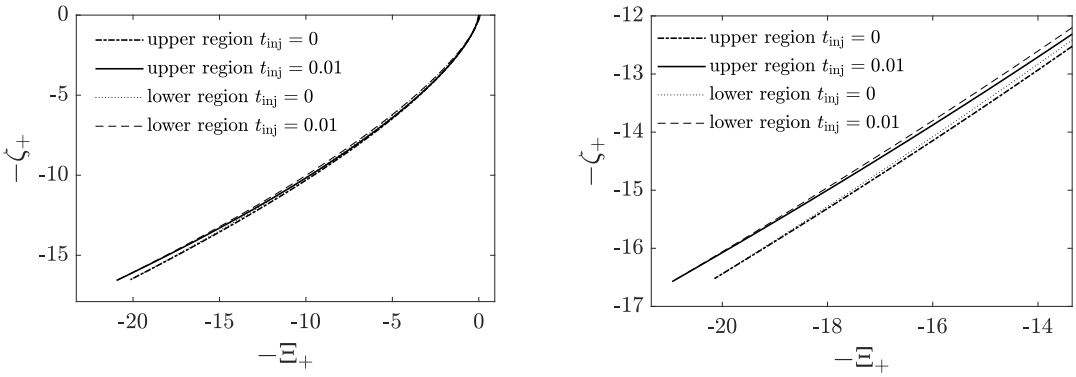

Figure B.2: (a) Determining the matching point between the lower and the upper region of the front for two values of t_{inj}. Here, $-\zeta_+$ and $-\Xi_+$ are the rescaled vertical y and horizontal x locations. (b) Inset zoomed view of (a) close to the cross over point.

(4.24)), and $\Xi_+^{\text{upper}}(\mathcal{T})$ (via equation (4.25)) in the upper region. Then, for the specified ζ_+^{upper}, we set $\zeta_+^{\text{lower}} = \zeta_+^{\text{upper}}$, and compute Ξ_+^{lower} via equation (4.26). For fixed time t_{inj}, we keep increasing $\mathcal{T}$ until the location of the upper region material point coincides with a material point in the lower region, so that $\Xi_+^{\text{upper}} = \Xi_+^{\text{lower}}$ (see also Figure B.3). For $t_{\text{inj}} \to 0$, we found that the matching point occurs at $\mathcal{T}_{\text{cross},0} \approx 0.9431$, with $\zeta_{+\text{cross},0} \approx 16.52$ and $\Xi_{+\text{cross},0} \approx 20.15$ (see the first-order solution in section 4.4 of Chapter 4). For $t_{\text{inj}} = 0.01$, we found that $\mathcal{T}_{\text{cross}} \approx 0.9458$, obtaining that $\zeta_+(\mathcal{T}_{\text{cross}}) \approx 16.57$ and $\Xi_+(\mathcal{T}_{\text{cross}}) \approx 20.95$. In Figure B.3 we see, for injected t_{inj}, that there are two values of $\mathcal{T}$ at which the upper and lower region intersect, the larger one being the correct value in each case. This verifies what is difficult to see on the scale of Figure B.2(a), i.e. that there are two intersections, with the intersection we require, giving specifically a concave corner, being the one that is lower down in Figure B.2(a), which corresponds here to the second intersection having the larger of the two $\mathcal{T}$ values. A zoomed view of the second intersection is shown in the inset of Figure B.3. We denote the intersection point by $\zeta_{+\text{cross}}$ and $\Xi_{+\text{cross}}$ and it has a corresponding y value $y_{\text{cross}}^{\text{inter}}$ as can be obtained

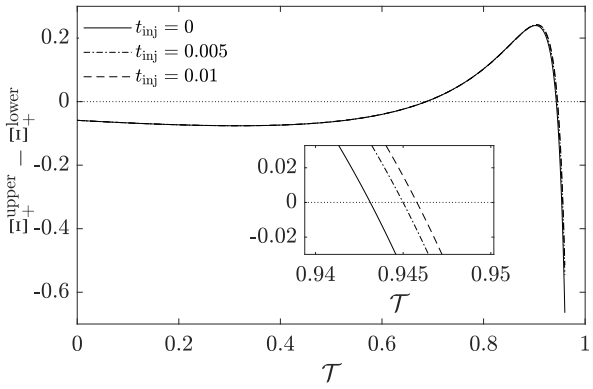

Figure B.3: Front rescaled horizontal displacement difference between upper and lower region $\Xi_+^{\rm upper} - \Xi_+^{\rm lower}$, as a function of $\mathcal{T}$.

via equation (4.33) in Chapter 4. Note that the $\mathcal{T}$ value corresponding to the intersection increases as $t_{\rm inj}$ increases (inset of Figure B.3), at least for $t_{\rm inj}$ up to 0.01.

B.7 Perturbed location of the concave corner at time t

In section 4.6 in Chapter 4 we demonstrated that the value of orientation angle $\mathcal{A}_+$ at the matching point, denoted $\mathcal{A}_{+\rm cross}$ could be expanded in the form of equation (4.32), as

$$\begin{aligned}\mathcal{A}_{+\rm cross} &\approx \mathcal{A}_{+,0}(\mathcal{T}_{\rm cross,0}) + t_{\rm inj}\left(\mathcal{T}_{\rm cross,1}\mathcal{A}'_{+,0}(\mathcal{T}_{\rm cross,0}) + \mathcal{A}_{+,1}(\mathcal{T}_{\rm cross,0})\right)\\ &\equiv \mathcal{A}_{+\rm cross,0} + t_{\rm inj}\mathcal{A}_{+\rm cross,1},\end{aligned} \tag{B.40}$$

where $\mathcal{A}'_{+,0}$ denotes the function $\mathrm{d}\mathcal{A}_{+,0}/\mathrm{d}\mathcal{T}$ (which is obtained via equations (4.15) and (4.23) as given in Chapter 4). Analogously, we can compute ζ_+ and Ξ_+ at the concave corner (denoted $\zeta_{+\rm cross}$ and $\Xi_{+\rm cross}$), via equations (4.24) and (4.25)

(also given in Chapter 4), as

$$\begin{aligned}\zeta_{+\text{cross}} &\approx \zeta_{+,0}(\mathcal{T}_{\text{cross},0}) + t_{\text{inj}}\left(\mathcal{T}_{\text{cross},1}\zeta'_{+,0}(\mathcal{T}_{\text{cross},0}) + \zeta_{+,1}(\mathcal{T}_{\text{cross},0})\right)\\ &\equiv \zeta_{+\text{cross},0} + t_{\text{inj}}\zeta_{+\text{cross},1}, \qquad \text{(B.41)}\\ \Xi_{+\text{cross}} &\approx \Xi_{+,0}(\mathcal{T}_{\text{cross},0}) + t_{\text{inj}}\left(\mathcal{T}_{\text{cross},1}\Xi'_{+,0}(\mathcal{T}_{\text{cross},0}) + \Xi_{+,1}(\mathcal{T}_{\text{cross},0})\right)\\ &\equiv \Xi_{+\text{cross},0} + t_{\text{inj}}\Xi_{+\text{cross},1}, \qquad \text{(B.42)}\end{aligned}$$

where $\zeta'_{+,0}$ and $\Xi'_{+,0}$, denote the functions $\mathrm{d}\zeta_{+,0}/\mathrm{d}\mathcal{T}$ and $\mathrm{d}\Xi_{+,0}/\mathrm{d}\mathcal{T}$, respectively (obtained via equations (4.16), (4.17), (4.24) and (4.25), as given in Chapter 4). We can also obtain analogous expressions in terms of t instead of t_{inj}. Via equation (4.19) (given in Chapter 4), the value $\mathcal{A}$ at the corner (denoted $\mathcal{A}_{\text{cross}}$), is given by (using also equation (4.28), as given in Chapter 4)

$$\mathcal{A}_{\text{cross}} \approx \mathcal{A}_0(\mathcal{T}_{\text{cross},0} + t\,(1-\mathcal{T}_{\text{cross},0})\mathcal{T}_{\text{cross},1}) + t\,\mathcal{A}_1(\mathcal{T}_{\text{cross},0} + t\,(1-\mathcal{T}_{\text{cross},0})\mathcal{T}_{\text{cross},1}) \qquad \text{(B.43)}$$

which upon expanding gives

$$\begin{aligned}\mathcal{A}_{\text{cross}} &\approx \mathcal{A}_0(\mathcal{T}_{\text{cross},0}) + t\,((1-\mathcal{T}_{\text{cross},0})\mathcal{T}_{\text{cross},1}\mathcal{A}'_0(\mathcal{T}_{\text{cross},0}) + \mathcal{A}_1(\mathcal{T}_{\text{cross},0}))\\ &\equiv \mathcal{A}_{\text{cross},0} + t\,\mathcal{A}_{\text{cross},1}, \qquad \text{(B.44)}\end{aligned}$$

where $\mathcal{A}'_0$ denotes the function $\mathrm{d}\mathcal{A}_0/\mathrm{d}\mathcal{T}$ (obtained via equation (4.15)). Analogously, we can compute $\zeta \equiv \zeta_{\text{cross}}$ and $\Xi \equiv \Xi_{\text{cross}}$, via equations (4.20) and (4.21) (given in Chapter 4), as

$$\begin{aligned}\zeta_{\text{cross}} &\approx \zeta_0(\mathcal{T}_{\text{cross},0}) + t\,((1-\mathcal{T}_{\text{cross},0})\mathcal{T}_{\text{cross},1}\zeta'_0(\mathcal{T}_{\text{cross},0}) + \zeta_1(\mathcal{T}_{\text{cross},0}))\\ &\equiv \zeta_{\text{cross},0} + t\,\zeta_{\text{cross},1}, \qquad \text{(B.45)}\\ \Xi_{\text{cross}} &\approx \Xi_0(\mathcal{T}_{\text{cross},0}) + t\,((1-\mathcal{T}_{\text{cross},0})\Xi_{\text{cross},1}\Xi'_0(\mathcal{T}_{\text{cross},0}) + \Xi_1(\mathcal{T}_{\text{cross},0}))\\ &\equiv \Xi_{\text{cross},0} + t\,\Xi_{\text{cross},1}, \qquad \text{(B.46)}\end{aligned}$$

where ζ_0' and Ξ_0', denote the functions $\mathrm{d}\zeta_0/\mathrm{d}\mathcal{T}$ and $\mathrm{d}\Xi_0/\mathrm{d}\mathcal{T}$, respectively (obtained via equations (4.16) and (4.17)). Predictions that arise from equations (B.40)–(B.42) and (B.44)–(B.46) are presented in section 4.7 of Chapter 4.

A comparison between equations (B.40)–(B.42) and (B.44)–(B.46) can be made using equations (4.23)–(4.25) to identify the relationships between $\mathcal{A}_{+,0}$, $\zeta_{+,0}$, $\Xi_{+,0}$, $\mathcal{A}_{+,1}$, $\zeta_{+,1}$ and $\Xi_{+,1}$, and $\mathcal{A}_0$, ζ_0, Ξ_0, $\mathcal{A}_1$, ζ_1 and Ξ_1, noting also via (4.23)–(4.25) that

$$\mathcal{A}'_{+,0} = \frac{\mathcal{A}'_0}{(1-\mathcal{T})^{1/2}} + \frac{\mathcal{A}_0}{2(1-\mathcal{T})^{3/2}}, \tag{B.47}$$

$$\zeta'_{+,0} = \frac{\zeta'_0}{(1-\mathcal{T})} + \frac{\zeta_0}{(1-\mathcal{T})^2}, \tag{B.48}$$

$$\Xi'_{+,0} = \frac{\Xi'_0}{(1-\mathcal{T})^{3/2}} + \frac{3\Xi_0}{2(1-\mathcal{T})^{5/2}}. \tag{B.49}$$

Equations (B.40)–(B.42) now become

$$\begin{aligned}\mathcal{A}_{+\mathrm{cross}} \approx\ & \frac{\mathcal{A}_0(\mathcal{T}_{\mathrm{cross},0})}{(1-\mathcal{T}_{\mathrm{cross},0})^{1/2}} \\ & + t_{\mathrm{inj}}\left(\mathcal{T}_{\mathrm{cross},1}\left(\frac{\mathcal{A}'_0(\mathcal{T}_{\mathrm{cross},0})}{(1-\mathcal{T}_{\mathrm{cross},0})^{1/2}} + \frac{\mathcal{A}_0(\mathcal{T}_{\mathrm{cross},0})}{2(1-\mathcal{T}_{\mathrm{cross},0})^{3/2}}\right) + \frac{\mathcal{A}_1(\mathcal{T}_{\mathrm{cross},0})}{(1-\mathcal{T}_{\mathrm{cross},0})^{3/2}}\right),\end{aligned} \tag{B.50}$$

$$\begin{aligned}\zeta_{+\mathrm{cross}} \approx\ & \frac{\zeta_0(\mathcal{T}_{\mathrm{cross},0})}{(1-\mathcal{T}_{\mathrm{cross},0})} \\ & + t_{\mathrm{inj}}\left(\mathcal{T}_{\mathrm{cross},1}\left(\frac{\zeta'_0(\mathcal{T}_{\mathrm{cross},0})}{(1-\mathcal{T}_{\mathrm{cross},0})} + \frac{\zeta_0(\mathcal{T}_{\mathrm{cross},0})}{(1-\mathcal{T}_{\mathrm{cross},0})^2}\right) + \frac{\zeta_1(\mathcal{T}_{\mathrm{cross},0})}{(1-\mathcal{T}_{\mathrm{cross},0})^2}\right),\end{aligned} \tag{B.51}$$

$$\begin{aligned}\Xi_{+\mathrm{cross}} \approx\ & \frac{\Xi_0(\mathcal{T}_{\mathrm{cross},0})}{(1-\mathcal{T}_{\mathrm{cross},0})^{3/2}} \\ & + t_{\mathrm{inj}}\left(\mathcal{T}_{\mathrm{cross},1}\left(\frac{\Xi'_0(\mathcal{T}_{\mathrm{cross},0})}{(1-\mathcal{T}_{\mathrm{cross},0})^{3/2}} + \frac{3\Xi_0(\mathcal{T}_{\mathrm{cross},0})}{2(1-\mathcal{T}_{\mathrm{cross},0})^{5/2}}\right) + \frac{\Xi_1(\mathcal{T}_{\mathrm{cross},0})}{(1-\mathcal{T}_{\mathrm{cross},0})^{3/2}}\right),\end{aligned} \tag{B.52}$$

which are written in a form that can be readily contrasted with equations (B.44)–(B.46), with the various functions needed to evaluate all of these being specified in equations (4.15)–(4.17) and ((B.28), (B.37) and (B.39)). The following rela-

tionships can now be derived (replacing terms in (B.47)–(B.49) by counterparts from equations (B.44)–(B.46))

$$\mathcal{A}_{+\mathrm{cross},0} = \mathcal{A}_{\mathrm{cross},0}/(1-\mathcal{T}_{\mathrm{cross},0})^{1/2}, \tag{B.53}$$

$$\zeta_{+\mathrm{cross},0} = \zeta_{\mathrm{cross},0}/(1-\mathcal{T}_{\mathrm{cross},0}), \tag{B.54}$$

$$\Xi_{+\mathrm{cross},0} = \Xi_{\mathrm{cross},0}/(1-\mathcal{T}_{\mathrm{cross},0})^{3/2}, \tag{B.55}$$

$$\mathcal{A}_{+\mathrm{cross},1} = \frac{\mathcal{A}_{\mathrm{cross},1}}{(1-\mathcal{T}_{\mathrm{cross},0})^{3/2}} + \mathcal{T}_{\mathrm{cross},1}\frac{\mathcal{A}_{\mathrm{cross},0}}{2(1-\mathcal{T}_{\mathrm{cross},0})^{3/2}}, \tag{B.56}$$

$$\zeta_{+\mathrm{cross},1} = \frac{\zeta_{\mathrm{cross},1}}{(1-\mathcal{T}_{\mathrm{cross},0})^{2}} + \mathcal{T}_{\mathrm{cross},1}\frac{\zeta_{\mathrm{cross},0}}{(1-\mathcal{T}_{\mathrm{cross},0})^{2}}, \tag{B.57}$$

$$\Xi_{+\mathrm{cross},1} = \frac{\Xi_{\mathrm{cross},1}}{(1-\mathcal{T}_{\mathrm{cross},0})^{5/2}} + \mathcal{T}_{\mathrm{cross},1}\frac{3\Xi_{\mathrm{cross},0}}{2(1-\mathcal{T}_{\mathrm{cross},0})^{5/2}}. \tag{B.58}$$

Consulting Table 4.1 in Chapter 4, the terms $\mathcal{A}_{+\mathrm{cross},1}$, $\zeta_{+\mathrm{cross},1}$, $\Xi_{+\mathrm{cross},1}$ turn out to have opposite sign from $\mathcal{A}_{\mathrm{cross},1}$, $\zeta_{\mathrm{cross},1}$, $\Xi_{\mathrm{cross},1}$. It is clear from equations (B.56)–(B.58) that any sign changes must originate from the second term on each right hand side. In each expression, the origin of this second term is due $\mathcal{T}_{\mathrm{cross}}$ increasing (by an amount $t_{\mathrm{inj}}\mathcal{T}_{\mathrm{cross},1}$) to a value greater than $\mathcal{T}_{\mathrm{cross},0}$ coupled to the tendency of $\mathcal{A}_{+,0}$, $\zeta_{+,0}$ and $\Xi_{+,0}$ to increase with increasing $\mathcal{T}$ even without accounting for increases in $\mathcal{A}_0$, ζ_0, Ξ_0 (due to the second term on the right hand side of equations (B.47)–(B.49)).

B.8 Tracking lower region material points to achieve matching

In Chapter 4 and also in section B.6 above, we used a procedure of second-order accuracy in time to track the trajectory of an injected material point (injected at time t_{inj}) through the upper region in terms of ζ_+ and Ξ_+, as the rescaled y and x location. We followed its location over time until it coincided with the current location of a material point in the lower region, thereby allowing us to

estimate the location of the concave corner. Once we know when and where the two regions coincide, we can figure out which material point in the lower region meets up with any given material point in the upper region. Then it is possible to track the trajectory of a lower region material point up to the matching point with the upper region material point labelled by t_{inj}: this is what Figure 4.3 in Chapter 4 achieves. In what follows we identify material points in the lower region by their original location on the front y_0 on the front at time $t = 0$, and we explain how to find a relation between the lower region y_0 and the upper region t_{inj}, this relation then being used to produce the trajectories in Figure 4.3.

B.8.1 Identifying the value of $\mathfrak{z}_0$

As we are interested in early-time solutions, and hence small values of t_{inj} and t, we expect that the material points of interest will be comparatively close to the top of the solution domain, hence y_0 values are expected to be close to unity. Accordingly (and in line with section B.3) we define $\mathfrak{z}_0 = 1 - y_0$ as the vertical distance (measured down from the top of the solution domain) of a material point at its original location at time $t = 0$. We anticipate that $\mathfrak{z}_0$ will be rather smaller than unity. In principle we can consider not only values $\mathfrak{z}_0 > 0$ (points already present on the front at $t = 0$), but also $\mathfrak{z}_0 < 0$ (denoting a "virtual" material points not yet physically present on the front at time $t = 0$, but which might be extracted from the concave corner later on [104]). Comparing equations (4.11) and (4.12) in Chapter 4 (and remembering that $5t^2/(48y_0)$ can be approximated by $5t^2/48$ when t is small and y_0 is close to unity), it follows that a lower region point released at $t = 0$ from $y = y_0$, follows a trajectory given by

$$y \approx y_0 - 1 + y_{\text{2nd,lower}}(t) = -\mathfrak{z}_0 + y_{\text{2nd,lower}}(t), \tag{B.59}$$

with the specific formula for $y_{\mathrm{2nd,lower}}(t)$ (the trajectory of a point initially at the top of the solution domain) given by equation (4.12) in Chapter 4. If we suppose that the concave corner is at location $y_{\mathrm{2nd,cross}}(t)$ (see equation (4.34)) at any given time t, we can determine the $\mathfrak{z}_0$ value instantaneously at the corner via

$$\mathfrak{z}_0 \approx y_{\mathrm{2nd,lower}}(t) - y_{\mathrm{2nd,cross}}(t). \tag{B.60}$$

Here however we are interested in the first instance in obtaining $\mathfrak{z}_0$ as a function of t_{inj} rather than as a function of t. Within the expression for $y_{\mathrm{2nd,lower}}(t)$ (see equation (4.12)) it is a simple matter to replace t by $t_{\mathrm{inj}}/(1-\mathcal{T}_{\mathrm{cross}}(t_{\mathrm{inj}}))$ where $\mathcal{T}_{\mathrm{cross}}$ as a function of t_{inj} is obtained by the procedure outlined in section B.6. If we are specifically interested in the time at which the point $\mathfrak{z}_0$ reaches the concave corner tracked via the aforementioned procedure to a location $y = y^{\mathrm{inter}}_{\mathrm{cross}}(t_{\mathrm{inj}})$ at which upper and lower regions intersect, it now follows that

$$\mathfrak{z}_0 \approx y_{\mathrm{2nd,lower}}(t_{\mathrm{inj}}/(1-\mathcal{T}_{\mathrm{cross}}(t_{\mathrm{inj}}))) - y^{\mathrm{inter}}_{\mathrm{cross}}(t_{\mathrm{inj}}). \tag{B.61}$$

Meanwhile employing equation (4.33) in Chapter 4, $y^{\mathrm{inter}}_{\mathrm{cross}}$ can simply be written as $1-(t_{\mathrm{inj}}/2)\zeta_{+\mathrm{cross}}(t_{\mathrm{inj}})$ where again $\zeta_{+\mathrm{cross}}$ as a function of t_{inj} is obtained by the procedure outlined in section B.6. Hence

$$\mathfrak{z}_0 \approx -\frac{t_{\mathrm{inj}}}{2}\left(\frac{1}{(1-\mathcal{T}_{\mathrm{cross}})} - \zeta_{+\mathrm{cross}}\right) + \frac{5t^2_{\mathrm{inj}}}{48(1-\mathcal{T}_{\mathrm{cross}})^2}. \tag{B.62}$$

This has been plotted in Figure B.4 presented later on. This equation (B.62) can also be simplified in small t_{inj} limit by first recognising that $\zeta_{+\mathrm{cross}} = \zeta_{\mathrm{cross}}/(1-\mathcal{T}_{\mathrm{cross}})$. Then ζ_{cross} is expanded as $\zeta_{\mathrm{cross},0} + t\,\zeta_{\mathrm{cross},1}$ (see equation (B.45)), with the factor t (which appears here within the perturbation term $t\,\zeta_{\mathrm{cross},1}$) approximated at leading order by $t_{\mathrm{inj}}/(1-\mathcal{T}_{\mathrm{cross},0})$. In addition the factor $(1-\mathcal{T}_{\mathrm{cross}})^{-1}$ in

equation (B.62) can be approximated via

$$\frac{1}{(1-\mathcal{T}_{\mathrm{cross}})} \approx \frac{1}{(1-\mathcal{T}_{\mathrm{cross},0}-t_{\mathrm{inj}}\mathcal{T}_{\mathrm{cross},1})} \approx \frac{1}{(1-\mathcal{T}_{\mathrm{cross},0})} + \frac{t_{\mathrm{inj}}\mathcal{T}_{\mathrm{cross},1}}{(1-\mathcal{T}_{\mathrm{cross},0})^2}. \quad \text{(B.63)}$$

Retaining only terms out to order t_{inj}^2 within equation (B.62) gives

$$\mathfrak{z}_0 \approx -\frac{(1-\zeta_{\mathrm{cross},0})}{(1-\mathcal{T}_{\mathrm{cross},0})}\frac{t_{\mathrm{inj}}}{2} + \left(\frac{5}{24} + \zeta_{\mathrm{cross},1} - (1-\zeta_{\mathrm{cross},0})\mathcal{T}_{\mathrm{cross},1}\right)\frac{t_{\mathrm{inj}}^2}{2(1-\mathcal{T}_{\mathrm{cross},0})^2}. \quad \text{(B.64)}$$

Inserting parameter values from Table 4.1 (as provided in Chapter 4) now gives

$$\mathfrak{z}_0 \approx -0.530\, t_{\mathrm{inj}} + 1.845\, t_{\mathrm{inj}}^2. \quad \text{(B.65)}$$

Again this has been plotted in Figure B.4. As can be seen in that figure, although equations (B.62) and (B.65) agree in the small t_{inj} limit, for larger t_{inj} they behave rather differently. Equation (B.65) predicts $\mathfrak{z}_0$ decreasing from zero reaching a minimum value of -0.0382 at $t_{\mathrm{inj}} \approx 0.144$ and returning to $\mathfrak{z}_0 = 0$ at $t_{\mathrm{inj}} \approx 0.288$. Negative $\mathfrak{z}_0$ values correspond to material points with $y_0 > 1$ that were not on the lower region of front originally but rather which have been extracted from the concave corner sometime after time $t = 0$. The minimum (i.e. most negative) $\mathfrak{z}_0$ corresponds to the last extracted material point. After this, as $\mathfrak{z}_0$ begins to increase, the corner starts consuming previously extracted material points, and when $\mathfrak{z}_0 = 0$ all extracted points have now been consumed and the corner is beginning to consume points originally on the front $y_0 \leq 1$. By contrast, equation (B.62) predicts a monotonically decreasing $\mathfrak{z}_0$, the magnitude of the derivative $|\mathrm{d}\mathfrak{z}_0/\mathrm{d}t_{\mathrm{inj}}|$ initially decreases with increasing t_{inj} but then an inflection occurs and $|\mathrm{d}\mathfrak{z}_0/\mathrm{d}t_{\mathrm{inj}}|$ increases again. The reason for this can be traced back to the behaviour of $\zeta_{+\mathrm{cross}}$ as predicted by the procedure of section B.6. For small t_{inj}, we find that $\zeta_{+\mathrm{cross}}$ is an increasing function of t_{inj}, but for larger t_{inj} the predicted value of $\zeta_{+\mathrm{cross}}$ decreases (see Figure 4.6(b) in Chapter 4). The

decrease in $\zeta_{+\text{cross}}$ is what then drives equation (B.62) towards more negative $\mathfrak{z}_0$ values.

B.8.2 Relating $\mathfrak{z}_0$ to the location of the concave corner

One of the issues we face with increasing t_{inj} is that the procedure in section B.6 for tracking an upper region material point up to the corner actually yields a poor estimate for the corner's location, at least when compared with a numerical Eulerian approach (see Figure 4.7 in Chapter 4). In that case Figure 4.7 reveals that the function $y_{2\text{nd,cross}}(t)$ (equation (4.37)) actually gives a far better estimate of the location of the corner for any given t than a formula based on tracking material points through the upper region would. That suggests returning to equation (B.60) which gives $\mathfrak{z}_0$ directly as a function of t. To the extent that the formula (4.34) for $y_{2\text{nd,cross}}(t)$ is reliable, this enables us to identify which material point in the lower region is being extracted or consumed by the concave corner at any instant t, without even having to specify the corresponding material point in the upper region. Using the specific formulae for $y_{2\text{nd,lower}}(t)$ and $y_{2\text{nd,cross}}(t)$ from equations (4.12) and (4.37) in Chapter 4, equation (B.60) predicts a minimum value of $\mathfrak{z}_0$ equal to -0.0114 at time $t \approx 0.759$ and predicts $\mathfrak{z}_0 = 0$ at time $t \approx 1.518$, i.e. the time at which $y_{2\text{nd,lower}} = y_{2\text{nd,cross}}$ as discussed in section 4.7.3 in Chapter 4. To plot the resulting equation (B.60) on Figure B.4 we need however to provide a relation between t and t_{inj}. If we choose to approximate $\mathcal{T}_{\text{cross}} \approx \mathcal{T}_{\text{cross},0} + t_{\text{inj}}\mathcal{T}_{\text{cross},1}$ as in equation (4.28) in Chapter 4, we deduce

$$t \approx t_{\text{inj}}/(1 - \mathcal{T}_{\text{cross},0} - t_{\text{inj}}\mathcal{T}_{\text{cross},1}). \tag{B.66}$$

This is now inserted into equation (B.60). If we were to Taylor expand the resulting equation in powers of t_{inj}, and discard all powers higher than order

t_{inj}^2, then equation (B.65) would result. Here however we do not carry out that formal expansion, retaining instead equations (B.60) and (B.66). The result is now plotted in Figure B.4: qualitatively the shape is similar to equation B.65 but over a more compressed t_{inj} scale. Using the values for $\mathcal{T}_{\text{cross},0}$ and $\mathcal{T}_{\text{cross},1}$ reported in Table 4.1 in Chapter 4, the time $t \approx 0.759$ giving the minimum $\mathfrak{z}_0$ is now considered to correspond to $t_{\text{inj}} \approx 0.0320$. Meanwhile the time $t \approx 1.518$ at which $\mathfrak{z}_0 = 0$ corresponds to $t_{\text{inj}} \approx 0.0508$.

B.8.3 Tracking a particular material point in the lower region

When t_{inj} is sufficiently small, all the various methodologies discussed above to estimate $\mathfrak{z}_0$ give nearly the same prediction, so matching material points in the upper and lower region becomes straightforward again. Once we have identified, for any particular upper region material point t_{inj}, the corresponding lower region material point $\mathfrak{z}_0$, we can track the vertical motion this material point executes via

$$y \approx 1 - \mathfrak{z}_0 - t/2 + 5t^2/48, \tag{B.67}$$

where equations (B.59) and (4.12) have been used, and all t values are considered up to the time at which intersection occurs between the specified upper and lower region material points. Equivalently defining $\zeta_+ = (1-y)/(t_{\text{inj}}/2)$, $Z_0 = \mathfrak{z}_0/(t_{\text{inj}}/2)$ and $\mathcal{T} = 1 - t_{\text{inj}}/t$ (now with $\mathcal{T} \leq \mathcal{T}_{\text{cross}}$), we deduce

$$\zeta_+ = Z_0 + \frac{1}{1-\mathcal{T}} - t_{\text{inj}} \frac{5}{24\,(1-\mathcal{T})^2}. \tag{B.68}$$

This then can be inserted into equation (4.26) to predict the ζ_+ vs Ξ_+ trajectory that the lower region material point executes as $\mathcal{T}$ and hence t varies. This is what we plot in Figure 4.3 in Chapter 4 for the cases $t_{\text{inj}} \to 0$ and $t_{\text{inj}} = 0.01$. The values

Appendix B. Supplementary material: Foam-liquid front propagation in Lagrangian coordinates

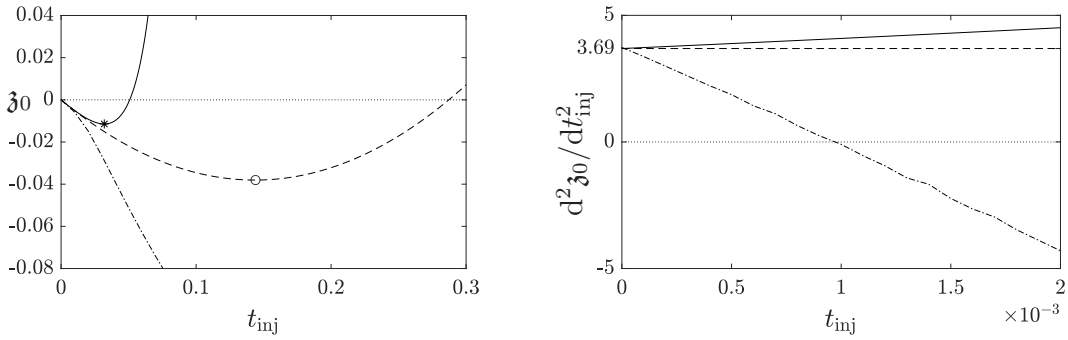

Figure B.4: $\mathfrak{z}_0$ vs t_{inj} obtained via three different methodologies. Solid line: equations (B.60) (along with (B.66)). Dash-dotted line: equation (B.62). Dashed lined: equation (B.65). Points "$*$" and "$\circ$" show the (t_{inj}, $\mathfrak{z}_0$) value corresponding to the minimum $\mathfrak{z}_0$ given by equations (B.60) and (B.65), respectively. (b) $\mathrm{d}^2\mathfrak{z}_0/\mathrm{d}t_{\text{inj}}^2$ vs t_{inj} for $t_{\text{inj}} < 0.002$.

of $\mathfrak{z}_0$ and hence $Z_0 \equiv \mathfrak{z}_0/(t_{\text{inj}}/2)$ reported in Figure 4.3 in each instance have been obtained from equation (B.62). Note that as $t_{\text{inj}} \to 0$, the value of $\mathfrak{z}_0 \to 0$ also, but Z_0 remains finite, turning out to have a value of $Z_0 \equiv \mathfrak{z}_0/(t_{\text{inj}}/2) \approx -1.06$, as also follows from (B.65) in the $t_{\text{inj}} \to 0$ limit. For small $t_{\text{inj}} < 0.01$ values, equations (B.60), (B.62) and (B.65) predict almost the same $\mathfrak{z}_0$ value, however the amount that they disagree increases as t_{inj} increases. In the case of equation (B.60), a minimum is found at $t_{\text{inj}} \approx 0.0320$ (assuming (B.66) applies) the minimum value being $\mathfrak{z}_0 \approx -0.0114$ (point with asterisk "$*$" on the solid line in Figure B.4). To the left of $*$, material points at the concave corner were not in the original solution domain of the lower region: they only appear when they are extracted from the concave corner. To the right of $*$, we start consuming material points again. At $t_{\text{inj}} \approx 0.0508$ (still using equation (B.60)), the value of $\mathfrak{z}_0$ reaches zero: all the extracted material points have been consumed. Hence for values of $\mathfrak{z}_0 > 0$ we start consuming material points that were originally on the front since time $t = 0$. Similarly, when the formula given by equation (B.65) is used, a minimum is found at $t_{\text{inj}} \approx 0.114$ and $\mathfrak{z}_0 \approx -0.0382$ (point with "$\circ$" on the dashed line

in Figure B.4). This also predicts that at $t_{\text{inj}} \approx 0.288$ all the extracted material points have been consumed ($\mathfrak{z}_0$ reaches zero here). In contrast, when equation (B.62) is used $\mathfrak{z}_0$ just becomes more negative as t_{inj} increases. In Figure B.4 we compute $\mathrm{d}^2\mathfrak{z}_0/\mathrm{d}t_{\text{inj}}^2$ vs t_{inj} with $t_{\text{inj}} < 0.002$, for equations (B.62), (B.65), and (B.60). For equation (B.62) (dash-dotted line in Figure B.4), this starts positive and then becomes negative for $t_{\text{inj}} \sim 0.001$: this indicates an inflection for $\mathfrak{z}_0$ vs t_{inj} (albeit difficult to see on the scale of in Figure B.4(a)). For equation (B.65) this corresponds to a constant $\mathrm{d}^2\mathfrak{z}_0/\mathrm{d}t_{\text{inj}}^2$ value of 3.69. Finally for equation (B.60) (solid line in Figure B.4), it starts positive and keeps increasing.

B.9 Front upper region extrapolation

Although equation (B.45) estimates ζ_{cross} for any given t, it only approximates the nominal ζ_{cross} value that would be computed via the intersection of equations (4.20), (4.21), and (4.22), as Figure 4.6(e) (in Chapter 4) makes clear when comparing predictions. It may be necessary to extrapolate the solution of equations (4.20) and (4.21) over an interval of ζ from the vertical location where it intersects with equation (4.22) to an estimated ζ_{cross} value by equation (B.45). As we saw in Chapter 4, the estimated ζ_{cross} obtained via (B.45) actually gives a better indication (see e.g. equation (4.34)) of how the vertical location of the concave corner evolves. Here we explain a simple way in which an extrapolation with respect to ζ can be achieved. We extrapolate the rescaled front's upper region shape $\zeta(\mathcal{T}, t)$ vs $\Xi(\mathcal{T}, t)$, and rescaled front orientation $\mathcal{A}(\mathcal{T}, t)$ vs $\zeta(\mathcal{T}, t)$ at any given time t (as described by equations (4.19)–(4.21)), beyond the intercept between the upper (given by equation (4.20) and (4.21)) and the lower (given by equation (4.22)) region of the front, by considering a straight line extrapolation between the nominal ζ_{cross} at the intercept itself and the estimate of ζ_{cross} from

equation (B.45). Specifically, we can expand equations (4.19)–(4.21), to obtain

$$\mathcal{A} \approx \mathcal{A}_0(\mathcal{T}_{\text{cross},0}) + t\,\mathcal{A}_1(\mathcal{T}_{\text{cross},0}) + \chi\, t\,(1-\mathcal{T}_{\text{cross},0})\mathcal{T}_{\text{cross},1}\mathcal{A}_0'(\mathcal{T}_{\text{cross},0}), \tag{B.69}$$

$$\zeta \approx \zeta_0(\mathcal{T}_{\text{cross},0}) + t\,\zeta_1(\mathcal{T}_{\text{cross},0}) + \chi\, t\,(1-\mathcal{T}_{\text{cross},0})\mathcal{T}_{\text{cross},1}\zeta_0'(\mathcal{T}_{\text{cross},0}), \tag{B.70}$$

$$\Xi \approx \Xi_0(\mathcal{T}_{\text{cross},0}) + t\,\Xi_1(\mathcal{T}_{\text{cross},0}) + \chi\, t\,(1-\mathcal{T}_{\text{cross},0})\mathcal{T}_{\text{cross},1}\Xi_0'(\mathcal{T}_{\text{cross},0}). \tag{B.71}$$

Here, $\mathcal{A}_0'$, ζ_0' and Ξ_0', denote $\mathrm{d}\mathcal{A}_0/\mathrm{d}\mathcal{T}$, $\mathrm{d}\zeta_0/\mathrm{d}\mathcal{T}$ and $\mathrm{d}\Xi_0/\mathrm{d}\mathcal{T}$, respectively (with A_0, ζ_0 and Ξ_0 as given by equations (4.15)–(4.17)). Moreover, χ is a parameter that varies from 0 to unity, as $\mathcal{T}$ varies from $\mathcal{T}_{\text{cross},0}$ to $\mathcal{T}_{\text{cross},0} + t_{\text{inj}}\,\mathcal{T}_{\text{cross},1} \approx \mathcal{T}_{\text{cross},0} + t\,(1-\mathcal{T}_{\text{cross},0})\,\mathcal{T}_{\text{cross},1}$. We can obtain a straight line relation between $\mathcal{A}$ and ζ, and between Ξ and ζ as

$$\mathcal{A} \approx \frac{\mathcal{A}_0'(\mathcal{T}_{\text{cross},0})}{\zeta_0'(\mathcal{T}_{\text{cross},0})}\left(\zeta - \zeta_0(\mathcal{T}_{\text{cross},0}) - t\,\zeta_1(\mathcal{T}_{\text{cross},0})\right) + \mathcal{A}_0(\mathcal{T}_{\text{cross},0}) + t\,\mathcal{A}_1(\mathcal{T}_{\text{cross},0}), \tag{B.72}$$

$$\Xi \approx \frac{\Xi_0'(\mathcal{T}_{\text{cross},0})}{\zeta_0'(\mathcal{T}_{\text{cross},0})}\left(\zeta - \zeta_0(\mathcal{T}_{\text{cross},0}) - t\,\zeta_1(\mathcal{T}_{\text{cross},0})\right) + \Xi_0(\mathcal{T}_{\text{cross},0}) + t\,\Xi_1(\mathcal{T}_{\text{cross},0}). \tag{B.73}$$

Equations (B.72) and (B.73) are what we have plotted in Figure 4.8 (see Chapter 4 for details) at fixed time $t = 1$, with $\mathcal{T}_{\text{cross}} \approx 0.9003$, for values of ζ from the computed $\zeta(\mathcal{T}_{\text{cross}}) \approx 0.5839$ (i.e. the intersection between (4.20)–(4.21) and (4.22)) up to the prediction that equation (B.45) estimates namely $\zeta_{\text{cross}} \approx 0.7711$.

Appendix C

Supplementary material: Foam flow in confined straight channels

This appendix consists of the supplementary material of the manuscript presented in Chapter 5: "Viscous froth model applied to the motion of two-dimensional bubbles in a channel: The three-bubble case". Here a detailed deduction of the main equation used in Chapter 5 is presented, in addition to further analysis and discussion about limiting cases of the studied phenomena.

Appendix C. Supplementary material: Foam flow in confined straight channels

Summary: In these supplementary sections, we start by deriving the formulae to compute the three-bubble system structure at equilibrium, given in section C.1. Then we proceed in section C.2, to obtain the coordinates for moving films, either when the system is parametrized in terms of orientation angles or distances along films. Then in section C.3 we carry out further analysis of the inherently stable system moving at high velocity. In section C.4 by contrast, we deduce a weakly-driven migration solution for the variables that define the system as it moves at very low velocities. Results for out-of-equilibrium systems migrating at a finite velocity are presented in section C.5: these expand upon the results already presented in section 5.5 in Chapter 5.

C.1 Determining the equilibrium structure

In this section, we compute the initial symmetric static state, or so-called, equilibrium structure, where there is not any external driving pressure applied. Hence, the imposed back pressure $p_b = 0$. The (equilibrium) pressures of each of the bubbles $\mathcal{B}_1$, $\mathcal{B}_2$ and $\mathcal{B}_3$ will be denoted by p_1°, p_2° and p_3°, where the superscript "$\circ$" is used in this work to refer to the value of variables in the initial equilibrium state. The bubble pressures are fixed by the constrained bubble areas A_1, A_2 and A_3, respectively, with $A_1 = A_3$ in the symmetric state considered here.

C.1.1 Equilibrium film coordinates

As described in Chapter 5 (see section 5.2), films are connected three by three at vertices, each film subtending an angle of $2\pi/3$ with respect to its neighbours, as required by Plateau's law for dry foams (see Figure 5.1(a) in Chapter 5 section 5.2). The angles through which a film turns, measured in the case of films $\jmath_{02}$, $\jmath_{13}$ and $\jmath_{20}$ from a channel side wall to a vertex either V_1, V_2 or V_3 are denoted $\delta\phi_{02}$, $\delta\phi_{13}$ and $\delta\phi_{20}$, all other film turning angles being determined in terms of

these according to Table 5.1 in Chapter 5. The turning angles are measured in the anticlockwise direction from the vertical, implying that for film $\jmath_{02}$ at equilibrium, the value of $\delta\phi^\circ_{02}$ is negative and equal to $-\delta\phi^\circ_{20}$ (see Figure 5.1 in Chapter 5). Meanwhile on symmetry grounds at equilibrium $\delta\phi^\circ_{13} = 0$. For migration velocity $v = 0$, we obtain for each film $\jmath_{ij}$ (using equations (5.3)–(5.4))

$$\frac{\mathrm{d}x^\circ_{ij}}{\mathrm{d}\phi_{ij}} = -\frac{\sin(\phi_{ij})}{\Delta p^\circ_{ij}}, \tag{C.1}$$

$$\frac{\mathrm{d}y^\circ_{ij}}{\mathrm{d}\phi_{ij}} = \frac{\cos(\phi_{ij})}{\Delta p^\circ_{ij}}. \tag{C.2}$$

Remember that Δp°_{ij} here corresponds to the left side minus right side pressure. The ranges of variation of ϕ_{ij} for each film, are summarized in Table 5.1 in Chapter 5.

Since at equilibrium the system is symmetric, we just need to integrate equations (C.1) and (C.2) for three of the films $\jmath_{23}$, $\jmath_{20}$ and $\jmath_{30}$, in order to characterize the whole structure. Then, we obtain

$$y^\circ_{23} = 1 - l^\circ_2 - \frac{\sqrt{3}}{2(p^\circ_2 - p^\circ_3)} + \frac{\sin(\phi_{23})}{(p^\circ_2 - p^\circ_3)}, \quad \frac{\pi}{3} \leq \phi_{23} \leq \frac{\pi}{3} + \delta\phi^\circ_{20}, \tag{C.3}$$

$$y^\circ_{30} = 1 + \frac{\sin(\phi_{30})}{p^\circ_3}, \quad 0 \geq \phi_{30} \geq -\frac{\pi}{3} + \delta\phi^\circ_{20}, \tag{C.4}$$

$$y^\circ_{20} = \frac{\sin(\phi_{20})}{p^\circ_2}, \quad 0 \leq \phi_{20} \leq \delta\phi^\circ_{20}. \tag{C.5}$$

Since the films $\jmath_{23}$, $\jmath_{30}$ and $\jmath_{20}$ join at the vertex V_3, we know that $y^\circ_{23}(\pi/3+\delta\phi^\circ_{20}) = y^\circ_{30}(-\pi/3 + \delta\phi^\circ_{20}) = y^\circ_{20}(\delta\phi^\circ_{20}) \equiv 1 - l^\circ_1$. Using these relations, we can calculate p°_3

and p_2°, in terms of l_1° and l_2°, as

$$p_3^\circ = \frac{\sqrt{3}(1-l_2^\circ)\sqrt{4{l_2^\circ}^2(1-l_1^\circ+{l_1^\circ}^2)-4l_1^\circ l_2^\circ(1+l_1^\circ)+{l_1^\circ}^2(1+6l_1^\circ-3{l_1^\circ}^2)}}{4{l_1^\circ}^2-4l_1^\circ l_2^\circ(1+l_1^\circ)+4{l_2^\circ}^2(1-l_1^\circ+{l_1^\circ}^2)} + \frac{\sqrt{3}l_2^\circ(2-3l_1^\circ+{l_1^\circ}^2)-\sqrt{3}l_1^\circ(1-l_1^\circ)}{4{l_1^\circ}^2-4l_1^\circ l_2^\circ(1+l_1^\circ)+4{l_2^\circ}^2(1-l_1^\circ+{l_1^\circ}^2)}, \quad \text{(C.6)}$$

$$p_2^\circ = \frac{\sqrt{3}-2p_3^\circ l_2^\circ}{2(1-l_2^\circ)}. \quad \text{(C.7)}$$

Here both equation (C.3) and equation (C.4) were matched at vertex V_3 to $(1-l_1^\circ)$, to obtain, after some manipulation, equations (C.6) and (C.7), respectively. Here in each case by using equation (C.5) the turning angle $\delta\phi_{20}^\circ$ was replaced by $\delta\phi_{20}^\circ = \text{asin}(p_2^\circ(1-l_1^\circ))$.

In Figure C.1 we show the equilibrium pressures and also a film turning angle for two fixed values of l_1° and different values of l_2°/l_1°. Observe how the pressures $p_1^\circ = p_3^\circ$ tend to exceed p_2°, and decreasing l_1° causes $p_1^\circ = p_3^\circ$ to increase even more. Meanwhile increasing l_2°/l_1° tends to decrease both p_2° and $\delta\phi_{20}^\circ$. Note that increasing l_1° decreases the length of film $\jmath_{20}$ and hence decreases the turning angle $\delta\phi_{20}^\circ$ likewise. Once the pressures are calculated for the equilibrium structure, given l_1° and l_2° as the control variables, we can compute the x_{ij} and y_{ij} coordinate of each film using equations (C.1) and (C.2).

C.1.2 System energy in the equilibrium

We can compute the system's energy in equilibrium (the sum of all film lengths) E° by integrating equation (5.2) (as given in section 5.2.2 in Chapter 5) with $v = 0$, for films $\jmath_{23}$, $\jmath_{30}$ and $\jmath_{20}$. Then by adding together (on symmetry grounds) twice the $\mathcal{L}_{23}^\circ$, $\mathcal{L}_{30}^\circ$ and $\mathcal{L}_{20}^\circ$ of these films, with the vertical film $\jmath_{13}$ of length l_2°,

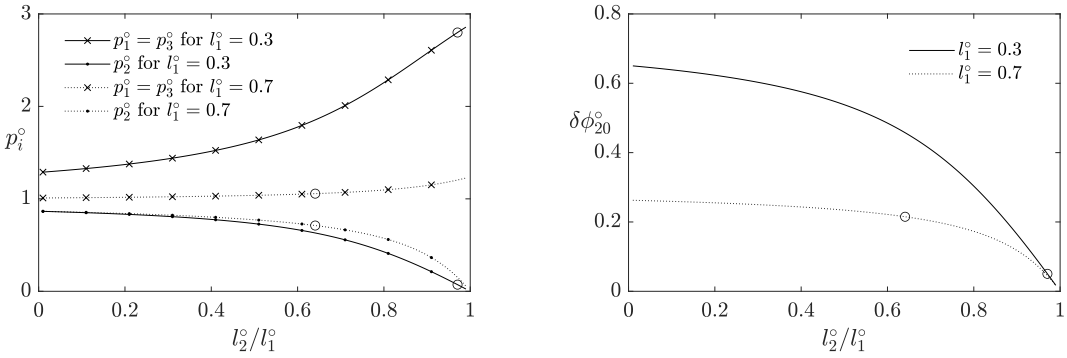

Figure C.1: (a) Equilibrium pressures $p_1^\circ = p_3^\circ$ and p_2°, and (b) total turning angle $\delta\phi_{20}^\circ = -\delta\phi_{02}^\circ$. In each case we plot for two values of l_1°, and $l_2^\circ/l_1^\circ \in [0.01, 0.99]$. In (a) and (b) in each curve the monodisperse scenario has been highlighted with "$\circ$".

we can obtain E°, which is given by

$$E^\circ = 2\left(\frac{\pi}{3\,p_3^\circ} + \delta\phi_{20}^\circ\left(\frac{1}{p_2^\circ} + \frac{1}{p_3^\circ - p_2^\circ} - \frac{1}{p_3^\circ}\right)\right) + l_2^\circ, \tag{C.8}$$

where $\delta\phi_{20}^\circ$, p_2° and p_3° are functions of l_1° and l_2°. This E° is plotted in Figure C.2(b) for different values of l_1° and l_2°. Qualitatively E° shows a similar trend to the perimeter of a circular bubble with the same A_{tot} i.e. with the same total area.

C.1.3 Setting bubble areas

In this work we do not consider gas diffusion between bubbles, i.e. areas will remain constant even when the system is set in motion. Once the equilibrium pressures and film turning angles are determined as a function of l_1° and l_2°, we can compute bubble areas considering that in the equilibrium state all films are

Appendix C. Supplementary material: Foam flow in confined straight channels

l_1° \ l_2°/l_1°	0	0.1	0.2	0.3	0.4	0.5	0.6	0.7	0.8	0.9	1
0	*0.121*	*0.077*	*0.044*	*0.019*	0.005	*0.000*	*0.000*	*0.000*	*0.000*	*0.000*	*0.000*
0.1	*0.196*	*0.151*	*0.112*	*0.080*	*0.053*	*0.033*	*0.020*	*0.012*	*0.008*	*0.005*	0.004
0.2	*0.277*	*0.233*	*0.192*	*0.154*	*0.120*	*0.089*	*0.064*	*0.044*	*0.030*	*0.021*	0.016
0.3	*0.365*	*0.324*	*0.282*	*0.241*	*0.201*	*0.162*	*0.125*	*0.093*	*0.066*	*0.048*	0.037
0.4	*0.460*	*0.423*	*0.382*	*0.340*	*0.295*	*0.248*	*0.202*	*0.157*	*0.117*	*0.085*	0.066
0.5	*0.565*	*0.532*	*0.493*	*0.449*	*0.401*	*0.348*	*0.293*	*0.236*	*0.181*	0.134	0.102
0.6	*0.679*	*0.651*	*0.615*	*0.571*	*0.520*	*0.462*	*0.397*	*0.328*	*0.258*	0.193	0.147
0.7	*0.806*	*0.782*	*0.749*	*0.705*	*0.651*	*0.588*	*0.516*	0.435	0.349	0.265	0.201
0.8	*0.945*	*0.927*	*0.896*	*0.853*	*0.797*	0.728	0.648	0.557	0.455	0.350	0.262
0.9	*1.101*	*1.088*	*1.059*	1.016	0.958	0.884	0.797	0.694	0.578	0.450	0.333
1	*1.276*	*1.265*	1.239	1.196	1.135	1.057	0.961	0.849	0.719	0.571	0.410

Table C.1: Area of bubbles $A_1 = A_3$ for different values of l_1° and l_2°/l_1°. Cases shown in italics have A_1 and A_3 smaller than A_2. The cases $l_1^\circ \to 1$ or $l_2^\circ/l_1^\circ \to 0$ reported here are limiting cases that are easy to compute. Meanwhile in the limiting case $l_2^\circ/l_1^\circ \to 1$, $A_1 = A_3 \approx (2\pi/9 - 1/(2\sqrt{3}))l_1^{\circ 2}$. The limiting case $l_1^\circ \to 0$ is discussed later on (see section C.1.4): areas $A_1 = A_3$ vanish unless $l_2^\circ/l_1^\circ < 0.5$.

arcs of circles. It is possible to deduce that

$$A_2 = 2\left(\frac{1}{\Delta p_{23}^\circ}\left(1 - \frac{(l_1^\circ + l_2^\circ)}{2}\right)\left(\cos\left(\frac{\pi}{3} + \delta\phi_{20}^\circ\right) - \frac{1}{2}\right) - \frac{1}{2{\Delta p_{23}^\circ}^2}\left(\delta\phi_{20}^\circ - \sin(\delta\phi_{20}^\circ)\right)\right.$$
$$\left. + \frac{1}{2{\Delta p_{20}^\circ}^2}\left(\delta\phi_{20}^\circ - \sin\left(\delta\phi_{20}^\circ\right)\right) + \frac{(1 - l_1^\circ)}{2\Delta p_{20}^\circ}\left(1 - \cos\left(\delta\phi_{20}^\circ\right)\right)\right), \tag{C.9}$$

$$A_3 = \frac{1}{2{\Delta p_{23}^\circ}^2}\left(\delta\phi_{20}^\circ - \sin(\delta\phi_{20}^\circ)\right) + \frac{(l_1^\circ + l_2^\circ)}{2\Delta p_{23}^\circ}\left(\cos\left(\frac{\pi}{3} + \delta\phi_{20}^\circ\right) - \frac{1}{2}\right)$$
$$+ \frac{1}{2{\Delta p_{30}^\circ}^2}\left(\frac{\pi}{3} - \delta\phi_{20}^\circ - \sin\left(\frac{\pi}{3} - \delta\phi_{20}^\circ\right)\right) + \frac{l_1^\circ}{2\Delta p_{30}^\circ}\left(1 - \cos\left(\frac{\pi}{3} - \delta\phi_{20}^\circ\right)\right). \tag{C.10}$$

Remember that a symmetric system entails that $A_1 = A_3$. Although equations (C.9) and (C.10) are given here as functions of l_1°, l_2°, $\delta\phi_{20}^\circ$, p_2°, and p_3°, by using equations (C.6) and (C.7), and the fact that $\delta\phi_{20}^\circ = \mathrm{asin}(p_2^\circ(1 - l_1^\circ))$, they can be written solely in terms of l_1° and l_2°. Equations (C.9) and (C.10) are therefore nonlinear equations relating A_2 and $A_1 = A_3$ to l_1° and l_2°.

Appendix C. Supplementary material: Foam flow in confined straight channels

l_1° \ l_2°/l_1°	0	0.1	0.2	0.3	0.4	0.5	0.6	0.7	0.8	0.9	1
0	*2.887*	*2.512*	*2.118*	*1.704*	*1.271*	*0.819*	*0.599*	*0.415*	*0.259*	*0.122*	*0.000*
0.1	*2.752*	*2.414*	*2.069*	*1.720*	*1.374*	*1.042*	*0.744*	*0.495*	*0.296*	*0.135*	0.000
0.2	*2.629*	*2.312*	*1.994*	*1.678*	*1.367*	*1.066*	*0.783*	*0.531*	*0.317*	*0.143*	0.000
0.3	*2.512*	*2.207*	*1.907*	*1.611*	*1.323*	*1.044*	*0.780*	*0.537*	*0.324*	*0.145*	0.000
0.4	*2.399*	*2.100*	*1.809*	*1.528*	*1.256*	*0.996*	*0.750*	*0.522*	*0.317*	*0.141*	0.000
0.5	*2.288*	*1.990*	*1.705*	*1.433*	*1.174*	*0.930*	*0.701*	*0.489*	*0.298*	0.133	0.000
0.6	*2.177*	*1.878*	*1.595*	*1.328*	*1.080*	*0.848*	*0.635*	*0.441*	*0.268*	0.119	0.000
0.7	*2.069*	*1.763*	*1.479*	*1.217*	*0.976*	*0.756*	*0.558*	0.382	0.229	0.100	0.000
0.8	*1.958*	*1.646*	*1.360*	*1.099*	*0.864*	0.655	0.471	0.313	0.182	0.077	0.000
0.9	*1.846*	*1.526*	*1.236*	0.976	0.746	0.546	0.377	0.237	0.128	0.049	0.000
1	*1.732*	*1.404*	1.109	0.849	0.624	0.433	0.277	0.156	0.069	0.017	0.000

Table C.2: Area of bubble A_2 for different values of l_1° and l_2°/l_1°. Cases shown in italics are those for which A_1 and A_3 are smaller than A_2. Limiting cases either $l_1^\circ \to 1$ or $l_2^\circ/l_1^\circ \to 0$ are easy to compute. In the limiting case $l_2^\circ/l_1^\circ \to 1$, A_2 vanishes. However area A_2 is finite in the $l_1^\circ \to 0$ limit, see section C.1.4 for details.

Tables C.1 and C.2 show for a wide range of values of l_1° and l_2°, the corresponding bubble areas $A_1 = A_3$ and A_2, respectively. Increasing l_1° or decreasing l_2°/l_1° leads to increased $A_1 = A_3$. Meanwhile increasing l_1° or increasing l_2°/l_1° leads to decreased A_2. In Figure 5.3(c) in Chapter 5 we plot the bubble area for polydisperse bubble systems for three fixed values of $l_1^\circ = [0.1, 0.5, 0.9]$ and values of $l_2^\circ/l_1^\circ \in [0.01, 0.99]$, in effect plotting data from selected rows of Table C.1 and Table C.2.

Figure C.2(a) shows for that same system the total area of all bubbles $A_{\text{tot}} = 2\,A_1 + A_2$ using the same set of l_1° and again with values of $l_2^\circ/l_1^\circ \in [0.01, 0.99]$. Here the edges of the bubbles on the channel walls are not included in the computation of E°, so there is no requirement for E° to exceed $(4\pi\, A_{\text{tot}})^{1/2}$. In both Figure C.2(a) and C.2(b) (for each l_1°) the particular l_2°/l_1° values giving monodispersity are highlighted with "$\circ$". In the case of $l_1^\circ = 0.01$ however, this value is strictly speaking out of the studied domain since it involves $l_2^\circ/l_1^\circ = 0.997$. Certain combinations of l_1° and l_2° (see Figure 5.4(a) in Chapter 5) lead to monodisperse

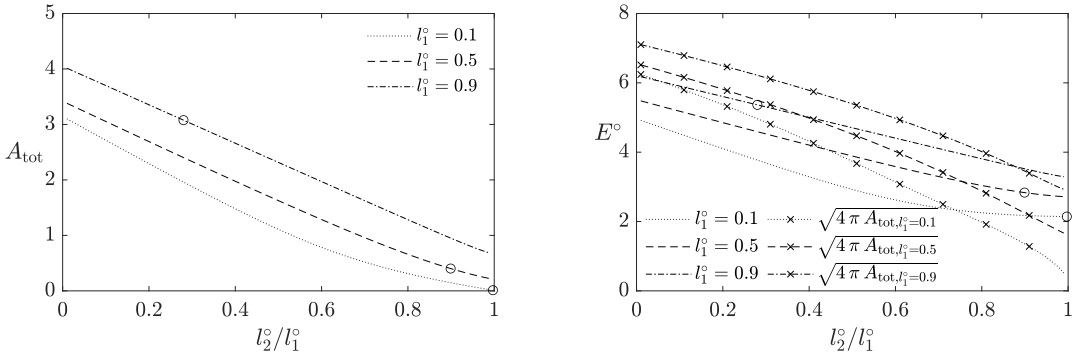

Figure C.2: (a) Total bubble area $A_{\rm tot} = 2\,A_1 + A_2$ for three fixed values of l_1° and values of $l_2^\circ/l_1^\circ \in [0.01, 0.99]$. (b) System energy in equilibrium E° for different three values of l_1° and values of $l_2^\circ/l_1^\circ \in [0.01, 0.99]$, in comparison with $(4\pi\,A_{\rm tot})^{1/2}$ (which is the perimeter of a circular bubble with the same total area).

systems for which $A_1 = A_2 = A_3$, the resulting monodisperse bubble areas being plotted in Figure 5.4(b) (also in Chapter 5). For any given l_1°, the requisite l_2°/l_1° value to attain the monodisperse state can be estimated by reading off areas from the corresponding rows of Table C.1 and C.2 until a l_2°/l_1° value is found at which the areas are roughly equal. This then provides a starting guess for solving the nonlinear equation obtained by equating (C.9) and (C.10).

C.1.4 Setting bubble areas in limiting cases

Equations (C.9)–(C.10) indicate that bubble areas $A_1 = A_3$ are complex nonlinear functions of l_1° and l_2°. There are certain limiting cases however in which these relations simplify considerably. Here we consider a number of such limiting cases for the system in equilibrium.

C.1.4.1 $l_1^\circ \ll 1$ limit

The limiting case $l_1^\circ \ll 1$ turns out to have very different behaviour depending upon whether $\chi < 1/2$ or $1/2 < \chi < 1$ (with $\chi = l_2^\circ/l_1^\circ$). In the former case, it can

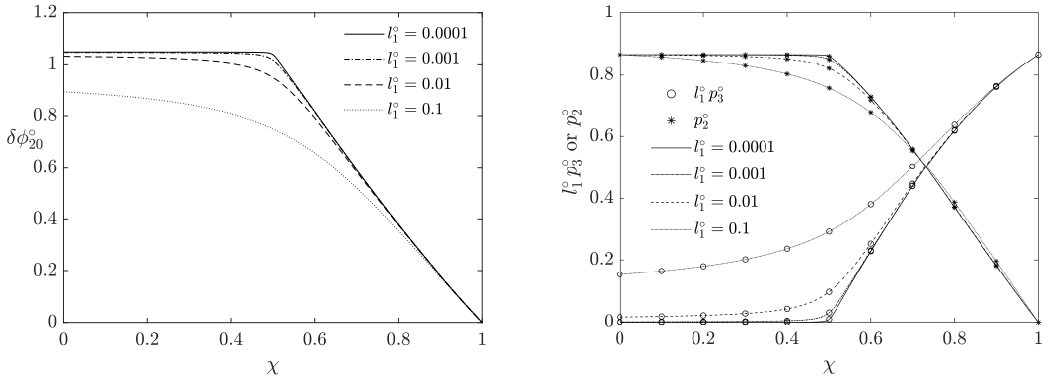

Figure C.3: (a) Total turning angle $\delta\phi_{20}^{\circ}$, and (b) bubble pressures $l_1^{\circ} p_1^{\circ} = l_1^{\circ} p_3^{\circ}$ and p_2°, as a function of $\chi \equiv l_2^{\circ}/l_1^{\circ}$ for four fixed values of l_1° in the equilibrium. Here for bubbles $\mathcal{B}_1$ and $\mathcal{B}_3$ we plot a rescaled pressure (rescaled by l_1°) since in the $l_1^{\circ} \to 0$ limit, with $\chi > 1/2$, $p_1^{\circ} = p_3^{\circ}$ might be orders of magnitude bigger than p_2°. The data shown here obtained by using equations (C.6) and (C.7).

be shown that film $\jmath_{20}$ turns through an angle $\pi/3$ and bubble pressure $p_2^{\circ} \approx \sqrt{3}/2$ (see Figure C.3(a)). Meanwhile bubble $\mathcal{B}_3$ (which is a symmetric mirror image of bubble $\mathcal{B}_1$) need not be particularly small, the pressure p_3° (whilst larger than p_2°) need not be orders of magnitude larger (see Figure C.3(b)), and film $\jmath_{30}$ (which is very short in this $l_1^{\circ} \ll 1$ limit) turns through a negligible angle (see Figure C.4 (a)). In the latter case however, film $\jmath_{20}$ turns through an angle significantly less than $\pi/3$ and bubble pressure p_2° can likewise be less than $\sqrt{3}/2$. Film $\jmath_{30}$ despite being very short, now turns through a non-negligible angle. This requires that pressure p_3° is orders of magnitude larger than p_2° (see Figure C.3(b)). Films $\jmath_{30}$ and $\jmath_{23}$ both have nearly the same curvature, and both these films are highly curved. This then requires that bubble $\mathcal{B}_3$ and also its symmetric mirror image bubble $\mathcal{B}_1$ have vanishingly small area in the limit $l_1^{\circ} \to 0$ (see Figure C.4(b)). As seen in Figure C.3(b), small l_1° means that p_1° and p_3° are very large (much bigger than p_2°), which causes that $\jmath_{12}$ and $\jmath_{23}$ to turn through a noticeable angle, especially when $\chi < 0.5$.

Approximated results can then be derived in this limiting case, taking note in what follows of the turning angles at the start and end of each film as given in Table 5.1 in Chapter 5. Film $\jmath_{20}$ at equilibrium satisfies (see equation (C.5))

$$1 - l_1^\circ = \frac{\sin(\delta\phi_{20}^\circ)}{p_2^\circ}. \tag{C.11}$$

Hence if $l_1^\circ \ll 1$, we can either have $\delta\phi_{20}^\circ \approx \pi/3$ and $p_2^\circ = \sqrt{3}/2$ (as suggested by equation (C.7), provided $p_3^\circ l_2^\circ \to 0$ as $l_2^\circ \to 0$), or we can have a smaller value of $\delta\phi_{20}^\circ$ and a correspondingly smaller p_2°. Film $\jmath_{30}$ meanwhile satisfies (see equation (C.4))

$$l_1^\circ = \frac{\sin(\pi/3 - \delta\phi_{20}^\circ)}{p_3^\circ}. \tag{C.12}$$

In a situation in which $\delta\phi_{20}^\circ = \pi/3 - \Delta\phi_{20}$ where by assumption $\Delta\phi_{20} \ll 1$, we have to a good approximation

$$l_1^\circ \approx \frac{\Delta\phi_{20}}{p_3^\circ}. \tag{C.13}$$

Meanwhile film $\jmath_{23}$ satisfies (see equation (C.3))

$$l_2^\circ - l_1^\circ = \frac{\sin(\pi/3)}{p_3^\circ - p_2^\circ} - \frac{\sin(\pi/3 + \delta\phi_{20}^\circ)}{p_3^\circ - p_2^\circ}. \tag{C.14}$$

If we set $l_2^\circ = \chi l_1^\circ$ (for some $\chi < 1$) and we also set $\delta\phi_{20}^\circ = \pi/3 - \Delta\phi_{20}$ we discover upon Taylor expanding in terms of $\Delta\phi_{20}$ that

$$(1 - \chi) l_1^\circ \approx \frac{\Delta\phi_{20}}{2(p_3^\circ - p_2^\circ)}. \tag{C.15}$$

Solutions of the above equations are

$$p_3^\circ \approx \frac{(2 - 2\chi)}{(1 - 2\chi)} p_2^\circ, \tag{C.16}$$

Appendix C. Supplementary material: Foam flow in confined straight channels

$$\Delta\phi_{20} \approx l_1^\circ p_3^\circ \approx \frac{(2-2\chi)}{(1-2\chi)} l_1^\circ p_2^\circ. \tag{C.17}$$

These equations have physically sensible solutions as long as $\chi < 1/2$. In that case it is clear that p_3° is not orders of magnitude larger than p_2° and since $\Delta\phi_{20}$ is then small it follows by equation (C.11) that $p_2^\circ \approx \sqrt{3}/2$.

It is only in the limit as $\chi \to 1/2$ that we find $p_3^\circ \gg p_2^\circ$ and $\Delta\phi_{20}$ ceases to be small (which means $\delta\phi_{20}^\circ$ starts to become significantly less than $\pi/3$). In the limit when $p_3^\circ \gg p_2^\circ$ we have the following approximation for film $\jmath_{23}$ (see equation (C.14))

$$l_1^\circ - l_2^\circ \approx \frac{\sin(\pi/3 + \delta\phi_{20}^\circ) - \sqrt{3}/2}{p_3^\circ}. \tag{C.18}$$

If we take a ratio between the relations for $\jmath_{30}$ and $\jmath_{23}$ (see equations (C.12) and (C.18)) we obtain

$$1 - \chi \equiv \frac{l_1^\circ - l_2^\circ}{l_1^\circ} \approx \frac{\sin(\pi/3 + \delta\phi_{20}^\circ) - \sqrt{3}/2}{\sin(\pi/3 - \delta\phi_{20}^\circ)}. \tag{C.19}$$

For any value of $1/2 < \chi < 1$ we should be able to find a corresponding $\delta\phi_{20}^\circ$. Close to $\chi = 1$, we expect $\delta\phi_{20}^\circ \to 0$ whereas close to $\chi = 1/2$ we expect $\delta\phi_{20}^\circ$ to be slightly smaller than $\pi/3$. Once the value of $\delta\phi_{20}^\circ$ is obtained, the pressure p_2° follows via equation (C.11) as $p_2^\circ \approx \sin(\delta\phi_{20}^\circ)$.

Based on the arguments above, it is now possible to determine formulae for bubble areas with $l_1^\circ \ll 1$, both in the regime $\chi \equiv l_2^\circ/l_1^\circ < 1/2$ and in the regime $1/2 < \chi < 1$. These are the data we already reported in Table C.1 and Table C.2. One feature of the $l_1^\circ \ll 1$ geometry, which is particularly noticeable when χ is also small, is that vertices V_1 and V_3 are no longer necessarily the most distant points of film $\jmath_{12}$ and film $\jmath_{23}$ from the upper channel wall. Instead films $\jmath_{12}$ and $\jmath_{23}$ sweep downwards starting from vertex V_2 and then sweep upwards a little to reach vertices V_1 and V_3, respectively: see Figure C.4(a)–(b) for detail. Here (since films $\jmath_{01}$, $\jmath_{13}$ and $\jmath_{30}$ are all nearly vertical, with $\chi < 1/2$ in this

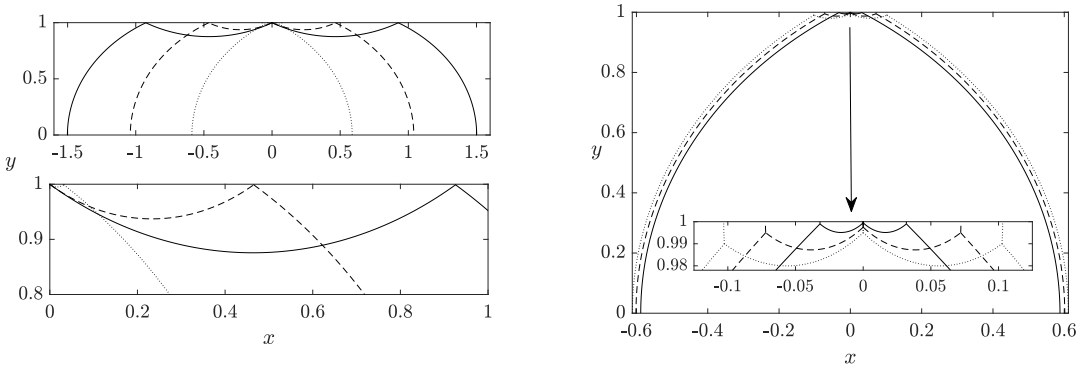

(a) (b)

Figure C.4: (a) System in equilibrium for $l_1^\circ = 0.001$ and $l_2^\circ/l_1^\circ = 0.1$ (solid line), $l_2^\circ/l_1^\circ = 0.3$ (dashed line), and $l_2^\circ/l_1^\circ = 0.5$ (dotted line), with $A_1 = A_3 \approx 0.0780$ and $A_2 \approx 2.5109$; $A_1 = A_3 \approx 0.0198$ and $A_2 \approx 1.7049$; and $A_1 = A_3 \approx 1.1318 \times 10^{-4}$ and $A_2 \approx 0.8483$, respectively. (b) System in equilibrium for $l_2^\circ/l_1^\circ = 0.5$ and $l_1^\circ = 0.001$ (solid line), $l_1^\circ = 0.005$ (dashed line), and $l_1^\circ = 0.01$ (dotted line). Here the areas are $A_1 = A_3 = 1.1318 \times 10^{-4}$ and $A_2 = 0.8483$; $A_1 = A_3 = 7.0803 \times 10^{-4}$ and $A_2 = 0.8832$; and $A_1 = A_3 = 0.0016$ and $A_2 = 0.9080$, respectively.

figure), it follows that films $\jmath_{12}$ and $\jmath_{23}$ turn through an angle of roughly $\pi/3$, so we can deduce that the pressure difference across these films can be estimated as $\pi/(3\mathcal{L}_{23}^\circ)$. Based on this, we can determine that

$$\mathcal{L}_{23}^\circ \approx 2\pi \sqrt{\frac{A_1}{3(2\pi - 3\sqrt{3})}}, \tag{C.20}$$

and that the vertex V_2 to V_3 separation Δx_{23}° can be determined as $\Delta x_{23}^\circ \approx 1/\Delta p_{23}^\circ \approx 3\mathcal{L}_{23}^\circ/\pi$, hence $\Delta x_{23}^\circ \approx 2\sqrt{3\,A_1/(2\pi - 3\sqrt{3})}$. All these values $\mathcal{L}_{23}^\circ$, $\Delta p_{23}^\circ \equiv p_2^\circ - p_3^\circ$, Δx_{23}° and A_1 are of course sensitive to the value of χ. On the other hand, considering that the turning angle of films $\jmath_{02}$ and $\jmath_{20}$ correspond to $|\delta\phi_{02}^\circ| = \delta\phi_{20}^\circ \approx \pi/3$, we can deduce that the area of bubble $\mathcal{B}_2$ can be obtained as a leading-order term (formed by the "wings" swept out by films $\jmath_{02}$ and $\jmath_{20}$ in Figure C.4(a)–(b)) plus an order $A_1^{1/2}$ correction (formed by the rectangle of width $2\Delta x_{12}^\circ$ and unit height, i.e. the part of the channel enclosed between vertices

V_1 and V_3), minus order A_1 corrections (from bubbles $\mathcal{B}_1$ and $\mathcal{B}_3$ bulging into the aforementioned rectangle). Therefore, we can compute that

$$A_2 \approx \left(\frac{4\pi}{9} - \frac{1}{\sqrt{3}}\right) + 12\sqrt{\frac{A_1}{3(2\pi - 3\sqrt{3})}} - 2\,A_1 \approx 0.8189 + 6.6451\sqrt{A_1} - 2A_1. \tag{C.21}$$

The values of A_1 here are in the domain $A_1 \to 0$ (corresponding to $\chi \to 1/2$) to $A_1 \approx 0.1208$ (corresponding to $\chi \to 0$). The domain of A_2 therefore is $0.8189 \leq A_2 \leq 2.8868$. If we now increase χ above the value $1/2$, A_1 remains zero, and A_2 falls from 0.8189 to zero. These are the domains shown in Table C.1 and Table C.2 in the $l_1^\circ \ll 1$ limit. Equation (C.21) has been also plotted in Figure 5.8 in Chapter 5. For any choice of A_1 (and hence, in this instance, A_2 via (C.21)), equations (C.9)–(C.10) are ordinarily used to obtain the values of l_1° and l_2°. However, the structures plotted in Figure C.4 were obtained selecting small but arbitrary values of l_1° and l_2° in the equilibrium (then using equations (C.9)–(C.10) merely to report the areas A_1 and A_2). In Figure C.4(a) we see how when l_1°/l_2° is very small, the order $A_1^{1/2}$ contribution to equation (C.21) (i.e. the part of the enclosed channel between vertices V_1 and V_3) makes a very significant contribution to A_2. A variant of the scenario seen in Figure C.4(b) is that in which the value of l_2°/l_1° is maintained fixed (with a value 0.5) for different arbitrary small $l_1^\circ \ll 1$ values. This is what Figure C.4(b) shows. The area A_1 is now tiny, and A_2 changes comparatively little with l_1°. On the other hand, if $l_1^\circ \ll 1$, but χ increases beyond 0.5, values of A_2 do change. An extreme case occurs with $l_2^\circ \to l_1^\circ$, i.e. $\chi = l_2^\circ/l_1^\circ \to 1$ (see Figure C.5(c) for details). This particular structure, although not easy to set up experimentally (given that bubble $\mathcal{B}_2$ is highly elongated, so bubbles would likely stack in a different fashion, not in a staircase), can be determined analytically as follows. Bubbles $\mathcal{B}_1$ and $\mathcal{B}_3$

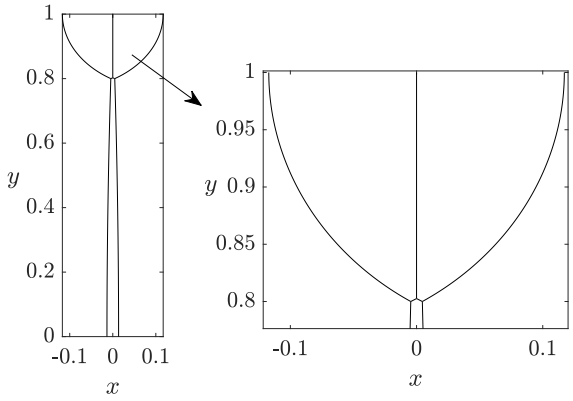

Figure C.5: System in equilibrium for $l_1^\circ = 0.2$ and $l_2^\circ/l_1^\circ \approx 0.9871$, with $A_1 = A_2 = A_3 \approx 0.0168$. The horizontal distance between vertices V_1 and V_3 corresponds to 0.0092 while the horizontal spacing between film $\jmath_{02}$ and $\jmath_{20}$ at the lower channel wall corresponds to 0.0270, indicating that most of the area of A_2 is in the parabolic wings to the left of V_1 and to the right of V_3. The proportion of the area A_2 in the parabolic wings becomes even more significant as $l_1^\circ \to 0$.

can be considered as half a simple lens each, Therefore we find that

$$A_1 = A_3 \approx \frac{1}{2}\left(\frac{4\pi}{9} - \frac{1}{\sqrt{3}}\right) l_1^{\circ 2}, \tag{C.22}$$

so their areas are proportional to $l_1^{\circ 2}$. The pressure of bubbles $\mathcal{B}_1$ and $\mathcal{B}_3$ can be approximated as $p_1^\circ = p_3^\circ \approx \sqrt{3}/(2\,l_1^\circ)$, and the pressure of bubble $\mathcal{B}_2$ can be considered as $p_2^\circ \ll p_3^\circ$, such that film $\jmath_{23}$ with a length $\mathcal{L}_{23}^\circ$ of roughly $2(l_1^\circ - l_2^\circ)$ turns through an angle of $\delta\phi_{23}^\circ \approx \sqrt{3}(1 - l_2^\circ/l_1^\circ)$. Film $\jmath_{20}$ therefore, must turn through exactly the same angle but over a much longer distance, so its curvature is comparatively small. Based on the aforementioned, the area of bubble $\mathcal{B}_2$ can be estimated as the area enclosed by two "wings" of a parabola formed by films $\jmath_{02}$ and $\jmath_{20}$ these wings covering almost all the height of the channel, and almost meeting one another. Hence, we can deduce that

$$A_2 \approx \frac{1}{\sqrt{3}}\left(1 - \frac{l_2^\circ}{l_1^\circ}\right). \tag{C.23}$$

There is an additional contribution to A_2 coming from the region between vertices V_1, V_2 and V_3 and the lower channel wall, but equation (C.23) dominates when l_1° is small. A special case of interest is the monodisperse case in which all bubble areas are equal. By matching equations (C.22) with (C.23), we obtain that for monodispersity.

$$l_2^\circ \approx l_1^\circ - \left(\frac{2\pi}{3\sqrt{3}} - \frac{1}{2}\right) l_1^{\circ 3}. \tag{C.24}$$

This is what we plot in Figure 5.4(a) in Chapter 5.

Although the $l_1^\circ \ll 1$ structures considered above are permissible three-bubble structures, some of them (see e.g. Figure C.4(a)–(b)), do not strictly speaking match the geometrical notion of a staircase in which bubble $\mathcal{B}_1$ would extend furthest to the left out of all the bubbles, and $\mathcal{B}_3$ would extend furthest to the right. As such those structures are less likely to exhibit properties similar to an infinite staircase. A limiting case which is however geometrically more similar to an infinite staircase is the opposite limit $l_1^\circ \to 1$, which we discuss next.

C.1.4.2 $l_1^\circ \to 1$ limit

In the case $l_1^\circ \to 1$, films $\jmath_{02}$ and $\jmath_{20}$ are now very short and almost vertical, whilst film $\jmath_{13}$ is always vertical (in the equilibrium state): see Figure C.6. If we now consider how films $\jmath_{12}$ and $\jmath_{23}$ are oriented at either end, it follows that those films are necessarily flat, in other words the pressure of bubble $\mathcal{B}_2$ is the same as that of bubbles $\mathcal{B}_1$ and $\mathcal{B}_3$. Moreover the area of bubbles $\mathcal{B}_1$ and $\mathcal{B}_3$ tends to be very significant when compared with the opposite cases for which $l_1^\circ \ll 1$. In the first instance we consider a case for which l_1° is close to unity, but $1 - l_2^\circ \gg 1 - l_1^\circ$ (see Figure C.6(a) for details). Here, as we have said, films $\jmath_{12}$ and $\jmath_{23}$ are relatively flat with their curvature approaching zero, so the area of bubble A_1 can be approximated by the area swept out by the arc $\jmath_{01}$ plus a trapezium joining the upper channel wall to vertices V_1 and V_2: the trapezium

area is $\sqrt{3}(l_1^\circ - l_2^\circ)(l_1^\circ + l_2^\circ)/2$. We can deduce that

$$A_1 \approx \frac{1}{2}\left(\frac{4\pi}{9} - \frac{1}{\sqrt{3}}\right) l_1^{\circ 2} + \frac{\sqrt{3}}{2}(l_1^\circ - l_2^\circ)(l_1^\circ + l_2^\circ), \tag{C.25}$$

where recall l_1° is close to unity here. The area of bubble A_2 can be approximated as a pentagon (a leading-order term given by a triangle enclosed by vertices V_1, V_2 and V_3, plus a small rectangle between vertices V_1 and V_3 and the lower channel wall), so we can compute

$$A_2 \approx \sqrt{3}(l_1^\circ - l_2^\circ)^2 + 2\sqrt{3}(l_1^\circ - l_2^\circ)(1 - l_1^\circ). \tag{C.26}$$

Note that A_2 vanishes as $l_2^\circ \to l_1^\circ$, but decreasing l_2° at fixed $l_1^\circ \to 1$, causes both A_1 and A_2 to increase. If $l_2^\circ \to 0$ whilst $l_1^\circ \to 1$, we find $A_1 \approx 1.2755$ and $A_2 \approx 1.7321$. By matching equations (C.25) with (C.26) (i.e. imposing monodispersity), still with $l_1^\circ \to 1$, we determine that

$$l_2^\circ \to \frac{6 - 2\sqrt[4]{3}\sqrt{\pi}}{9} \approx 0.1483. \tag{C.27}$$

This is essentially the situation we plot in Figure C.6(a). Equations (C.25) and (C.26) however are only strictly valid in the limit of $l_1^\circ \to 1$. Therefore, to obtain a relation for the monodisperse l_2° as a function of $(1 - l_1^\circ)$ in the limit of small but finite $(1 - l_1^\circ)$, we need to consider a different set of equations. These equations recognize that for $(1 - l_1^\circ)$ small but non-zero, films $\jmath_{12}$ and $\jmath_{23}$ are not entirely flat. Hence, using equations (C.3)–(C.5) we can determine an order $(1 - l_1^\circ)$ correction for bubble pressures as $p_1^\circ = p_3^\circ \approx \sqrt{3}/2 + (\sqrt{3}/2)(1 - l_1^\circ)$, and $p_2 \approx \sqrt{3}/2 - (\sqrt{3}/4)l_2^\circ(1 - l_1^\circ)/(1 - l_2^\circ)$. Then via equation (C.1) we can deduce the order $(1 - l_1^\circ)$ correction for the horizontal extent of film $\jmath_{01}$ (the same applies to $\jmath_{30}$), so we obtain $\Delta x_{01}^\circ = \Delta x_{30}^\circ \approx 1/\sqrt{3} - (2/\sqrt{3})(1 - l_1^\circ)$. The horizontal distance between vertices V_1 and V_2 (the same applies for V_2 and V_3) is

$$\Delta x_{12}^{\circ} = \Delta x_{23}^{\circ} \approx \sqrt{3}(1 - l_2^{\circ}) - (\sqrt{3}/2) l_2^{\circ}(1 - l_1^{\circ}).$$

Finally the bubble areas $A_1 = A_3$ can be obtained using an order $(1-l_1^{\circ})$ correction to the area of the arc segment of film $\jmath_{01}$ (or $\jmath_{30}$) which can be approximated as the sum of the area in $\mathcal{B}_1$ to the left of V_1 (half a simple lens plus a $(1 - l_1^{\circ})$ correction due to a perturbation in the turning angle of $\delta\phi_{01}^{\circ}$) and the area in $\mathcal{B}_1$ to the right of V_1 which corresponds to a trapezium and a bulge from film $\jmath_{12}$. The area of bubble A_2 can be determined in a similar fashion to C.26, so it can be approximated as pentagon of height $1 - l_2^{\circ}$, enclosed by vertices V_1, V_2 and V_3, minus the bulges from films $\jmath_{12}$ and $\jmath_{23}$. Therefore, by keeping terms up to order $(1 - l_1^{\circ})$ we can determine

$$A_1 \approx \frac{9(2 - 3l_2^{\circ 2}) + 4\sqrt{3}\pi}{18\sqrt{3}} - \frac{(9(l_2^{\circ 2} + l_2^{\circ} + 8) + 8\sqrt{3}\pi)(1 - l_1^{\circ})}{36\sqrt{3}}, \tag{C.28}$$

$$A_2 \approx \sqrt{3}(1 - l_2^{\circ})^2 + \frac{(1 - l_2^{\circ})(4 - l_2^{\circ})(1 - l_1^{\circ})}{2\sqrt{3}}. \tag{C.29}$$

By matching equations (C.28) and (C.29) for monodispersity, again keeping the terms up to order $(1 - l_1^{\circ})$ we can deduce that

$$l_2^{\circ} \approx \frac{6 - 2\sqrt[4]{3}\sqrt{\pi}}{9} + \frac{((14\sqrt[4]{3}\sqrt{\pi} + 15)\pi + 51\sqrt[4]{27}\sqrt{\pi})(1 - l_1^{\circ})}{108\pi}. \tag{C.30}$$

This is what we have plotted in Figure 5.4(a) in Chapter 5.

On the other hand, we can also consider the limit $l_1^{\circ} \to 1$ in a very polydisperse scenario, with bubble $\mathcal{B}_2$ much smaller than bubbles $\mathcal{B}_1$ and $\mathcal{B}_3$. In this case $1-l_2^{\circ}$ (whilst larger than $1 - l_1^{\circ}$) is not considered to be orders of magnitude larger. In this case we can put $l_1^{\circ} \to 1$ and $l_2^{\circ} \to 1$ in equation (C.25) to deduce A_1 whereas A_2 remains a pentagon so equation (C.26) continues to apply. Indeed we are free to fix the area of bubbles $A_1 = A_3$ and change the area of bubble A_2, by changing l_1°, without l_2° changing too much (see Figure C.6(b) for details). It is interesting

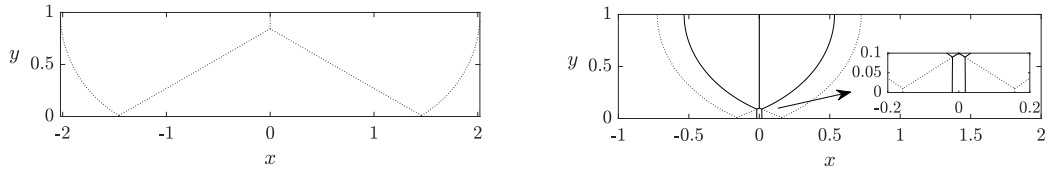

(a) (b)

Figure C.6: (a) System in equilibrium for $l_1^\circ = 0.99$ and $l_2^\circ/l_1^\circ \approx 0.1584$, with $A_1 = A_2 = A_3 \approx 1.2343$. (b) System in equilibrium for $l_1^\circ = 0.99$ and $l_2^\circ = 0.9$ (dotted line), with $A_1 = A_3 \approx 0.5458$, and $A_2 \approx 0.0173$ (when pushed out of equilibrium, this system is expected to undergo a $T1_{l3}$). We also plot a system in the equilibrium for $l_1^\circ = 0.95$ and $l_2^\circ = 0.9$ (solid line), with $A_1 = A_3 \approx 0.3483$, and $A_2 \approx 0.0034$ (when pushed out of equilibrium, this system is expected to undergo a $T1_c$).

to contrast the structure for $l_1^\circ \ll 1$ and comparatively large l_2°/l_1° ($\chi > 1/2$), with the structure in Figure C.6(b) (both l_1° and l_2°/l_1° close to unity). In the former case, bubbles $\mathcal{B}_1$ and $\mathcal{B}_3$ are small, and have 4 sides each, including the channel wall. Films $\jmath_{01}$ and $\jmath_{30}$ turn through very significant angles, due to large pressures in p_1° and p_3°. This is reminiscent of what happens in a simple lens with small area [19]. Hence we expect this system might have a behaviour akin to that of a simple lens: in particular decreasing the size of the small bubble might make the system (when pushed out of equilibrium) better able to resist $T1$. On the other hand, in Figure C.6(b) it is bubble $\mathcal{B}_2$ that has small area. This bubble now has 5 sides, including the channel wall. The pressure p_2° is comparatively small, and none of the films now turns through a significant angle, at least as long as l_1° and l_2°/l_1° remain close to unity. The resulting shape is no longer reminiscent of a simple lens, so there is no guarantee that shrinking bubble $\mathcal{B}_2$ will make the out-of-equilibrium system better able to resist $T1$. We will return to this point in section C.5.4.

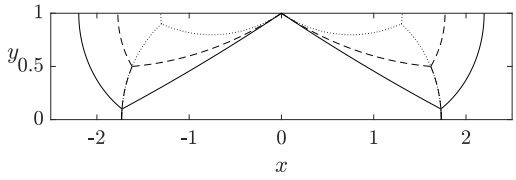

Figure C.7: $l_2^\circ \to 0$ limit. Dotted line: $l_1^\circ = 0.1$, with $A_1 = A_3 = 0.1953$ and $A_2 = 2.7482$. Dash-dotted line: $l_1^\circ = 0.5$, with $A_1 = A_3 = 0.5647$ and $A_2 = 2.2878$. Solid line: $l_1^\circ = 0.9$, with $A_1 = A_3 = 1.1009$ and $A_2 = 1.8458$.

C.1.4.3 $l_2^\circ \to 0$ limit

Note that the system considered above $l_1^\circ \to 1$, gives (for any chosen l_2° or analogously for any chosen A_2) the largest possible A_1 for an equilibrium staircase structure to exist. Is it is also possible to consider, for any chosen l_1° or analogously any chosen A_1, a maximum allowed A_2. This corresponds to the limit $l_2^\circ \to 0$. This limit is easy to compute given that in the limit $l_2^\circ \to 0$, equation (C.7) gives $p_2^\circ = \sqrt{3}/2$. Hence the amount that film $\jmath_{20}$ turns (over a vertical distance $1 - l_1^\circ$) is well defined. This in turn fixes the amount that film $\jmath_{30}$ turns over a vertical distance l_1° (specifically $\delta\phi_{20}^\circ = \mathrm{asin}((\sqrt{3}/2)(1 - l_1^\circ))$), and hence the value p_3° is fixed too (specifically $p_1^\circ = p_3^\circ = (\sqrt{3}\sqrt{1 - 3\,l_1^{\circ 2} + 6\,l_1^\circ})/(4\,l_1^\circ) - \sqrt{3}/(4\,l_1^\circ) + \sqrt{3}/4$). Knowing the two pressures p_2° and p_3° then defines the shape of film $\jmath_{23}$. Formulae for A_1 and A_2, as given by equations (C.9) and (C.10), then result, and since $l_2^\circ \to 0$ here, areas can therefore be computed solely in terms of l_1°. As mentioned in section C.1.4.1, and given in Tables C.1 and C.2, these give the largest allowed A_2 for any chosen l_1° and its value varies between 2.8868 when $l_1^\circ \to 0$ and 1.7321 when $l_1^\circ \to 1$, while $A_1 \approx 0.1208$ when $l_1^\circ \to 0$ (albeit still with $l_2^\circ / l_1^\circ \ll 1$), and $A_1 \approx 1.2755$ when $l_1^\circ \to 1$. In Figure C.7 we plot sample bubble shapes for a selection of l_1°.

C.1.4.4 $l_2^\circ \to l_1^\circ$ limit

The last case we consider here, consists of the limit of $l_2^\circ \to l_1^\circ$ for arbitrary l_1°. In this limit, the shape of bubble $\mathcal{B}_2$ (except when $l_1^\circ \to 1$) is highly elongated (hence not easy to realise experimentally). In this case the bubbles $\mathcal{B}_1$ and $\mathcal{B}_3$ are both half-lenses, so they have a well-defined formula for area in terms of l_1° (see equation (C.22)). Meanwhile bubble $\mathcal{B}_2$ has a negligible area when $l_2^\circ \to l_1^\circ$ (see Table C.2). When l_1° is small, most of the area of $\mathcal{B}_2$ is in the parabolic wings (as discussed in section C.1.4.1), but when l_1° is larger, most of the area of $\mathcal{B}_2$ is in the pentagon underneath vertices V_1, V_2 and V_3 (see section C.1.4.2 for details). The reason that the parabolic wings become less important when l_1° is larger, is that the pressures p_1° and p_3° are not quite so large, and hence pressure differences $p_1^\circ - p_2^\circ$ and $p_3^\circ - p_2^\circ$ are not so large either. Hence, for a given value of $l_1^\circ - l_2^\circ$, films $\jmath_{12}$ and $\jmath_{23}$ turn through a lesser angle, as do therefore $\jmath_{02}$ and $\jmath_{20}$, and the area in the parabolic wings is proportionately less. Nevertheless, regardless of whether l_1° is small or large, A_2 vanishes in the limit $l_2^\circ \to l_1^\circ$, making the details how that area is distributed across bubble $\mathcal{B}_2$ be of limited interest.

Out-of-equilibrium configurations for all the various types of structures described above will be studied in section C.5. The different structures we explore here exhibit different types of $T1$, as presented in section 5.5 in Chapter 5. Moreover, in section C.5 we will study how $p_{b,T1}$ (and also the critical imposed back pressure p_b^*) changes as different values of l_1° and l_2° are considered, implying therefore different values of A_1 and A_2. What we will find is that certain of these structures (particularly those with small $l_1^\circ \to 0$ and l_2° neither too small nor too close to l_1°) can resist $T1$ out to very large p_b values whereas others undergo $T1$ at much more modest $p_{b,T1}$ (particularly those with $l_1^\circ \to 0$ and $l_2^\circ \to l_1^\circ$ leading to a $T1_c$, or those with $l_1^\circ \to 0$ and $l_2^\circ \ll l_1^\circ$ leading to $T1_u$).

C.2 Displacement of film coordinates due to motion

In this section we compute x and y coordinates for moving films, parametrically in terms of orientation angle ϕ_{ij}, as explained in section C.2.1. Then, in section C.2.2 we obtain expressions to compute film length $\mathfrak{s}_{ij}$ as a function of orientation angle ϕ_{ij}, expressions that can be inverted to obtain ϕ_{ij} as a function of $\mathfrak{s}_{ij}$. The equations obtained are used to compute x and y coordinates for moving films, parametrically in terms of $\mathfrak{s}_{ij}$, as explained in section C.2.3. The various results presented here are used by section 5.4 in Chapter 5.

C.2.1 Film coordinates expressed as a function of orientation angle ϕ_{ij}

Here, we integrate equations (5.7) and (5.8) given in Chapter 5 in terms of ϕ_{ij}, in the domain of orientation angles established in Table 5.1 (see Chapter 5), in order to obtain $x_{ij}(\phi_{ij})$ vs $y_{ij}(\phi_{ij})$ film coordinates. The shape of the moving films, is then given by the bubble pressures (p_1, p_2 and p_3), turning angles ($\delta\phi_{02}$, $\delta\phi_{13}$ and $\delta\phi_{20}$, which govern the domain of ϕ_{ij} values for each and every film) and the migration velocity v. In addition, it is convenient to define a mobility parameter a_{ij} as

$$a_{ij} = \frac{v}{\Delta p_{ij}}, \tag{C.31}$$

which is the ratio between the migration velocity v and the driving pressures across films Δp_{ij} (where recall Δp_{ij} is measured from left to right). Therefore, we can express equation (5.7) as

$$\frac{\mathrm{d}x_{ij}}{\mathrm{d}\phi_{ij}} = -\frac{1}{v}\left(\frac{a_{ij}\sin(\phi_{ij})}{1 - a_{ij}\cos(\phi_{ij})}\right), \tag{C.32}$$

and equation (5.8) as

$$\frac{\mathrm{d}y_{ij}}{\mathrm{d}\phi_{ij}} = \frac{1}{v}\left(\frac{a_{ij}\cos\phi_{ij}}{1 - a_{ij}\cos(\phi_{ij})}\right). \tag{C.33}$$

Hence, integrating equation (C.32) in terms of ϕ_{ij}, from some initial orientation $\phi_{ij,0}$ to ϕ_{ij}, we obtain that

$$x_{ij}(\phi_{ij}) = x_{ij,0} + \frac{1}{v}\log\left(1 - \frac{a_{ij}\ \cos(\phi_{ij,0})}{1 - a_{ij}\ \cos(\phi_{ij})}\right). \tag{C.34}$$

To integrate equation (C.33), we have to consider two different cases, firstly for values of $|a_{ij}| < 1$ and then for $|a_{ij}| > 1$. In both cases we integrate in terms of ϕ_{ij}, from $\phi_{ij,0}$ to ϕ_{ij} (see Table 5.1 in Chapter 5). Hence, for $|a_{ij}| < 1$ we obtain that

$$y_{ij}(\phi_{ij}) = y_{ij,0} + \frac{1}{v}\left(\phi_{ij,0} - \phi_{ij} + \frac{2\,\mathrm{atan}\left(\bar{a}_{ij}\tan\left(\frac{\phi_{ij}}{2}\right)\right) - 2\,\mathrm{atan}\left(\bar{a}_{ij}\tan\left(\frac{\phi_{ij,0}}{2}\right)\right)}{\sqrt{1 - a_{ij}^2}}\right), \tag{C.35}$$

$$\bar{a}_{ij} = \sqrt{\frac{1 + a_{ij}}{1 - a_{ij}}},$$

and when $|a_{ij}| > 1$, that

$$y_{ij}(\phi_{ij}) = y_{ij,0} + \frac{1}{v}\left(\phi_{ij,0} - \phi_{ij} + \frac{2\,\mathrm{atanh}\left(\hat{a}_{ij}\tan\left(\frac{\phi_{ij}}{2}\right)\right) - 2\,\mathrm{atanh}\left(\hat{a}_{ij}\tan\left(\frac{\phi_{ij,0}}{2}\right)\right)}{\hat{a}_{ij}(1 - a_{ij})}\right), \tag{C.36}$$

$$\hat{a}_{ij} = \sqrt{\frac{a_{ij} + 1}{a_{ij} - 1}}.$$

Equations (C.34) and (C.35)–(C.36) (when expressed in a short hand notation) correspond to equations (C.34) and (C.35) in Chapter 5. Once we know the x_{ij} and y_{ij} coordinates for each film, we can compute the shape of the moving

structure.

C.2.2 Distance along film $\mathfrak{s}_{ij}$ and its relation to orientation angle ϕ_{ij}

We measure each film's energy via its length $\mathcal{L}_{ij}$ and therefore the system's energy (as already mentioned in section C.1.2) as the sum of all film lengths. When the system is set in motion by imposing a back pressure p_b, the energy typically increases up to the point where a topological transformation occurs. Some systems exhibit (as already mentioned where in section 5.2.4 in Chapter 5), at a certain critical pressure, a saddle-node bifurcation at which a stable solution branch meets an unstable branch, the latter typically with higher energy than the former. It is therefore of interest to track how the energy changes after the saddle-node bifurcation. In order to compute energy, we need a formula to relate film length $\mathcal{L}_{ij}$ to the total angle $\delta\phi_{ij}$ through which films turn along their length. To obtain that we need, in turn, a formula relating distance $\mathfrak{s}_{ij}$ measured to an arbitrary point along a film to the orientation angle ϕ_{ij} at that same point. Additionally, as the migration velocity increases, films of a system comprised of large bubbles and therefore with long films, might become flat. In such cases we can no longer readily parametrize films in terms of orientation angle ϕ_{ij}. Nevertheless if (as mentioned in section 5.4.2 in Chapter 5) we know distance measured along a film $\mathfrak{s}_{ij}$ we can obtain how orientation angles ϕ_{ij} depend on location even if the film asymptotes towards being entirely flat. The above arguments highlight that having a relation between the variables $\mathfrak{s}_{ij}$ and ϕ_{ij} is very valuable.

Such a relation can be obtained by integrating equation (5.2) (given in Chapter 5), as before, for each film from $\phi_{ij,0}$ (film's initial point) to ϕ_{ij} (with $\phi_{ij,0}$ as

Appendix C. Supplementary material: Foam flow in confined straight channels

specified in Table 5.1 of Chapter 5). First we rearrange equation (5.2), to obtain

$$\frac{\mathrm{d}\mathfrak{s}_{ij}}{\mathrm{d}\phi_{ij}} = \pm\frac{a_{ij}}{v}\left(\frac{1}{1-a_{ij}\cos(\phi_{ij})}\right), \tag{C.37}$$

and then we integrate it. For $|a_{ij}| < 1$ we obtain that

$$\mathfrak{s}_{ij}(\phi_{ij}) = \pm\frac{2\,a_{ij}}{v\,\bar{a}_{ij}(1-a_{ij})}\left(\operatorname{atan}\left(\bar{a}_{ij}\tan\left(\frac{\phi_{ij}}{2}\right)\right) - \operatorname{atan}\left(\bar{a}_{ij}\tan\left(\frac{\phi_{ij,0}}{2}\right)\right)\right), \tag{C.38}$$

$$\bar{a}_{ij} = \sqrt{\frac{1+a_{ij}}{1-a_{ij}}},$$

and for $|a_{ij}| > 1$, we obtain

$$\mathfrak{s}_{ij}(\phi_{ij}) = \pm\frac{2\,a_{ij}}{v\,\hat{a}_{ij}(1-a_{ij})}\left(\operatorname{atanh}\left(\hat{a}_{ij}\tan\left(\frac{\phi_{ij}}{2}\right)\right) - \operatorname{atanh}\left(\hat{a}_{ij}\tan\left(\frac{\phi_{ij,0}}{2}\right)\right)\right), \tag{C.39}$$

$$\hat{a}_{ij} = \sqrt{\frac{a_{ij}+1}{a_{ij}-1}}.$$

In equations (C.38) and (C.39), the sign of "$\pm$" is set as $-$ if $\mathfrak{s}_{ij}$ is measured downwards, and as $+$ if $\mathfrak{s}_{ij}$ is measured upwards, such that $\mathfrak{s}_{ij}$ is always a positive quantity. Equations (C.38) and (C.39) evaluated at $\phi_{ij} = \phi_{ij,\mathcal{L}}$ are then used to obtain film lengths $\mathcal{L}_{ij}$, which are in turn used to compute system energy E.
In the above, we have obtained the length of a film $\mathfrak{s}_{ij}$ as a function of orientation angle ϕ_{ij}. Now we can invert equations (C.38) and (C.39), to express ϕ_{ij} as a function of $\mathfrak{s}_{ij}$. Hence, when $|a_{ij}| < 1$, we find that

$$\phi_{ij}(\mathfrak{s}_{ij}) = 2\operatorname{atan}\left(\frac{1}{\bar{a}_{ij}}\tan\left(\pm\mathfrak{s}_{ij}\frac{v\bar{a}_{ij}(1-a_{ij})}{2\,a_{ij}} + \operatorname{atan}\left(\bar{a}_{ij}\tan\left(\frac{\phi_{ij,0}}{2}\right)\right)\right)\right), \tag{C.40}$$

and when $|a_{ij}| > 1$ we find that

$$\phi_{ij}(\mathfrak{s}_{ij}) = 2\,\mathrm{atan}\left(\frac{1}{\hat{a}_{ij}}\tanh\left(\pm\mathfrak{s}_{ij}\frac{v\,\hat{a}_{ij}(1-a_{ij})}{2\,a_{ij}} + \mathrm{atanh}\left(\hat{a}_{ij}\tan\left(\frac{\phi_{ij,0}}{2}\right)\right)\right)\right). \tag{C.41}$$

Given values of $\mathfrak{s}_{ij}$ in the domain $0 \leq \mathfrak{s}_{ij} \leq \mathcal{L}_{ij}$, the corresponding range of orientations ϕ_{ij} can be determined and values of film turning angles $\delta\phi_{ij}$ then follow.

C.2.3 Film coordinates expressed as a function of distance along film $\mathfrak{s}_{ij}$

Substituting (C.40) and (C.41) into equations (5.3), (5.4), (5.5) and (5.6) in Chapter 5, as applicable, we obtain for $|a_{ij}| < 1$ that

$$x_{ij}(\mathfrak{s}_{ij}) = x_{ij,0} - \frac{\bar{\alpha}_{ij}}{\bar{\beta}_{ij}(1-\bar{\alpha}_{ij}^2)}\log\left(\frac{(1+\tan^2(\pm\mathfrak{s}_{ij}\,\bar{\beta}_{ij}+\bar{\gamma}_{ij}))(1+\bar{\alpha}_{ij}^2\tan^2(\bar{\gamma}_{ij}))}{(1+\bar{\alpha}_{ij}^2\tan^2(\pm\mathfrak{s}_{ij}\,\bar{\beta}_{ij}+\bar{\gamma}_{ij}))(1+\tan^2(\bar{\gamma}_{ij}))}\right), \tag{C.42}$$

and

$$y_{ij}(\mathfrak{s}_{ij}) = y_{ij,0} + \frac{1}{\bar{\beta}_{ij}(\bar{\alpha}_{ij}^2-1)}\Big(-(\pm\mathfrak{s}_{ij}\,\bar{\beta}_{ij}(1+\bar{\alpha}_{ij}^2)) + 2\bar{\alpha}_{ij}\Big(\mathrm{atan}(\bar{\alpha}_{ij}\tan(\pm s\,\bar{\beta}_{ij}+\bar{\gamma}_{ij})) - \mathrm{atan}(\bar{\alpha}_{ij}\tan(\bar{\gamma}_{ij}))\Big)\Big), \tag{C.43}$$

with $\bar{\alpha}_{ij} = 1/\bar{a}_{ij}$, $\bar{\beta}_{ij} = v\,\bar{a}_{ij}(1-a_{ij})/(2\,a_{ij})$, and $\bar{\gamma}_{ij} = \mathrm{atan}(\bar{a}_{ij}\tan(\phi_{ij,0}/2))$. Meanwhile for $|a_{ij}| > 1$ we obtain that

$$x_{ij}(\mathfrak{s}_{ij}) = x_{ij,0} - \frac{\hat{\alpha}_{ij}}{\hat{\beta}_{ij}(1+\hat{\alpha}_{ij}^2)}\log\left(\frac{(1+\hat{\alpha}_{ij}^2\tanh(\pm\mathfrak{s}_{ij}\,\hat{\beta}_{ij}+\hat{\gamma}_{ij}))(1-\tanh^2(\hat{\gamma}_{ij}))}{(1-\tanh^2(\pm\mathfrak{s}_{ij}\,\hat{\beta}_{ij}+\hat{\gamma}_{ij}))(1+\hat{\alpha}_{ij}^2\tanh^2(\hat{\gamma}_{ij}))}\right), \tag{C.44}$$

and

$$y_{ij}(\mathfrak{s}_{ij}) = y_{ij,0} + \frac{1}{\hat{\beta}_{ij}(1+\hat{\alpha}_{ij}^2)}\Big((\pm\mathfrak{s}_{ij}\,\hat{\beta}_{ij}(1-\hat{\alpha}_{ij}^2)) + 2\hat{\alpha}_{ij}\Big(\operatorname{atan}(\hat{\alpha}_{ij}\tanh(\pm\mathfrak{s}_{ij}\,\hat{\beta}_{ij}+\hat{\gamma}_{ij})) - \operatorname{atan}(\bar{\alpha}_{ij}\tanh(\bar{\gamma}_{ij}))\Big)\Big), \tag{C.45}$$

with $\hat{\alpha}_{ij} = 1/\hat{a}_{ij}$, $\hat{\beta}_{ij} = v\,\hat{a}_{ij}(1-a_{ij})/(2\,a_{ij})$, and $\hat{\gamma}_{ij} = \operatorname{atanh}(\hat{a}_{ij}\tan(\phi_{ij,0}/2))$. As before the $-$ sign applies if $\mathfrak{s}_{ij}$ is measured downwards, and the $+$ sign applies if it is measured upwards, as specified in Chapter 5. Using equations (C.42)–(C.45), we can obtain film coordinates x_{ij} and y_{ij} as a function of film length $\mathfrak{s}_{ij}$. These relationships, which are represented in short hand notation in equations (C.42)–C.43, can be used even when the films become asymptotically flat.

C.3 Inherently stable structure additional results

Some systems as specified in section 5.3 in Chapter 5, might reach a so-called inherently stable structure without undergoing any topological transformation, even for an arbitrarily large imposed back pressure. This structure is characterized by the fact that films do not suffer any further deformation as the imposed back pressure keeps increasing. In this limit, film curvature along them vanishes, films then becoming entirely flat, apart from sharp curvature at one of their end points. Here we obtain expressions to compute the area of bubbles in this limit, which are the same expression from those discussed in section C.3.1, but written in a different fashion. This is done with the objective of determining how bubble areas $A_1 = A_3$ and A_2 are related with each each other for a fixed $\mathcal{L}_{30}$ variable, but varying $\mathcal{L}_{12}$ (recalling $\mathcal{L}_{ij}$ is the length of film $\jmath_{ij}$). This relation, for each fixed $\mathcal{L}_{30}$ as seen by the thin dotted lines in Figure 5.8 in Chapter 5. Then, in sec-

tion C.3.2 we compute the system energy for a given set of bubble areas, related with a specific structure in the equilibrium state, obtained via the corresponding l_1° and l_2° values.

C.3.1 Bubble areas in terms of $\mathcal{L}_{12}$

As seen in section 5.3 in Chapter 5, for a fixed value of $\mathcal{L}_{30}$, we can obtain the area of bubbles A_1 and A_2 as a function of $\mathcal{L}_{12}$. In Figure 5.8 two limiting cases are plotted, for $\mathcal{L}_{12} \to 0$ and for $\mathcal{L}_{02} \to 0$ (the last implying that $\mathcal{L}_{12} \to (1-\mathcal{L}_{30})/\cos(\phi_{12,0})$). For any specified $\mathcal{L}_{30}$, a thin line in Figure 5.8 connects these two limit points, relating bubble areas A_1 and A_2 as $\mathcal{L}_{12}$ varies. Here we reexpress equations (5.11)–(5.12) from Chapter 5 as a leading-order term (obtained as a function of $\mathcal{L}_{30}$) plus order $\mathcal{L}_{12}$ and $\mathcal{L}_{12}^2$ terms. Therefore we obtain,

$$A_1 = A_{1(0)} + A_{1(1)}\mathcal{L}_{12} + A_{1(2)}\mathcal{L}_{12}^2, \tag{C.46}$$

$$A_2 = A_{2(0)} + A_{2(1)}\mathcal{L}_{12} + A_{2(2)}\mathcal{L}_{12}^2, \tag{C.47}$$

where

$$A_{1(0)} = \mathcal{L}_{30}^2(\tan(\delta\phi_{01}) - \tan(\delta\phi_{13}))/2, \tag{C.48}$$

$$A_{1(1)} = \mathcal{L}_{30}(\sin(|\phi_{12,0}|) + \tan(\delta\phi_{01})\cos(\phi_{12,0})), \tag{C.49}$$

$$A_{1(2)} = (\cos(\phi_{12,0})\sin(|\phi_{12,0}|) + \tan(\delta\phi_{01})\cos(\phi_{12,0})^2)/2, \tag{C.50}$$

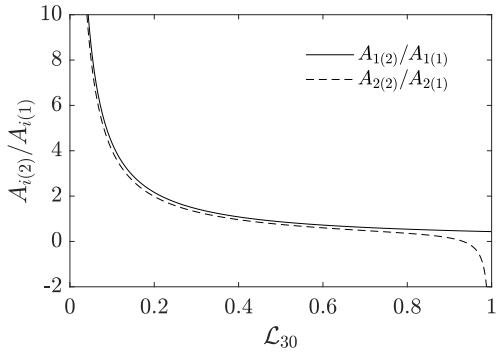

Figure C.8: Value of $A_{1(2)}/A_{1(1)}$ for bubble A_1 vs value of $A_{2(2)}/A_{2(1)}$ for bubble A_2, for values of $\mathcal{L}_{30} \in (0, 1)$.

and

$$A_{2(0)} = (\mathcal{L}_{30}(1-\mathcal{L}_{30})\tan(\delta\phi_{01}) - 2\mathcal{L}_{30}(1-\mathcal{L}_{30})\tan(\delta\phi_{30}))/2, \tag{C.51}$$

$$A_{2(1)} = (2(1-\mathcal{L}_{30})\sin(|\phi_{12,0}|) + (1-\mathcal{L}_{30})\tan(\delta\phi_{30})\cos(\phi_{12,0})), \tag{C.52}$$

$$A_{2(2)} = ((1-2\mathcal{L}_{30})\cos(\phi_{12,0})\sin(|\phi_{12,0}|) + (1-\mathcal{L}_{30})\tan(\delta\phi_{01})\cos(\phi_{12,0})^2)/(2\mathcal{L}_{30}) \tag{C.53}$$

where the values of $\delta\phi_{01}$, $\delta\phi_{13}$ and $\phi_{12,0}$ are given in section 5.3.1 in Chapter 5. To determine if the thin dotted lines in Figure 5.8 in Chapter 5 are exactly straight lines or merely almost straight, we compute $A_{1(2)}/A_{1(1)}$ vs $A_{2(2)}/A_{2(1)}$. As seen in Figure C.8 these two ratios are almost equal over nearly the entire $\mathcal{L}_{30}$ domain. This implies that if $\mathcal{L}_{30}$ is held fixed but $\mathcal{L}_{12}$ varies, the amount that A_1 changes is very nearly proportional to the amount that A_2 changes, which explains the almost straight lines in Figure 5.8 in Chapter 5. The aforementioned ratios $A_{1(2)}/A_{1(1)}$ vs $A_{2(2)}/A_{2(1)}$ only differ significantly when $\mathcal{L}_{30} \to 1$. However in that limit, it is necessarily the case that $\mathcal{L}_{12} \ll 1$, so the order $\mathcal{L}_{12}^2$ terms do not affect the areas much in equations (C.46)–(C.47), and a near straight relation between A_2 vs A_1 is recovered regardless of the values of $A_{1(2)}$ and $A_{2(2)}$.

C.3.2 System energies for $p_b \gg 1$

Now we continue to consider inherently stable states in which $\mathcal{L}_{30}$ is given, and neither $\mathcal{L}_{12} \to 0$, nor $\mathcal{L}_{02} \to 0$ (section 5.3.2 in Chapter 5). As shown in Figure 5.8(b) in Chapter 5, there is well specified domain of values of A_2 vs A_1 that can in principle generate the migration configuration corresponding to an inherently stable structure. This A_2 vs A_1 domain can also be expressed in terms a well defined domain in l_1° vs l_2°/l_1° space. This is what Figure 5.10(b) in Chapter 5 shows. We compute the energy E_{inh} for the inherently stable system in these permitted domains as follows. Once $\mathcal{L}_{12}$, $\mathcal{L}_{23}$ and $\mathcal{L}_{30}$ have been obtained as explained in section 5.3 in Chapter 5 we can compute $\mathcal{L}_{01}$, $\mathcal{L}_{02}$, $\mathcal{L}_{13}$ and $\mathcal{L}_{20}$ by simple geometry as

$$\mathcal{L}_{01} = \frac{\mathcal{L}_{30} + \mathcal{L}_{12}\cos(\phi_{12,0})}{\cos(\delta\phi_{01})}, \tag{C.54}$$

$$\mathcal{L}_{02} = 1 - (\mathcal{L}_{30} + \mathcal{L}_{12}\cos(\phi_{12,0})), \tag{C.55}$$

$$\mathcal{L}_{13} = \frac{\mathcal{L}_{30}}{\cos(\delta\phi_{13})}, \tag{C.56}$$

$$\mathcal{L}_{20} = 1 - \mathcal{L}_{30}, \tag{C.57}$$

where recall values for $\delta\phi_{01}$, $\delta\phi_{13}$ and $\phi_{12,0}$ are found in section 5.3.1 in Chapter 5. Then the energy E_{inh} can be computed as the sum of all the $\mathcal{L}_{ij}$.

Here we compute the system energy E_{inh} for three fixed values of l_1° values of l_2°/l_1° as given in Figure 5.8(b), in each case for the selected values of l_2°/l_1° (see Figure 5.8 for details). In addition we also plot, as a comparison, the energy E° of those systems in the equilibrium. This is what Figure C.9 shows. Here as expected the energy in the equilibrium E° is less than the energy E_{inh}. The value of E_{inh} in this case shows us the maximum energy that such a system might reach as the inherently stable state is approached.

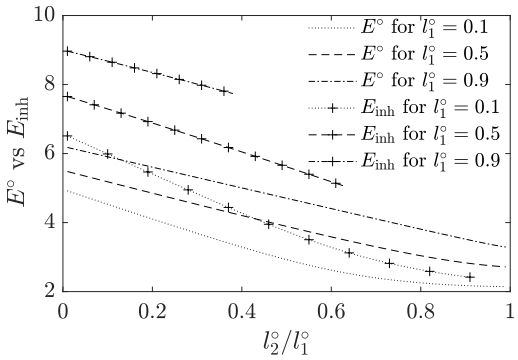

Figure C.9: System energy $E_{\rm inh}$ for the structures that survive up to arbitrary large velocities (also known as the inherently stable state) vs system energies in the equilibrium E°. Note that for each l_1°, the inherently stable structure itself (and hence the value of $E_{\rm inh}$) is only defined over a limited domain of l_2°/l_1°.

C.4 Weakly driven system: $p_b \ll 1$ limit

Here we explain how to go from a system at equilibrium, to one slightly perturbed away from equilibrium. Consider, in the first instance, a three-bubble system at equilibrium, as given in section 5.2.3 in Chapter 5, set by fixing l_1° and l_2°. For such a system the pressure difference across the structure is equal to zero. If we now impose back pressure $p_b > 0$ upon the structure, this will move at an unknown migration velocity v. A steady state solution for this migration must then be obtained. If we consider that $p_b \ll 1$, we can find the values of the variables that define the system structure out of equilibrium via perturbations in terms of the variables at equilibrium. Therefore, perturbed response variables are $p_i \approx p_i^\circ + \hat{\delta} p_i$ for the bubble pressures, $\delta\phi_{ij} \approx \delta\phi_{ij}^\circ + \hat{\delta}(\delta\phi_{ij})$ for the film total turning angles, and $\phi_{ij,0} \approx \phi_{ij,0}^\circ + \hat{\delta}\phi_{ij,0}$ for the orientation angle at the start of each film: note that $\phi_{ij,0}$ is known for films that start on walls, but not known a priori for films that start at vertices (specifically in this system those starting at vertex V_2), but can be determined in terms of the film turning angle $\delta\phi_{13}$. We need to deal with 11 response variables: a velocity, 3 bubble pressures and 7 turning angles. However, there are 4 relations between turning angles (2 at vertex

V_1 and 2 at vertex V_2: the relations are found in Table 5.1 in Chapter 5), so 4 of the total turning angles $\delta\phi_{ij}$ can be eliminated, leaving just $\delta\phi_{02}$, $\delta\phi_{20}$ and $\delta\phi_{13}$ as the unknown angles. We also consider that pressure differences across films $\Delta p_{ij} = \Delta p_{ij}^{\circ} + \hat{\delta}(\Delta p_{ij})$ where $\hat{\delta}(\Delta p_{ij}) = \hat{\delta}p_i - \hat{\delta}p_j$, with i denoting the bubble on the left and j the one on the right. Here p_b, v, $\hat{\delta}p_i$, $\hat{\delta}\phi_{ij,\mathcal{L}}$, and $\hat{\delta}\phi_{ij,0}$ are all first-order quantities. Additionally, since $\delta\phi_{13}^{\circ} = 0$, we can express $\hat{\delta}\phi_{13,\mathcal{L}} \equiv \delta\phi_{13}$ (another first-order quantity). Then, via first-order Taylor expansion of equation (5.2) in powers of the small parameter ϕ_{13} (with $0 \leq \phi_{13} \leq \delta\phi_{13}$), it is obtained after integration that

$$\delta\phi_{13} \approx (l_2^{\circ} + \hat{\delta}L_2)(v - (\hat{\delta}p_1 - \hat{\delta}p_3)) \approx l_2^{\circ}(v - (\hat{\delta}p_1 - \hat{\delta}p_3)), \tag{C.58}$$

where $\hat{\delta}L_2$ is the perturbation of the film length l_2°. Therefore, as established in Table 5.1 we can readily express $\hat{\delta}\phi_{12,0} \approx -\delta\phi_{13}$ and $\hat{\delta}\phi_{23,0} \approx \delta\phi_{13}$. Hence, it is possible to obtain approximated system variables for an arbitrary small $p_b \ll 1$, by using the seven system constraints established in section 5.4.3. The procedure starts by substituting the previously defined perturbed response variables in equations (5.7) and (5.8) as given in Chapter 5. Then via a first-order Taylor expansion in terms of the small parameters $\hat{\delta}(\Delta p_{ij})$ and v, retaining the first-order terms, we obtain

$$\frac{\mathrm{d}x_{ij}}{\mathrm{d}\phi_{ij}} \approx \left(v\frac{\mathrm{d}y_{ij}^{\circ}}{\mathrm{d}\phi_{ij}} - \frac{\hat{\delta}(\Delta p_{ij})}{\Delta p_{ij}^{\circ}} + 1 \right) \frac{\mathrm{d}x_{ij}^{\circ}}{\mathrm{d}\phi_{ij}}, \tag{C.59}$$

$$\frac{\mathrm{d}y_{ij}}{\mathrm{d}\phi_{ij}} \approx \left(v\frac{\mathrm{d}y_{ij}^{\circ}}{\mathrm{d}\phi_{ij}} - \frac{\hat{\delta}(\Delta p_{ij})}{\Delta p_{ij}^{\circ}} + 1 \right) \frac{\mathrm{d}y_{ij}^{\circ}}{\mathrm{d}\phi_{ij}}, \tag{C.60}$$

where $y_{ij}^{\circ} = y_{ij}^{\circ}(\phi_{ij})$ corresponds to the y coordinate of a film in the equilibrium. This has been obtained already in section C.1. Then integrating (C.60) in terms

of ϕ_{ij} from $\phi^\circ_{ij,0}+\hat{\delta}\phi_{ij,0}$ to ϕ_{ij}, and Taylor expanding in terms of $\hat{\delta}\phi_{ij,0}$, we obtain

$$y_{ij} \approx y^\circ_{ij,0} + \hat{\delta}y_{ij,0} + v\frac{\sin(2\phi_{ij}) - \sin(2\phi^\circ_{ij,0}) + 2(\phi_{ij}-\phi^\circ_{ij,0})}{4{\Delta p^\circ_{ij}}^2} - \hat{\delta}(\Delta p_{ij})\frac{\sin(\phi_{ij})-\sin(\phi^\circ_{ij,0})}{{\Delta p^\circ_{ij}}^2} - \hat{\delta}\phi_{ij,0}\frac{\cos(\phi^\circ_{ij,0})}{\Delta p^\circ_{ij}} + \frac{\sin(\phi_{ij})-\sin(\phi^\circ_{ij,0})}{\Delta p^\circ_{ij}}, \tag{C.61}$$

where $y^\circ_{ij,0} = y^\circ_{ij}(\phi^\circ_{ij,0})$, such that $y_{ij}(\phi_{ij,0}) \approx y_{ij}(\phi^\circ_{ij,0}+\hat{\delta}\phi_{ij,0}) \approx y^\circ_{ij,0}+\hat{\delta}y_{ij,0}$. Here the vertical $y_{ij,0}$ location at the start of each film is known for films that start on walls, but not known a priori for films that start at a vertex. Then, we can obtain $y_{ij}(\phi_{ij,\mathcal{L}}) \approx y_{ij}(\phi^\circ_{ij,\mathcal{L}}+\hat{\delta}\phi_{ij,\mathcal{L}}) \approx y^\circ_{ij,\mathcal{L}}+\hat{\delta}y_{ij,\mathcal{L}}$ by substituting $\phi_{ij,\mathcal{L}} \approx \phi^\circ_{ij,\mathcal{L}}+\hat{\delta}\phi_{ij,\mathcal{L}}$ in place of ϕ_{ij} in equation (C.61), and Taylor expanding in powers of the small parameter $\hat{\delta}\phi_{ij,\mathcal{L}}$, considering just the first-order terms, we deduce

$$\begin{aligned} y_{ij}(\phi_{ij,\mathcal{L}}) \approx y^\circ_{ij,0} + \hat{\delta}y_{ij,0} + v\frac{\sin(2\phi^\circ_{ij,\mathcal{L}}) - \sin(2\phi^\circ_{ij,0}) + 2(\phi^\circ_{ij,\mathcal{L}}-\phi^\circ_{ij,0})}{4{\Delta p^\circ_{ij}}^2} \\ - \hat{\delta}(\Delta p_{ij})\frac{\sin(\phi^\circ_{ij,\mathcal{L}})-\sin(\phi^\circ_{ij,0})}{{\Delta p^\circ_{ij}}^2} - \hat{\delta}\phi_{ij,0}\frac{\cos(\phi^\circ_{ij,0})}{\Delta p^\circ_{ij}} + \hat{\delta}\phi_{ij,\mathcal{L}}\frac{\cos(\phi^\circ_{ij,\mathcal{L}})}{\Delta p^\circ_{ij}} \\ \frac{\sin(\phi^\circ_{ij,\mathcal{L}})-\sin(\phi^\circ_{ij,0})}{\Delta p^\circ_{ij}}, \end{aligned}$$

$$y_{ij}(\phi_{ij,\mathcal{L}}) \approx y^\circ_{ij,0} + Y_{ij}(v, \hat{\delta}(\Delta p_{ij}), \hat{\delta}\phi_{ij,0}, \hat{\delta}\phi_{ij,\mathcal{L}}), \tag{C.62}$$

where Y_{ij} is a first-order quantity, that gives the variation in the vertical location of each film. Exceptionally, since in equilibrium, film $\jmath_{13}$ is a straight line, we can approximate $y_{13}(\phi_{13,\mathcal{L}}) \approx 1 - l^\circ_2 - \hat{\delta}L_2$, where $\hat{\delta}L_2$ is the perturbation to the length of this film, so the initial film points for films $\jmath_{12}$ and $\jmath_{23}$ can be estimated as $y_{12}(\phi_{12,0}) = y_{23}(\phi_{23,0}) \approx 1 - l^\circ_2 - \hat{\delta}L_2$, with $y^\circ_{12,0} = 1 - l^\circ_2$, and $\hat{\delta}y_{12,0} = -\hat{\delta}L_2$ (similarly for film $\jmath_{23}$). All other films start on walls at known y locations and with known orientations. Using equation (C.62), in combination with vertex meeting rule constraints on y coordinates, and the angle relations given in Table 5.1, we

can determine four linear equations in terms of the equilibrium parameters and seven unknown variables v, $\hat{\delta}p_1$, $\hat{\delta}p_2$, $\hat{\delta}p_3$, $\hat{\delta}\phi_{02,\mathcal{L}}$, $\hat{\delta}\phi_{20,\mathcal{L}}$, $\hat{\delta}L_2$, with $\delta\phi_{13}$ having already been given by equation (C.58). The symbols without $\hat{\delta}$ are already first-order quantities. Hence, we can deduce the following equations

$$\begin{aligned} Y_{12}(v,\hat{\delta}(\Delta p_{12}),\hat{\delta}\phi_{12,0},\hat{\delta}\phi_{12,\mathcal{L}}) &= Y_{01}(v,\hat{\delta}(\Delta p_{01}),\hat{\delta}\phi_{01,0},\hat{\delta}\phi_{01,\mathcal{L}}) \\ &= Y_{02}(v,\hat{\delta}(\Delta p_{02}),\hat{\delta}\phi_{02,0},\hat{\delta}\phi_{02,\mathcal{L}}), \quad \text{(C.63)} \end{aligned}$$

$$\begin{aligned} Y_{23}(v,\hat{\delta}(\Delta p_{23}),\hat{\delta}\phi_{23,0},\hat{\delta}\phi_{23,\mathcal{L}}) &= Y_{30}(v,\hat{\delta}(\Delta p_{30}),\hat{\delta}\phi_{30,0},\hat{\delta}\phi_{30,\mathcal{L}}) \\ &= Y_{20}(v,\hat{\delta}(\Delta p_{20}),\hat{\delta}\phi_{20,0},\hat{\delta}\phi_{20,\mathcal{L}}). \quad \text{(C.64)} \end{aligned}$$

In addition we can obtain three more equations, based on bubble area constraints. Therefore, we obtain

$$\begin{aligned} A_1 \approx \int_0^{\phi^\circ_{01,\mathcal{L}}+\hat{\delta}\phi_{01,\mathcal{L}}} (1-y_{01})\frac{\mathrm{d}x_{01}}{\mathrm{d}\phi_{01}}\mathrm{d}\phi_{01} + \int_{\phi^\circ_{12,\mathcal{L}}+\hat{\delta}\phi_{12,\mathcal{L}}}^{\phi^\circ_{12,0}+\hat{\delta}\phi_{12,0}} (1-y_{12})\frac{\mathrm{d}x_{12}}{\mathrm{d}\phi_{12}}\mathrm{d}\phi_{12} \\ + \int_{l^\circ_2+\hat{\delta}L_2}^{0} (x_{13,v}-x_{13}(s))\mathrm{d}\mathfrak{s}_{13}, \quad \text{(C.65)} \end{aligned}$$

$$\begin{aligned} A_2 \approx \int_0^{\phi^\circ_{02,\mathcal{L}}+\hat{\delta}\phi_{02,\mathcal{L}}} y_{02}\frac{\mathrm{d}x_{02}}{\mathrm{d}\phi_{02}}\mathrm{d}\phi_{02} + \int_{\phi^\circ_{12,\mathcal{L}}+\hat{\delta}\phi_{12,\mathcal{L}}}^{\phi^\circ_{12,0}+\hat{\delta}\phi_{12,0}} y_{12}\frac{\mathrm{d}x_{12}}{\mathrm{d}\phi_{12}}\mathrm{d}\phi_{12} + \int_{\phi^\circ_{23,0}+\hat{\delta}\phi_{23,0}}^{\phi^\circ_{23,\mathcal{L}}+\hat{\delta}\phi_{23,\mathcal{L}}} y_{23}\frac{\mathrm{d}x_{23}}{\mathrm{d}\phi_{23}}\mathrm{d}\phi_{23} \\ + \int_{\phi^\circ_{20,\mathcal{L}}+\hat{\delta}\phi_{20,\mathcal{L}}}^{0} y_{20}\frac{\mathrm{d}x_{20}}{\mathrm{d}\phi_{20}}\mathrm{d}\phi_{20}, \\ \text{(C.66)} \end{aligned}$$

Appendix C. Supplementary material: Foam flow in confined straight channels

$$A_3 \approx \int_{\phi^\circ_{23,0}+\hat{\delta}\phi_{23,0}}^{\phi^\circ_{23,\mathcal{L}}+\hat{\delta}\phi_{23,\mathcal{L}}} (1-y_{23})\frac{\mathrm{d}x_{23}}{\mathrm{d}\phi_{23}}\mathrm{d}\phi_{23} + \int_{\phi^\circ_{30,\mathcal{L}}+\hat{\delta}\phi_{30,\mathcal{L}}}^{0} (1-y_{30})\frac{\mathrm{d}x_{30}}{\mathrm{d}\phi_{30}}\mathrm{d}\phi_{30} + \int_0^{l_2^\circ+\hat{\delta}L_2} (x_{13,v}-x_{13}(s))\mathrm{d}\mathfrak{s}_{13}, \quad \text{(C.67)}$$

where $x_{13,v}$ is the location where film $\jmath_{13}$ meets the vertex V_2. Here an arbitrary point on that same film has $x_{13}(\mathfrak{s}_{13}) \approx x_{13,w}+|\kappa_{13}|\mathfrak{s}_{13}^2/2$, with $x_{13,w}$ here denoting the location where film $\jmath_{13}$ meets the wall, and with κ_{13} denoting curvature. Hence $x_{13,v} \approx x_{13,w}+|\kappa_{13}|l_2^{\circ 2}/2$. Here, as in Chapter 5, the distance along films $\jmath_{13}$ is measured downwards, so that the curvature $\kappa_{13} \equiv -\mathrm{d}\phi_{13}/\mathrm{d}\mathfrak{s}_{13}$ as defined in Chapter 5 is negative for this film. Hence, $|\kappa_{13}| = v-(\hat{\delta}p_1-\hat{\delta}p_3) > 0$, as obtained via equation (5.2) (given in Chapter 5) with $\cos(\phi_{13}) \approx 1$ since $\phi_{13} \ll 1$ along film $\jmath_{13}$. This verifies incidentally that κ_{13} is near uniform along this film. Taylor expanding equations (C.65)–(C.67) up to first-order terms in the seven unknown small variables v, $\hat{\delta}p_1$, $\hat{\delta}p_2$, $\hat{\delta}p_3$, $\hat{\delta}\phi_{02,\mathcal{L}}$, $\hat{\delta}L_2$ and $\hat{\delta}\phi_{20,\mathcal{L}}$, we can obtain three linear equations in terms of the equilibrium parameters and seven unknown variables (all remaining unknowns being expressed in terms of these). Therefore, we obtain

$$A_1 \approx A_1^\circ + \hat{\delta}A_1, \quad \text{(C.68)}$$

$$A_2 \approx A_2^\circ + \hat{\delta}A_2, \quad \text{(C.69)}$$

$$A_2 \approx A_3^\circ + \hat{\delta}A_3, \quad \text{(C.70)}$$

where equations (C.68)–(C.70) must match the bubble areas given by equations (C.9) and (C.10). Finally, by solving the seven linear equations (equations (C.63), (C.64) and (C.68)–(C.70)), it is possible to calculate the value of the perturbation variables v, $\hat{\delta}p_1$, $\hat{\delta}p_2$, $\hat{\delta}p_3$, $\hat{\delta}\phi_{02,\mathcal{L}}$, $\hat{\delta}L_2$ and $\hat{\delta}\phi_{20,\mathcal{L}}$, as a function of any arbitrary

small $p_b \ll 1$. Thus we obtain all the perturbed values that we require $p_1 \approx p_1^\circ + \hat{\delta}p_1$, $p_2 \approx p_2^\circ + \hat{\delta}p_2$, $p_3 \approx p_3^\circ + \hat{\delta}p_3$, $\delta\phi_{02} \approx \delta\phi_{02}^\circ + \hat{\delta}(\delta\phi_{02})$, $\delta\phi_{13} \approx l_2^\circ(v - (\hat{\delta}p_1 - \hat{\delta}p_3))$ (via (C.58)) and $\delta\phi_{20} = \delta\phi_{20}^\circ + \hat{\delta}(\delta\phi_{20})$, as a function of the equilibrium variables. Note in particular that $\hat{\delta}(\delta\phi_{02}) = \hat{\delta}\phi_{02,\mathcal{L}}$ and $\hat{\delta}(\delta\phi_{20}) = \hat{\delta}\phi_{20,\mathcal{L}}$ which follows because $\phi_{02,0} = \phi_{20,0} \equiv 0$.

C.5 Steady state out-of-equilibrium additional results

As the system moves faster due to an increasing imposed driving pressure, not only do films deform and reorient as seen in section 5.5 in Chapter 5, but also the internal bubble pressures increase. This is what we show in section C.5.1. Then in section C.5.2 we compute the film energy for various systems again as they move and deform as a driving pressure is increased. Finally in sections C.5.3–C.5.4 we study how $p_{b,T1}$ (or p_b^*) varies for systems in a number of special cases, including limiting cases as defined in section C.1.4. The results discussed here thereby supplement those already shown in section 5.5.

C.5.1 Imposed back pressure p_b vs p_1, p_2 and p_3

In this section we study, for four particular systems set up at equilibrium by fixing l_1° and l_2°, how the pressures p_1, p_2 and p_3 change as p_b increases, up to the systems reaching a topological transformation quasistatically, or else reaching a saddle-node bifurcation, or alternatively attaining an inherently stable structure that does not change anymore as we keep increasing p_b. In Figure C.10(a) we plot data for $l_1^\circ = 0.5$, with $l_2^\circ/l_1^\circ = 0.41$. Here we track the steady state solution along the stable solution branch by using p_b as control variable, eventually the system reaches a saddle-node bifurcation with $p_b^* \approx 7.86$ (solid lines in Figure

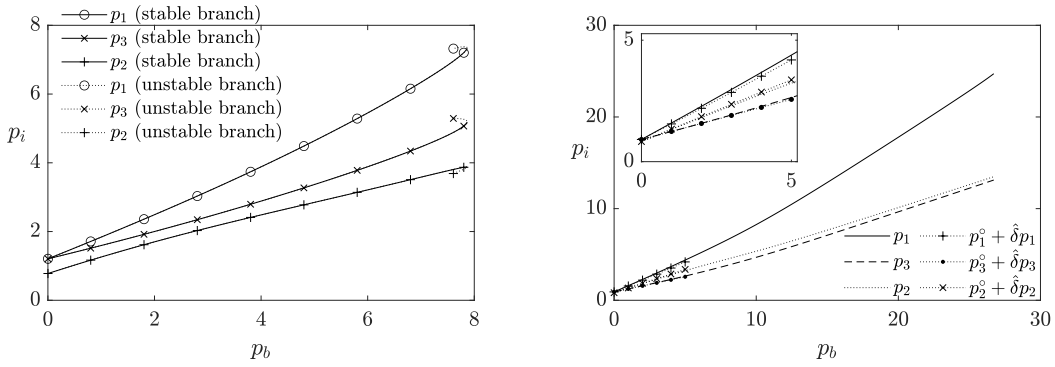

(a) (b)

Figure C.10: (a) Steady state pressures p_1, p_2 and p_3 as a function of the imposed back pressure p_b. (a) $l_1^\circ = 0.5$ with $l_2^\circ/l_1^\circ = 0.41$. (b) $l_1^\circ = 0.9$ with $l_2^\circ/l_1^\circ = 0.5$. Here we also plot the bubble pressures obtained via the weakly driven solution.

C.10(a)), where by switching control variable as explained in Chapter 5 section 5.4.5, we track the steady state solution through the unstable solution branch up to $T1^{\phi}_{u,\delta\phi_{20}}$ now with p_1 and p_3 increasing as p_b decreases down to a $T1$ at $p_{b,T1} \approx 7.61$. In contrast p_2 decreases on this branch.

In Figure C.10(b) we plot data for $l_1^\circ = 0.9$, with $l_2^\circ/l_1^\circ = 0.5$. Here we track p_1, p_2 and p_3 vs p_b, up to $p_b^* \approx 26.71$, the system undergoing a $T1^s_{c,p_b}$ topological transformation. In addition we have also included the values of bubble pressures obtained via the weakly driven solution, as deduced in section C.4. This is shown up to pressures of $p_b = 5$. Even though this is formally a low velocity (and hence low p_b) approximate solution, it still manages to fit the data comparatively well (see inset of Figure C.10(b)). On the other hand, as mentioned before, there is a set of systems that do not undergo any topological transformation, for any arbitrarily large imposed back pressure. These systems are intrinsically stable, and the structures keep their shape for any imposed back pressure. Hence, as explained in section 5.3 in Chapter 5 we can still obtain solutions for these systems no matter how large p_b becomes. Here, when we impose back pressure $p_b \gg 1$, we can approximate pressures p_2 and p_3, by $p_2 \approx p_3 \approx p_b/2$ and $p_1 \approx p_b(\sqrt{3}/2+1)/2$,

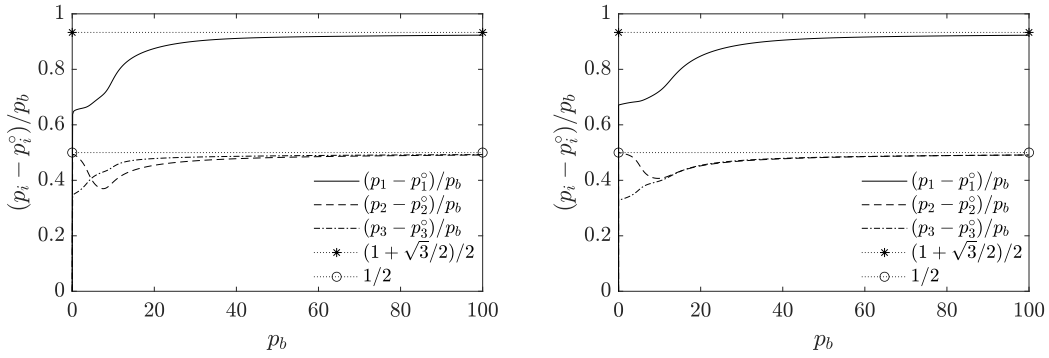

Figure C.11: (a) Steady state pressures p_1, p_2 and p_3 (normalised here as $(p_i - p_i^\circ)/p_b$) as a function of the imposed back pressure p_b for systems that attain inherently stable structures. (a) $l_1^\circ = 0.78$ with $l_2^\circ/l_1^\circ = 0.21$. (b) $l_1^\circ = 0.9$ with $l_2^\circ/l_1^\circ = 0.23$. In the large p_b limit, known values of p_i/p_b and hence of $(p_i - p_i^\circ)/p_b$ are predicted in section 5.3 of Chapter 5.

while the imposed back pressure and velocity can be related as $v \approx p_b/2$. These results are plotted in Figure C.11. In Figure C.11(a) we plot for $l_1^\circ = 0.78$ with $l_2^\circ/l_1^\circ = 0.21$, while in Figure C.11(b) we plot for $l_1^\circ = 0.9$ with $l_2^\circ/l_1^\circ = 0.23$. For large imposed back pressures, each case matches with what was obtained in section 5.3.

C.5.2 System energy

We now compute the energy for systems with values of $l_1^\circ \in [0.5, 0.9]$, as considered before (see e.g. Figure C.10 in section C.5.1), and different values of l_2°/l_1°. As mentioned earlier, we calculate the energy E of a given system as the total length of the films that comprise it. To determine this, we use equations (C.38)–(C.39), whichever corresponds to each film, evaluating $\mathfrak{s}_{ij}$ for $\phi_{ij} = \phi_{ij,\mathcal{L}}$ (see Table 5.1 in Chapter 5) to obtain $\mathcal{L}_{ij}$. From Figure C.12 we can see that, in cases which exhibit saddle-node bifurcations, beyond the bifurcation, the energy continues to increase even though the back pressure decreases. High energy branches like these

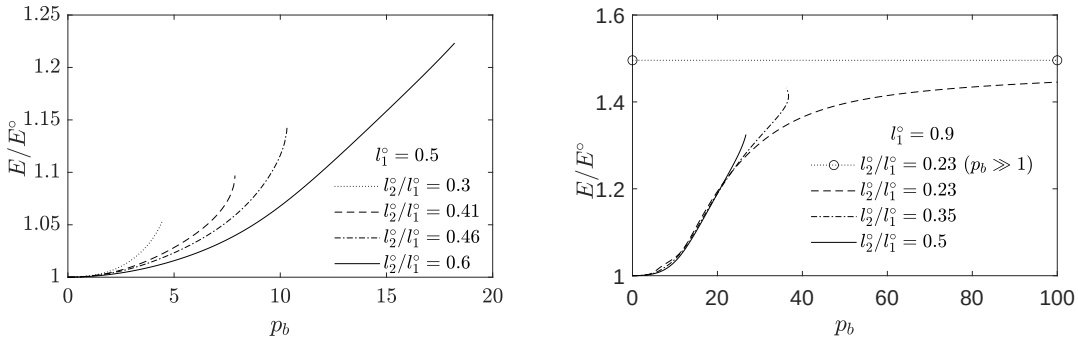

Figure C.12: System energy E (relative to equilibrium energy E°) vs imposed back pressure p_b computed for (a) $l_1^\circ = 0.5$, and (b) $l_1^\circ = 0.9$ and various l_2°/l_1° values. In particular, for $l_1^\circ = 0.5$ and $l_2^\circ/l_1^\circ = 0.41$ and $l_2^\circ/l_1^\circ = 0.46$ (in (a)) and for $l_1^\circ = 0.9$ and $l_2^\circ/l_1^\circ = 0.35$ (in (b)) the systems reach saddle-node bifurcations even before reaching the maximum possible energy (where they undergo topological transformations). Here we also plot the energy for an inherently stable structure ($p_b \gg 1$), as given by the system in (b) with $l_2^\circ/l_1^\circ = 0.23$. In this case the energy $E/E^\circ \approx 1.496$ as predicted for the selected l_1° and l_2° values by the theory presented in section 5.3.1 and section C.3.2.

are expected to be unstable. This same behaviour was found in [19], for the simple lens system. An additional behaviour we see in Figure C.12 is that for systems that are inherently stable, energy eventually approaches a final limiting state associated with the flat film structure analysed in section 5.3.1 and section C.3.2.

C.5.3 Critical imposed back pressure for monodisperse systems

In Chapter 5 (section 5.5.2) we examined values of critical imposed back pressure for $T1$ for a number of combinations of l_1° and l_2°. In the present section, we do the same for a monodisperse system with $A_1 = A_2 = A_3$. In each studied case, for any selected l_1°, the value of l_2° is set to ensure monodispersity (see Figure 5.4(a) in Chapter 5 for details). In Figure C.13, we plot $p_{b,T1}$ for values

Appendix C. Supplementary material: Foam flow in confined straight channels

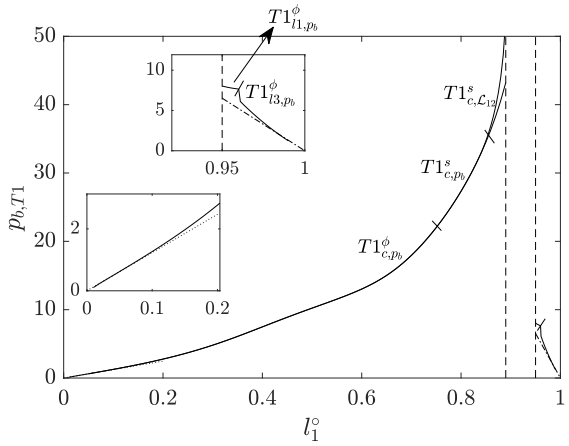

Figure C.13: Imposed back pressure $p_{b,T1}$ (in the majority of the cases it coincides with p_b^*) for monodisperse systems. Here we consider systems set up in the equilibrium for values of $l_1^{\circ} \in [0.01, 0.99]$ and values of l_2° to ensure monodispersity (see Figure 5.4(a) in Chapter 5). The dotted line corresponds to a numerical approximation $p_{b,T1} \approx 12.35\, l_1^{\circ}$ obtained for small $l_1^{\circ} \in [0.001, 0.01]$ values. The dash-dotted line corresponds to a numerical approximation $p_{b,T1} \approx 121.3(1 - l_1^{\circ})$ obtained for values of $l_1^{\circ} \in [0.99, 0.999]$.

of $l_1^{\circ} \in [0.01, 0.99]$. Here we can see that as l_1° increases from zero, $p_{b,T1}$ also increases, the system undergoing $T1^{\phi}_{c,p_b}$ (and eventually $T1^{s}_{c,p_b}$). There is however a band of l_1° values between $l_1^{\circ} \approx 0.89$ and $l_1^{\circ} \approx 0.95$ (see the vertical dashed lines in Figure C.13) for which an inherently stable state is possible, with the three-bubble system surviving out to arbitrarily large pressure. Then, for even larger values of l_1°, $p_{b,T1}$ decreases to zero as l_1° approaches unity. In the case of $l_1^{\circ} \ll 1$ we obtain that $p_{b,T1} \approx 12.35\, l_1^{\circ}$ (dotted lined), the system undergoing $T1^{\phi}_{c,p_b}$ in all the studied cases. Meanwhile when $l_1^{\circ} \to 1$ we find that $p_{b,T1} \approx 121.3(1 - l_1^{\circ})$ (dash-dotted line), the system undergoing $T1^{\phi}_{l3,p_b}$ in all the studied cases. Thus neither in the limit when $l_1^{\circ} \to 0$ nor in the limit when $l_1^{\circ} \to 1$ is the monodisperse case particularly stable. This is an interesting contrast from the simple lens which was highly stable in the $l_1^{\circ} \to 0$ limit in particular [19]. However in both instances ($l_1^{\circ} \to 0$ and $l_1^{\circ} \to 1$) discussed here, the (monodisperse) three-bubble system is exhibiting a type of $T1$ (respectively a $T1_c$ or a $T1_{l3}$) that the simple lens did not

exhibit. Further analysis of (polydisperse) systems in the $l_1^\circ \ll 1$, $l_1^\circ \to 1$, and the $l_2^\circ \to 0$ limiting cases, as described in sections C.1.4, are offered in the follow section.

C.5.4 Critical imposed back pressure in limiting cases

An interesting analysis to consider consists of determining how $p_{b,T1}$ (or p_b^*) behaves with bubble size in some of the limiting cases described in section C.1.4. In what follows we treat cases with with $l_1^\circ \ll 1$, then cases with $l_1^\circ \to 1$ and finally we study the $l_2^\circ \to 0$ limit. The $l_2^\circ \to l_1^\circ$ limiting case (with arbitrary l_1°) is not considered here for reasons already explained in section C.1.4.4 (bubble $\mathcal{B}_2$ despite having tiny area is highly elongated, which would be a difficult state to set up).

C.5.4.1 $l_1^\circ \ll 1$ limit

We start by considering cases in which $l_1^\circ \ll 1$ for $l_2^\circ = \chi\, l_1^\circ$, with $0 < \chi < 1$. Here we have computed $p_{b,T1}$ for four different small values of $l_1^\circ \in [0.01, 0.04, 0.07, 0.1]$ (see Figure C.14). In this limit, the relation between $A_1 = A_3$ and A_2 is sensitive to χ (see section C.1.4.1 for details). For values of $0 < \chi < 0.5$, regardless of how small l_1° becomes, A_2 and A_1 attain finite areas, but in all cases A_2 exceeds A_1. Moreover, in this case, the point of attachment of vertex V_3 is close to the right hand end of $\mathcal{B}_3$ as Figure C.4(a) shows.

The case of $1/2 < \chi < 1$, meanwhile permits the size of bubble $A_1 = A_3$ to shrink as l_1° shrinks, although A_2 is typically larger, except in the limit as χ also becomes very close to unity (see e.g. Figure C.4(c)). In what follows the $p_{b,T1}$ data are presented, with Figure C.14(a)–(b) focussing on $0 < \chi < 0.5$ and Figure C.14(c)–(d) focussing on $0.5 < \chi < 1$. The data are also subjected to various different rescalings. In Figure C.14(b)–(d) we plot for instance $l_1^\circ p_{b,T1}$ rather than just $p_{b,T1}$, which allows us to compare the effect of having different small but finite

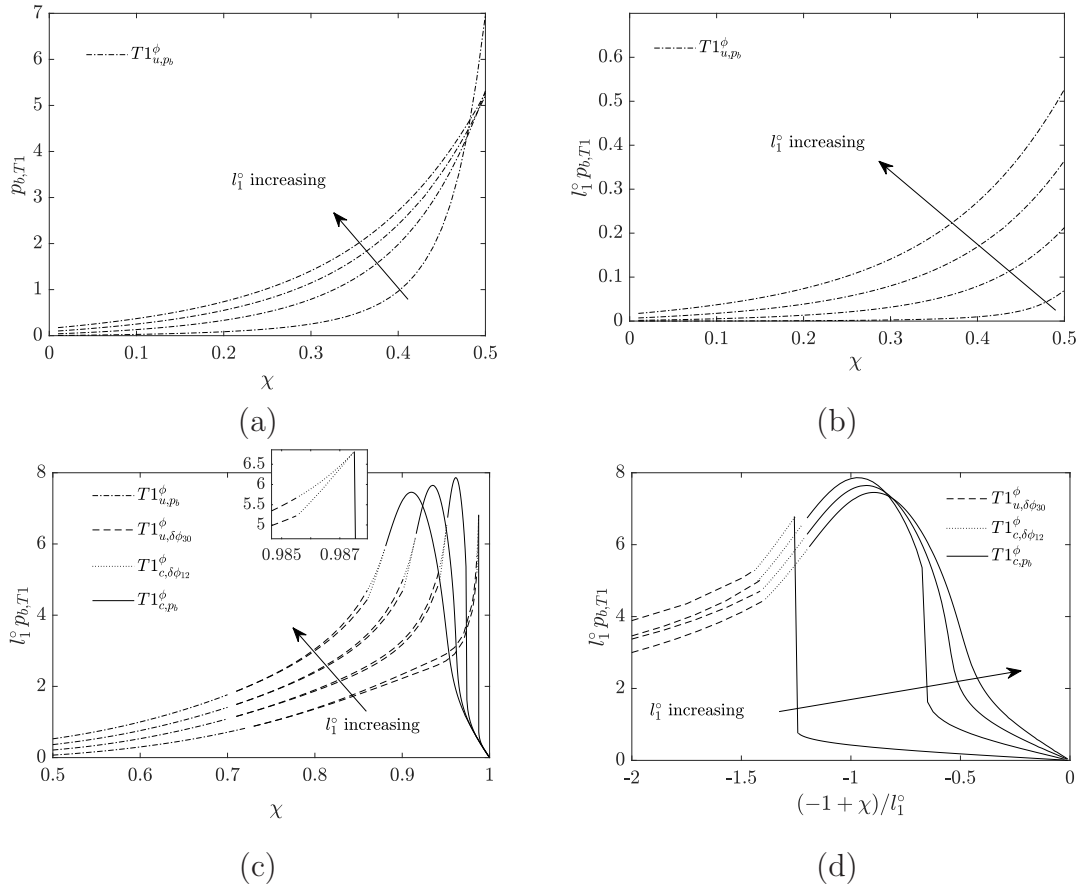

Figure C.14: Imposed back pressure at the topological transformation point $p_{b,T1}$ (which for the most part coincides with p_b^*) for values of $l_1^\circ \in [0.01, 0.04, 0.07, 0.1]$. Data are plotted against $\chi \equiv l_2^\circ/l_1^\circ$. In (a), plotted on the domain $0 < \chi < 0.5$ (or more specifically for $\chi \in [0.01, 0.5]$). In (b), again on the domain $0 < \chi < 0.5$, we plot $l_1^\circ p_{b,T1}$ instead of just $p_{b,T1}$: now values of l_1° increase uniformly from bottom to the top. In (c) we continue to plot $l_1^\circ p_{b,T1}$ but now on the domain $0.5 < \chi < 1$, or more specifically $\chi \in [0.5, 0.99]$. Moreover in (d), we plot $l_1^\circ p_{b,T1}$ vs $(-1+\chi)/l_1^\circ$.

values of l_1°. For $\chi < 0.5$ in all the studied cases the system undergoes $T1^{\phi}_{u,p_b}$ topological transformations (see Figure C.14(a) and (b)). This is unsurprising given that (even at equilibrium) vertex V_3 is already far towards the right of bubble $\mathcal{B}_3$, making it easy for that vertex and that bubble to slip apart when the system starts moving, and that then produces a $T1_u$.
Moreover, as Figure C.4(a) shows, decreasing χ causes bubble $\mathcal{B}_3$ to grow in area, meaning that in relative terms (i.e. relative to either the horizontal end-to-end length of bubble $\mathcal{B}_3$ or the vertical distance $\mathcal{B}_3$ protrudes into the channel) the point of attachment of vertex V_3 on bubble $\mathcal{B}_3$, shifts increasingly far to the right and upwards as $\chi = l_2^\circ/l_1^\circ$ decreases. This makes the system even weaker, i.e. even more susceptible to $T1_u$, so that $p_{b,T1}$ falls as χ decreases. The simple lens [19] with small $l_1^\circ \ll 1$ did not exhibit anywhere near this level of weakness to $T1_u$, because at equilibrium the vertex always attached at the point on the lens bubble furthest from the upper channel wall: it was not then so easy for the vertex and bubble to slip apart.

In Figure C.14(a)–(b), we see that as χ increases towards 0.5 and (in Figure C.14(c)) even beyond that into the domain $\chi > 0.5$, the system becomes much stronger, in the sense that the value of $p_{b,T1}$ corresponding to $T1^{\phi}_{u,p_b}$ increases greatly. Moreover as χ increases well above 0.5, the systems eventually start to exhibit $T1^{\phi}_{u,\delta\phi_{30}}$ (on an assumed unstable solution branch) or $T1^{\phi}_{c,\delta\phi_{12}}$ (again on an assumed unstable solution branch). On these unstable solution branches we show $p_{b,T1}$ with the lower down lines (pressure at which the system undergoes a topological transformation), and p_b^* with the higher up lines (maximum imposed back pressure corresponding here to a saddle-node bifurcation). As χ continues to increase, the system eventually switches again to a $T1^{\phi}_{c,p_b}$.

For any l_1°, observe that there is a well defined $\chi = l_2^\circ/l_1^\circ$ (dependent upon l_1°)

at which $p_{b,T1}$ attains an overall maximum allowed value: this corresponds to the strongest or most stable system that is permitted for that l_1° values. Figure C.14(d) makes it clear that this occurs at a χ value that is relatively close to $1 - l_1^\circ$. Note also that, since in Figure C.14(c)–(d) we have plotted $l_1^\circ p_{b,T1}$ rather than just $p_{b,T1}$, by comparing the data at different l_1°, it is clear that this maximum allowed $p_{b,T1}$ scales proportionally to $(l_1^\circ)^{-1}$. A similar scaling is seen for the strength of the simple lens system in [19]. The similar behaviour is not surprising since (as already noted in section C.1.4.1) the three-bubble system with small l_1° but $1/2 < \chi < 1$ has a number of similarities with the simple lens. The pressures in bubbles $\mathcal{B}_1$ and $\mathcal{B}_3$ are now very large, and as a result of this, films $\jmath_{01}$ and $\jmath_{30}$ despite having small length, turn through significant angles.

Increasing χ even further beyond the point at which $p_{b,T1}$ has its maximum allowed value, we see that $p_{b,T1}$ drops several orders of magnitude as we approach $\chi \to 1$ (see right hand side of Figure C.14(c)). The system is now very susceptible indeed to $T1^{\phi}_{c,p_b}$ topological transformation (a type of transformation that incidentally is not even available to the simple lens). The reason for this high susceptibility to $T1_c$ is that for χ extremely close to unity, at equilibrium film $\jmath_{12}$ has now become very short indeed (Figure C.4(c) shows a typical shape). It is this film that, when the system driven out-of-equilibrium, shrinks away to produce the $T1_c$.

C.5.4.2 $l_1^\circ \to 1$ and $l_2^\circ \to 1$ limit

In Figure C.15(a) and (b), we show $p_{b,T1}$, and $p_{b,T1}/(1 - l_2^\circ)$, respectively, considering systems with values of $l_1^\circ \to 1$ and with $l_2^\circ \to l_1^\circ$ (which makes $A_1 = A_3 \gg A_2$). More specifically we consider a set of comparatively large values of l_2° ($l_2^\circ \in [0.9, 0.93, 0.96, 0.99]$), with l_1° varying in the domain from $l_2^\circ < l_1^\circ < 1$. Consequently $(1 - l_1^\circ)/(1 - l_2^\circ)$ increases from 0 to 1 as l_1° decreases. Here we see

that as l_1° moves closer to a fixed l_2° i.e. as we change the aspect ratio of bubble A_2 from nearly a triangle to a much thinner pentagon of the same height (see Figure C.6(b)), the system switches, at certain value of $(1-l_1^\circ)/(1-l_2^\circ)$ which is weakly dependent on l_2°, from undergoing a $T1^\phi_{l3,p_b}$ topological transformation to undergoing a $T1^\phi_{c,p_b}$. This is expected since we move from a system in which $\jmath_{20}$ is the shortest edge to a system in which $\jmath_{12}$ is shortest. On the $T1^\phi_{l3,p_b}$ branch, as $(1-l_1^\circ)/(1-l_2^\circ)$ increases, the system becomes more stable, but after switching to $T1^\phi_{c,p_b}$, it becomes less stable again. Hence the maximum possible stability is at the $(1-l_1^\circ)/(1-l_2^\circ)$ value at which the two branches meet.

Note that this maximum allowed $p_{b,T1}$ decreases as l_2° increases, seeming to scale roughly like $1-l_2^\circ$. Hence (by contrast with section C.5.4.1) shrinking the smallest bubble ($\mathcal{B}_2$ in this case), i.e. increasing l_2°, makes the system weaker, not stronger. In Figure C.15(b) we plot a rescaled $p_{b,T1}/(1-l_2^\circ)$ so as to compare more readily the effect of changing l_1°, and therefore $(1-l_1^\circ)/(1-l_2^\circ)$ for various different l_2°. Here we appreciate that as l_2° increases, the value of $(1-l_1^\circ)/(1-l_2^\circ)$ at which the system switch from undergoing a $T1^\phi_{l3,p_b}$ to a $T1^\phi_{c,p_b}$ approaches 0.5. As we have noted, this exhibits a different behaviour from what is seen in section C.5.4.1 in the limit of $l_1^\circ \ll 1$ (and also the simple lens [19]): shrinking the smallest bubbles ($\mathcal{B}_1$ and $\mathcal{B}_3$) made that system more stable. This difference between these scenarios can be explained (see section C.1.4.2 for details) by the very different shape of four-sided bubbles $\mathcal{B}_1$ and $\mathcal{B}_3$ when they are small, versus the five-sided bubble $\mathcal{B}_2$ when it is small. In the former case, the pressures p_1° and p_3° can be large, and films $\jmath_{01}$ and $\jmath_{30}$ turn through very significant amounts, as can films $\jmath_{12}$ and $\jmath_{23}$. In the latter case however, p_2° decreases towards zero, whilst the pressures $p_1^\circ = p_3^\circ$ turn out to approach a finite value $\sqrt{3}/2$. All the films on bubble small $\mathcal{B}_2$, namely $\jmath_{02}$, $\jmath_{12}$, $\jmath_{23}$ and $\jmath_{20}$ then barely turn through any angle whatsoever.

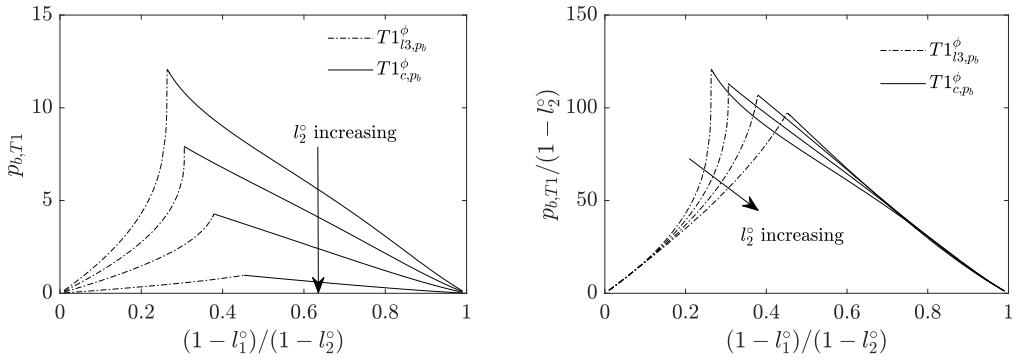

Figure C.15: Imposed back pressure at the topological transformation point $p_{b,T1}$ (which coincides with p_b^*) in the limit of $l_2^\circ \to 1$ and $(1-l_1)^\circ/(1-l_2^\circ) \in (0,1)$. Here we plot for $l_2^\circ \in [0.9, 0.93, 0.96, 0.99]$ (values of l_2° increasing from top to bottom), where the dash-dotted lines show $T1^{\phi}_{l3,p_b}$, and solid lines show $T1^{\phi}_{c,p_b}$ topological transformations.

C.5.4.3 $l_2^\circ \to 0$ limit

In the previous section we looked at $p_{b,T1}$ values in a situation in which bubbles $\mathcal{B}_1$ and $\mathcal{B}_3$ were made comparatively large by taking the limit $l_1^\circ \to 1$. Now we consider a situation in which bubble $\mathcal{B}_2$ is made comparatively large by setting $l_2^\circ \to 0$, as already introduced in section C.1.4.3. However, for the purpose of numerical computations, since film $\jmath_{13}$ cannot be shorter than the minimum established in the numerical method, i.e. less than 10^{-6} (see section 5.4.6 in Chapter 5). Hence we set $l_2^\circ = 0.0001$ and vary $l_1^\circ \in [0.01, 0.99]$, determining $p_{b,T1}$ in each case. This is what Figure C.16 shows. Here we can see that for small l_1° values, the system undergoes $T1^{\phi}_{u,p_b}$, consistently with what is shown in section C.5.4.1. Recall that this happens since, when both l_1° and l_2°/l_1° are small, vertex V_3 is far over towards the right of bubble $\mathcal{B}_3$, making it easy for the vertex and bubble to slip apart as the three-bubble structure moves. As l_1° increases the system eventually starts to undergo $T1^{\phi}_{u,\delta\phi_{30}}$, and then switches to $T1^{\phi}_{l1,\delta\phi_{02}}$. In these cases the lower down lines on Figure C.16 show $p_{b,T1}$, while the higher up lines show p_b^*. Finally as $l_1^\circ \to 1$, the system undergoes $T1^{\phi}_{l3,p_b}$. This was also seen in section

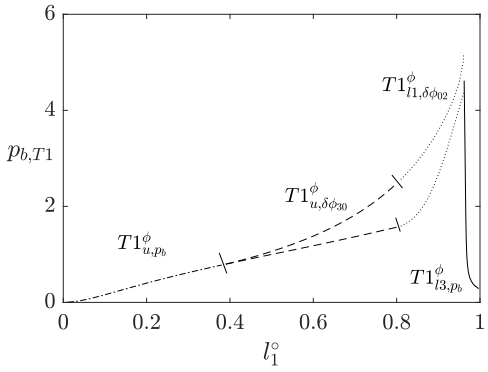

Figure C.16: $p_{b,T1}$ (and where relevant p_b^*, upper line) vs l_1° for a fixed small $l_2^\circ = 0.0001$.

C.5.4.2, but since the values of l_2° there were close to l_1° (rather than $l_2^\circ \ll 1$ as considered here), the observed transition was from $T1^\circ_{c,p_b}$ to $T1^{\phi}_{l3,p_b}$.

Bibliography

[1] D. Weaire and R. Phelan, "The physics of foam," *Journal of Physics: Condensed Matter*, vol. 8, no. 47, pp. 9519–9524, 1996.

[2] I. Cantat, S. Cohen-Addad, F. Elias, F. Graner, R. Höhler, O. Pitois, F. Rouyer, and A. Saint-Jalmes, *Foams: Structure and Dynamics*. OUP Oxford, 2013.

[3] P. Stevenson, *Foam Engineering: Fundamentals and Applications*. John Wiley & Sons, 2012.

[4] S. A. Jones, B. Dollet, Y. Méheust, S. J. Cox, and I. Cantat, "Structure-dependent mobility of a dry aqueous foam flowing along two parallel channels," *Physics of Fluids*, vol. 25, no. 6, p. 63101, 2013.

[5] D. Weaire and S. Hutzler, *The Physics of Foams*. New York: Oxford University Press Inc., 1999. [Online]. Available: http://books.google.co.uk/books?id=VxXwAAAAMAAJ

[6] D. Exerowa and P. M. Kruglyakov, Eds., *Chapter 7 - Foam Stability and the Stabilising Ability of Surfactants*, ser. Studies in Interface Science. Elsevier, 1998, vol. 5, pp. 502–570. [Online]. Available: http://www.sciencedirect.com/science/article/pii/S1383730398800100

[7] C. T. Nguyen, H. M. Gonnermann, Y. Chen, C. Huber, A. A. Maiorano, A. Gouldstone, and J. Dufek, "Film drainage and the lifetime of bubbles," *Geochemistry Geophysics Geosystems*, vol. 14, no. 9, pp. 3616–3631, 2013.

[8] R. V. Craster and O. K. Matar, "Dynamics and stability of thin liquid films," *Reviews of Modern Physics*, vol. 81, no. 3, pp. 1131–1198, 2009.

[9] R. Höhler and S. Cohen-Addad, "Rheology of liquid foam," *Journal of Physics: Condensed Matter*, vol. 17, no. 41, p. R1041, 2005.

[10] M. J. Rosen and J. T. Kunjappu, *Surfactants and interfacial phenomena*. John Wiley & Sons, 2012.

[11] L. L. Schramm, *Surfactants: fundamentals and applications in the petroleum industry*. Cambridge University Press, 2000.

[12] K. Ma, G. Ren, K. Mateen, D. Morel, and P. Cordelier, "Modeling techniques for foam flow in porous media," *SPE Journal*, vol. 20, pp. 453–470, 2015, doi.org/10.2118/169104-PA. [Online]. Available: https://doi.org/10.2118/169104-PA

[13] R. J. Pugh, "Foaming, foam films, antifoaming and defoaming," *Advances in Colloid and Interface Science*, vol. 64, pp. 67–142, 1996.

[14] B. Embley and P. Grassia, "Viscous froth simulations with surfactant mass transfer and Marangoni effects: Deviations from Plateau's rules," *Colloids and Surfaces A: Physicochemical and Engineering Aspects*, vol. 382, no. 1, pp. 8–18, 2011, a collection of papers from the 8th EUFOAM Conference and the Meetings of COST Actions D43 and P21. [Online]. Available: http://www.sciencedirect.com/science/article/pii/S0927775711000392

[15] D. Vitasari, S. Cox, P. Grassia, and R. Rosario, "Effect of surfactant redistribution on the flow and stability of foam films," *Proceedings*

of the Royal Society A: Mathematical, Physical and Engineering Sciences, vol. 476, no. 2234, p. 20190637, 2020. [Online]. Available: https://royalsocietypublishing.org/doi/abs/10.1098/rspa.2019.0637

[16] J. E. Taylor, "The structure of singularities in soap-bubble-like and soap-film-like minimal surfaces," *Annals of Mathematics*, pp. 489–539, 1976.

[17] F. Morgan, "Mathematicians, including undergraduates, look at soap bubbles," *The American Mathematical Monthly*, vol. 101, no. 4, pp. 343–351, 1994. [Online]. Available: https://doi.org/10.1080/00029890.1994.11996953

[18] S. Cohen-Addad, R. Höhler, and O. Pitois, "Flow in foams and flowing foams," *Annual Review of Fluid Mechanics*, vol. 45, no. 45, pp. 241–267, 2013.

[19] T. E. Green, A. Bramley, L. Lue, and P. Grassia, "Viscous froth lens," *Physical Review E*, vol. 74, no. 5, p. 051403, 2006.

[20] P. Grassia, G. Montes-Atenas, L. Lue, and T. E. Green, "A foam film propagating in a confined geometry: analysis via the viscous froth model," *The European Physical Journal E*, vol. 25, no. 1, pp. 39–49, 2008.

[21] N. Kern, D. Weaire, A. Martin, S. Hutzler, and S. J. Cox, "Two-dimensional viscous froth model for foam dynamics," *Physical Review E*, vol. 70, no. 4, p. 041411, 2004.

[22] D. Vitasari, P. Grassia, and P. Martin, "Surfactant transport onto a foam lamella," *Chemical Engineering Science*, vol. 102, pp. 405–423, 2013. [Online]. Available: http://www.sciencedirect.com/science/article/pii/S0009250913005848

[23] D. Vitasari and S. Cox, "A viscous froth model adapted to wet foams," *Colloids and Surfaces A: Physicochemical and Engineering Aspects*, vol. 534, pp. 8–15, 2017.

[24] S. Cox, D. Weaire, and J. A. Glazier, "The rheology of two-dimensional foams," *Rheologica Acta*, vol. 43, no. 5, pp. 442–448, 2004.

[25] W. Drenckhan and S. Hutzler, "Structure and energy of liquid foams." *Advances in Colloid and Interface Science*, vol. 224, pp. 1–16, 2015.

[26] S. A. Koehler, H. A. Stone, M. P. Brenner, and J. Eggers, "Dynamics of foam drainage," *Phys. Rev. E*, vol. 58, pp. 2097–2106, Aug 1998. [Online]. Available: https://link.aps.org/doi/10.1103/PhysRevE.58.2097

[27] E. Rio, W. Drenckhan, A. Salonen, and D. Langevin, "Unusually stable liquid foams," *Advances in Colloid and Interface Science*, vol. 205, pp. 74–86, 2014, Special Issue in honor of Bjorn Lindman. [Online]. Available: http://www.sciencedirect.com/science/article/pii/S0001868613001383

[28] A. S. Aronson, V. Bergeron, M. E. Fagan, and C. J. Radke, "The influence of disjoining pressure on foam stability and flow in porous media," *Colloids and Surfaces A: Physicochemical and Engineering Aspects*, vol. 83, no. 2, pp. 109–120, 1994. [Online]. Available: http://www.sciencedirect.com/science/article/pii/0927775794800944

[29] Z. I. Khatib, G. J. Hirasaki, and A. H. Falls, "Effects of capillary pressure on coalescence and phase mobilities in foams flowing through porous media," *SPE Reservoir Engineering*, vol. 3, no. 03, pp. 919–926, 1988, https://doi.org/10.2118/15442-PA.

[30] J. Von Neumann, "Metal interfaces," *American Society for Metals, Cleveland*, vol. 108, 1952.

[31] S. Cox, "A viscous froth model for dry foams in the surface evolver," *Colloids and Surfaces A: Physicochemical and Engineering Aspects*, vol. 263, no. 1, pp. 81–89, 2005. [Online]. Available: https://www.sciencedirect.com/science/article/pii/S0927775704010210

[32] W. Drenckhan, S. J. Cox, G. Delaney, H. Holste, D. Weaire, and N. Kern, "Rheology of ordered foams: on the way to discrete microfluidics," *Colloids and Surfaces A: Physicochemical and Engineering Aspects*, vol. 263, no. 1-3, pp. 52–64, 2005.

[33] T. E. Green, P. Grassia, L. Lue, and B. Embley, "Viscous froth model for a bubble staircase structure under rapid applied shear: An analysis of fast flowing foam," *Colloids and Surfaces A: Physicochemical and Engineering Aspects*, vol. 348, no. 1–3, pp. 49–58, 2009.

[34] D. Weaire, "The rheology of foam," *Current Opinion in Colloid and Interface Science*, vol. 13, no. 3, pp. 171–176, 2008. [Online]. Available: http://www.sciencedirect.com/science/article/pii/S1359029407001562

[35] M. Durand and H. A. Stone, "Relaxation time of the topological $T1$ process in a two-dimensional foam," *Physical Review Letters*, vol. 97, p. 226101, 2006. [Online]. Available: https://link.aps.org/doi/10.1103/PhysRevLett.97.226101

[36] W. R. Rossen, "Foams in enhanced oil recovery," in *Foams: Theory, Measurements and Applications*, ser. Surfactant Science Series, R. K. Prud'homme and S. A. Khan, Eds. New York: Marcel Dekker, 1996, ch. 2, pp. 99–187.

[37] A. Agarwal, W. J. Ng, and Y. Liu, "Principle and applications of microbubble and nanobubble technology for water treatment," *Chemosphere*, vol. 84, no. 9, pp. 1175–1180, 2011.

[38] M. M. Kotb, H. K. Shakiban, and A. F. Sawaby, "Foam treatment for varicose veins; efficacy and safety," *Alexandria Journal of Medicine*, vol. 49, no. 3, pp. 249–253, 2013. [Online]. Available: https://doi.org/10.1016/j.ajme.2012.11.003

[39] B. Burghoff, "Foam fractionation applications," *Journal of Biotechnology*, vol. 161, no. 2, pp. 126–137, 2012.

[40] R. Lemlich, "Adsorptive bubble separation methods—foam fractionation and allied techniques," *Industrial & Engineering Chemistry*, vol. 60, no. 10, pp. 16–29, 1968.

[41] R. A. Leonard and R. Lemlich, "A study of interstitial liquid flow in foam. part I. theoretical model and application to foam fractionation," *AICHE Journal*, vol. 11, no. 1, pp. 18–25, 1965.

[42] S. R. Rao, *Surface chemistry of froth flotation: Volume 1: Fundamentals*. Springer Science & Business Media, 2013.

[43] M. C. Fuerstenau, G. J. Jameson, and R.-H. Yoon, *Froth flotation: a century of innovation*. SME, 2007.

[44] B. J. Shean and J. J. Cilliers, "A review of froth flotation control," *International Journal of Mineral Processing*, vol. 100, no. 3–4, pp. 57–71, 2011.

[45] N. Barbian, E. Ventura-Medina, and J. Cilliers, "Dynamic froth stability in froth flotation," *Minerals Engineering*, vol. 16, no. 11, pp. 1111–1116, 2003.

[46] A. Madani, S. Zeinoddini, S. Varahmi, H. Turnbull, A. B. Phillion, J. Olson, and D. M. Martinez, "Ultra-lightweight paper foams: processing and properties," *Cellulose*, vol. 21, no. 3, pp. 2023–2031, 2014.

[47] T. Lappalainen and J. Lehmonen, "Paper physics: Determinations of bubble size distribution of foam-fibre mixture using circular Hough transform," *Nordic Pulp and Paper Research Journal*, vol. 27, no. 5, pp. 930–939, 2012. [Online]. Available: https://www.degruyter.com/view/journals/npprj/27/5/article-p930.xml

[48] C. O. Au and I. Thorn, *Applications of wet-end paper chemistry*. Springer Science & Business Media, 2013.

[49] A. Hajimohammadi, T. Ngo, and P. Mendis, "Enhancing the strength of pre-made foams for foam concrete applications," *Cement and Concrete Composites*, vol. 87, pp. 164–171, 2018. [Online]. Available: http://www.sciencedirect.com/science/article/pii/S0958946517307758

[50] R. C. R. Figueredo and E. Sabadini, "Firefighting foam stability: the effect of the drag reducer poly(ethylene) oxide," *Colloids and Surfaces A: Physicochemical and Engineering Aspects*, vol. 215, no. 1, pp. 77–86, 2003. [Online]. Available: http://www.sciencedirect.com/science/article/pii/S0927775702004259

[51] B. Y. Lattimer and J. Trelles, "Foam spread over a liquid pool," *Fire Safety Journal*, vol. 42, no. 4, pp. 249–264, 2007.

[52] S. Kobielak and Z. Zamiar, "Oval concrete domes," *Archives of Civil and Mechanical Engineering*, vol. 17, pp. 486–501, 2017.

[53] N. Senses, "Foam structures: A comparative structural efficiency analysis based on the building case "watercube"," MSc thesis, TU Wien, 2007.

[54] A. K. Asghari, I. Norton, T. Mills, P. Sadd, and F. Spyropoulos, "Interfacial and foaming characterisation of mixed protein-starch particle systems for food-foam applications," *Food Hydrocolloids*, vol. 53, pp. 311–319, 2016,

Functional Hydrocolloids: A Key to Human Health. [Online]. Available: http://www.sciencedirect.com/science/article/pii/S0268005X15300825

[55] A. D. Rudin, "Measurement of the foam stability of beers," *Journal of the Institute of Brewing*, vol. 63, no. 6, pp. 506–509, 1957. [Online]. Available: https://onlinelibrary.wiley.com/doi/abs/10.1002/j.2050-0416.1957.tb06291.x

[56] A. Ellis and A. Lazidis, "Foams for food applications," in *Polymers for Food Applications*. Springer, 2018, pp. 271–327.

[57] M. Elsayed, J. Huang, and M. Edirisinghe, "Bioinspired preparation of alginate nanoparticles using microbubble bursting," *Materials Science and Engineering: C*, vol. 46, pp. 132–139, 2015.

[58] R. Ran, Q. Sun, T. Baby, D. Wibowo, A. P. J. Middelberg, and C.-X. Zhao, "Multiphase microfluidic synthesis of micro- and nanostructures for pharmaceutical applications," *Chemical Engineering Science*, vol. 169, pp. 78–96, 2017.

[59] M. X. Tan and K. P. Hapgood, "Mapping of regimes for the key processes in wet granulation: Foam vs. spray," *AIChE Journal*, vol. 59, no. 7, pp. 2328–2338, 2013. [Online]. Available: https://aiche.onlinelibrary.wiley.com/doi/abs/10.1002/aic.14024

[60] N. Shadid, R. Ceulen, P. Nelemans, C. Dirksen, J. Veraart, G. W. Schurink, P. van Neer, J. vd Kley, E. de Haan, and A. Sommer, "Randomized clinical trial of ultrasound-guided foam sclerotherapy versus surgery for the incompetent great saphenous vein," *BJS (British Journal of Surgery)*, vol. 99, no. 8, pp. 1062–1070, 2012. [Online]. Available: https://bjssjournals.onlinelibrary.wiley.com/doi/abs/10.1002/bjs.8781

[61] J. Rodríguez-Rodríguez, A. Sevilla, C. Martínez-Bazán, and J. M. Gordillo, "Generation of microbubbles with applications to industry and medicine," *Annual Review of Fluid Mechanics*, vol. 47, no. 1, pp. 405–429, 2015.

[62] E. C. Unger, T. Porter, W. Culp, R. Labell, T. Matsunaga, and R. Zutshi, "Therapeutic applications of lipid-coated microbubbles," *Advanced Drug Delivery Reviews*, vol. 56, no. 9, pp. 1291–1314, 2004.

[63] S. Wang and C. N. Mulligan, "An evaluation of surfactant foam technology in remediation of contaminated soil," *Chemosphere*, vol. 57, no. 9, pp. 1079–1089, 2004.

[64] D. Shan and W. R. Rossen, "Optimal injection strategies for foam IOR," *SPE Journal*, vol. 9, no. 02, pp. 132–150, 2004, https://doi.org/10.2118/75180-MS.

[65] B. Géraud, S. A. Jones, I. Cantat, B. Dollet, and Y. Méheust, "The flow of a foam in a two-dimensional porous medium," *Water Resources Research*, vol. 52, no. 2, pp. 773–790, 2016. [Online]. Available: https://doi.org/10.1002/2015WR017936

[66] X. Shen, L. Zhao, Y. Ding, B. Liu, H. Zeng, L. Zhong, and X. Li, "Foam, a promising vehicle to deliver nanoparticles for vadose zone remediation," *Journal of Hazardous Materials*, vol. 186, pp. 1773–1780, 2011. [Online]. Available: https://doi.org/10.1016/j.jhazmat.2010.12.071

[67] L. Zhong, J. E. Szecsody, F. Zhang, and S. V. Mattigod, "Foam delivery of amendments for vadose zone remediation: propagation performance in unsaturated sediments." *Vadose Zone Journal*, vol. 9, no. 3, pp. 757–767, 2010. [Online]. Available: https://doi.org/10.2136/vzj2010.0007

[68] W. Rossen and Z. Zhou, "Modeling foam mobility at the limiting capillary pressure," *SPE Adv. Technol*, vol. 3, no. 1, pp. 146–153, 1995.

[69] R. Farajzadeh, A. Andrianov, R. Krastev, G. J. Hirasaki, and W. R. Rossen, "Foam–oil interaction in porous media: Implications for foam assisted enhanced oil recovery," *Advances in Colloid and Interface Science*, vol. 183-184, pp. 1–13, 2012, https://doi.org/10.1016/j.cis.2012.07.002. [Online]. Available: http://www.sciencedirect.com/science/article/pii/S0001868612001121

[70] R. M. de Velde Harsenhorst, A. S. Dharma, A. Andrianov, and W. R. Rossen, "Extension of a simple model for vertical sweep in foam SAG displacements," *SPE Reservoir Evaluation & Engineering*, vol. 17, no. 03, pp. 373–383, 2014. [Online]. Available: https://doi.org/10.2118/164891-PA

[71] R. Farajzadeh, H. Bertin, and W. R. Rossen, "Editorial to the special issue: foam in porous media for petroleum and environmental engineering—experience sharing," *Transport in Porous Media*, vol. 131, no. 1, pp. 1–3, 2020.

[72] J. Gong, S. Vincent-Bonnieu, R. K. Bahrim, C. C. Mamat, J. Groenenboom, R. Farajzadeh, and W. Rossen, "Laboratory investigation of liquid injectivity in surfactant-alternating-gas foam enhanced oil recovery," *Transport in Porous Media*, vol. 131, no. 1, pp. 85–99, 2020.

[73] A. Skauge, J. Solbakken, P. A. Ormehaug, and M. G. Aarra, "Foam generation, propagation and stability in porous medium," *Transport in Porous Media*, vol. 131, no. 1, pp. 5–21, 2020.

[74] C. Boeije, C. Portois, M. Schmutz, and O. Atteia, "Tracking a foam front in a 3d, heterogeneous porous medium," *Transport in Porous Media*, vol. 131, no. 1, pp. 23–42, 2020.

[75] S. Thomas, "Enhanced oil recovery: an overview," *Oil & Gas Science and Technology-Revue de l'IFP*, vol. 63, no. 1, pp. 9–19, 2008.

[76] E. Ashoori, T. van der Heijden, and W. Rossen, "Fractional-flow theory of foam displacements with oil," *SPE Journal*, vol. 15, no. 02, pp. 260–273, 2010.

[77] W. R. Rossen, S. C. Zeilinger, J. X. Shi, and M. T. Lim, "Simplified mechanistic simulation of foam processes in porous media," *SPE Journal*, vol. 4, no. 03, pp. 279–287, 1999.

[78] Y. Kawagoe, T. Oshima, K. Tomarikawa, T. Tokumasu, T. Koido, and S. Yonemura, "A study on pressure-driven gas transport in porous media: from nanoscale to microscale," *Microfluidics and Nanofluidics*, vol. 20, no. 12, pp. 1–18, 2016.

[79] L. Cheng, A. Reme, D. Shan, D. Coombe, and W. Rossen, "Simulating foam processes at high and low foam qualities," ser. SPE Improved Oil Recovery Conference, 04 2000. [Online]. Available: https://doi.org/10.2118/59287-MS

[80] P. Grassia, E. Mas-Hernández, N. Shokri, S. J. Cox, G. Mishuris, and W. R. Rossen, "Analysis of a model for foam improved oil recovery," *Journal of Fluid Mechanics*, vol. 751, pp. 346–405, 2014, https://doi.org/10.1017/jfm.2014.287.

[81] S. I. Chou, "Percolation theory of foam in porous media," in *SPE/DOE Enhanced Oil Recovery Symposium*. Society of Petroleum Engineers, 1990.

[82] M. N. Zanganeh, S. I. Kam, T. LaForce, and W. R. Rossen, "The method of characteristics applied to oil displacement by foam," *SPE Journal*, vol. 16, no. 01, pp. 8–23, 2011.

[83] M. Eneotu and P. Grassia, "Modelling foam improved oil recovery: towards a formulation of pressure-driven growth with flow reversal," *Proceedings of the Royal Society A: Mathematical, Physical and Engineering Sciences*, vol. 476, no. 2244, p. 20200573, 2020. [Online]. Available: https://royalsocietypublishing.org/doi/abs/10.1098/rspa.2020.0573

[84] John Wiley and Sons, "Oil demand and stocks," *Oil and Energy Trends*, vol. 45, no. 10, pp. 29–37, 2020. [Online]. Available: https://onlinelibrary.wiley.com/doi/abs/10.1111/oet.8_12669

[85] L. W. Lake, *Enhanced oil recovery.* Prentice Hall, Englewood Cliffs, NJ, 1989.

[86] D. W. Green and G. P. Willhite, *Enhanced Oil Recovery.* Richardson, TX: Henry L. Doherty Memorial Fund of AIME, Society of Petroleum Engineers, 1998, vol. 6.

[87] E. Tzimas, A. Georgakaki, C. G. Cortes, and S. D. Peteves, "Enhanced oil recovery using carbon dioxide in the European energy system," *Report EUR*, vol. 21895, no. 6, 2005.

[88] J. Salager, "Recuperación mejorada del petróleo," *ULA.[S357-C]*, 2005.

[89] G. Hirasaki and J. Lawson, "Mechanisms of foam flow in porous media: Apparent viscosity in smooth capillaries," *SPE Journal*, vol. 25, pp. 176–190, 04 1985, https://doi.org/10.2118/12129-PA.

[90] K. Ma, K. Mateen, G. Ren, H. Luo, G. Bourdarot, and D. Morel, "Mechanistic modeling of foam flow through porous media in the presence of oil: Review of foam-oil interactions and an improved bubble population-balance model," *SPE Annual Technical Conference and Exhibition, Dallas, TX, 24th–26th Sep.*, September 2018, https://doi.org/10.2118/191564-MS.

[91] E. Mas-Hernández, P. Grassia, and N. Shokri, "Foam improved oil recovery: Foam front displacement in the presence of slumping," *Colloids and Surfaces A: Physicochemical and Engineering Aspects*, vol. 473, pp. 123–132, 2015. [Online]. Available: https://doi.org/10.1016/j.colsurfa.2014.12.023

[92] A. R. Kovscek, T. W. Patzek, and C. J. Radke, "A mechanistic population balance model for transient and steady-state foam flow in Boise sandstone," *Chemical Engineering Science*, vol. 50, no. 23, pp. 3783–3799, 1995, https://doi.org/10.1023/A:1010740811277.

[93] A. H. Falls, G. J. Hirasaki, T. W. Patzek, D. A. Gauglitz, D. D. Miller, and T. Ratulowski, "Development of a mechanistic foam simulator: The population balance and generation by snap-off," *SPE Reservoir Engineering*, vol. 3, no. 03, pp. 884–892, 1988, https://doi.org/10.2118/14961-PA.

[94] R. F. Li, W. Yan, S. Liu, G. Hirasaki, and C. A. Miller, "Foam mobility control for surfactant enhanced oil recovery," *SPE Journal*, vol. 15, no. 04, pp. 928–942, 2010.

[95] A. Bera, K. Ojha, and A. Mandal, "Synergistic effect of mixed surfactant systems on foam behavior and surface tension," *Journal of Surfactants and Detergents*, vol. 16, no. 4, pp. 621–630, 2013, https://doi.org/10.1007/s11743-012-1422-4. [Online]. Available: https://aocs.onlinelibrary.wiley.com/doi/abs/10.1007/s11743-012-1422-4

[96] K. Osei-Bonsu, N. Shokri, and P. Grassia, "Fundamental investigation of foam flow in a liquid-filled Hele-Shaw cell," *Journal of Colloid and Interface Science*, vol. 462, pp. 288–296, Jan. 2016, https://doi.org/10.1016/j.jcis.2015.10.017.

[97] S. Kumar and A. Mandal, "Investigation on stabilization of CO_2 foam by ionic and nonionic surfactants in presence of different additives for applica-

tion in enhanced oil recovery," *Applied Surface Science*, vol. 420, pp. 9–20, 2017, https://doi.org/10.1016/j.apsusc.2017.05.126. [Online]. Available: http://www.sciencedirect.com/science/article/pii/S0169433217314496

[98] K. Osei-Bonsu, P. Grassia, and N. Shokri, "Relationship between bulk foam stability, surfactant formulation and oil displacement efficiency in porous media," *Fuel*, vol. 203, pp. 403–410, 2017, https://doi.org/10.1016/j.fuel.2017.04.114. [Online]. Available: http://www.sciencedirect.com/science/article/pii/S0016236117305422

[99] ——, "Investigation of foam flow in a 3D printed porous medium in the presence of oil," *Journal of Colloid and Interface Science*, vol. 490, pp. 850–858, 2017, https://doi.org/10.1016/j.jcis.2016.12.015. [Online]. Available: http://www.sciencedirect.com/science/article/pii/S0021979716310086

[100] A. Fisher, R. Foulser, and S. Goodyear, "Mathematical modeling of foam flooding," ser. SPE Improved Oil Recovery Conference, 04 1990. [Online]. Available: https://doi.org/10.2118/20195-MS

[101] S. E. Buckley and M. C. Leverett, "Mechanism of fluid displacement in sands," *Transactions of the AIME*, vol. 146, no. 01, pp. 107–116, 1942.

[102] Z. Zhou and W. Rossen, "Applying fractional-flow theory to foam processes at the limiting capillary pressure," *SPE Advanced Technology Series*, vol. 3, no. 01, pp. 154–162, 1995.

[103] R. Farajzadeh, M. Lotfollahi, A. Eftekhari, W. Rossen, and G. Hirasaki, "Effect of permeability on implicit-texture foam model parameters and the limiting capillary pressure," *Energy & fuels*, vol. 29, no. 5, pp. 3011–3018, 2015.

[104] P. Grassia, L. Lue, C. Torres-Ulloa, and S. Berres, "Foam front advance during improved oil recovery: Similarity solutions at early times near the top of the front," *Journal of Fluid Mechanics*, vol. 828, pp. 527–572, 2017. [Online]. Available: https://doi.org/10.1017/jfm.2017.541

[105] A. R. Kovscek and H. J. Bertin, "Foam mobility in heterogeneous porous media. I. Scaling concepts," *Transport in Porous Media*, vol. 52, pp. 17–35, 2003, https://doi.org/10.1023/A:1022312225868.

[106] A. R. Kovscek, T. W. Patzek, and C. J. Radke, "Mechanistic foam flow simulation in heterogeneous and multidimensional porous media," *SPE Journal*, vol. 2, pp. 511–526, 1997. [Online]. Available: https://doi.org/10.2118/39102-PA

[107] R. O. Salazar Castillo, S. F. Ter Haar, C. G. Ponners, M. Bos, and W. Rossen, "Fractional-flow theory for non-Newtonian surfactant-alternating-gas foam processes," *Transport in Porous Media*, vol. 131, no. 2, pp. 399–426, 2020, https://doi.org/10.1007/s11242-019-01351-6.

[108] Y. Zeng, A. Muthuswamy, K. Ma, L. Wang, R. Farajzadeh, M. Puerto, S. Vincent-Bonnieu, A. A. Eftekhari, Y. Wang, C. Da, J. C. Joyce, S. L. Biswal, and G. J. Hirasaki, "Insights on foam transport from a texture-implicit local-equilibrium model with an improved parameter estimation algorithm," vol. 55, pp. 7819–7829, 2016, doi.org/10.1021/acs.iecr.6b01424.

[109] C. D. Erle and T. Djebbar, "Applications of Darcy's law," in *Petrophysics - Theory and Practice of Measuring Reservoir Rock and Fluid Transport Properties*, 3rd ed. Elsevier, 2012, pp. 1–2.

[110] S. Whitaker, "Flow in porous media I: A theoretical derivation of Darcy's law," *Transport in Porous Media*, vol. 1, no. 1, pp. 3–25, 1986.

[111] K. Ma, J. L. Lopez-Salinas, M. C. Puerto, C. A. Miller, S. L. Biswal, and G. J. Hirasaki, "Estimation of parameters for the simulation of foam flow through porous media. Part 1: The dry-out effect," *Energy and Fuels*, vol. 27, no. 5, pp. 2363–2375, 2013, https://doi.org/10.1021/ef302036s.

[112] P. Grassia, "Pressure-driven growth in strongly heterogeneous systems," *The European Physical Journal E*, vol. 41:10, no. 1, 2018. [Online]. Available: https://doi.org/10.1140/epje/i2018-11618-7

[113] E. Mas-Hernández, P. Grassia, and N. Shokri, "Modelling foam improved oil recovery within a heterogeneous reservoir," *Colloids and Surfaces A: Physicochemical and Engineering Aspects*, vol. 510, pp. 43–52, 2016. [Online]. Available: https://10.1016/j.colsurfa.2016.07.064

[114] P. Grassia, C. Torres-Ulloa, S. Berres, E. Mas-Hernández, and N. Shokri, "Foam front propagation in anisotropic oil reservoirs," *The European Physical Journal E*, vol. 39:42, no. 4, 2016. [Online]. Available: https://doi.org/10.1140/epje/i2016-16042-5

[115] E. Mas-Hernández, P. Grassia, and N. Shokri, "Foam-improved oil recovery: Modelling the effect of an increase in injection pressure," *The European Physical Journal E*, vol. 38, no. 6, pp. 1–7, 2015.

[116] C. Torres-Ulloa, S. Berres, and P. Grassia, "Foam-liquid front motion in Eulerian coordinates," *Proceedings of the Royal Society A: Mathematical, Physical and Engineering Sciences*, vol. 474, no. 2220, pp. 2018–0290, 2018. [Online]. Available: https://doi.org/10.1098/rspa.2018.0290

[117] C. Torres-Ulloa and P. Grassia, "Breakdown of similarity solutions: a perturbation approach for front propagation during foam-improved oil recovery," *Proceedings of the Royal Society A: Mathematical, Physical and*

Engineering Sciences, vol. 477, no. 2245, p. 20200691, 2021. [Online]. Available: https://royalsocietypublishing.org/doi/abs/10.1098/rspa.2020.0691

[118] J. Atencia and D. J. Beebe, "Controlled microfluidic interfaces," *Nature*, vol. 437, pp. 648–55, 10 2005.

[119] I. Cantat, N. Kern, and R. Delannay, "Dissipation in foam flowing through narrow channels," *EPL*, vol. 65, no. 5, pp. 726–732, 2004.

[120] F. P. Bretherton, "The motion of long bubbles in tubes," *Journal of Fluid Mechanics*, vol. 10, no. 2, pp. 166–188, 1961.

[121] J.-P. Raven, P. Marmottant, and F. Graner, "Dry microfoams: formation and flow in a confined channel," *The European Physical Journal B - Condensed Matter and Complex Systems*, vol. 51, no. 1, pp. 137–143, 2006.

[122] G. F. Christopher and S. L. Anna, "Microfluidic methods for generating continuous droplet streams," *Journal of Physics D: Applied Physics*, vol. 40, no. 19, p. R319, 2007.

[123] C.-H. Yang, K.-S. Huang, and J.-Y. Chang, "Manufacturing monodisperse chitosan microparticles containing ampicillin using a microchannel chip," *Biomedical microdevices*, vol. 9, no. 2, pp. 253–259, 2007.

[124] P. Marmottant and J.-P. Raven, "Microfluidics with foams," *Soft Matter*, vol. 5, pp. 3385–3388, 2009. [Online]. Available: http://dx.doi.org/10.1039/B903276B

[125] P. Grassia, "Motion of an oil droplet through a capillary with charged surfaces," *Journal of Fluid Mechanics*, vol. 866, pp. 721–758, 2019.

[126] S. L. Anna, N. Bontoux, and H. A. Stone, "Formation of dispersions using "flow focusing" in microchannels," *Applied Physics Letters*, vol. 82, no. 3, pp. 364–366, 2003.

[127] P. Garstecki, I. Gitlin, W. DiLuzio, G. M. Whitesides, E. Kumacheva, and H. A. Stone, "Formation of monodisperse bubbles in a microfluidic flow-focusing device," *Applied Physics Letters*, vol. 85, no. 13, pp. 2649–2651, 2004.

[128] P. Garstecki and G. M. Whitesides, "Flowing crystals: nonequilibrium structure of foam," *Physical Review Letters*, vol. 97, no. 2, p. 024503, 2006.

[129] R. Gabbrielli, A. J. Meagher, D. Weaire, K. A. Brakke, and S. Hutzler, "An experimental realization of the weaire–phelan structure in monodisperse liquid foam," *Philosophical Magazine Letters*, vol. 92, no. 1, pp. 1–6, 2012. [Online]. Available: https://doi.org/10.1080/09500839.2011.645898

[130] A. M. Kraynik, "Foam flows," *Annual Review of Fluid Mechanics*, vol. 20, no. 1, pp. 325–357, 1988.

[131] A. M. Kraynik and D. Reinelt, "Foam microrheology: from honeycombs to random foams," in *15th Annual Meeting Polymer Processing Sosiety*, 1999.

[132] T. Okuzono and K. Kawasaki, "Intermittent flow behavior of random foams: a computer experiment on foam rheology," *Physical Review E*, vol. 51, no. 2, p. 1246, 1995.

[133] M. A. Spencer, Z. Jabeen, and D. K. Lubensky, "Vertex stability and topological transitions in vertex models of foams and epithelia," *The European Physical Journal E*, vol. 40, no. 1, pp. 1–17, 2017.

[134] P. S. Stewart and S. H. Davis, "Dynamics and stability of metallic foams: Network modeling," *Journal of Rheology*, vol. 56, no. 3, pp. 543–574, 2012. [Online]. Available: https://doi.org/10.1122/1.3695029

[135] D. J. Durian, "Foam mechanics at the bubble scale," *Phys. Rev. Lett.*, vol. 75, pp. 4780–4783, Dec 1995. [Online]. Available: https://link.aps.org/doi/10.1103/PhysRevLett.75.4780

[136] D. J. Durian, "Bubble-scale model of foam mechanics: Melting, nonlinear behavior, and avalanches," *Physical Review E*, vol. 55, pp. 1739–1751, Feb 1997. [Online]. Available: https://link.aps.org/doi/10.1103/PhysRevE.55.1739

[137] S. A. Langer and A. J. Liu, "Effect of random packing on stress relaxation in foam," *The Journal of Physical Chemistry B*, vol. 101, no. 43, pp. 8667–8671, 1997.

[138] Y. Jiang, "Extended large-Q Potts model simulation of foam drainage," *Philosophical Magazine Letters*, vol. 74, no. 2, pp. 119–128, 1996.

[139] Y. Jiang and J. A. Glazier, "Foam drainage: Extended large-Q Potts model simulation," in *Materials Research Society Symposium Proceedings*, vol. 463. Materials Research Society, 1997, pp. 307–312.

[140] Y. Jiang, P. J. Swart, A. Saxena, M. Asipauskas, and J. A. Glazier, "Hysteresis and avalanches in two-dimensional foam rheology simulations," *Physical Review E*, vol. 59, no. 5, pp. 5819–5832, 1999.

[141] D. Weaire and J. P. Kermode, "Computer simulation of a two-dimensional soap froth ii. Analysis of results," *Philosophical Magazine B*, vol. 50, no. 3, pp. 379–395, 1984.

[142] P. S. Stewart, S. H. Davis, and S. Hilgenfeldt, "Microstructural effects in aqueous foam fracture," *Journal of Fluid Mechanics*, vol. 785, p. 425–461, 2015.

[143] A. Huerre, V. Miralles, and M.-C. Jullien, "Bubbles and foams in microfluidics," *Soft Matter*, vol. 10, no. 36, pp. 6888–6902, 2014.

[144] S. J. Cox, D. Weaire, and G. Mishuris, "The viscous froth model: steady states and the high-velocity limit," *Proceedings of the Royal Society A: Mathematical, Physical and Engineering Sciences*, vol. 465, no. 2108, pp. 2391–2405, 2009.

[145] R. Satomi, P. Grassia, S. Cox, G. Mishuris, and L. Lue, "Diffusion of curvature on a sheared semi-infinite film," *Proceedings of the Royal Society A: Mathematical, Physical and Engineering Sciences*, vol. 469, no. 2159, p. 20130359, 2013.

[146] D. Weaire and S. McMurry, "Some fundamentals of grain growth," *Solid state Physics (New York. 1955)*, vol. 50, pp. 1–36, 1996.

[147] H. Flyvbjerg, "Dynamics of soap froth," *Physica A: Statistical Mechanics and its Applications*, vol. 194, no. 1-4, pp. 298–306, 1993.

[148] D. Weaire and J. A. Glazier, "Modelling grain growth and soap froth coarsening: past, present and future," in *Materials Science Forum*, vol. 94. Trans Tech Publ, 1992, pp. 27–38.

[149] W. W. Mullins, "Two-dimensional motion of idealized grain boundaries," *Journal of Applied Physics*, vol. 27, no. 8, pp. 900–904, 1956.

[150] B. Dollet and C. Bocher, "Flow of foam through a convergent channel," *The European Physical Journal E*, vol. 38, no. 11, pp. 123–123, 2015.

[151] J. A. Sethian, "Fast marching methods," *SIAM Review*, vol. 41, no. 2, pp. 199–235, 1999. [Online]. Available: https://doi.org/10.1137/S0036144598347059

[152] C. Li, C. Xu, C. Gui, and M. D. Fox, "Distance regularized level set evolution and its application to image segmentation," *IEEE Transactions on Image Processing*, vol. 19, no. 12, pp. 3243–3254, 2010. [Online]. Available: https://doi.org/10.1109/TIP.2010.2069690

[153] A. S. Bova, W. E. Mell, and C. M. Hoffman, "A comparison of level set and marker methods for the simulation of wildland fire front propagation," *International Journal of Wildland Fire*, vol. 25, no. 2, pp. 229–241, 2015.

[154] D. Adalsteinsson and J. A. Sethian, "A fast level set method for propagating interfaces," *Journal of Computational Physics*, vol. 118, no. 2, pp. 269–277, 1995. [Online]. Available: https://doi.org/10.1006/jcph.1995.1098

[155] J. A. Boon, C. J. Budd, and G. W. Hunt, "Level set methods for the displacement of layered materials," vol. 463, no. 2082, pp. 1447–1466, 2007. [Online]. Available: https://doi.org/10.1098/rspa.2007.1827

[156] S. Osher and R. Fedkiw, *Level Set Methods and Dynamic Implicit Surfaces*. Springer New York, 2006. [Online]. Available: https://doi.org/10.1007/b98879

[157] S. Osher and J. A. Sethian, "Fronts propagating with curvature-dependent speed: algorithms based on Hamilton-Jacobi formulations," *Journal of Computational Physics*, vol. 79, no. 1, pp. 12–49, 1988. [Online]. Available: https://doi.org/10.1016/0021-9991(88)90002-2

[158] A. Kurganov, S. Noelle, and G. Petrova, "Semidiscrete central-upwind schemes for hyperbolic conservation laws and Hamilton–Jacobi equations," *SIAM Journal on Scientific Computing*, vol. 23, no. 3, pp. 707–740, 2001. [Online]. Available: https://doi.org/10.1137/S1064827500373413

[159] A. Coronel, P. Cumsille, and R. Quezada, "Un método numérico híbrido para capturar los choques en leyes de conservación escalares," *Revista Integración*, vol. 28, no. 2, pp. 111–132, 2010.

[160] D. Peng, B. Merriman, S. Osher, H. Zhao, and M. Kang, "A PDE-based fast local level set method," *Journal of Computational Physics*, vol. 155, no. 2, pp. 410–438, 1999. [Online]. Available: https://doi.org/10.1006/jcph.1999.6345

[161] S. Bidadi and S. L. Rani, "Quantification of numerical diffusivity due to TVD schemes in the advection equation," *Journal of Computational Physics*, vol. 261, pp. 65–82, 2014. [Online]. Available: https://doi.org/10.1016/j.jcp.2013.12.011